Experimental and Computational Explorations of Structure/Catalytic Activity Relationships in Functional Nanocarbons Derived from Polyacrylonitrile Containing Polymers

Submitted in partial fulfillment of the requirements for

The degree of

Doctor of Philosophy

In the subject of

Chemistry

Eric R. Gottlieb

Carnegie Mellon University

Pittsburgh, PA

June 2018

Examining committee:

Advisor: Prof. Tomasz Kowalewski

Advisor: Prof. David Yaron

Prof. Krzysztof Matyjaszewski

External: Prof. Michael Bockstaller

Abstract

Carbons are increasingly important as possible alternatives to expensive metal catalysts owing to the wide range of chemical properties they can exhibit and the growing set of synthetic methods available to produce them. This thesis explores the use of polyacrylonitrile-containing precursors in the controlled synthesis of nanostructured, heteroatom enriched carbons. Using these well-defined carbons, features that affect catalytic activity were determined for a variety of catalytic applications. Computational studies were also used to probe for catalytic active sites, and the electronic and spin properties of carbon systems were explored. The results presented provide insight into how nanostructure and microstructure affect catalytic activity and possible ways in which the electronic properties that lead to catalytic activity might emerge.

Acknowledgements

I would like to thank my friends and family who have been incredibly supportive throughout my time as a PhD student. I also would like to thank Tomek and Dave for being great advisors, pushing me to new intellectual levels, and helping me be successful in my research. Most of all, I want to thank my fiancée, Erica, who has been there to keep me going, even while first across the state and then across an ocean. I am excited that I will have the opportunity to do the same for her over the next few years.

Table of Contents

List of Abbreviations

AC	Activated carbon
AFM	Atomic force microscopy
AN	Acrylonitrile
ATRP	Atom transfer radical polymerization
BA	Butyl Acylate
BE	Binding Energy
BET	Brunauer-Emmett-Teller
BJH	Barett-Joyner-Halenda
CNT	Carbon nanotube
CTNC	Copolymer-templated nitrogen-enriched carbon
CV	Cyclic voltammetry
CVD	Chemical vapor deposition
DLS	Dynamic light scattering
DMF	Dimethylformamide
DMSO	Dimethylsulfoxide
DSC	Differential Scanning Calorimetry
DFT	Density functional theory
DP	Degree of polymerization
FTIR	Fourier transform infrared
GBP	Graphene basal plane
GO	Graphene Oxide
GPC	Gel permeation chromatography
GR	Graphene Ribbon
HDPE	High Density Poly Ethylene
HOMO	Highest Occupied Molecular Orbital
l_p	Porod length of inhomogeneity
LUMO	Lowest unoccupied Molecular Orbital
MW	Molecular Weight
NMR	Nuclear Magnetic Resonance
PAN	Polyacrylonitrile
PBA	Poly(n-butyl acrylate)
PBA-b-PAN	Poly(n-Butyl Acrylate)-block-Polyacrylonitrile
PE	Polyethylene
PEG	Poly(ethylene glycol)
PS	Polystyrene
PSD	Pore size distribution
RAFT	Reversible addition-fragmentation chain-transfer polymerization
ReaxFF	Reactive Force Field
rGO	Reduced Graphene Oxide
SAXS	Small angle X-ray scattering
SCE	Saturated Calomel Electrode

SHE	Standard hydrogen electrode
SEM	Scanning electron microscopy
TEM	Transmission electron microscopy
TGA	Thermogravimetric analysis
WAXS	Wide-Angle X-ray Scattering
WRC	Water reducing catalyst
XPS	X-ray Photoelectron Spectroscopy
XRD	X-ray Diffraction

List of Figures

List of Tables

Chapter 1: Introduction

This thesis consists of multiple papers and early drafts of paper, each with brief preambles to contextualize them with respect to my time as a PhD student and my specific contributions to the works being presented. The introduction is adapted from a "Progress Report" review on using polymers as precursors to catalytically active carbons.

1.1 Introduction

As global energy demand has grown, so has the interest in and importance of alternative energy technologies such as fuel cells. At the center of all alternative energy systems are reversible processes that store or release energy, many of which require a catalyst to drive a redox reaction. While tremendous progress has been made in improving the catalysts for these systems, many of them are still precious-metals. They are currently the most economical materials to use as the active components despite suffering from poor selectivity and durability as well as dramatically increased costs.[1, 2] In recent years, carbon materials have emerged as possible alternatives to precious-metal catalysts with the promise of leading to lower material costs such that wide adoption would be possible.[3-7] To realize this goal, catalytic activity needs to be sufficiently high and the cost of synthesis needs to be sufficiently low to realize this goal. Both of these conditions have yet to be achieved in a single material. To overcome these challenges, there are many facets of metal-free catalysis that still need to be developed. This includes the fundamental principles that lead to metal-free catalytic activity, synthetic tools to produce materials from inexpensive precursors that leverage such principles, and engineering of all these components in the context of a given applied system, like a PEM fuel cell.[8-12]

In this chapter, polymer-based synthetic routes to metal-free carbon catalysts are assessed. Specifically, underlying mechanisms and considerations when forming a carbon

from macromolecules are discussed, such as the stabilization process and polymer microstructure. Then, challenges associated with controlling heteroatom active sites produced from heteroatom containing macromolecular precursors is considered, followed by an assessment of the merits of using polymer/carbon hybrids to make functional carbons with more effective blends of properties. Finally, factors in nanostructuring polymeric precursors and the effects/limitations of different nanostructuring methods is explored.

1.1.1 Background and Current Understanding in Metal-Free Catalysis

The fundamental principles that lead to metal-free catalytic activity are still actively being investigated, but certain features are generally applicable in all of catalysis. For a compound to catalyze a reaction, it has to lower the activation energy required for a reaction to proceed.[13, 14] This can be manifested in many ways, but in the broadest view it involves at least one reactant binding to the catalyst. In the case of energy reactions such as hydrogen evolution, an ideal catalytic site is one with an intermediate bound state that matches the energy of the products and reactants when at thermal equilibrium.[15, 16] In heterogeneous catalysis, another factor is the bulk of the material, which can affect the electronic structure of the active site and how it binds with a reactant. Both features, the bulk's electronic structure and the active sites, are necessary to exhibit catalytic activity (though the details of how these idealized models and real catalysis relate is still being explored).[17] This is why neither pristine graphite nor small molecules have appreciable catalytic activity towards alternative energy reactions.

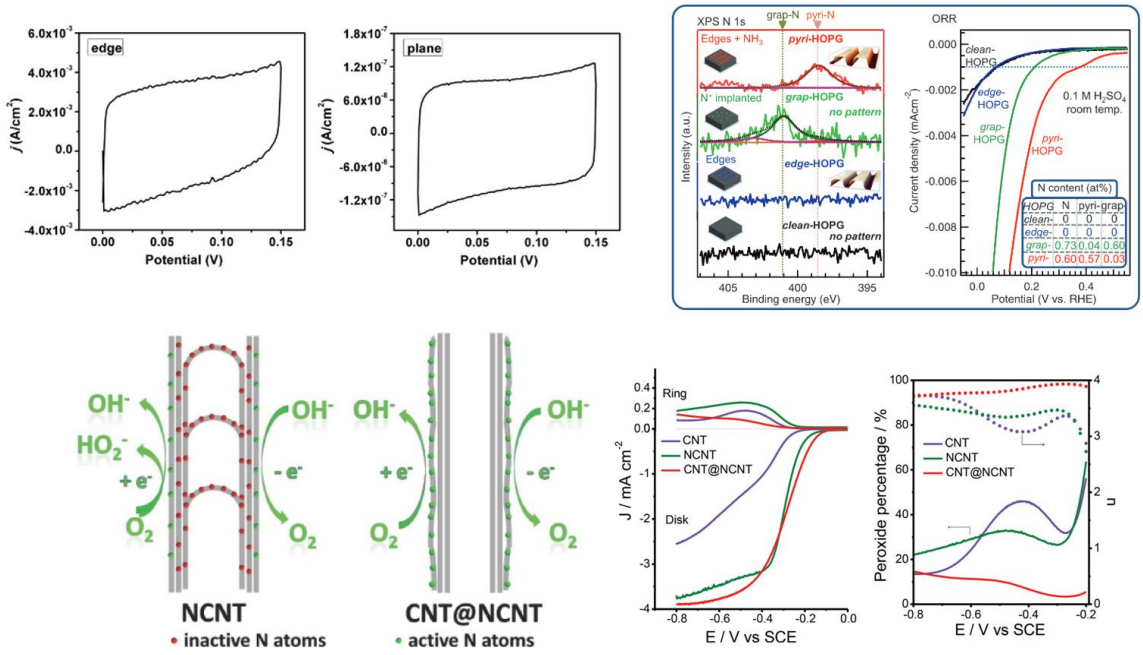

Figure 1.1 Studies of various carefully controlled carbon systems have revealed some of the features that are import for electrocatalytic activity. These features have included carbon edges (top left), pyridinic nitrogens (top right), and preference for heteroatom sites to be exposed while leaving the bulk carbon in unaffected (bottom). Top left) Reproduced with permission.[18] Copyright 2013, Nature Publishing Group. Top right) Reproduced with permission.[19] Copyright 2016, AAAS. Bottom row) Reproduced with permission.[20] Copyright 2014, Wiley-VCH.

To more deeply probe the origins of metal-free catalytic activity, carefully controlled model catalysts are needed. One of the many current challenges with carbon catalysts is the chemical heterogeneity they exhibit, which makes it difficult to determine active sites, tune them for improved performance, or selectively synthesize them within the material. While studies of many different carbon systems have contributed towards determining features of effective metal-free catalysts, the definitive experimental evidence has come from probing electrochemical activity of structurally simple, carefully controlled carbon systems. Through such studies, edges have been identified as being dramatically more electrochemically active than the basal plane, carbons adjacent to pyridinic nitrogens have been identified as the active sites in metal-free ORR, and the importance of retaining the bulk graphitic structure in non-surface sites (**Figure 1.1**). The key takeaways in these

studies then need to be applied to the design of metal-free catalysts that are approached with commercial viability in mind.

1.1.2 Tools for Synthesizing Catalytic Carbons

Currently, targeting certain features in synthesizing a carbon from inexpensive precursors is a difficult task. Commodity activated carbons today primarily come from biomass, especially fibrous sources.[21-24] While cost effective, the resulting carbons also have a high degree of structural and chemical heterogeneity. Furthermore, the mechanisms that drive carbon synthesis are not understood with the degree of nuance necessary to control features that may lead to more efficient catalytic activity.[25, 26] This is where synthetic polymers can provide valuable insight. In contrast to biomass, synthetic polymers have well-defined structures and can yield carbons with relatively well controlled structures and content. Furthermore, there is an immense body of research that already exists on polymer structures, properties, and reactions, providing a foundation for understanding the carbons they produce. In particular, the use of controlled polymerization methods such as atom transfer radical polymerization (ATRP) and reversible addition-fragmentation chain-transfer polymerization (RAFT) enable the synthesis of polymers with controlled degrees of polymerization (DP), low dispersity, and complex but well-defined arrangements and architectures.[27-30] This provides a useful way to investigate the formation of a carbon that more closely reflects the types of carbons that may one day be adopted commercially while retaining more control over the structures being studied.

1.2 Crosslinking and Microstructure of Polymers for Carbonization

In comparison to many of the carbon systems that have been recently developed, graphite does not exhibit significant catalytic activity. In contrast to graphite and other

carbon materials such as carbon fibers from organic molecule or polymers, catalytically active carbons can be thought of as having undergone early stages of graphitization, *e.g.* are partially graphitic, because they need to have an abundance of defect sites, heteroatoms, and edge states.[31, 32] The more graphitized a carbon is, the fewer features it retains from its precursor, such as pore structure, edge states and heteroatom content.[33-35] There is a wealth of research regarding more complete graphitization from a range of precursors because of their use as sorbents,[36-38] separation membranes,[39] catalyst support,[40, 41] electrodes,[42-44] and mechanically robust fibers.[45-47] These works can be drawn upon and applied to partial graphitization for catalysis, but the scopes mean that factors of importance to catalysis are often left out. In contrast to these applications, it could be said that there is more emphasis on the starting materials and their features, because the goal is to produce a carbon that retains certain components of that precursor like heteroatom content.

Polymers used as precursors for carbons typically contain unsaturated bonds and heteroatoms that provide thermally susceptible groups to react and produce a carbon.[24, 48, 49] With that said, almost any polymer can be used to synthesize a carbon given the right conditions or pretreatments. The formation of a graphitic carbon can be thought of as a controlled degradation process. Some polymers have a propensity for thermally decomposing into a carbon, while other polymers normally degrade into gaseous small molecules but can be "coaxed" to form a carbon instead.[50-53] For example, polyethylene (PE) lacks clear reactive pathways to crosslink and form aromatic rings and thus mostly gasifies if thermally treated.[50, 53-55] Despite this, PE has been successfully made into a carbon through a variety of harsh conditions, such as hot sulfuric acid, room temperature

chlorosulphonic acid, or high pressure.[56, 57] Even polymers with chemical groups that make them susceptible to thermal decomposition, such as by having oxygen in the backbone of the polymer can be made into a carbon. Poly(ethylene glycol) (PEG) has been successfully used as a precursor for carbon nanotubes (CNTs) by CoO_x nanoparticle catalyzed growth.

Precursors that more easily form carbons undergo a stabilization step (*e.g.* crosslinking) that can occur thermally, chemically, or by some combination of the two, before reaching pyrolytic temperatures.[58, 59] Without this step, the polymer will either depolymerize or decompose into gaseous compounds. In the case of polyacrylonitrile (PAN), thermal oxidation under air leads to crosslinks and ladder polymers that can fuse under subsequent pyrolytic treatment. These stabilization reactions in many ways determine how effective a polymer will be at becoming a carbon.[60-63]

1.2.1 Computational Studies of Polymer Pyrolysis

The early reactions that occur over the course of the thermal treatment of a polymer can dramatically affect how the polymer as a whole degrades and the yield of pyrolysis. Computationally, this has been studied by assessing mechanisms of carbonization in polymers by Reactive Force Field (ReaxFF) molecular dynamics simulations because the method uses bond order in calculating the potential, resulting in a smooth transition over bond dissociation and formation. PAN,[64, 65] polyimide,[66, 67] polycarbonate,[68] phenolic resin,[69] and high-density polyethylene (HDPE)[70] have all been studied by such means at different stages in their pyrolytic process. These studies provide valuable insights into chemical features that affect the carbonization process. For instance, while both polycarbonate and polyimide both have oxygen in their backbones and in fact show

bond breaking of the backbone at high temperatures, [66-68] polyimide is still successfully used as a carbon precursor.[71, 72] The carbonization of polyimide, as opposed to degradation to small molecules, was in shown using ReaxFF under constant mass, volume, and temperature with high pressures (**Figure 1.2**).[67] Under these conditions, Dong *et.al.* showed that bond cleavage at heteroatom sites leave the radical heteroatoms attached to the main structure, which subsequently undergo cyclization reactions, fusing the system together.

These patterns, small molecule formation with heteroatoms and subsequent crosslinking from by the groups left behind, hold in other systems such as phenolic resin carbonization.[69] In some cases, these studies reveal pathways to small molecule formation and crosslinking that have yet to be found by other means. Understanding underlying mechanisms of crosslinking is important to rationally designing carbons and effectively modifying them to improve their carbonization behavior.

1.2.2 Crosslinking Methods

Crosslinking is the first step in carbonization, occurring at milder conditions to direct the system to carbonize as opposed to break down into small molecules. There are many different ways to crosslink a polymer, and the types that can be employed for a polymer will depend heavily on the chemical moieties present in the system. Crosslinking can proceed without any other components, as is the case with UV crosslinking[73, 74] or gamma crosslinking,[73, 75] but in most cases, crosslinking requires the use of some kind of additive. Crosslinkers can be incorporated into the system, as is typically the case with oxygen in thermal oxidative stabilization,[61, 76-79] carbonyls,[55] or resol,[80] but do not necessarily have to be. There are also cases where crosslinking occurs because of an

additive that acts as a sacrificial component, with a catalyst, or a reactant that does not necessarily get incorporated into the system, such as using iodine doping,[81-83] acid-catalyzation,[84] or $FeCl_3$ crosslinking.[85-87]

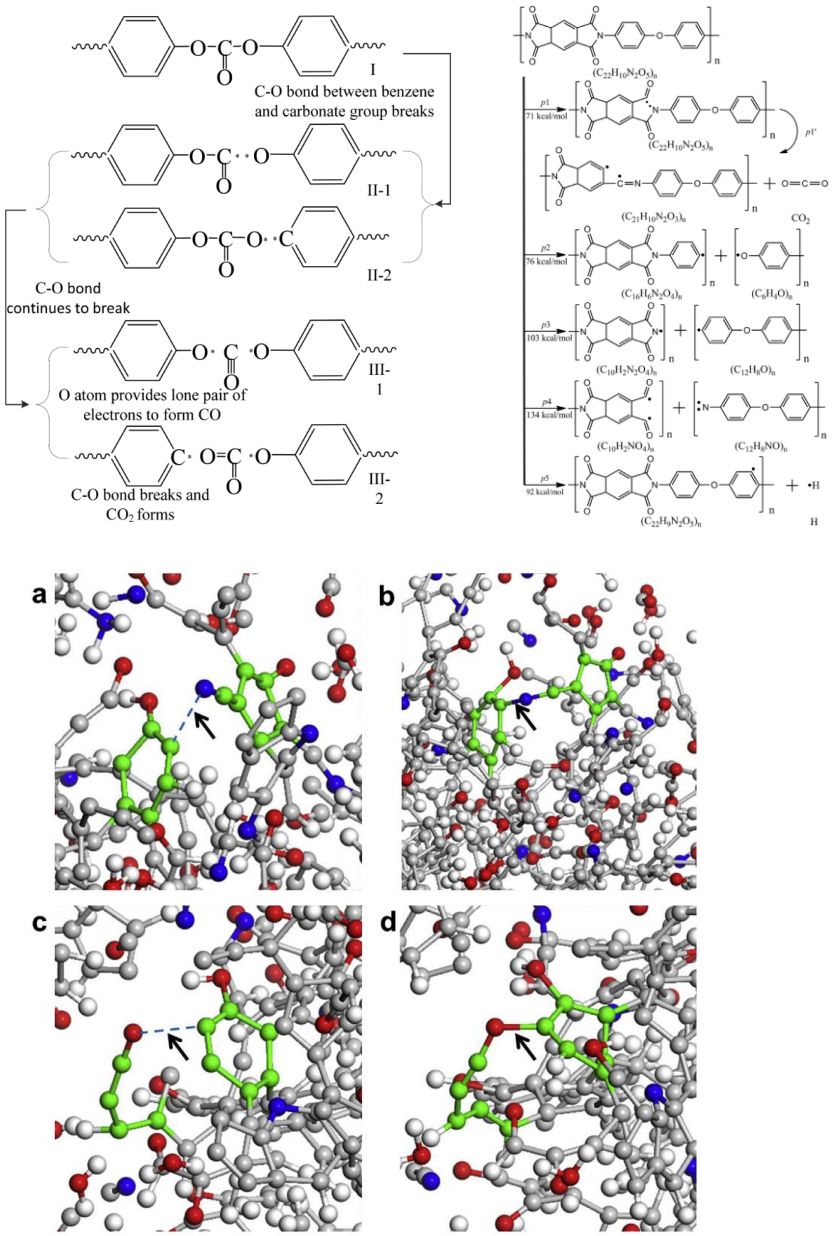

Figure 1.2 Initial pyrolysis mechanisms for polycarbonate (top left) and polyimide (top right) by ReaxFF. Despite both polymers showing backbone breakage as a primary reaction occurring at elevated temperatures, polyimide is still successfully used as a carbon precursor. This has been shown to be because of heteroatoms remaining as components of the monomer, after which they crosslink with other nearby polyimides, forming a fused structure (bottom set). Top left) Reproduced with permission.[68] Copyright 2018, American Chemical Society. Top right) Reproduced with permission.[66] Copyright 2015, Elsevier. Bottom set) Reproduced with permission.[67] Copyright 2016, Elsevier.

The method and conditions used for stabilization has a dramatic effect on the resulting carbon, from percent yields, to heteroatom content, and nano/micro structure. The polymer composition also directly affects the types and efficacy of crosslinking methods that can be used. Furthermore, polymer composition can be modified to enhance the crosslinking process — a common approach for carbon fiber synthesis from PAN.[88] The use of small quantities of a comonomer such as itaconic acid for the polymerization has been shown to reduce the temperature necessary to initiate cyclization of PAN during thermal oxidative stabilization.[89] The small amounts of itaconic acid from other chains act as initiators that catalyze the cyclization process at lower temperatures (**Figure 1.3**).[90] This is important for soft templating, where entropy can overcome the interactions that induce nanostructuring, leading to a loss of nanostructure (discussed in more detail in a later section).

Modifications or additives to polymeric precursors can be effective in improving the polymer's effectiveness in carbonization.[91] Unmodified polyacetylene has a very low carbonization yield, producing many small hydrocarbons such as benzene, toluene, and ethylene over the course of pyrolysis.[92] This can be overcome by iodine doping the polyacetylene prior to pyrolysis, providing a path to crosslinking and subsequent high yield carbonization.[81-83] Additionally, the carbonization yield goes up with the fraction of iodine incorporated. It is also worth noting that iodine doping of polyacetylene does not result in iodine doped carbon since all of the iodine reacts during thermal treatment to allow the polyacetylene to crosslink.

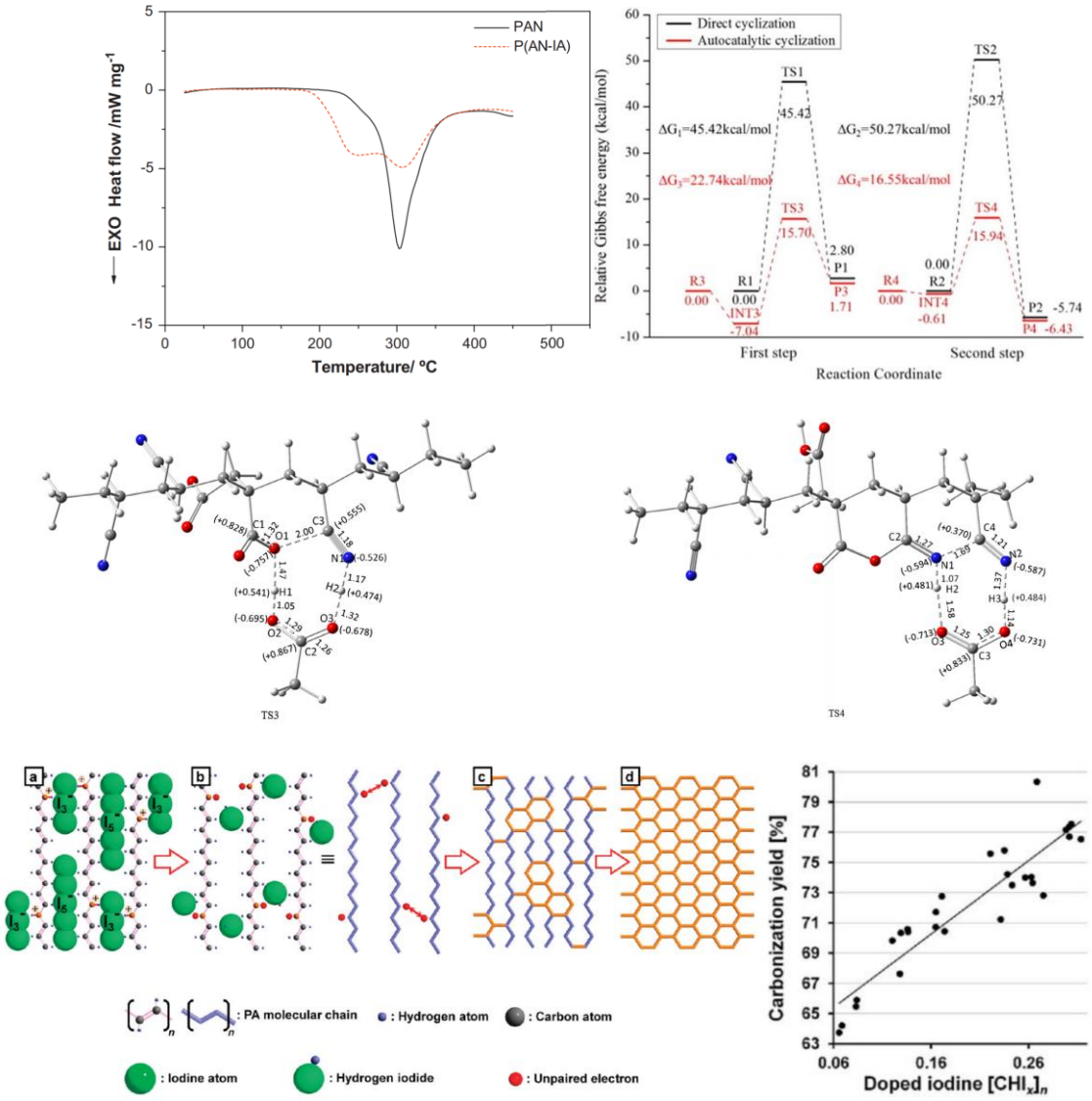

Figure 1.3 Stabilization is a critical first step to effectively synthesize a carbon, and by adding an extra component to a pre-carbon system, the stabilization process can be enhanced. In PAN, adding small amounts of itaconic acid can lower the temperature at which cyclization occurs, as shown by differential scanning calorimetry (DSC) (top left). DFT calculations show that the transition state barriers to cyclize PAN are dramatically lowered by the presence of itaconic acid from a nearby chain as opposed to a neighboring monomer unit from the same chain (top right), with hydrogens stabilizing the cyclization (middle left) and propagating along the formed ladder system (middle right). Carbonization yields from pyrolysis of polyacetylene is also enhanced by an additive. Iodine doping provides a means for removing hydrogen to then form crosslinks (bottom left), thereby increasing carbonization yield (bottom right). Top left) Reproduced with permission.[89] Copyright 2008, Elsevier. Top right and middle row) Reproduced with permission.[90] Copyright 2017, Elsevier. Bottom left) Reproduced with permission.[83] Copyright 2011, American Chemical Society. Bottom right) Reproduced with permission.[82] Copyright 2015, American Chemical Society.

1.2.3 Microstructure in Carbon Precursors and Synthetic Control Over Types of Carbon Edges

A determining feature of polymeric precursors is the microstructure and molecular orientation of the polymer and resulting carbon. Carbonization of PAN in particular has been the subject of extensive studies on microstructure, largely due to its role as a carbon fiber precursor.[63] For example, microstructural differences between "normal" coiled PAN and uncoiled PAN manifest themselves in the final carbon by forming higher curvature carbon species in coiled versus uncoiled producing more graphitic structures.[93] Aligning the polymer chains prior to stabilization lowered the curvature of the structures, thereby suppressing the formation of fullerenes and increasing the extent of graphitization achievable (**Figure 1.4**). This is also seen in studies of PAN tacticity and the effect on microstructure, and by extension the carbon produced. Ghorpade *et. al.* showed that compared to atactic PAN, isotactic PAN exhibits larger crystallites, more easily undergoes cyclization under thermal oxidation, and ultimately produces a carbon with higher electrical conductivity.[94]

The types of edges exposed are particularly important to electrocatalytic activity. A well-known aspect of carbons is the armchair edges exhibit semiconducting band structures while zigzag edges are conducting. As studies have steadily indicated edges as also being the source of catalytic activity, controlling the types of edges formed in carbons has become an important but poorly understood aspect of developing carbon catalysts. Using molecular dynamics to screen precursors which were then experimentally explored, Yamada *et. al.* showed both that the types of edges formed could be controlled to some extent based on the precursors' structure and the extent of that control is related to the H/N

ratio in the precursor. Precursors with lower H/N ratios retained more of the edges present before pyrolysis. This pattern is also consistent with the active site retention in graphitic carbon nitrides, which contain very low H/N ratios.[6, 95-97]

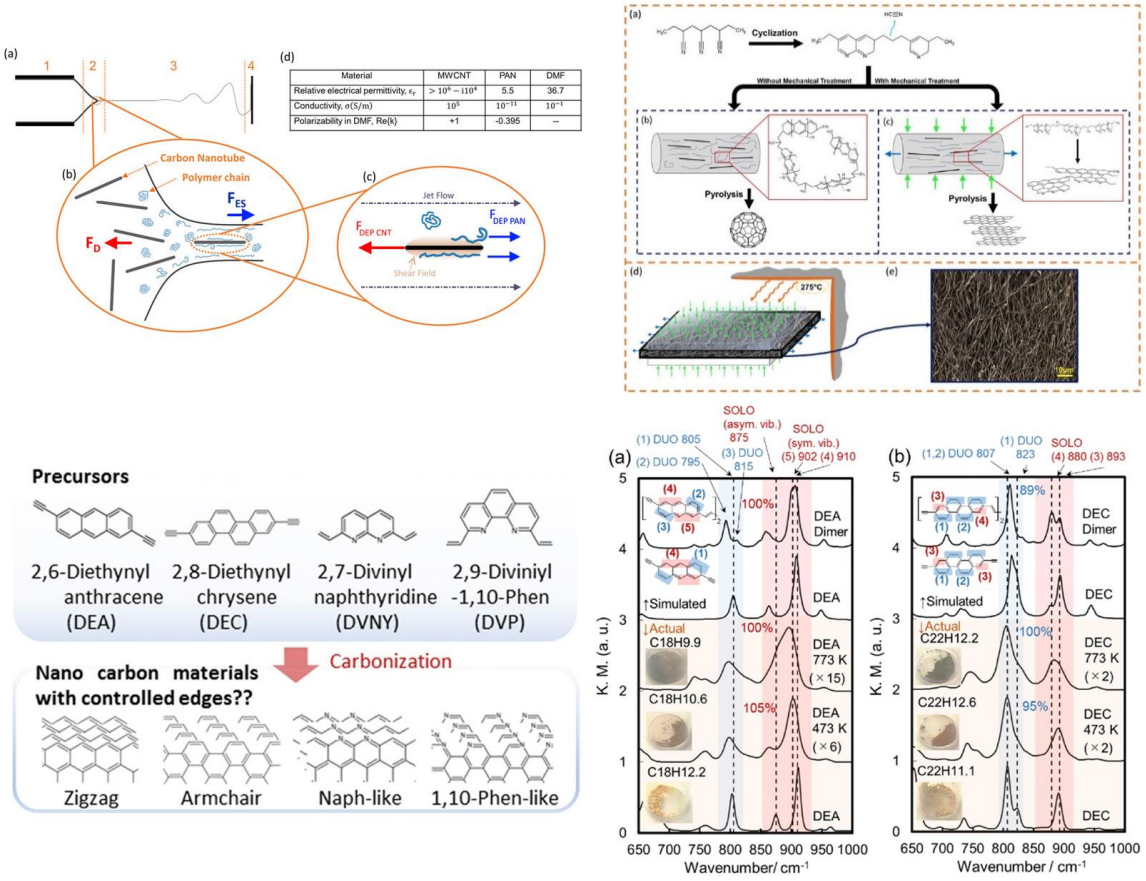

Figure 1.4 Microstructure of the precursor can strongly affect the resulting carbon, since the microstructure in many ways dictates the way the carbon atoms fuse together. By processing PAN chains such that they are uncoiled, the system is able to more extensively graphitize in comparison to PAN chains that are still coiled (top row). This indicates that features of the final carbon can be tuned by tuning the microstructure of the polymer precursor. Edges play a critical role in almost all applications of carbons, and synthesizing carbons with preferentially formed edges is important to optimizing carbons for an application. By using polyaromatic precursors, the edges present in precursors are partially retained in the resulting carbons, with more retention in systems with fewer hydrogens (bottom row). Top row) Reproduced with permission.[93] Copyright 2017, Nature Publishing Group. Bottom row) Reproduced with permission.[98] Copyright 2017, Elsevier.

1.3 Limitations in Heteroatom Active Site Control from Polymeric Precursors

Heteroatoms are recognized as being critical to a carbon's catalytic activity by providing active sites themselves, modifying the overall electronic structure of the carbon, or "activating" a nearby carbon atom.[19, 99] Some methods for heteroatoms incorporation

include the use of heteroatom rich precursors, crosslinking/non-crosslinking pre-pyrolysis additives, or post-pyrolysis modifications, like ball milling or ammonia activation. A wide range of heteroatoms have been successfully incorporated into graphitic structures to date including B,[100-102] N,[72, 103, 104] O,[105] F,[106, 107], Si,[108] P,[109-111] S,[91, 112] Cl,[113] Br,[114, 115] and I.[116-118] Some of these heteroatoms are limited to doping after pyrolysis treatment due to reactivity or volatility, while others are readily incorporated, but specific chemical functionality can be more difficult to control. Dual heteroatom doping is also of note for "synergistic" effects that have been seen in catalytic activity.[119-122]

Controlling the chemical state of heteroatoms incorporated during pyrolysis is particularly difficult, and even more challenging when considering distinctions between the heteroatom at the surface to be active sites and the bulk of the material.[20] The mechanisms will also vary depending on the process by which stabilization and carbonization proceed. In many cases, the heteroatoms in precursors act as activating groups that facilitate carbonization, and while this can also lead to heteroatom incorporation in to the resulting carbon, it results in less control over the heteroatom content chemical states for those atoms. This is apparent in pyrolysis of PAN, in which the idealized mechanism shows the carbon forming from fusing of stabilized PAN ladders, removing nitrogen in the process, but leaving pyridinic nitrogens on the edges.[76] Experimentally though, there is a distribution of chemical states observed for nitrogens in such carbons, forming as kinetically trapped defects during the fusing of ladder polymers (**Figure 1.5**).[123]

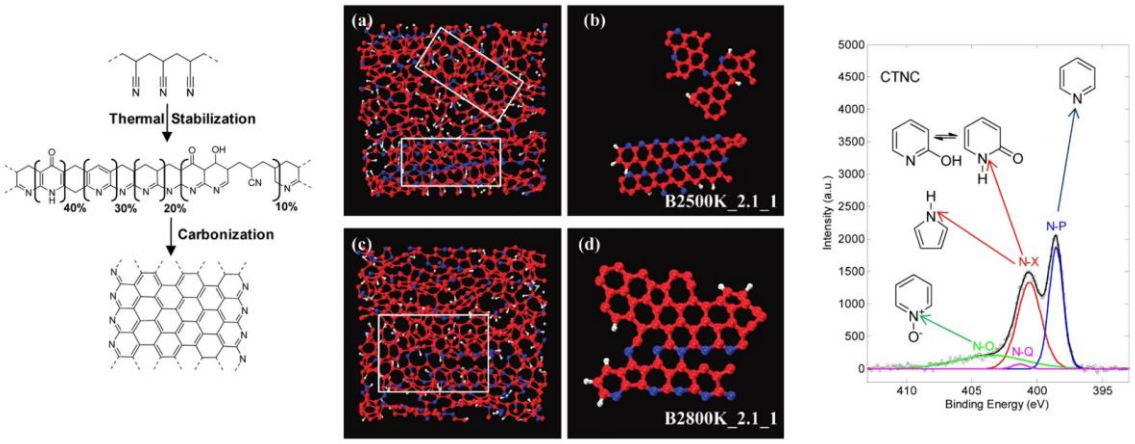

Figure 1.5 The idealized process that is depicted for PAN stabilization and carbonization should result in graphitic ribbons that have pyridinic nitrogens on zigzag edges (left). ReaxFF simulations of oxygen-free stabilized PAN carbonization show significant deviations from that mechanism, in the form of 5 and 7 member rings and quaternary nitrogens (middle). Experimentally, PAN derived carbons show a distribution of nitrogen species, with pyridinic nitrogen content decreasing with higher pyrolysis temperature (right). Left and right) Reproduced with permission.[124] Copyright 2012, American Chemical Society. Middle) Reproduced with permission.[64] Copyright 2012, American Chemical Society.

1.4 Carbon Composite Precursors

Across studies of properties that lead to effective catalysis, it seems that a mix of highly graphitized carbon and defect rich carbon can lead to more efficient catalysts than pristine or defect rich carbons could alone.[125] Synthesis of such carbons can use carbon/polymer composite precursors that are then further pyrolyzed. These precursors can be effective for multiple reasons: as mentioned, they can lead to a combination of material properties that would be difficult to synthesize from a single precursor, and the carbon could also assist in the carbonizing the polymer. This approach would enable the synthesis of carbon materials with both more graphitized components that provide higher conductivity and more disordered components that can be designed to contain specific functionalities.[20] Another potential benefit of using such composites as precursors could be in the pyrolysis itself, whereby interactions between the already formed graphitic carbon aids in forming a carbon.[65]

Even simply using carbon nanotubes as a filler component in PAN carbonization seems to aid in the process, forming more ordered graphitic structures than PAN carbonized without them. This has been investigated by Saha, *et. al.* using ReaxFF, showing that the nanofiller's π–conjugated system and the π – electrons from C≡N groups interact by van der Waals forces, and covalent bonding between the filler and polymer provides more stabilization for intermediates during carbonization.[65]

By starting with a carbon, functionalization may be achieved by incorporation and subsequent pyrolysis of a polymer under more moderate conditions.[126-128] This approach can be attractive to maximize the number of functional moieties that either may not survive higher pyrolysis conditions or are lost progressively during pyrolysis. Such "hybrid" templating methods can use chemical modifications of pre-formed carbons to graft polymers,[129] or polymers can be adsorbed onto the carbon surface.[120, 127, 128, 130-134] Hybrid templating can effectively meld the properties of an already formed carbon, such as conductivity, with functionalities provided by pyrolyzing a polymer, like heteroatoms or increased surface area.[112, 131, 135] The combination of conductivity and active sites has been especially effective at enhancing the electrocatalytic activity otherwise semiconducting materials like g-C_3N_4 for hydrogen evolution and even CO_2 reduction.[95, 125]

1.5 Factors in Nanostructuring Carbons from Polymers

Perhaps the material feature that has received the most attention when designing and discussing catalytic carbons is surface area. While many studies focus on using nanostructure to maximizing surface area, less has been said about how nanostructuring affects other features, such as microstructure of the polymer and thereby the resulting

carbon, or the types of exposed surfaces formed. As mentioned earlier, the basal plane of graphite and graphene have been shown to be dramatically less electrochemically active compared to the edges;[18] furthermore, it is important to keep in mind that some methods, like N_2 adsorption measurements or Porod Analysis of small angle X-ray scattering, only measure total surface area. The values they obtain do not necessarily correlate with catalytic activity, and if the exposed surfaces are not optimal, surface area could be an inefficient way to improve activity compared to improving preferential exposure on surfaces. The surfaces exposed on a carbon surface are critical to exhibiting significant catalytic activity, and nanostructuring affect the propensity for forming and exposing different types of surfaces. The approaches taken to produce nanostructure can be approximately categorized into either untemplated, hard templated, or soft templated.

Untemplated carbons can get their structure from the polymer precursors' microstructure, crosslinkers, or spun fibers. Hard templates impose a structure similarly to how a mold does in manufacturing, while soft templating produces a structure through weak interactions that spontaneously organize. It is important to note that most hard templates have to be removed with a post-pyrolysis etching step, most often using HF, NaOH, or HCl depending on the material used for the template.[8, 136-139] Beyond the cost and toxicity of most etching steps, there is still the question of how these treatments may be affecting the carbon structure and catalytically active sites in particular. For example, HF can remove oxygen functionalities from carbon nanotubes.[140] Similarly, "activating" steps such as with CO_2 or KOH to increase surface area can remove much of the nitrogen content.[124]

The types of pores formed are also important in catalysis applications, and beyond maximizing active site accessibility, the synthetic ability to tune them is also necessary to effectively engineer their mass transport for an application.

1.5.1Types of Interfaces Formed During Nanostructuring

In any templating, there is a component that acts as a carbon source and a component that occupies space to then become pores after pyrolysis. Thus, the interface between the two constitutes what becomes the exposed surface of the carbon, assuming the pyrolysis or etching processes do not decompose the carbon near the interface. This means that the nature of that interface can have a direct effect on the type of surface formed and exposed during synthesis. For example, polymer precursors can be polymerized by grafting from a silica for hard templating.[141] This could lead to a very different exposed carbon surface compared to unbounded polymers within a silica template (**Figure 1.6**).

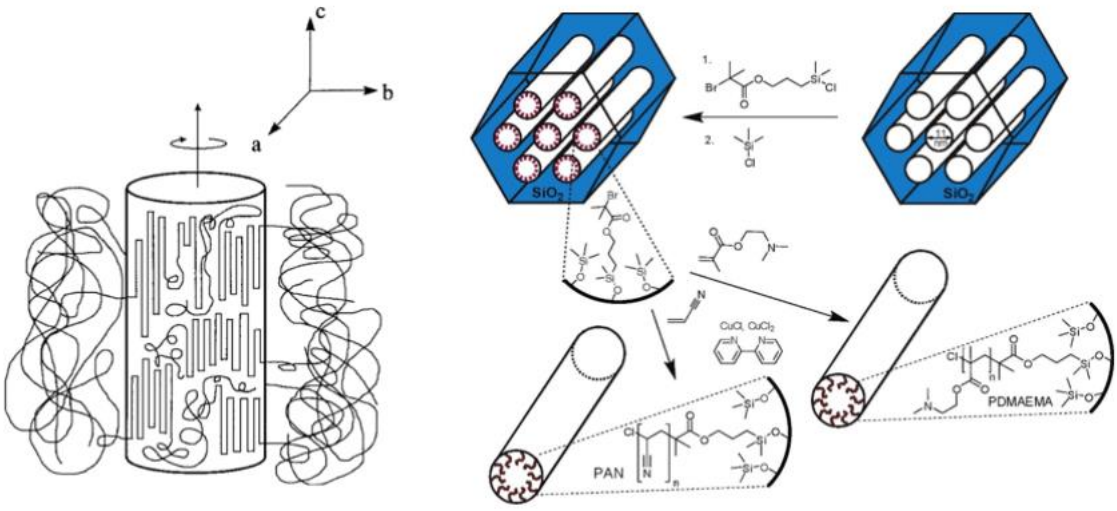

Figure 1.6 Polymer nanostructures can develop different types of interfaces between components depending on the nature of interaction between them. At the interface between block copolymers (left), the different polymer blocks orient themselves based on their microstructure, which may cause different types of edges or defects to form in the carbon. Polymers grafted from silica will have chains coming off of the silica surface, which can be expected to produce a different local microstructure, and thus produce a different type of exposed surface from pyrolysis. Left) Reproduced with permission.[142] Copyright 1998, American Chemical Society. Right) Reproduced with permission.[141] Copyright 2008, American Chemical Society.

Local to the interface of a nanostructured system, the different components can be chemically bound to each other or free. In a block copolymer template, there is always portions of the interface that are chemically bound, where the polymer goes from one block to the other (**Figure 1.6**).[142] Depending on features such as volume fractions, there can be regions of the block polymer where the different blocks are interacting at an interface but not chemically bound to each other, and these areas are going to have very different chain orientations. This can also be seen in hard templating where the template can be filled or grafted from.

1.5.2 Segregation Strength and Surface Energy in Soft Templated Systems

A key constraint in soft templating is the strength of the forces that lead to nanostructuring, especially when the heat is needed to induce crosslinking. This can be seen in block copolymer templating, in which smaller pores and therefore larger surface area can hypothetically be achieved by reducing the overall degree of polymerization while maintaining the approximate block ratios. In practice, the efficacy of this approach is limited, as the smaller degree of polymerization also leads to weaker segregation between the blocks.[103] This is particularly important when using a carbon precursor such as PAN, which typically is stabilized by thermal oxidation.

This is also a challenge with block copolymer templating for retention of morphology when attempting to use shorter polymers and/or to fabricate ultra-thin thin film structures. One approach to improve the structural stability of a templated polymer system is the use of covalently linked architectures. The ability to create complex polymeric architectures is one of the many unique aspects of controlled polymerization methods, and owing to the covalent linkages that partially induce their overall ordering, the

nanostructures of such polymer precursor systems are generally less susceptible to weakening phase boundaries or transitioning into disorder.[143] These polymer architectures include stars, brushes, and dendrimers.[144] In bottlebrush polymers with BCP arms, for example, the exterior block can be either sacrificial or a carbon precursor. The former results in a protective shell to isolate the cores from fusing during pyrolysis and the latter localizes the sacrificial component near the backbone while carbonizing block forms an interconnected structure with other brushes.[145, 146] The strong steric repulsion that comes from covalent linkages and high grafting density successfully hinders partial miscibility typical of low DP BCPs (**Figure 1.7**).

High surface area structures that are desirable for catalysis are necessarily formed out of high curvature systems, which can create some complications. The strength of the nanostructure, as well as how and when the carbon structure is rigidified are major considerations in soft templating. Since structures arise spontaneously out of weak intermolecular interactions, the phase segregation between the components that form those structures are susceptible to weakening at higher temperatures. Furthermore, the filler component of the system leaves via volatilization or decomposition during or leading up to pyrolysis. This can leave high surface area carbons susceptible to structural collapse during the carbonization process in cases where there is a substrate to reduce surface energy with respect to.[10]

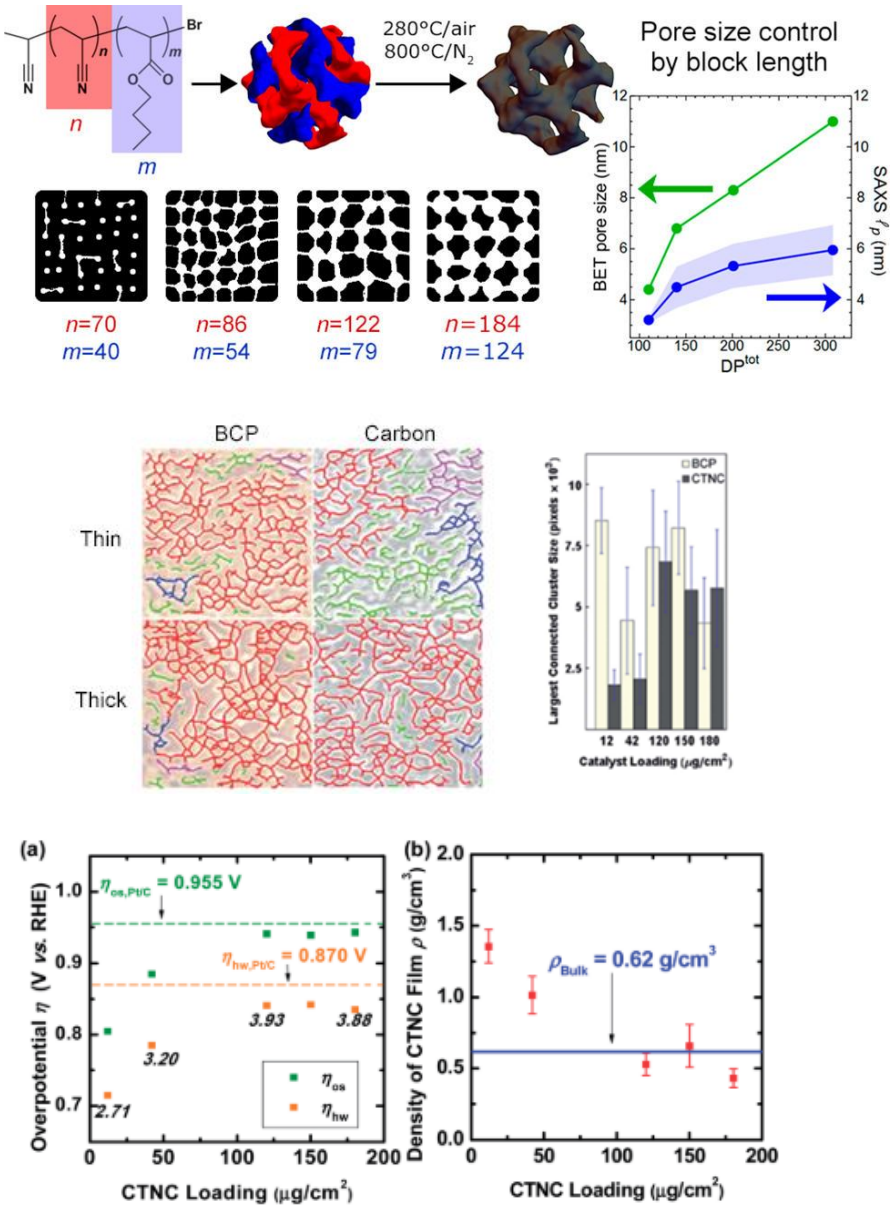

Figure 1.7 Block copolymer templating uses one block as a carbon precursor and another as a porogen. By changing the overall degree of polymerization of the block copolymer, the mesopore size can be controlled. This approach is limited at lower degrees of polymerization, where segregation strength is too weak to retain sharp boundaries under stabilization temperatures (top). Pyrolyzing thin films of polymeric precursors can have very strong interactions with the surface, causing the nanostructure to collapse. (Middle row) Morphological connectivity analysis of CTNC films from before and after thermal treatments show a reduction in connectivity for thin films, which results in lower performance for ORR (bottom row). Top row) Reproduced with permission.[103] Copyright 2017, American Chemical Society. Middle and bottom rows) Reproduced with permission.[10] Copyright 2014, Royal Society of Chemistry.

1.5.3 Nanostructuring and Confinement Effects on Microstructure and Atomic Content

There are many ways in which nanostructuring and confinement can affect the resulting carbon beyond simply the surface area and pore structure it provides. Within a confined space, the polymerization reaction can potentially proceed with different kinetics, the polymers can end up with a different microstructure, and heteroatoms can end up trapped during the pyrolysis process, resulting in a very different distribution of chemical environment for the heteroatoms. These derivative effects on the polymer and resulting carbon are of course important to catalytic activity but have only been explored to a limited extent.

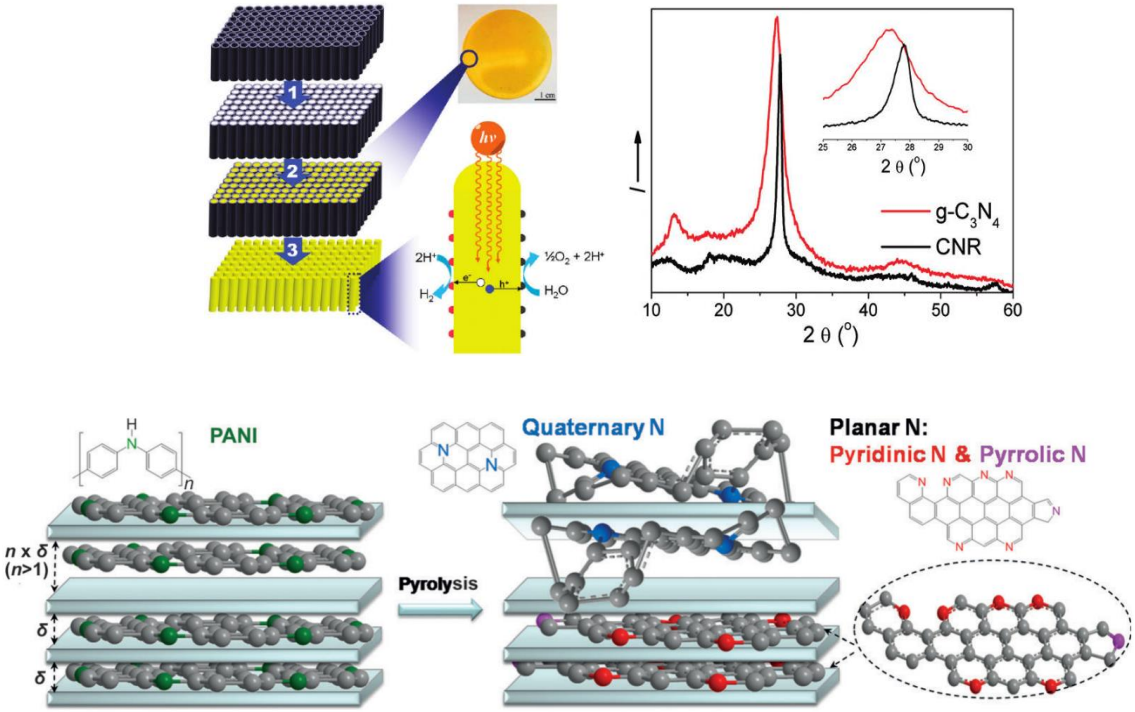

Figure 1.8 Confinement of the precursor before and during pyrolysis can heavily affect the microstructure and heteroatom content of the resulting carbon. Top) Using anodic alumina oxide as a hard template to make graphitic carbon nitride resulted in sharper X-ray diffraction (XRD) [002] peaks, which indicates larger crystallite sizes. Bottom) Pyrolysis of thin polyaniline stacks between montmorillonite resulted in differing nitrogen chemical states due to the limitations the confinement imposed during the pyrolysis process. Top row) Reproduced with permission.[8] Copyright 2011, American Chemical Society. Bottom row) Reproduced with permission.[147] Copyright 2013, Wiley-VCH.

The interactions between polymers incorporated into a hard template and the surface of the template may affect the polymer's microstructure near the interface.[148-152] These interactions occurring at the template/polymer interface also means that any induced changes to the carbon would be primarily at surfaces exposed after template removal.[8, 153-159] Such interactions may have a positive effect on the resulting carbon, such as improved crystallinity (**Figure 1.8**) [8] the overall phenomena as they apply to polymer derived carbons are relatively unexplored. For polymer systems in general, there are indications that polymers are susceptible to confinement effects, the extent of which will depend on polymer backbone rigidity, resulting in modified glass transition temperatures and local ordering.[153] There are also reports of confinement affecting polymer crystallization, and surface interactions affecting the microstructure of a polymer near that surface.[157-159] Despite the wealth of evidence in general polymer systems, the extent of the impact of confinement/interfacial effects on pyrolysis and properties of the resulting carbon is still largely unexplored.

Unfortunately, elucidating the result of interactions between templates and polymers on the resulting carbon's microstructure is not a straightforward task because of the difficulties associated with designing and synthesizing a directly analogous system. One such set of systems does exist, in which the carbons can be derived from PAN grafted from either silica nanoparticles or crosslinked PMMA.[160-162] The precursors only differ by the composition of their cores and the sites that link PAN to the nanoparticle. Comparing between these two systems could also potentially aid in assessing the effects of etching, since the PMMA core does not survive pyrolysis.[160, 163, 164]

1.6 Context of this Thesis in the Field

This thesis contains studies of PAN-containing polymers and PAN-derived carbons, focusing on understanding the relationships between structure and catalytic. The goal was to provide produce insights into factors that affect catalytic activity that translate to from PAN-derived carbons to other carbons, thereby improving the foundational knowledge that is used to design metal-free catalytic systems

1.7 References

[1] Y.P. Zhu, C. Guo, Y. Zheng, S.-Z. Qiao, Surface and Interface Engineering of Noble-Metal-Free Electrocatalysts for Efficient Energy Conversion Processes, *Acc. Chem. Res.* **2017,** *50* (4), 915-923, 10.1021/acs.accounts.6b00635.

[2] D. Banham, S. Ye, K. Pei, J.-i. Ozaki, T. Kishimoto, Y. Imashiro, A review of the stability and durability of non-precious metal catalysts for the oxygen reduction reaction in proton exchange membrane fuel cells, *J. Power Sources* **2015,** *285*, 334-348, 10.1016/j.jpowsour.2015.03.047.

[3] F. Rodriguez-Reinoso, The role of carbon materials in heterogeneous catalysis, *Carbon* **1998,** *36* (3), 159-175, Doi 10.1016/S0008-6223(97)00173-5.

[4] P. Serp, J.L.s. Figueiredo, Carbon materials for catalysis, John Wiley & Sons, Hoboken, N.J., 2009.

[5] P. Serp, Carbon nanotubes and nanofibers in catalysis, *Appl. Catal., A* **2003,** *253* (2), 337-358, 10.1016/s0926-860x(03)00549-0.

[6] Y. Zheng, J. Liu, J. Liang, M. Jaroniec, S.Z. Qiao, Graphitic carbon nitride materials: controllable synthesis and applications in fuel cells and photocatalysis, *Energy and Environmental Science*
2012, *5* (5), 6717, 10.1039/c2ee03479d.

[7] C. Hu, Y. Xiao, Y. Zou, L. Dai, Carbon-Based Metal-Free Electrocatalysis for Energy Conversion, Energy Storage, and Environmental Protection, *Electrochemical Energy Reviews* **2018,** *1* (1), 84-112, 10.1007/s41918-018-0003-2.

[8] X.H. Li, J.S. Zhang, X.F. Chen, A. Fischer, A. Thomas, M. Antonietti, X.C. Wang, Condensed Graphitic Carbon Nitride Nanorods by Nanoconfinement: Promotion of Crystallinity on Photocatalytic Conversion, *Chem. Mater.* **2011,** *23* (19), 4344-4348, 10.1021/cm201688v.

[9] N.R. Sahraie, U.I. Kramm, J. Steinberg, Y. Zhang, A. Thomas, T. Reier, J.P. Paraknowitsch, P. Strasser, Quantifying the density and utilization of active sites in non-precious metal oxygen electroreduction catalysts, *Nat Commun* **2015,** *6*, 8618, 10.1038/ncomms9618.

[10] M.J. Zhong, S.Y. Jiang, Y.F. Tang, E. Gottlieb, E.K. Kim, A. Star, K. Matyjaszewski, T. Kowalewski, Block copolymer-templated nitrogen-enriched nanocarbons with morphology-dependent electrocatalytic activity for oxygen reduction, *Chem. Sci.* **2014,** *5* (8), 3315-3319, 10.1039/c4sc01477d.

[11] E. Gottlieb, M. Kopec, M. Banerjee, J. Mohin, D. Yaron, K. Matyjaszewski, T. Kowalewski, In-Situ Platinum Deposition on Nitrogen-Doped Carbon Films as a Source of Catalytic Activity in a Hydrogen Evolution Reaction, *Acs Appl Mater Inter* **2016,** *8* (33), 21531-8, 10.1021/acsami.6b03924.

[12] B. Kumar, M. Asadi, D. Pisasale, S. Sinha-Ray, B.A. Rosen, R. Haasch, J. Abiade, A.L. Yarin, A. Salehi-Khojin, Renewable and metal-free carbon nanofibre catalysts for carbon dioxide reduction, *Nat. Commun.* **2013,** *4*, 2819, ARTN 2819 10.1038/ncomms3819.

[13] J.K. Norskov, F. Abild-Pedersen, F. Studt, T. Bligaard, Density functional theory in surface chemistry and catalysis, *Proc Natl Acad Sci U S A* **2011,** *108* (3), 937-43, 10.1073/pnas.1006652108.

[14] Z.W. Seh, J. Kibsgaard, C.F. Dickens, I. Chorkendorff, J.K. Nørskov, T.F. Jaramillo, Combining theory and experiment in electrocatalysis: Insights into materials design, *Science* **2017,** *355* (6321), eaad4998, 10.1126/science.aad4998.

[15] J. Durst, A. Siebel, C. Simon, F. Hasché, J. Herranz, H.A. Gasteiger, New insights into the electrochemical hydrogen oxidation and evolution reaction mechanism, *Energy & Environmental Science* **2014,** *7* (7), 2255-2260, 10.1039/c4ee00440j.

[16] X. Zou, Y. Zhang, Noble metal-free hydrogen evolution catalysts for water splitting, *Chem. Soc. Rev.* **2015,** *44* (15), 5148-5180, 10.1039/c4cs00448e.

[17] Y. Sun, S. Gao, F. Lei, Y. Xie, Atomically-thin two-dimensional sheets for understanding active sites in catalysis, *Chem. Soc. Rev.* **2015,** *44* (3), 623-636, 10.1039/c4cs00236a.

[18] W. Yuan, Y. Zhou, Y. Li, C. Li, H. Peng, J. Zhang, Z. Liu, L. Dai, G. Shi, The edge- and basal-plane-specific electrochemistry of a single-layer graphene sheet, *Sci. Rep.* **2013,** *3* (1), 10.1038/srep02248.

[19] D. Guo, R. Shibuya, C. Akiba, S. Saji, T. Kondo, J. Nakamura, Active sites of nitrogen-doped carbon materials for oxygen reduction reaction clarified using model catalysts, *Science* **2016,** *351* (6271), 361-365, 10.1126/science.aad0832.

[20] G.-L. Tian, Q. Zhang, B. Zhang, Y.-G. Jin, J.-Q. Huang, D.S. Su, F. Wei, Toward Full Exposure of "Active Sites": Nanocarbon Electrocatalyst with Surface Enriched Nitrogen for Superior Oxygen Reduction and Evolution Reactivity, *Adv. Funct. Mater.* **2014,** *24* (38), 5956-5961, 10.1002/adfm.201401264.

[21] F.X. Collard, J. Blin, A review on pyrolysis of biomass constituents: Mechanisms and composition of the products obtained from the conversion of cellulose, hemicelluloses and lignin, *Renew Sust Energ Rev* **2014,** *38*, 594-608, 10.1016/j.rser.2014.06.013.

[22] A.V. Bridgwater, Review of fast pyrolysis of biomass and product upgrading, *Biomass Bioenergy* **2012,** *38*, 68-94, 10.1016/j.biombioe.2011.01.048.

[23] M.J. Antal, M. Gronli, The art, science, and technology of charcoal production, *Ind. Eng. Chem. Res.* **2003,** *42* (8), 1619-1640, 10.1021/ie0207919.

[24] Suhas, P.J. Carrott, M.M. Ribeiro Carrott, Lignin--from natural adsorbent to activated carbon: a review, *Bioresour. Technol.* **2007,** *98* (12), 2301-12, 10.1016/j.biortech.2006.08.008.

[25] J.P. Abrahamson, A. Jain, A.C.T. van Duin, R.L. Vander Wal, Carbon structure and resulting graphitizability upon oxygen evolution, *Carbon* **2018,** *135*, 171-179, 10.1016/j.carbon.2018.04.055.

[26] A. Allahbakhsh, A.R. Bahramian, Self-assembled and pyrolyzed carbon aerogels: an overview of their preparation mechanisms, properties and applications, *Nanoscale* **2015,** *7* (34), 14139-14158, 10.1039/c5nr03855c.

[27] K. Matyjaszewski, N.V. Tsarevsky, Macromolecular engineering by atom transfer radical polymerization, *J. Am. Chem. Soc.* **2014,** *136* (18), 6513-33, 10.1021/ja408069v.

[28] K. Matyjaszewski, Atom Transfer Radical Polymerization (ATRP): Current Status and Future Perspectives, *Macromolecules* **2012,** *45* (10), 4015-4039, 10.1021/ma3001719.

[29] K. Matyjaszewski, Advanced Materials by Atom Transfer Radical Polymerization, *Adv. Mater.* **2018**, 1706441, 10.1002/adma.201706441.

[30] C. Tang, A. Tracz, M. Kruk, R. Zhang, D.M. Smilgies, K. Matyjaszewski, T. Kowalewski, Long-range ordered thin films of block copolymers prepared by zone-casting and their thermal conversion into ordered nanostructured carbon, *J. Am. Chem. Soc.* **2005,** *127* (19), 6918-9, 10.1021/ja0508929.

[31] M. Kruk, K.M. Kohlhaas, B. Dufour, E.B. Celer, M. Jaroniec, K. Matyjaszewski, R.S. Ruoff, T. Kowalewski, Partially graphitic, high-surface-area mesoporous carbons from polyacrylonitrile templated by ordered and disordered mesoporous silicas, *Microporous Mesoporous Mater.* **2007,** *102* (1-3), 178-187, 10.1016/j.micromeso.2006.12.027.

[32] W. Gao, Y. Wan, Y. Dou, D. Zhao, Synthesis of Partially Graphitic Ordered Mesoporous Carbons with High Surface Areas, *Adv. Energy Mater.* **2011,** *1* (1), 115-123, 10.1002/aenm.201000009.

[33] J. Goma, M. Oberlin, Graphitization of thin carbon films, *Thin Solid Films* **1980,** *65* (2), 221-232, 10.1016/0040-6090(80)90256-4.

[34] A. Oberlin, Carbonization and graphitization, *Carbon* **1984,** *22* (6), 521-541, 10.1016/0008-6223(84)90086-1.

[35] J.J. Kipling, J.N. Sherwood, P.V. Shooter, N.R. Thompson, Factors influencing the graphitization of polymer carbons, *Carbon* **1964,** *1* (3), 315-320, 10.1016/0008-6223(64)90285-4.

[36] M.D. Hornbostel, J. Bao, G. Krishnan, A. Nagar, I. Jayaweera, T. Kobayashi, A. Sanjurjo, J. Sweeney, D. Carruthers, M.A. Petruska, L. Dubois, Characteristics of

an advanced carbon sorbent for CO2 capture, *Carbon* **2013,** *56*, 77-85, 10.1016/j.carbon.2012.12.082.

[37] M. Uchimiya, L.H. Wartelle, K.T. Klasson, C.A. Fortier, I.M. Lima, Influence of Pyrolysis Temperature on Biochar Property and Function as a Heavy Metal Sorbent in Soil, *J. Agric. Food. Chem.* **2011,** *59* (6), 2501-2510, 10.1021/jf104206c.

[38] M. Michel, B. Buszewski, Porous graphitic carbon sorbents in biomedical and environmental applications, *Adsorption* **2009,** *15* (2), 193-202, 10.1007/s10450-009-9170-0.

[39] T.A. Centeno, J.L. Vilas, A.B. Fuertes, Effects of phenolic resin pyrolysis conditions on carbon membrane performance for gas separation, *J. Membr. Sci.* **2004,** *228* (1), 45-54, 10.1016/j.memsci.2003.09.010.

[40] E. Antolini, Carbon supports for low-temperature fuel cell catalysts, *Appl. Catal., B* **2009,** *88* (1-2), 1-24, 10.1016/j.apcatb.2008.09.030.

[41] Y. Shao, J. Liu, Y. Wang, Y. Lin, Novel catalyst support materials for PEMfuelcells: current status and future prospects, *J. Mater. Chem.* **2009,** *19* (1), 46-59, 10.1039/b808370c.

[42] R.L. McCreery, Advanced Carbon Electrode Materials for Molecular Electrochemistry, *Chem. Rev.* **2008,** *108* (7), 2646-2687, 10.1021/cr068076m.

[43] C.E. Banks, R.G. Compton, New electrodes for old: from carbon nanotubes to edge plane pyrolytic graphite, *The Analyst* **2006,** *131* (1), 15-21, 10.1039/b512688f.

[44] Z. Wu, W. Li, Y. Xia, P. Webley, D. Zhao, Ordered mesoporous graphitized pyrolytic carbon materials: synthesis, graphitization, and electrochemical properties, *J. Mater. Chem.* **2012,** *22* (18), 8835, 10.1039/c2jm30192j.

[45] M. Suzuki, Activated Carbon-Fiber - Fundamentals and Applications, *Carbon* **1994,** *32* (4), 577-586, Doi 10.1016/0008-6223(94)90075-2.

[46] T. Maitra, S. Sharma, A. Srivastava, Y.-K. Cho, M. Madou, A. Sharma, Improved graphitization and electrical conductivity of suspended carbon nanofibers derived from carbon nanotube/polyacrylonitrile composites by directed electrospinning, *Carbon* **2012,** *50* (5), 1753-1761, 10.1016/j.carbon.2011.12.021.

[47] C. Kim, Y.-J. Kim, Y.-A. Kim, Fabrication and structural characterization of electro-spun polybenzimidazol-derived carbon nanofiber by graphitization, *Solid State Commun.* **2004,** *132* (8), 567-571, 10.1016/j.ssc.2004.08.035.

[48] M. Sevilla, A.B. Fuertes, The production of carbon materials by hydrothermal carbonization of cellulose, *Carbon* **2009,** *47* (9), 2281-2289, 10.1016/j.carbon.2009.04.026.

[49] Y.S. Yun, S.Y. Cho, J. Shim, B.H. Kim, S.J. Chang, S.J. Baek, Y.S. Huh, Y. Tak, Y.W. Park, S. Park, H.J. Jin, Microporous carbon nanoplates from regenerated silk proteins for supercapacitors, *Adv. Mater.* **2013,** *25* (14), 1993-8, 10.1002/adma.201204692.

[50] D.C. Wu, C.M. Hui, H.C. Dong, J. Pietrasik, H.J. Ryu, Z.H. Li, M.J. Zhong, H.K. He, E.K. Kim, M. Jaroniec, T. Kowalewski, K. Matyjaszewski, Nanoporous Polystyrene and Carbon Materials with Core-Shell Nanosphere-Interconnected Network Structure, *Macromolecules* **2011,** *44* (15), 5846-5849, 10.1021/ma2013207.

[51] Y. Ouyang, H. Shi, R. Fu, D. Wu, Highly monodisperse microporous polymeric and carbonaceous nanospheres with multifunctional properties, *Sci. Rep.* **2013,** *3* (1), 1430, 10.1038/srep01430.

[52] Y. Liang, L. Chen, D. Zhuang, H. Liu, R. Fu, M. Zhang, D. Wu, K. Matyjaszewski, Fabrication and nanostructure control of super-hierarchical carbon materials from heterogeneous bottlebrushes, *Chem Sci* **2017,** *8* (3), 2101-2106, 10.1039/c6sc03961h.

[53] Z. Li, D. Wu, Y. Liang, F. Xu, R. Fu, Facile fabrication of novel highly microporous carbons with superior size-selective adsorption and supercapacitance properties, *Nanoscale* **2013,** *5* (22), 10824-8, 10.1039/c3nr04236g.

[54] H.O. Pierson, Handbook of carbon, graphite, diamond, and fullerenes : properties, processing, and applications, Noyes Publications, Park Ridge, N.J., U.S.A., 1993.

[55] W.H. Lee, J.H. Moon, Monodispersed N-doped carbon nanospheres for supercapacitor application, *Acs Appl Mater Inter* **2014,** *6* (16), 13968-76, 10.1021/am5033378.

[56] K.W. Kim, H.M. Lee, B.S. Kim, S.H. Hwang, L.K. Kwac, K.H. An, B.J. Kim, Preparation and thermal properties of polyethylene-based carbonized fibers, *Carbon Letters* **2015,** *16* (1), 62-66, 10.5714/Cl.2015.16.1.062.

[57] M.J. Behr, B.G. Landes, B.E. Barton, M.T. Bernius, G.F. Billovits, E.J. Hukkanen, J.T. Patton, W. Wang, C. Wood, D.T. Keane, J.E. Rix, S.J. Weigand, Structure-property model for polyethylene-derived carbon fiber, *Carbon* **2016,** *107*, 525-535, 10.1016/j.carbon.2016.06.032.

[58] E. Fitzer, W. Schäfer, The effect of crosslinking on the formation of glasslike carbons from thermosetting resins, *Carbon* **1970,** *8* (3), 353-364, 10.1016/0008-6223(70)90075-8.

[59] K.A. Trick, T.E. Saliba, Mechanisms of the pyrolysis of phenolic resin in a carbon/phenolic composite, *Carbon* **1995,** *33* (11), 1509-1515, 10.1016/0008-6223(95)00092-r.

[60] J.W. To, Z. Chen, H. Yao, J. He, K. Kim, H.H. Chou, L. Pan, J. Wilcox, Y. Cui, Z. Bao, Ultrahigh Surface Area Three-Dimensional Porous Graphitic Carbon from Conjugated Polymeric Molecular Framework, *ACS Central Science* **2015,** *1* (2), 68-76, 10.1021/acscentsci.5b00149.

[61] B. Saha, G.C. Schatz, Carbonization in polyacrylonitrile (PAN) based carbon fibers studied by ReaxFF molecular dynamics simulations, *J. Phys. Chem. B* **2012,** *116* (15), 4684-92, 10.1021/jp300581b.

[62] Y. Xue, J. Liu, J. Liang, Correlative study of critical reactions in polyacrylonitrile based carbon fiber precursors during thermal-oxidative stabilization, *Polym. Degrad. Stab.* **2013,** *98* (1), 219-229, 10.1016/j.polymdegradstab.2012.10.018.

[63] E. Frank, L.M. Steudle, D. Ingildeev, J.M. Spörl, M.R. Buchmeiser, Carbon Fibers: Precursor Systems, Processing, Structure, and Properties, *Angew. Chem. Int. Ed.* **2014,** *53* (21), 5262-5298, 10.1002/anie.201306129.

[64] B. Saha, G.C. Schatz, Carbonization in Polyacrylonitrile (PAN) Based Carbon Fibers Studied by ReaxFF Molecular Dynamics Simulations, *J. Phys. Chem. B* **2012,** *116* (15), 4684-4692, 10.1021/jp300581b.

[65] B. Saha, A.o. Furmanchuk, Y. Dzenis, G.C. Schatz, Multi-step mechanism of carbonization in templated polyacrylonitrile derived fibers: ReaxFF model uncovers origins of graphite alignment, *Carbon* **2015,** *94*, 694-704, 10.1016/j.carbon.2015.07.048.

[66] X. Lu, X. Wang, Q. Li, X. Huang, S. Han, G. Wang, A ReaxFF-based molecular dynamics study of the pyrolysis mechanism of polyimide, *Polym. Degrad. Stab.* **2015,** *114*, 72-80, 10.1016/j.polymdegradstab.2015.02.004.

[67] Y. Dong, S.C. Rismiller, J. Lin, Molecular dynamic simulation of layered graphene clusters formation from polyimides under extreme conditions, *Carbon* **2016,** *104*, 47-55, 10.1016/j.carbon.2016.03.050.

[68] T. Zhao, T. Li, Z. Xin, L. Zou, L. Zhang, A ReaxFF-Based Molecular Dynamics Simulation of the Pyrolysis Mechanism for Polycarbonate, *Energy Fuels* **2018,** *32* (2), 2156-2162, 10.1021/acs.energyfuels.7b03332.

[69] D.-e. Jiang, A.C.T. van Duin, W.A. Goddard, S. Dai, Simulating the Initial Stage of Phenolic Resin Carbonization via the ReaxFF Reactive Force Field, *J. Phys. Chem. A* **2009,** *113* (25), 6891-6894, 10.1021/jp902986u.

[70] X. Liu, X. Li, J. Liu, Z. Wang, B. Kong, X. Gong, X. Yang, W. Lin, L. Guo, Study of high density polyethylene (HDPE) pyrolysis with reactive molecular dynamics, *Polym. Degrad. Stab.* **2014,** *104*, 62-70, 10.1016/j.polymdegradstab.2014.03.022.

[71] M. Inagaki, S. Harada, T. Sato, T. Nakajima, Y. Horino, K. Morita, Carbonization of polyimide film "Kapton", *Carbon* **1989,** *27* (2), 253-257, 10.1016/0008-6223(89)90131-0.

[72] Y. Liu, Y. Chen, L. Tian, R. Hu, Hierarchical porous nitrogen-doped carbon materials derived from one-step carbonization of polyimide for efficient CO2 adsorption and separation, *J. Porous Mater.* **2016,** *24* (3), 583-589, 10.1007/s10934-016-0294-9.

[73] Y. Wang, J. Liu, S. Christiansen, D.H. Kim, U. Gösele, M. Steinhart, Nanopatterned Carbon Films with Engineered Morphology by Direct Carbonization of UV-Stabilized Block Copolymer Films, *Nano Lett.* **2008,** *8* (11), 3993-3997, 10.1021/nl802554h.

[74] M.C. Paiva, P. Kotasthane, D.D. Edie, A.A. Ogale, UV stabilization route for melt-processible PAN-based carbon fibers, *Carbon* **2003,** *41* (7), 1399-1409, 10.1016/s0008-6223(03)00041-1.

[75] W. Zhao, Y. Lu, J. Wang, Q. Chen, L. Zhou, J. Jiang, L. Chen, Improving crosslinking of stabilized polyacrylonitrile fibers and mechanical properties of carbon fibers by irradiating with γ-ray, *Polym. Degrad. Stab.* **2016,** *133*, 16-26, 10.1016/j.polymdegradstab.2016.07.018.

[76] P. Bajaj, A.K. Roopanwal, Thermal stabilization of acrylic precursors for the production of carbon fibers: An overview, *J. Macromol. Sci., Rev. Macromol. Chem. Phys.* **1997,** *C37* (1), 97-147, 10.1080/15321799708014734.

[77] Z.H. Wang, X.Q. Xiong, L. Qie, Y.H. Huang, High-performance lithium storage in nitrogen-enriched carbon nanofiber webs derived from polypyrrole, *Electrochim. Acta* **2013,** *106*, 320-326, 10.1016/j.electacta.2013.05.088.

[78] H.V. Shah, S.T. Brittain, Q. Huang, S.J. Hwu, G.M. Whitesides, D.W. Smith, Bis-o-diynylarene (BODA) derived polynaphthalenes as precursors to glassy carbon microstructures, *Chem. Mater.* **1999,** *11* (10), 2623-2625, DOI 10.1021/cm9903780.

[79] H. Suda, K. Haraya, Gas permeation through micropores of carbon molecular sieve membranes derived from Kapton polyimide, *J. Phys. Chem. B* **1997,** *101* (20), 3988-3994, DOI 10.1021/jp963997u.

[80] S.A. Hesse, J.G. Werner, U. Wiesner, One-Pot Synthesis of Hierarchically Macro- and Mesoporous Carbon Materials with Graded Porosity, *ACS Macro Lett.* **2015,** *4* (5), 477-482, 10.1021/acsmacrolett.5b00095.

[81] M. Kyotani, S. Matsushita, T. Nagai, Y. Matsui, M. Shimomura, A. Kaito, K. Akagi, Helical Carbon and Graphitic Films Prepared from Iodine-Doped Helical Polyacetylene Film Using Morphology-Retaining Carbonization, *J. Am. Chem. Soc.* **2008,** *130* (33), 10880-10881, 10.1021/ja803865e.

[82] S. Matsushita, K. Akagi, Macroscopically Aligned Graphite Films Prepared from Iodine-Doped Stretchable Polyacetylene Films Using Morphology-Retaining Carbonization, *J. Am. Chem. Soc.* **2015,** *137* (28), 9077-9087, 10.1021/jacs.5b04012.

[83] S. Matsushita, M. Kyotani, K. Akagi, Hierarchically Controlled Helical Graphite Films Prepared from Iodine-Doped Helical Polyacetylene Films Using Morphology-Retaining Carbonization, *J. Am. Chem. Soc.* **2011,** *133* (44), 17977-17992, 10.1021/ja2082922.

[84] J.W. Krumpfer, E. Giebel, E. Frank, A. Muller, L.M. Ackermann, C.N. Tironi, G. Mourgas, J. Unold, M. Klapper, M.R. Buchmeiser, K. Mullen, Poly(Methyl Vinyl Ketone) as a Potential Carbon Fiber Precursor, *Chem. Mater.* **2017,** *29* (2), 780-788, 10.1021/acs.chemmater.6b04774.

[85] S. Israel, I. Gurevitch, M.S. Silverstein, Carbons with a hierarchical porous structure through the pyrolysis of hypercrosslinked emulsion-templated polymers, *Polymer* **2015,** *72*, 453-463, 10.1016/j.polymer.2015.02.055.

[86] R. Castaldo, R. Avolio, M. Cocca, G. Gentile, M.E. Errico, M. Avella, C. Carfagna, V. Ambrogi, Synthesis and adsorption study of hyper-crosslinked styrene-based nanocomposites containing multi-walled carbon nanotubes, *Rsc Advances* **2017,** *7* (12), 6865-6874, 10.1039/c6ra25481k.

[87] H. Zhu, X. Wang, X. Liu, X. Yang, Integrated synthesis of poly(o-phenylenediamine)-derived carbon materials for high performance supercapacitors, *Adv. Mater.* **2012,** *24* (48), 6524-9, 10.1002/adma.201202461.

[88] A.K. Gupta, D.K. Paliwal, P. Bajaj, Acrylic Precursors for Carbon Fibers, *Polym. Rev.* **1991,** *31* (1), 1-89, 10.1080/15321799108021557.

[89] Q. Ouyang, L. Cheng, H. Wang, K. Li, Mechanism and kinetics of the stabilization reactions of itaconic acid-modified polyacrylonitrile, *Polym. Degrad. Stab.* **2008,** *93* (8), 1415-1421, 10.1016/j.polymdegradstab.2008.05.021.

[90] Q. Luo, Z. Shi, D. Li, C. Zhu, M. Wang, DFT study on the ionic cyclization mechanism of copolymers of acrylonitrile-itaconic acid: Direct or autocatalytic?, *Chem. Phys. Lett.* **2017,** *687*, 158-162, 10.1016/j.cplett.2017.09.011.

[91] Z.C. Xiao, D.B. Kong, J.X. Liang, B. Wang, R. Iqbal, Q.H. Yang, L.J. Zhi, Structure controllable carbon matrix derived from benzene-constructed porous organic polymers for high-performance Li-S batteries, *Carbon* **2017,** *116*, 633-639, 10.1016/j.carbon.2017.02.041.

[92] J.C.W. Chien, P.C. Uden, J.-L. Fan, Pyrolysis of polyacetylene, *J. Polym. Sci., Part A: Polym. Chem.* **1982,** *20* (8), 2159-2167, 10.1002/pol.1982.170200819.

[93] M. Ghazinejad, S. Holmberg, O. Pilloni, L. Oropeza-Ramos, M. Madou, Graphitizing Non-graphitizable Carbons by Stress-induced Routes, *Sci. Rep.* **2017,** *7* (1), 10.1038/s41598-017-16424-z.

[94] R.V. Ghorpade, D.W. Cho, S.C. Hong, Effect of controlled tacticity of polyacrylonitrile (co)polymers on their thermal oxidative stabilization behaviors and the properties of resulting carbon films, *Carbon* **2017,** *121*, 502-511, 10.1016/j.carbon.2017.06.015.

[95] X. Lu, T.H. Tan, Y.H. Ng, R. Amal, Highly Selective and Stable Reduction of CO2to CO by a Graphitic Carbon Nitride/Carbon Nanotube Composite Electrocatalyst, *Chemistry A European Journal* **2016,** *22* (34), 11991-11996, 10.1002/chem.201601674.

[96] J. Wei, D.D. Zhou, Z.K. Sun, Y.H. Deng, Y.Y. Xia, D.Y. Zhao, A Controllable Synthesis of Rich Nitrogen-Doped Ordered Mesoporous Carbon for CO2 Capture and Supercapacitors, *Adv. Funct. Mater.* **2013,** *23* (18), 2322-2328, 10.1002/adfm.201202764.

[97] X. Wang, K. Maeda, A. Thomas, K. Takanabe, G. Xin, J.M. Carlsson, K. Domen, M. Antonietti, A metal-free polymeric photocatalyst for hydrogen production from water under visible light, *Nat Mater* **2009,** *8* (1), 76-80, 10.1038/nmat2317.

[98] Y. Yamada, S. Gohda, K. Abe, T. Togo, N. Shimano, T. Sasaki, H. Tanaka, H. Ono, T. Ohba, S. Kubo, T. Ohkubo, S. Sato, Carbon materials with controlled edge structures, *Carbon* **2017,** *122*, 694-701, 10.1016/j.carbon.2017.07.012.

[99] T. Xing, Y. Zheng, L.H. Li, B.C. Cowie, D. Gunzelmann, S.Z. Qiao, S. Huang, Y. Chen, Observation of active sites for oxygen reduction reaction on nitrogen-doped multilayer graphene, *ACS Nano* **2014,** *8* (7), 6856-62, 10.1021/nn501506p.

[100] B. You, F. Kang, P.Q. Yin, Q. Zhang, Hydrogel-derived heteroatom-doped porous carbon networks for supercapacitor and electrocatalytic oxygen reduction, *Carbon* **2016,** *103*, 9-15, 10.1016/j.carbon.2016.03.009.

[101] W.X. Zhao, S. Han, X.D. Zhuang, F. Zhang, Y.Y. Mai, X.L. Feng, Cross-linked polymer-derived B/N co-doped carbon materials with selective capture of CO2, *J. Mater. Chem. A* **2015,** *3* (46), 23352-23359, 10.1039/c5ta06702b.

[102] W. Meng, L. Wen, Z. Song, N. Cao, X. Qin, Metal-free boron-doped carbon microspheres as excellent cathode catalyst for rechargeable Li–O2 battery, *J. Solid State Electrochem.* **2016,** *21* (3), 665-671, 10.1007/s10008-016-3412-3.

[103] M. Kopec, R. Yuan, E. Gottlieb, C.M.R. Abreu, Y. Song, Z. Wang, J.F.J. Coelho, K. Matyjaszewski, T. Kowalewski, Polyacrylonitrile-b-poly(butyl acrylate) Block Copolymers as Precursors to Mesoporous Nitrogen-Doped Carbons: Synthesis and Nanostructure, *Macromolecules* **2017,** *50* (7), 2759-2767, 10.1021/acs.macromol.6b02678.

[104] Q. Lai, Y. Zhao, Y. Liang, J. He, J. Chen, In Situ Confinement Pyrolysis Transformation of ZIF-8 to Nitrogen-Enriched Meso-Microporous Carbon Frameworks for Oxygen Reduction, *Adv. Funct. Mater.* **2016,** *26* (45), 8334-8344, 10.1002/adfm.201603607.

[105] S. Chen, J. Duan, M. Jaroniec, S.-Z. Qiao, Nitrogen and Oxygen Dual-Doped Carbon Hydrogel Film as a Substrate-Free Electrode for Highly Efficient Oxygen Evolution Reaction, *Adv. Mater.* **2014,** *26* (18), 2925-2930, 10.1002/adma.201305608.

[106] K. Kakaei, A. Balavandi, Hierarchically porous fluorine-doped graphene nanosheets as efficient metal-free electrocatalyst for oxygen reduction in gas diffusion electrode, *J. Colloid Interface Sci.* **2017,** *490*, 819-824, 10.1016/j.jcis.2016.12.011.

[107] Y. Wang, J. Zhang, X. Wang, M. Antonietti, H. Li, Boron- and fluorine-containing mesoporous carbon nitride polymers: metal-free catalysts for cyclohexane oxidation, *Angew. Chem. Int. Ed. Engl.* **2010,** *49* (19), 3356-9, 10.1002/anie.201000120.

[108] Z. Qian, X. Shan, L. Chai, J. Ma, J. Chen, H. Feng, Si-Doped Carbon Quantum Dots: A Facile and General Preparation Strategy, Bioimaging Application, and Multifunctional Sensor, *ACS Appl. Mater. Interfaces* **2014,** *6* (9), 6797-6805, 10.1021/am500403n.

[109] J. Zhang, Z. Zhao, Z. Xia, L. Dai, A metal-free bifunctional electrocatalyst for oxygen reduction and oxygen evolution reactions, *Nat. Nanotechnol.* **2015,** *10* (5), 444-452, 10.1038/nnano.2015.48.

[110] J. Wu, C. Jin, Z. Yang, J. Tian, R. Yang, Synthesis of phosphorus-doped carbon hollow spheres as efficient metal-free electrocatalysts for oxygen reduction, *Carbon* **2015,** *82*, 562-571, 10.1016/j.carbon.2014.11.008.

[111] T.Y. Ma, J. Ran, S. Dai, M. Jaroniec, S.Z. Qiao, Phosphorus-Doped Graphitic Carbon Nitrides Grown In Situ on Carbon-Fiber Paper: Flexible and Reversible Oxygen Electrodes, *Angew. Chem. Int. Ed.* **2015,** *54* (15), 4646-4650, 10.1002/anie.201411125.

[112] Z. Chang, H. Dou, B. Ding, J. Wang, Y. Wang, G.Y. Xu, C. Li, Interconnected core-shell pyrolyzed polyacrylonitrile@sulfur/carbon nanocomposites for rechargeable lithium-sulfur batteries, *New J. Chem.* **2016,** *40* (9), 7680-7686, 10.1039/c6nj00325g.

[113] K. Kakaei, M. Hamidi, S. Husseindoost, Chlorine-doped reduced graphene oxide nanosheets as an efficient and stable electrode for supercapacitor in acidic medium, *J. Colloid Interface Sci.* **2016,** *479*, 121-126, 10.1016/j.jcis.2016.06.058.

[114] Z.-A. Lan, G. Zhang, X. Wang, A facile synthesis of Br-modified g-C 3 N 4 semiconductors for photoredox water splitting, *Appl. Catal., B* **2016,** *192*, 116-125, 10.1016/j.apcatb.2016.03.062.

[115] S. Żarska, D. Kulawik, J. Drabowicz, W. Ciesielski, A review of procedures of purification and chemical modification of carbon nanotubes with bromine, *Fullerence, Nanotubes, and Carbon Nanostructures* **2017,** *25* (10), 563-569, 10.1080/1536383x.2017.1330266.

[116] Y. Zhan, J. Huang, Z. Lin, X. Yu, D. Zeng, X. Zhang, F. Xie, W. Zhang, J. Chen, H. Meng, Iodine/nitrogen co-doped graphene as metal free catalyst for oxygen reduction reaction, *Carbon* **2015,** *95*, 930-939, 10.1016/j.carbon.2015.09.024.

[117] Q. Han, C. Hu, F. Zhao, Z. Zhang, N. Chen, L. Qu, One-step preparation of iodine-doped graphitic carbon nitride nanosheets as efficient photocatalysts for visible light water splitting, *J. Mater. Chem. A* **2015,** *3* (8), 4612-4619, 10.1039/c4ta06093h.

[118] F. Du, M. Zhang, H. Ju, L. Zhang, M. Sun, Z. Zhou, Z. Dai, L. Zhang, A. Gong, C. Wu, Engineering iodine-doped carbon dots as dual-modal probes for fluorescence and X-ray CT imaging, *Int. J. Nanomed.* **2015**, 10.2147/ijn.s82778.

[119] Y. Zheng, Y. Jiao, L.H. Li, T. Xing, Y. Chen, M. Jaroniec, S.Z. Qiao, Toward Design of Synergistically Active Carbon-Based Catalysts for Electrocatalytic Hydrogen Evolution, *ACS Nano* **2014,** *8* (5), 5290-5296, 10.1021/nn501434a.

[120] R. Li, Z.D. Wei, X.L. Gou, Nitrogen and Phosphorus Dual-Doped Graphene/Carbon Nanosheets as Bifunctional Electrocatalysts for Oxygen Reduction and Evolution, *ACS Catal.* **2015,** *5* (7), 4133-4142, 10.1021/acscatal.5b00601.

[121] K. Qu, Y. Zheng, S. Dai, S.Z. Qiao, Graphene oxide-polydopamine derived N, S-codoped carbon nanosheets as superior bifunctional electrocatalysts for oxygen reduction and evolution, *Nano Energy* **2016,** *19*, 373-381, 10.1016/j.nanoen.2015.11.027.

[122] Z.X. Pei, H.F. Li, Y. Huang, Q. Xue, Y. Huang, M.S. Zhu, Z.F. Wang, C.Y. Zhi, Texturing in situ: N, S-enriched hierarchically porous carbon as a highly active reversible oxygen electrocatalyst, *Energy and Environmental Science* **2017,** *10* (3), 742-749, 10.1039/c6ee03265f.

[123] H. Jiang, J. Wang, S. Wu, Z. Yuan, Z. Hu, R. Wu, Q. Liu, The pyrolysis mechanism of phenol formaldehyde resin, *Polym. Degrad. Stab.* **2012,** *97* (8), 1527-1533, 10.1016/j.polymdegradstab.2012.04.016.

[124] M. Zhong, E.K. Kim, J.P. McGann, S.E. Chun, J.F. Whitacre, M. Jaroniec, K. Matyjaszewski, T. Kowalewski, Electrochemically active nitrogen-enriched nanocarbons with well-defined morphology synthesized by pyrolysis of self-assembled block copolymer, *J. Am. Chem. Soc.* **2012,** *134* (36), 14846-57, 10.1021/ja304352n.

[125] Y. Zheng, Y. Jiao, Y. Zhu, L.H. Li, Y. Han, Y. Chen, A. Du, M. Jaroniec, S.Z. Qiao, Hydrogen evolution by a metal-free electrocatalyst, *Nat. Commun.* **2014,** *5*, 10.1038/ncomms4783.

[126] S.H. Lee, H.W. Kim, J.O. Hwang, W.J. Lee, J. Kwon, C.W. Bielawski, R.S. Ruoff, S.O. Kim, Three-dimensional self-assembly of graphene oxide platelets into

mechanically flexible macroporous carbon films, *Angew. Chem. Int. Ed. Engl.* **2010,** *49* (52), 10084-8, 10.1002/anie.201006240.

[127] Y. Zhang, X.D. Zhuang, Y.Z. Su, F. Zhang, X.L. Feng, Polyaniline nanosheet derived B/N co-doped carbon nanosheets as efficient metal-free catalysts for oxygen reduction reaction, *J. Mater. Chem. A* **2014,** *2* (21), 7742-7746, 10.1039/c4ta00814f.

[128] X. Zhuang, F. Zhang, D. Wu, X. Feng, Graphene coupled Schiff-base porous polymers: towards nitrogen-enriched porous carbon nanosheets with ultrahigh electrochemical capacity, *Adv. Mater.* **2014,** *26* (19), 3081-6, 10.1002/adma.201305040.

[129] E. Andreoli, A.R. Barron, Correlating Carbon Dioxide Capture and Chemical Changes in Pyrolyzed Polyethylenimine-C60, *Energy Fuels* **2015,** *29* (7), 4479-4487, 10.1021/acs.energyfuels.5b00778.

[130] K. Qu, Y. Zheng, Y. Jiao, X. Zhang, S. Dai, S.-Z. Qiao, Polydopamine-Inspired, Dual Heteroatom-Doped Carbon Nanotubes for Highly Efficient Overall Water Splitting, *Adv. Energy Mater.* **2017,** *7* (9), 1602068, 10.1002/aenm.201602068.

[131] B.Y. Zhu, Z. Deng, W.L. Yang, H.B. Wang, L.J. Gao, Pyrolyzed polyaniline and graphene nano sheet composite with improved rate and cycle performance for lithium storage, *Carbon* **2015,** *92*, 354-361, 10.1016/j.carbon.2015.05.051.

[132] Z.Y. Lin, G.H. Waller, Y. Liu, M.L. Liu, C.P. Wong, 3D Nitrogen-doped graphene prepared by pyrolysis of graphene oxide with polypyrrole for electrocatalysis of oxygen reduction reaction, *Nano Energy* **2013,** *2* (2), 241-248, 10.1016/j.nanoen.2012.09.002.

[133] Z.Y. Lin, G.H. Waller, Y. Liu, M.L. Liu, C.P. Wong, Simple preparation of nanoporous few-layer nitrogen-doped graphene for use as an efficient electrocatalyst for oxygen reduction and oxygen evolution reactions, *Carbon* **2013,** *53*, 130-136, 10.1016/j.carbon.2012.10.039.

[134] K. Yuan, T. Hu, Y. Xu, R. Graf, L. Shi, M. Forster, T. Pichler, T. Riedl, Y. Chen, U. Scherf, Nitrogen-doped porous carbon/graphene nanosheets derived from two-dimensional conjugated microporous polymer sandwiches with promising capacitive performance, *Mater. Chem. Front.* **2017,** *1* (2), 278-285, 10.1039/c6qm00012f.

[135] M. Seredych, K. Laszlo, E. Rodriguez-Castellon, T.J. Bandosz, S-doped carbon aerogels/GO composites as oxygen reduction catalysts, *Journal of Energy Chemistry* **2016,** *25* (2), 236-245, 10.1016/j.jechem.2016.01.005.

[136] X. Huang, L.J. Zhou, D. Voiry, M. Chhowalla, X. Zou, T. Asefa, Monodisperse Mesoporous Carbon Nanoparticles from Polymer/Silica Self-Aggregates and Their Electrocatalytic Activities, *Acs Appl Mater Inter* **2016,** *8* (29), 18891-903, 10.1021/acsami.6b05739.

[137] T.Y. Yang, J. Liu, R.F. Zhou, Z.G. Chen, H.Y. Xu, S.Z. Qiao, M.J. Monteiro, N-doped mesoporous carbon spheres as the oxygen reduction reaction catalysts, *J. Mater. Chem. A* **2014,** *2* (42), 18139-18146, 10.1039/c4ta04301d.

[138] H.J. Liu, J. Wang, C.X. Wang, Y.Y. Xia, Ordered Hierarchical Mesoporous/Microporous Carbon Derived from Mesoporous Titanium-Carbide/Carbon Composites and its Electrochemical Performance in Supercapacitor, *Adv. Energy Mater.* **2011,** *1* (6), 1101-1108, 10.1002/aenm.201100255.

[139] S.W. Bian, Z. Ma, W.G. Song, Preparation and Characterization of Carbon Nitride Nanotubes and Their Applications as Catalyst Supporter, *J. Phys. Chem. C* **2009,** *113* (20), 8668-8672, 10.1021/jp810630k.

[140] X. Li, J.-S. Huang, S. Nejati, L. McMillon, S. Huang, C.O. Osuji, N. Hazari, A.D. Taylor, Role of HF in Oxygen Removal from Carbon Nanotubes: Implications for High Performance Carbon Electronics, *Nano Lett.* **2014,** *14* (11), 6179-6184, 10.1021/nl502401c.

[141] M. Kruk, B. Dufour, E.B. Celer, T. Kowalewski, M. Jaroniec, K. Matyjaszewski, Grafting Monodisperse Polymer Chains from Concave Surfaces of Ordered Mesoporous Silicas, *Macromolecules* **2008,** *41* (22), 8584-8591, 10.1021/ma801643r.

[142] D.J. Quiram, R.A. Register, G.R. Marchand, D.H. Adamson, Chain Orientation in Block Copolymers Exhibiting Cylindrically Confined Crystallization, *Macromolecules* **1998,** *31* (15), 4891-4898, 10.1021/ma971218h.

[143] K. Ishizu, K. Tsubaki, A. Mori, S. Uchida, Architecture of nanostructured polymers, *Prog. Polym. Sci.* **2003,** *28* (1), 27-54, 10.1016/s0079-6700(02)00025-4.

[144] H. Gao, K. Matyjaszewski, Synthesis of functional polymers with controlled architecture by CRP of monomers in the presence of cross-linkers: From stars to gels, *Prog. Polym. Sci.* **2009,** *34* (4), 317-350, 10.1016/j.progpolymsci.2009.01.001.

[145] C. Tang, B. Dufour, T. Kowalewski, K. Matyjaszewski, Synthesis and morphology of molecular brushes with polyacrylonitrile block copolymer side chains and their conversion into nanostructured carbons, *Macromolecules* **2007,** *40* (17), 6199-6205, 10.1021/ma070892o.

[146] R. Yuan, M. Kopeć, G. Xie, E. Gottlieb, J.W. Mohin, Z. Wang, M. Lamson, T. Kowalewski, K. Matyjaszewski, Mesoporous nitrogen-doped carbons from PAN-based molecular bottlebrushes, *Polymer* **2017**,

[147] W. Ding, Z. Wei, S. Chen, X. Qi, T. Yang, J. Hu, D. Wang, L.-J. Wan, S.F. Alvi, L. Li, Space-Confinement-Induced Synthesis of Pyridinic- and Pyrrolic-Nitrogen-Doped Graphene for the Catalysis of Oxygen Reduction, *Angew. Chem. Int. Ed.* **2013,** *52* (45), 11755-11759, 10.1002/anie.201303924.

[148] P. Huber, Soft matter in hard confinement: phase transition thermodynamics, structure, texture, diffusion and flow in nanoporous media, *J. Phys. Condens. Matter.* **2015,** *27* (10), 103102, 10.1088/0953-8984/27/10/103102.

[149] R.M. Michell, A.T. Lorenzo, A.J. Muller, M.C. Lin, H.L. Chen, I. Blaszczyk-Lezak, J. Martin, C. Mijangos, The Crystallization of Confined Polymers and Block Copolymers Infiltrated Within Alumina Nanotube Templates, *Macromolecules* **2012,** *45* (3), 1517-1528, 10.1021/ma202327f.

[150] T. Uyar, M. Rusa, A.E. Tonelli, Polymerization of Styrene in Cyclodextrin Channels: Can Confined Free-Radical Polymerization Yield Stereoregular Polystyrene?, *Macromol. Rapid Commun.* **2004,** *25* (15), 1382-1386, 10.1002/marc.200400165.

[151] F. Candau, O. Braun, F. Essler, K. Stahler, J. Selb, Polymerization in nanostructured media: Applications to the synthesis of associative polymers, *Macromolecular Symposia* **2002,** *179* (1), 13-25, Doi 10.1002/1521-3900(200203)179:1<13::Aid-Masy13>3.0.Co;2-Z.

[152] Y. Lee, R.S. Porter, Crystallization of poly(etheretherketone) (PEEK) in carbon fiber composites, *Polym. Eng. Sci.* **1986,** *26* (9), 633-639, 10.1002/pen.760260909.

[153] A. Shavit, R.A. Riggleman, Influence of Backbone Rigidity on Nanoscale Confinement Effects in Model Glass-Forming Polymers, *Macromolecules* **2013,** *46* (12), 5044-5052, 10.1021/ma400210w.

[154] Y.L. Loo, R.A. Register, A.J. Ryan, G.T. Dee, Polymer crystallization confined in one, two, or three dimensions, *Macromolecules* **2001,** *34* (26), 8968-8977, 10.1021/ma011521p.

[155] A.J. Muller, M.L. Arnal, M. Trujillo, A.T. Lorenzo, Super-nucleation in nanocomposites and confinement effects on the crystallizable components within block copolymers, miktoarm star copolymers and nanocomposites, *Eur. Polym. J.* **2011,** *47* (4), 614-629, 10.1016/j.eurpolymj.2010.09.027.

[156] W. Ding, Z. Wei, S. Chen, X. Qi, T. Yang, J. Hu, D. Wang, L.J. Wan, S.F. Alvi, L. Li, Space-confinement-induced synthesis of pyridinic- and pyrrolic-nitrogen-doped graphene for the catalysis of oxygen reduction, *Angew. Chem. Int. Ed. Engl.* **2013,** *52* (45), 11755-9, 10.1002/anie.201303924.

[157] S.V. Larin, S.G. Falkovich, V.M. Nazarychev, A.A. Gurtovenko, A.V. Lyulin, S.V. Lyulin, Molecular-dynamics simulation of polyimide matrix pre-crystallization near the surface of a single-walled carbon nanotube, *Rsc Advances* **2014,** *4* (2), 830-844, 10.1039/c3ra45010d.

[158] M. Trujillo, M.L. Arnal, A.J. Muller, M.A. Mujica, C.U. de Navarro, B. Ruelle, P. Dubois, Supernucleation and crystallization regime change provoked by MWNT addition to poly(epsilon-caprolactone), *Polymer* **2012,** *53* (3), 832-841, 10.1016/j.polymer.2011.12.028.

[159] E.D. Laird, C.Y. Li, Structure and Morphology Control in Crystalline Polymer-Carbon Nanotube Nanocomposites, *Macromolecules* **2013,** *46* (8), 2877-2891, 10.1021/ma400035j.

[160] D. Wu, Z. Li, M. Zhong, T. Kowalewski, K. Matyjaszewski, Templated synthesis of nitrogen-enriched nanoporous carbon materials from porogenic organic precursors prepared by ATRP, *Angew. Chem. Int. Ed. Engl.* **2014,** *53* (15), 3957-60, 10.1002/anie.201309836.

[161] Q. Sun, B. He, X.Q. Zhang, A.H. Lu, Engineering of Hollow Core-Shell Interlinked Carbon Spheres for Highly Stable Lithium-Sulfur Batteries, *ACS Nano* **2015,** *9* (8), 8504-13, 10.1021/acsnano.5b03488.

[162] J. Fu, Q. Xu, J. Chen, Z. Chen, X. Huang, X. Tang, Controlled fabrication of uniform hollow core porous shell carbon spheres by the pyrolysis of core/shell polystyrene/cross-linked polyphosphazene composites, *Chem. Commun.* **2010,** *46* (35), 6563-5, 10.1039/c0cc01185a.

[163] S. Kubo, R.J. White, K. Tauer, M.M. Titirici, Flexible Coral-like Carbon Nanoarchitectures via a Dual Block Copolymer-Latex Templating Approach, *Chem. Mater.* **2013,** *25* (23), 4781-4790, 10.1021/cm4029676.

[164] J.P. Han, G.Y. Xu, B. Ding, J. Pan, H. Dou, D.R. MacFarlane, Porous nitrogen-doped hollow carbon spheres derived from polyaniline for high performance supercapacitors, *J. Mater. Chem. A* **2014,** *2* (15), 5352-5357, 10.1039/c3ta15271e.

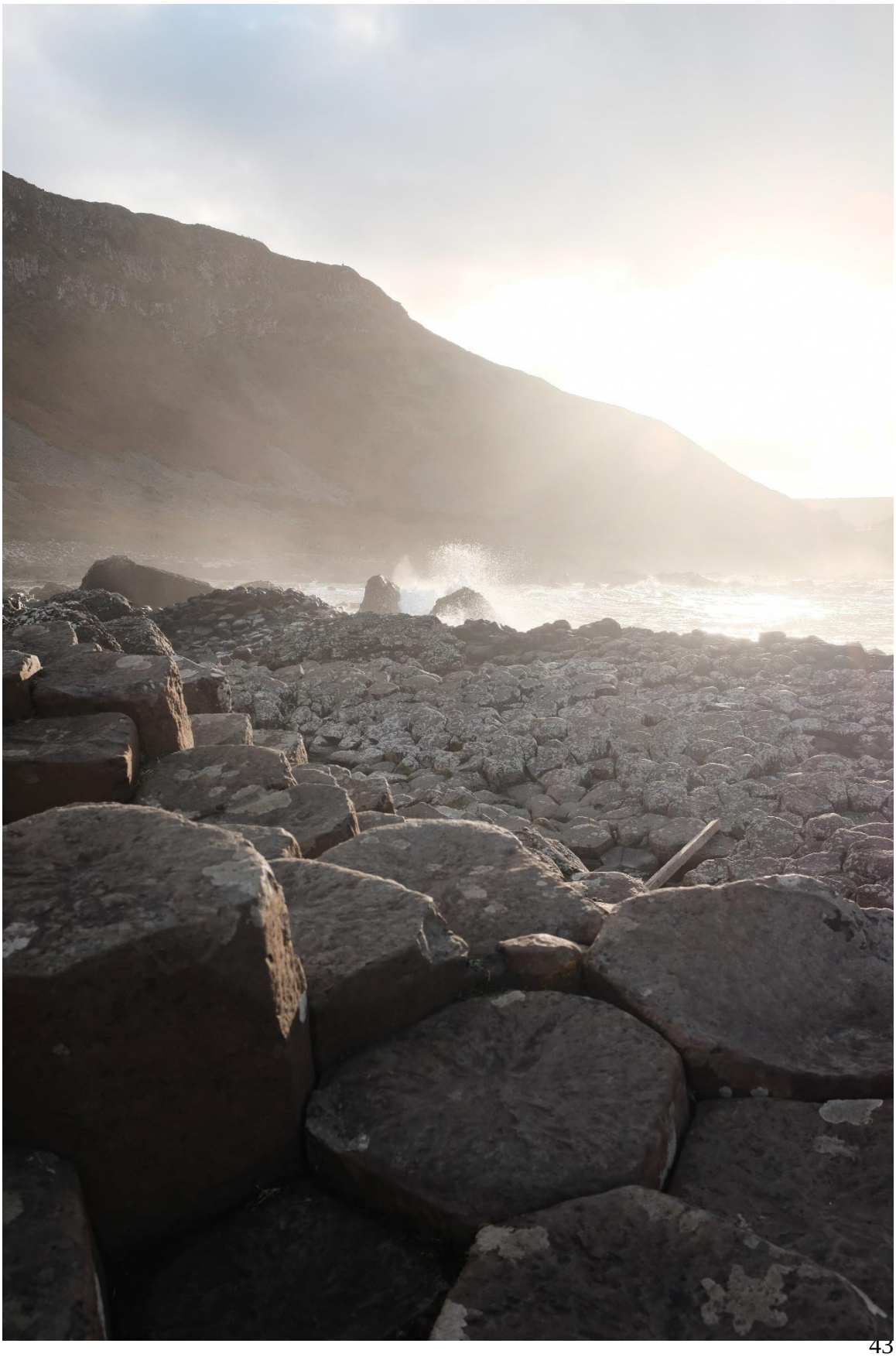

Chapter 2: Controlling Pore Size Through Block Copolymer Degree of Polymerization

This work was in collaboration with Dr. Maciej Kopeć and Rui Yuan with two main components: synthesis of polyacrylonitrile-*block*-poly(butyl acrylate) (PAN-*b*-PBA) copolymers with differing overall degrees of polymerization by supplemental activator reducing agent atom transfer radical polymerization (SARA ATRP), which was their contribution; and characterization of their micro/nanostructure evolution as a function of degree of polymerization.

The main challenge in in the characterization was to reconcile differences between measures of surface area and pore size obtained by analysis of N_2 adsorption, transmission electron microscopy (TEM), and small angle X-ray scattering (SAXS). Each method probed the carbon samples differently but led to a clearer picture of the structural evolution of the carbons across different block copolymer degrees of polymerization.

2.1 Abstract

A series of polyacrylonitrile-*block*-poly(butyl acrylate) (PAN-*b*-PBA) copolymers was prepared by supplemental activator reducing agent atom transfer radical polymerization (SARA ATRP). These copolymers were then used as precursors to pyrolytic nanostructured carbons with the PAN blocks serving as nitrogen-rich carbon precursors, and the PBA block acting as a sacrificial porogens. The study revealed that while the size of mesopores can be controlled by the size of the porogenic block, the connectivity of pores diminishes with the decrease of the overall molecular weight of the precursor. This partial loss of mesopore connectivity was attributed to the weaker phase segregation between the blocks of shorter lengths inferred from the shape of small angle x-ray scattering (SAXS) profiles, and from the crystallinity of polyacrylonitrile phase.

Table of Contents Figure

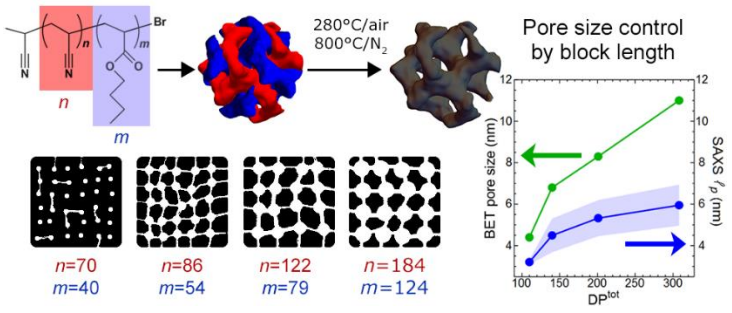

M. Kopec, R. Yuan, E. Gottlieb, C.M.R. Abreu, Y. Song, Z. Wang, J.F.J. Coelho, K. Matyjaszewski, T. Kowalewski, Polyacrylonitrile-b-poly(butyl acrylate) Block Copolymers as Precursors to Mesoporous Nitrogen-Doped Carbons: Synthesis and Nanostructure, *Macromolecules* **2017,** *50* (7), 2759-2767, 10.1021/acs.macromol.6b02678.

2.2 Introduction

Mesoporous, nitrogen-doped nanocarbons are currently receiving considerable attention, due to a range of electrochemical properties, which make these materials of particular interest in sustainable energy-related applications.[1-7] Over the past several years, we have developed a facile method to synthesize copolymer-templated nitrogen-enriched nanocarbons (CTNCs), through pyrolysis of nanostructured block copolymers (BCPs) containing polyacrylonitrile (PAN), namely poly(butyl acrylate)-*block*-polyacrylonitrile (PBA-*b*-PAN).[8-10] The well-defined structure of those copolymers resulted from the use of atom transfer radical polymerization (ATRP) which provided precise control over their molecular weight (MW) and molecular weight distribution (MWD).[11-16] Owing to the combination of high surface area and the presence of highly accessible electrochemically-active nitrogen atoms, CTNCs were successfully used as supercapacitors,[9, 10] electrocatalysts for oxygen reduction reaction (ORR)[17] and hydrogen evolution reaction (HER),[18] CO_2 sorbents[19] as well as cathodes in dye-sensitized solar cells (DSSC).[20]

The high surface areas desirable in abovementioned applications were achieved by the use of PBA-*b*-PAN BCPs of the composition assuring the formation of bicontinuous morphologies.[9] The preservation of BCP nanostructure upon pyrolysis, which involves heating the material to temperatures in excess of 600 ºC under anaerobic conditions, was realized through the use of a moderate temperature (200–300 ºC) oxidative annealing step, commonly used in the synthesis of PAN-derived carbon fibers.[21-23] Using this step allowed successful preservation of the BCP morphology in the synthesis of nanostructured carbon films,[8, 24] particles,[25] molecular brushes[26] and bulk mesoporous carbons.[9, 27] Other groups followed this approach and reported polyacrylonitrile-*b*-poly(methyl methacrylate) (PAN-*b*-PMMA),[28-30] polyacrylonitrile-*b*-polystyrene (PAN-*b*-PS)[31-33] or poly(*tert*-butyl acrylate)-*b*-polyacrylonitrile (P*t*BA-*b*-PAN)[34] BCPs as efficient carbon precursors. Furthermore, in our past studies of electrochemical applications of CTNCs, we have established that the desirable bicontinuous morphology can be obtained for BCPs containing ~40 wt % of PAN.[9, 17] Use of these precursors routinely yields CTNCs with surface areas of ~500 m^2/g. One question that has not been addressed so far is the extent to which the pore size and surface area of CTNCs could be varied by using precursors with the same PAN/PBA ratio but differing overall MW.

In the present study, we were able to address this issue by resorting to a newly developed synthetic approach *via* supplemental activator reducing agent (SARA) ATRP.[13, 35-37] Since the controlled synthesis of PAN-*b*-PBA copolymers is challenging due to different activities of AN and BA, and low solubility of PAN, the first part of this report is dedicated to the detailed description of the development of appropriate synthetic conditions. The SARA ATRP enabled preparation of BCPs with precisely

controlled block lengths and low dispersities (M_w/M_n < 1.2) at room temperature. Additionally, SARA ATRP allowed to reduce the copper catalyst concentration to only 50 ppm from previously used >1000 ppm.[9, 15] This is of particular importance for potential applications of CTNCs, as any residual metal may obscure the origin of catalytic activity in N-doped carbons.[38]

The structural studies described in the second part were focused on correlating BCP/CTNC nanostructure using the combination of small x-ray scattering (SAXS), transmission electron microscopy (TEM), and nitrogen adsorption. The impact of the overall molecular weight of BCPs on CTNC morphology was studied using a series of BCPs with the overall content demonstrated previously to yield bicontinuous morphologies. We show that while the size of mesopores in CTNCs can be indeed systematically varied by total MW, the accessible surface area is limited by the weak segregation in low-MW BCPs. In addition, thermal analysis was used to investigate the relationship between reactions occurring in both blocks during transformation into nanocarbon and wide-angle x-ray scattering (WAXS) revealed the dependence of the crystallinity of PAN blocks on the MW of the precursor.

2.3 Results and Discussion

Figure 2.1 shows the TEM images of CTNCs prepared from BCPs. All BCPs were of similar composition, between 38 and 42 wt.% of PAN. They all reveal the presence of characteristic features of progressively increasing size and definition, originating from BCP templating. Quantitative assessment of the relationship of BCP/CTNC morphology was carried out by comparison of SAXS patterns obtained for carbons and their copolymer precursors.

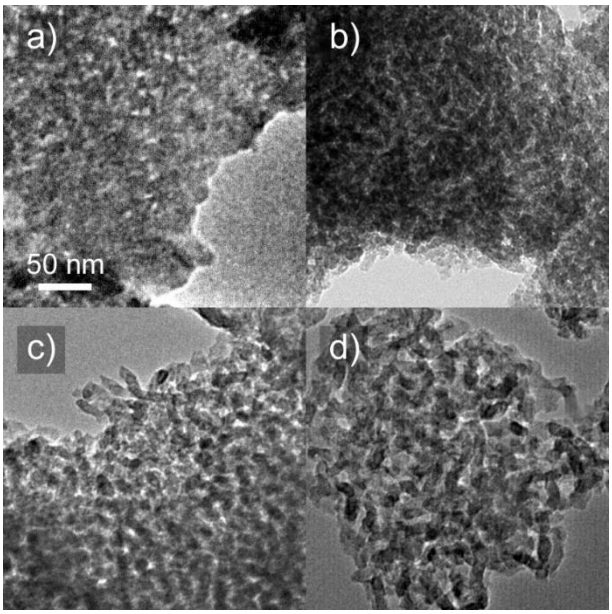

Figure 2.1 TEM images of mesoporous nanocarbons prepared by pyrolysis of (a) $(AN)_{70}$-*b*-$(BA)_{40}$ (b) $(AN)_{86}$-*b*-$(BA)_{54}$, (c) $(AN)_{122}$-*b*-$(BA)_{79}$ and (d) $(AN)_{184}$-*b*-$(BA)_{124}$.

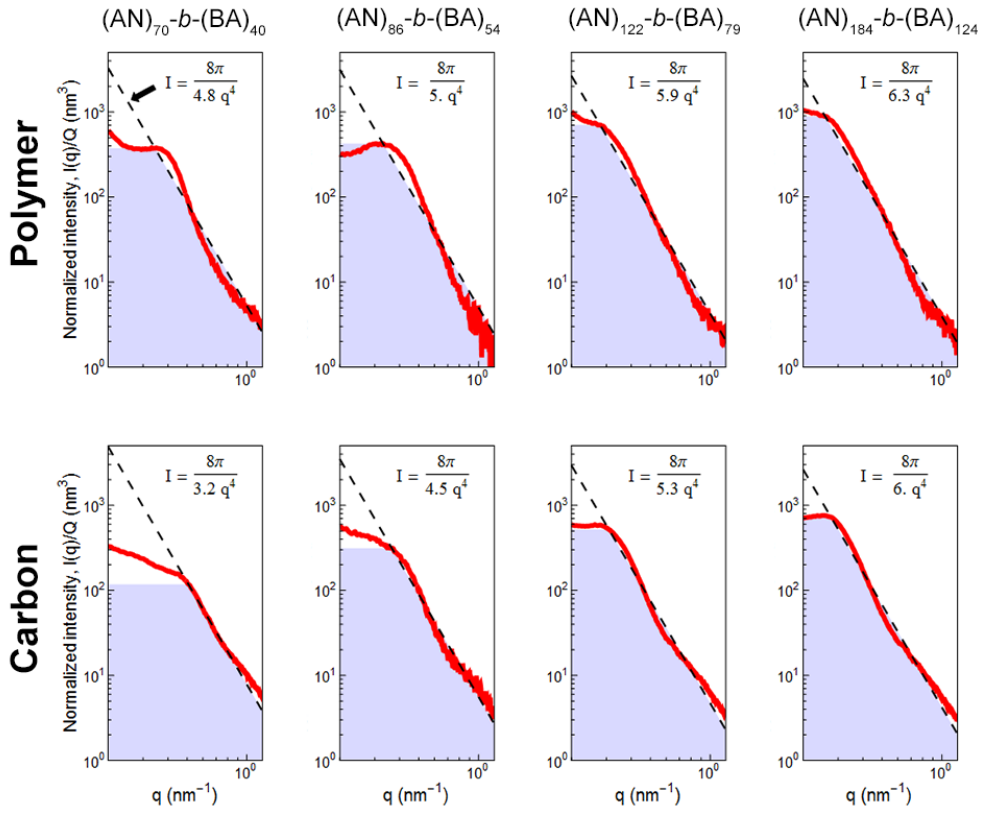

Figure 2.2 Invariant-normalized azimuthally-averaged SAXS scattering patterns (plotted in red) for BCPs (top row) and resulting CTNCs (bottom row). Blue areas show the regions used for calculating the invariant according to eq.1. Dashed lines show the results of fitting to q^{-4}. The inset slope equation shows the relationship between the fitting line and l_p, which is the denominator term.

Since the 2D patterns of all the samples were isotropic, they were azimuthally averaged and normalized by the invariant, yielding radial profiles of scattering intensity, I, as a function of momentum transfer, q, shown in **Figure 2.2**, as double logarithmic plots. In order to facilitate quantitative comparisons, all profiles were normalized by the scattering invariant, Q (eq.(2.1)).

$$Q = \frac{1}{2\pi^2}\int_0^\infty q^2\, I(q)dq \tag{2.1}$$

While the presented profiles do not show specific features such as Bragg peaks, which would be indicative of regular periodicity, they all follow the same pattern of decay, with the intensity decreasing as $I(q)\sim q^{-4}$, manifested in double logarithmic coordinates as straight lines (dashed lines in **Figure 2.2**). Given the evidence of nanostructures shown in TEM images (**Figure 2.1**), this decay pattern can be ascribed to the form predicted by the familiar Porod's law (eq.(2.2),

$$I_{norm}(q) = \frac{8\pi\, l_p^3}{\left(1 + l_p^2 q^2\right)^2} \approx \frac{8\pi}{l_p q^4} \tag{2.2}$$

which describes scattering from an isotropic, two phase system with sharp boundaries, characterized by some characteristic feature length (length of inhomogeneity, l_p).[39] The length of inhomogeneity in Porod's law is defined as

$$\frac{1}{l_p} = \frac{1}{\langle l_1\rangle} + \frac{1}{\langle l_2\rangle} \tag{2.3}$$

where $\langle l_1\rangle$ and $\langle l_2\rangle$ denote the average lengths traversed through phases 1 and 2 by a large number of *"rays"* cast through the structure in random directions. The dashed lines superimposed on the radial profiles shown in **Figure 2.2** represent fits to the limiting form of Porod's law, which predicts the linear behavior in double logarithmic coordinates.

Figure 2.3a shows the values of l_p obtained from those fits for BCPs (red) and CTNCs (blue), plotted against the total degree of polymerization of a copolymer precursor, DP^{tot}= DP^{PAN}+DP^{PBA}. The comparison of such constructed plots immediately points to the systematic increase of the characteristic length scale of the nanostructure with the increase of block lengths, and to the direct correspondence between the nanostructure of CTNCs and their respective precursors.

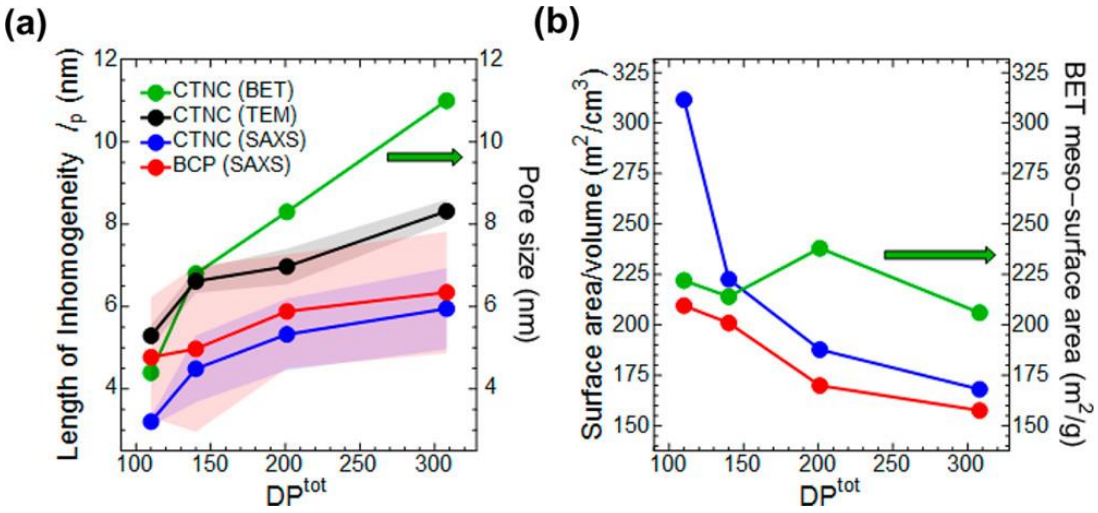

Figure 2.3 (a) Lengths of inhomogeneity for BCPs (red) and CTNCs (blue) from SAXS, as well as simulated lengths of inhomogeneity from TEM images (black) and pore sizes from BET (green). (b) Interfacial surface area to volume ratios from SAXS and gravimetric surface area from BET.

Similar values of l_p of CTNC samples were also obtained by quantitative analysis of TEM images, which followed the chord length geometry underlying Porod's analysis. As illustrated in **Figure 2.4**, the first step in this analysis involved digital extraction of multiple intensity profiles along randomly chosen straight paths across preprocessed TEM images. The profiles were then segmented according to their intensity into chords (n=300) passing through the dark and bright regions (carbon matrix and mesopores, respectively). The average lengths of the extracted chords were then used to calculate the l_p, according to eq.3, and plotted in **Figure 2.3a**. The obtained values of l_p were found to be in good

agreement with the values obtained by SAXS, increasing in a similar manner with the DP^{tot}. Altogether, this combined SAXS and TEM analysis of BCPs and resulting CTNCs confirmed the control of domain size with precursor molecular weights, and the preservation of that overall nanostructure upon stabilization and pyrolysis.

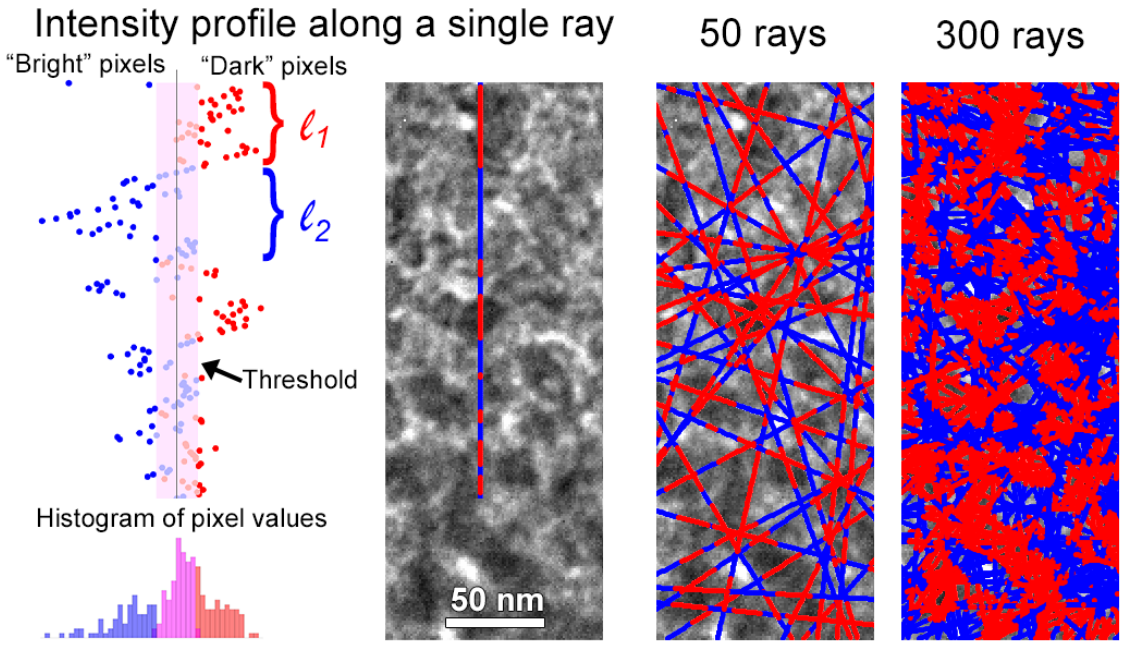

Figure 2.4 The ray casting process used to calculate lengths of inhomogeneity for each TEM carbon. Each ray was binarized by setting values above and below a half standard deviation from the mean, and using 0^{th} order interpolation for values within a half standard deviation of the mean.

Furthermore, the similar dependence of the characteristic length of CTNC nanostructures on the *DP* of the precursor was also revealed through pore size measurements carried out using nitrogen adsorption analysis by BET method. In all instances, the adsorption/desorption isotherms (**Figure 2.5a**) revealed the characteristic hysteresis, originating from capillary condensation within the mesopores of the material. As shown in **Figure 2.5** and **Table 3.1**, pore size distributions, calculated through BJH analysis of adsorption branches of isotherms, systematically shifted to higher values with the increase of the MW of the precursor. Pore size distribution maxima are used in **Table**

3.1 as a more reliable absolute measure, but to compare against trends in l_p values, average mesopore size is used as it is a more compatible metric (**Figure 2.3a**).

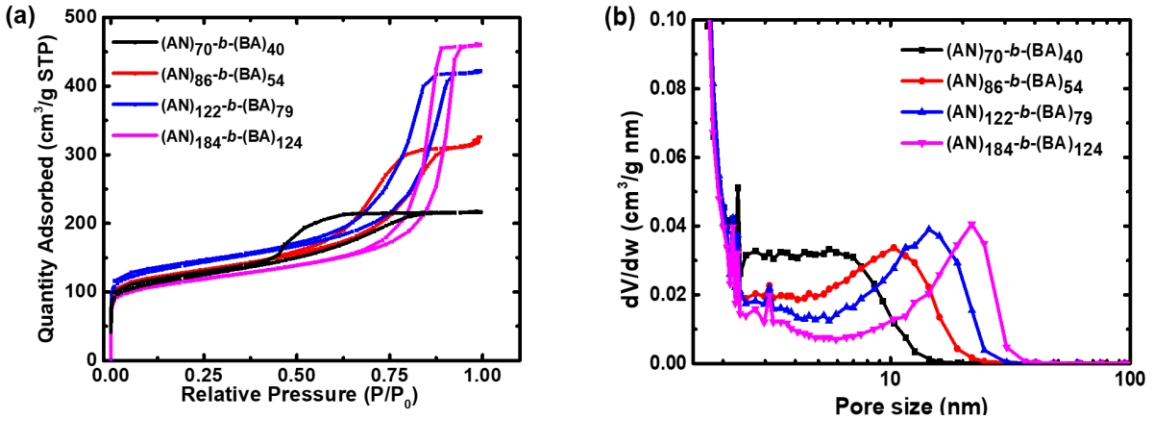

Figure 2.5 (a) Nitrogen adsorption isotherms and (b) pore size distribution of CTNCs synthesized from PAN-*b*-PBA block copolymers with different molecular weight.

Table 2.1 Specific surface areas and pore size distribution of mesoporous carbons prepared from PAN-*b*-PBA block copolymers

Sample	PAN (wt %)	Specific Surface Area (m^2/g)			Pore volume (cm^3/g)	Mesopore size distribution maxima[b] (nm)
		Micropores[a] (<2 nm)	Mesopores[b]	Total		
$(AN)_{70}$-*b*-$(BA)_{40}$	42.0	175	222	397	0.27	5.5
$(AN)_{86}$-*b*-$(BA)_{54}$	39.7	207	214	421	0.49	10.3
$(AN)_{122}$-*b*-$(BA)_{79}$	39.0	220	238	458	0.56	14.5
$(AN)_{184}$-*b*-$(BA)_{124}$	38.0	173	206	379	0.65	21.8

It should be pointed out, however, that while the trends in mesopore sizes and lengths of inhomogeneity in CTNCs were in agreement, no analogous trend has been observed for the overall gravimetric surface area of CTNCs (**Figure 2.3b**). While the surface area initially increased when moving from the CNTC obtained from the highest

MW precursor, namely $(AN)_{184}$-*b*-$(BA)_{124}$, to the $(AN)_{122}$-*b*-$(BA)_{79}$, the trend did not continue as expected for CTNCs obtained from precursors of lower MWs. One needs to keep in mind, however, that nitrogen adsorption measurements detect only physically accessible pores. On the other hand, inaccessible pores still contribute to the interfacial area between phases. As such, they should contribute to the overall scattering, the intensity of which depends on the interfacial area of phases with different electron densities. Porod's analysis provides the basis to quantify this *volumetric* interfacial area (m^2/cm^3) according to eq.(2.4), in which ϕ_1 and ϕ_2 denote volume fractions of respective phases ($\phi_1 + \phi_2 = 1$).

$$S_V = 4\,\frac{\phi_1\phi_2}{l_p} \tag{2.4}$$

Note that for $0.3 \leq \phi_1 \leq 0.5$ ($0.5 \leq \phi_2 \leq 0.7$), the product $\phi_1\phi_2$ varies between 0.21 and 0.25, which makes it possible to quite accurately estimate S_V from the length of inhomogeneity, even without knowledge of exact values of ϕ_1 and ϕ_2. This range applies to CTNCs discussed herein, since in all instances, pores account for approximately half of their volume. For comparison, values of volumetric interfacial area, calculated from eq.(2.4) (with $\phi_1 = \phi_2 = 0.5$) and expressed in m^2/cm^3, are shown in **Figure 2.3b**. Confirming our concern that nitrogen adsorption measurements might not have detected all the pores present it the material, the *volumetric* interfacial area calculated from SAXS profiles indeed exhibited the expected marked increase with the decrease of precursor DP^{tot}.

Since SAXS measurements provide the volumetric surface area, the direct comparison of interfacial areas requires the knowledge of the density of the carbon matrix, ρ_c. While the exact value of this quantity is not available, one can reverse the question,

asking what density value would yield consistency between volumetric and gravimetric areas. The estimate of the carbon matrix density performed in this manner, yields approximately $\rho_c = 2.08\text{-}2.80$ g/cm^3, which is close to the typical values for disordered carbon materials (2.2 g/cm^3).[40] This agreement indicates that the comparison of interfacial area from SAXS and gravimetric surface area from nitrogen adsorption can be carried out quantitatively.

Whereas the interfacial area analysis further confirms the preservation of the overall nanoscale morphology upon conversion of BCPs into CTNCs, materials prepared from the lowest MW precursor, namely $(AN)_{70}$-*b*-$(BA)_{40,}$ suffer from some loss of connectivity. The explanation of this loss emerges upon re-inspection of SAXS profiles of BCPs shown in **Figure 2.2**. Specifically, the scattering intensity profiles for the two lower molecular weight BCPs decay in the mid-q range faster than implied by the q^{-4} power law. Such faster decay patterns are usually indicative of the diffuse nature of the interface, as opposed to the sharp interface invoked in the Porod's law. In phase-separated block copolymers, the diffuse character of the interface usually points to a weak segregation between the blocks, due to a lower value of the χN product, which governs the strength of the segregation.[41] This dependence of phase segregation strength on the block lengths can thus explain the diffuse nature of the interface in lower molecular weight BCPs, inferred from the scattering profiles. It should be pointed out that no deviations from q^{-4} power law are evident in any of the CTNCs, which is consistent with the expected sharp boundaries between carbon matrix and pores. Further consequences of the deviations scattering by lower molecular weight BCPs from q^{-4} power law are also evident in deviations of the values of l_p (**Figure**

2.3a) and interfacial area (**Figure 2.3b**) for those samples from the trends exhibited by their counterparts.

In general, polymers with the overall structure $(CH_2CHR)_n$, where R is a side group, can crystallize only if they are sufficiently stereo-regular (e.g. isotactic or syndiotactic), which assures periodicity along the polymer backbone. PAN is one of the notable exceptions in this regard since WAXS patterns of atactic PAN (*a*-PAN) exhibit a combination of crystalline peaks and broad, amorphous halos, typical for partially crystalline systems.[42] As shown in **Figure 2.6**, patterns of this kind were also observed in the case of the studied BCP series. In all instances, the scattering profiles could be decomposed into components originating from PAN (two sharp peaks and a broad halo) and PBA (two broad halos). The ratio between the total areas under the respective peaks corresponding to PAN and PBA phases remained constant across the entire series, consistently with nearly identical overall composition of all the BCPs.

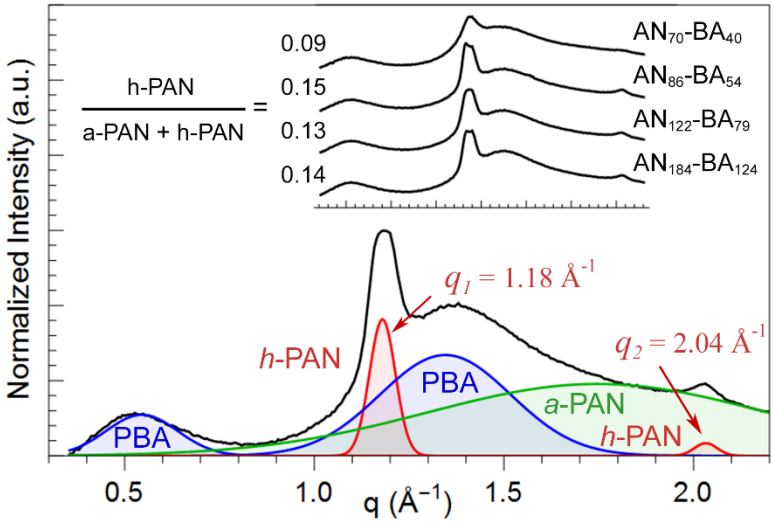

Figure 2.6 WAXS profile of $(AN)_{122}$-*b*-$(BA)_{79}$, and its decomposition into: amorphous halos of PBA (blue), amorphous halo of PAN (green), and Bragg peaks corresponding to hexagonal packing of PAN (red). *h*-PAN corresponds to the total area of the sharp Bragg peaks of PAN at q_1 and q_2, and *a*-PAN corresponds to the area under the broad peak determined through fitting and decomposition. Inset: WAXS profiles of all copolymers with crystalline fractions indicated on the left.

Sharp Bragg peaks in WAXS profiles, shown in **Figure 2.6**, originate from familiar hexagonal arrangement of PAN chains, adopting a predominantly extended all-trans conformation driven by nitrile dipole moments.[43, 44] The inter-planar spacing of 5.32 Å, inferred from the position of the first order Bragg peak, $q_2 = 1.18$ Å^{-1} is consistent with literature reports and corresponds to an inter-helical spacing of 6.13 Å.[42, 43, 45] Likewise, the position of the second order peak, $q_2 = 2.04$ Å^{-1}, is within 1% from the value of $q_2 = \sqrt{3}\, q_1$ expected for hexagonal packing. While the positions of Bragg peaks varied by less than 0.1% from sample to sample, the ratio of peak areas *h*-PAN/(*h*-PAN+*a*-PAN), providing the measure of PAN crystallinity was markedly lower for the lowest MW copolymer (0.09 vs. ~ 0.14). The lower overall crystallinity of this sample is consistent with weaker segregation between PAN and PBA blocks in the lowest MW system presented in the previous section.

At this point, it should be noted that partial crystallinity of PAN could make PAN/PBA copolymers behave as *de facto* three phase systems, with amorphous PBA and crystalline/amorphous PAN. Such a three-phase nature of BCPs could adversely affect the nanostructure preservation and overall yield of carbon upon pyrolysis. It should be kept in mind, however, that the distinct amorphous halo in WAXS profiles of PAN may arise from the rotational disorder about the chain axes of hexagonally packed chains, and does not necessarily have to indicate the presence of two phases within partially crystalline PAN.[45] Such a single phase nature of PAN would be beneficial to good preservation of nanostructure upon conversion of PAN-*b*-PBA copolymers to CTNCs.

2.4 Conclusion

A series of PAN-*b*-PBA copolymers, serving as precursor to nitrogen-enriched nanostructured carbons, was prepared by SARA ATRP and used to investigate the impact of precursor molecular weight on carbon nanostructure. The developed new synthetic conditions allowed to greatly diminish the copper catalyst concentration, a crucial aspect for potential applications of CTNC in energy storage/conversion, but also to prepare PAN-*b*-PBA block copolymers with precisely controlled block lengths.

Detailed structural studies of PAN-*b*-PBA precursors and their resulting carbons confirmed good preservation of BCP nanostructure upon pyrolysis. The length of inhomogeneity in both BCPs and nanocarbons as well as size of mesopores have been shown to systematically decrease accordingly with the molecular weight of precursors. However, the concomitant increase of the mesoscale area evident from SAXS studies has not been paralleled by the similar increase in the accessible gravimetric surface area, measured by nitrogen adsorption.

The reason for this discrepancy has been ascribed to some loss of mesopore connectivity, due to weaker block segregation in copolymers of the lowest molecular weight. The weaker segregation was also a likely cause of lower overall crystallinity of the PAN components revealed by WAXS studies for the lowest molecular weight for BCPs. The obtained results point to the immiscibility of the blocks as a limiting factor in increasing the surface area in CTNCs through the decrease of the molecular weight of BCP precursors. Nevertheless, the presented approach allows to finely tune mesopore size in CTNCs while maintaining relatively high surface area (up to 500 m^2/g), by simply adjusting block lengths of the PAN-*b*-PBA precursor.

2.5 Experimental

Materials. Acrylonitrile (AN, Sigma-Aldrich, >99%) and *n*-butyl acrylate (BA, Sigma-Aldrich, >99%) were purified by passing over a column of basic alumina to remove the inhibitor. 2-Bromopropionitrile (BPN, Sigma-Aldrich, 97%), 2,2'-bipyridine (bpy, Sigma-Aldrich, >99%), N,N,N',N",N"– pentamethyldiethylenetriamine (PMDETA, Sigma-Aldrich, 99%), copper (II) bromide ($CuBr_2$, Acros Organics, >99%), copper wire (diameter 1.0 mm, 99.9+%, Aldrich), dimethylformamide (DMF, Fisher, 99.9%), dimethyl sulfoxide (DMSO, Fisher, 99.9%), methanol (Fisher, 99.9%), and diethyl ether (Fischer, 99%) were used as received. Tris(2-pyridylmethyl)amine (TPMA) was synthesized according to a published procedure.[46, 47]

Polymerization of AN by SARA ATRP. In a typical procedure, copper wire (3cm × 1mm) was placed in a 10 mL Schlenk flask. Monomer (AN) was bubbled with nitrogen for 20 minutes and 3.0 mL (45.3 mmol) was injected into the reactor under nitrogen. Initiator (BPN, 31.3 mg, 0.227 mmol) was then injected into a mixture of $CuBr_2$ (0.51 mg, 0.002 mmol), bpy (1.06 mg, 0.007 mmol), DMF (0.5 mL, NMR standard) and DMSO (4.5 mL), previously bubbled with nitrogen for 20 minutes. The resulting mixture was transferred to the Schlenk flask under nitrogen. The reaction was conducted at room temperature. Samples of the reaction mixture were collected periodically during the polymerization by using an airtight syringe while purging the side arm of the Schlenk flask with nitrogen.

Chain extension of PAN-Br with BA by SARA ATRP. In a typical procedure, 8.23 g (1.75 mmol, 1 equiv.) of PAN-Br macroinitiator ($M_{n,\,NMR}$ = 4700, M_w/M_n = 1.25) was dissolved in 50 mL of DMF. Then, the solution was added to a 100 mL Schlenk flask

containing 1.37 mg $CuBr_2$ (0.0035 mmol, 0.01 equiv.), TPMA 5.34 mg (0.018 mmol, 0.0105 equiv) and bubbled with nitrogen for 30 min. 17.5 mL of deoxygenated BA (122 mmol, 70 equiv.) was then carefully added under vigorous stirring to prevent PAN precipitation. Cu wire (14 cm × 1 mm), previously cleaned with HCl:MeOH solution (1:1, v/v) was added to start polymerization at room temperature. The resulting block copolymer was precipitated into methanol/water (1:1, v/v), filtered and dried under vacuum overnight.

Preparation of porous carbons. Bulk carbons were prepared directly from precipitated powders. First, the BCP samples were stabilized by heating to 280 °C under air flow (150 mL/min) at a rate of 1 °C/min and kept at this temperature for 1 hour. Stabilized samples were then pyrolyzed under nitrogen gas flow (150 mL/min) by heating to 800 ºC at a rate of 10 °C/min and kept at this temperature for 30 min.

Characterization. ^{1}H NMR spectroscopy measurements were performed on a Bruker Avance 300 MHz spectrometer and used to determine the conversion of monomer in DMSO-d_6 and M_n of resulting (co)polymers in DMSO-d_6 for PAN homopolymer and DMF-d_7 for block copolymers. The molecular weights and molecular weight distributions (M_w/M_n) were determined by gel permeation chromatography (GPC). The GPC system used a Waters 515 HPLC pump and a Waters 2414 refractive index detector using Waters columns (Styrogel 10^2, 10^3, 10^5 Å) with 10 mM LiBr-containing DMF as the eluent at a flow rate of 1 mL/min at 50 °C using linear poly(ethylene oxide) (PEO) standards for PAN and PMMA for PAN-*b*-PBA copolymers.[48] Differential scanning calorimetry (DSC) was performed on a TA Instruments Q20 and a Q2000, as well as on a Seiko DSC2100. Gas flow was kept at 20 mL/min either purified air or N_2. Sample sizes were between 1 and 5 mg. Thermogravimetric analysis (TGA) was performed on a TA instruments Q50

with 60mL/min flow rate of air or nitrogen. Brunauer-Emmet-Taller (BET) specific surface area measurements were carried out using a Micromeritics Gemini VII 2390 Surface Area Analyzer with VacPrep 061 degasser. Carbon samples were degassed at 300 ºC and 20 mTorr vacuum for at least 8 hours prior to measurement. The adsorption isotherms were fitted to the Barrett-Joyner-Halenda (BJH) model with the Kruk-Jaroniec-Sayari (KJS) correction to yield pore-size distributions. The surface area of micropores was estimated using the *t*-plot method with the KJS thickness correction. Transmission electron microscopy (TEM) (HT-7700, Hitachi Ltd. Tokyo, Japan) was conducted at an accelerating voltage of 120 kV. Small Angle X-ray Scattering (SAXS) was performed using Rigaku S-MAX3000 instrument equipped with a 1.77 m sample to detector distance, a sealed microfocus source (Cu K-alpha, λ=0.15418 nm), and a wire-array detector (1024 by 1024, pixel size 0.1 mm). SAXS was collected with powders packed into a 5 mm thick sample holder, with scotch tape sealing the powders. All BCP samples analyzed were annealed prior to any measurements as described above. Since all samples were isotropic, 2D patterns were converted into 1D radial decay profiles in q space using custom procedures written in *Mathematica* (Wolfram Research, Inc.)

2.6 References

[1] C. Liang, Z. Li, S. Dai, Mesoporous Carbon Materials: Synthesis and Modification, *Angew. Chem. Int. Ed.* **2008,** *47* (20), 3696-3717, 10.1002/anie.200702046.

[2] Y. Zhai, Y. Dou, D. Zhao, P.F. Fulvio, R.T. Mayes, S. Dai, Carbon Materials for Chemical Capacitive Energy Storage, *Adv. Mater.* **2011,** *23* (42), 4828-4850, 10.1002/adma.201100984.

[3] H. Wang, T. Maiyalagan, X. Wang, Review on Recent Progress in Nitrogen-Doped Graphene: Synthesis, Characterization, and Its Potential Applications, *ACS Catal.* **2012,** *2* (5), 781-794, 10.1021/cs200652y.

[4] L. Dai, Y. Xue, L. Qu, H.-J. Choi, J.-B. Baek, Metal-Free Catalysts for Oxygen Reduction Reaction, *Chemical Reviews* **2015,** *115* (11), 4823-4892,

[5] T. Lin, I.W. Chen, F. Liu, C. Yang, H. Bi, F. Xu, F. Huang, Nitrogen-doped mesoporous carbon of extraordinary capacitance for electrochemical energy storage, *Science* **2015,** *350* (6267), 1508-1513,

[6] D. Guo, R. Shibuya, C. Akiba, S. Saji, T. Kondo, J. Nakamura, Active sites of nitrogen-doped carbon materials for oxygen reduction reaction clarified using model catalysts, *Science* **2016,** *351* (6271), 361-365,

[7] C. Hu, L. Dai, Carbon-Based Metal-Free Catalysts for Electrocatalysis beyond the ORR, *Angew. Chem. Int. Ed.* **2016,** *55* (39), 11736-11758, 10.1002/anie.201509982.

[8] T. Kowalewski, N.V. Tsarevsky, K. Matyjaszewski, Nanostructured Carbon Arrays from Block Copolymers of Polyacrylonitrile, *J. Am. Chem. Soc.* **2002,** *124*, 10632-10633,

[9] M. Zhong, E.K. Kim, J.P. McGann, S.E. Chun, J.F. Whitacre, M. Jaroniec, K. Matyjaszewski, T. Kowalewski, Electrochemically active nitrogen-enriched nanocarbons with well-defined morphology synthesized by pyrolysis of self-assembled block copolymer, *J. Am. Chem. Soc.* **2012,** *134* (36), 14846-57, 10.1021/ja304352n.

[10] J.P. McGann, M. Zhong, E.K. Kim, S. Natesakhawat, M. Jaroniec, J.F. Whitacre, K. Matyjaszewski, T. Kowalewski, Block Copolymer Templating as a Path to Porous Nanostructured Carbons with Highly Accessible Nitrogens for Enhanced (Electro)chemical Performance, *Macromol. Chem. Phys.* **2012,** *213* (10-11), 1078-1090, 10.1002/macp.201100691.

[11] K. Matyjaszewski, J. Xia, Atom Transfer Radical Polymerization, *Chem. Rev.* **2001,** *101* (9), 2921-2990, 10.1021/cr940534g.

[12] K. Matyjaszewski, N.V. Tsarevsky, Nanostructured functional materials prepared by atom transfer radical polymerization, *Nat. Chem.* **2009,** *1* (4), 276-288, 10.1038/nchem.257.

[13] K. Matyjaszewski, Atom Transfer Radical Polymerization (ATRP): Current Status and Future Perspectives, *Macromolecules* **2012,** *45* (10), 4015-4039, 10.1021/ma3001719.

[14] K. Matyjaszewski, N.V. Tsarevsky, Macromolecular engineering by atom transfer radical polymerization, *J. Am. Chem. Soc.* **2014,** *136* (18), 6513-33, 10.1021/ja408069v.

[15] C. Tang, T. Kowalewski, K. Matyjaszewski, Preparation of Polyacrylonitrile-block-poly(n-butyl acrylate) Copolymers Using Atom Transfer Radical Polymerization and Nitroxide Mediated Polymerization Processes, *Macromolecules* **2003,** *36* (5), 1465-1473, 10.1021/ma025894h.

[16] D.F. Grishin, I.D. Grishin, Radical-initiated controlled synthesis of homo- and copolymers based on acrylonitrile, *Russ. Chem. Rev.* **2015,** *84* (7), 712,

[17] M. Zhong, S. Jiang, Y. Tang, E. Gottlieb, E.K. Kim, A. Star, K. Matyjaszewski, T. Kowalewski, Block copolymer-templated nitrogen-enriched nanocarbons with morphology-dependent electrocatalytic activity for oxygen reduction, *Chemical Science* **2014,** *5* (8), 3315-3315,

[18] E. Gottlieb, M. Kopeć, M. Banerjee, J. Mohin, D. Yaron, K. Matyjaszewski, T. Kowalewski, In-Situ Platinum Deposition on Nitrogen-Doped Carbon Films as a Source of Catalytic Activity in a Hydrogen Evolution Reaction, *ACS Applied Materials & Interfaces* **2016,** *8* (33), 21531-21538, 10.1021/acsami.6b03924.

[19] M. Zhong, S. Natesakhawat, J.P. Baltrus, D. Luebke, H. Nulwala, K. Matyjaszewski, T. Kowalewski, Copolymer-templated nitrogen-enriched porous nanocarbons for CO2 capture, *Chem. Commun.* **2012,** *48* (94), 11516-8, 10.1039/c2cc36652e.

[20] M.J. Ju, I.T. Choi, M. Zhong, K. Lim, J. Ko, J. Mohin, M. Lamson, T. Kowalewski, K. Matyjaszewski, H.K. Kim, Copolymer-templated nitrogen-enriched nanocarbons as a low charge-transfer resistance and highly stable alternative to platinum cathodes in dye-sensitized solar cells, *J. Mater. Chem. A* **2015,** *3* (8), 4413-4419, 10.1039/C4TA07012G.

[21] E.A. Morris, C.W. Matthew, Solution Spinning of PAN-Based Polymers for Carbon Fiber Precursors, Polymer Precursor-Derived Carbon, American Chemical Society2014, pp. 189-213.

[22] E. Frank, L.M. Steudle, D. Ingildeev, J.M. Spörl, M.R. Buchmeiser, Carbon Fibers: Precursor Systems, Processing, Structure, and Properties, *Angew. Chem. Int. Ed.* **2014,** *53* (21), 5262-5298, 10.1002/anie.201306129.

[23] P. Bajaj, A.K. Roopanwal, Thermal Stabilization of Acrylic Precursors for the Production of Carbon Fibers: An Overview, *J. Macromol. Sci. Polym. Rev.* **1997,** *37* (1), 97-147, 10.1080/15321799708014734.

[24] C. Tang, A. Tracz, M. Kruk, R. Zhang, D.-M. Smilgies, K. Matyjaszewski, T. Kowalewski, Long-Range Ordered Thin Films of Block Copolymers Prepared by Zone-Casting and Their Thermal Conversion into Ordered Nanostructured Carbon, *J. Am. Chem. Soc.* **2005,** *127* (19), 6918-6919, 10.1021/ja0508929.

[25] C. Tang, K. Qi, K.L. Wooley, K. Matyjaszewski, T. Kowalewski, Well-Defined Carbon Nanoparticles Prepared from Water-Soluble Shell Cross-linked Micelles that Contain Polyacrylonitrile Cores, *Angew. Chem. Int. Ed.* **2004,** *116* (21), 2843-2847, 10.1002/ange.200353401.

[26] C. Tang, B. Dufour, T. Kowalewski, K. Matyjaszewski, Synthesis and Morphology of Molecular Brushes with Polyacrylonitrile Block Copolymer Side Chains and Their Conversion into Nanostructured Carbons, *Macromolecules* **2007,** *40* (17), 6199-6205, 10.1021/ma070892o.

[27] M. Zhong, C. Tang, E.K. Kim, M. Kruk, E.B. Celer, M. Jaroniec, K. Matyjaszewski, T. Kowalewski, Preparation of porous nanocarbons with tunable morphology and pore size from copolymer templated precursors, *Mater. Horiz.* **2014,** *1* (1), 121-124, 10.1039/c3mh00084b.

[28] C.T. Nguyen, D.-P. Kim, Direct preparation of mesoporous carbon by pyrolysis of poly(acrylonitrile-b-methylmethacrylate) diblock copolymer, *J. Mater. Chem.* **2011,** *21* (37), 14226-14230, 10.1039/C1JM10920K.

[29] K. Yan, L.-B. Kong, Y.-H. Dai, M. Shi, K.-W. Shen, B. Hu, Y.-C. Luo, L. Kang, Design and preparation of highly structure-controllable mesoporous carbons at the molecular level and their application as electrode materials for supercapacitors, *J. Mater. Chem. A* **2015,** *3* (45), 22781-22793, 10.1039/C5TA05947J.

[30] K. Yan, L.-B. Kong, K.-W. Shen, Y.-H. Dai, M. Shi, B. Hu, Y.-C. Luo, L. Kang, Facile preparation of nitrogen-doped hierarchical porous carbon with high

performance in supercapacitors, *Appl. Surf. Sci.* **2016,** *364*, 850-861, http://dx.doi.org/10.1016/j.apsusc.2015.12.193.

[31] M. Lazzari, O. Chiantore, R. Mendichi, M.A. López-Quintela, Synthesis of Polyacrylonitrile-block-Polystyrene Copolymers by Atom Transfer Radical Polymerization, *Macromol. Chem. Phys.* **2005,** *206* (14), 1382-1388, 10.1002/macp.200500159.

[32] M. Lazzari, D. Scalarone, C.E. Hoppe, C. Vazquez-Vazquez, M.A. Lòpez-Quintela, Tunable Polyacrylonitrile-Based Micellar Aggregates as a Potential Tool for the Fabrication of Carbon Nanofibers, *Chem. Mater.* **2007,** *19* (24), 5818-5820, 10.1021/cm7019894.

[33] M. Lazzari, D. Scalarone, C. Vazquez-Vazquez, M.A. López-Quintela, Cylindrical Micelles from the Self-Assembly of Polyacrylonitrile-Based Diblock Copolymers in Nonpolar Selective Solvents, *Macromol. Rapid Commun.* **2008,** *29* (4), 352-357, 10.1002/marc.200700818.

[34] Y. Lin, X. Wang, G. Qian, J.J. Watkins, Additive-Driven Self-Assembly of Well-Ordered Mesoporous Carbon/Iron Oxide Nanoparticle Composites for Supercapacitors, *Chem. Mater.* **2014,** *26* (6), 2128-2137, 10.1021/cm404199z.

[35] K. Matyjaszewski, N.V. Tsarevsky, W.A. Braunecker, H. Dong, J. Huang, W. Jakubowski, Y. Kwak, R. Nicolay, W. Tang, J.A. Yoon, Role of Cu0 in Controlled/"Living" Radical Polymerization, *Macromolecules* **2007,** *40* (22), 7795-7806, 10.1021/ma0717800.

[36] D. Konkolewicz, Y. Wang, M. Zhong, P. Krys, A.A. Isse, A. Gennaro, K. Matyjaszewski, Reversible-Deactivation Radical Polymerization in the Presence of Metallic Copper. A Critical Assessment of the SARA ATRP and SET-LRP Mechanisms, *Macromolecules* **2013,** *46* (22), 8749-8772, 10.1021/ma401243k.

[37] D. Konkolewicz, Y. Wang, P. Krys, M. Zhong, A.A. Isse, A. Gennaro, K. Matyjaszewski, SARA ATRP or SET-LRP. End of controversy?, *Polym. Chem.* **2014,** *5* (15), 4396-4417, 10.1039/C4PY00149D.

[38] J. Masa, W. Xia, M. Muhler, W. Schuhmann, On the Role of Metals in Nitrogen-Doped Carbon Electrocatalysts for Oxygen Reduction, *Angew. Chem. Int. Ed.* **2015,** *54* (35), 10102-10120, 10.1002/anie.201500569.

[39] R.J. Roe, Methods of X-ray and Neutron Scattering in Polymer Science, Oxford University Press2000.

[40] T.D. Burchell, Carbon Materials for Advanced Technologies, Elsevier Science1999.

[41] F.S. Bates, Polymer-Polymer Phase Behavior, *Science* **1991,** *251* (4996), 898,

[42] Z. Bashir, S. Rastogi, The Explanation of the Increase in Slope at the Tgin the Plot of d-Spacing Versus Temperature in Polyacrylonitrile, *J. Macromol. Sci. B* **2005,** *44* (1), 55-78, 10.1081/mb-200044588.

[43] Z. Bashir, The hexagonal mesophase in atactic polyacrylonitrile: a new interpretation of the phase transitions is the polymer, *J. Macromol. Sci. B* **2001,** *40* (1), 41-67, 10.1081/MB-100000053.

[44] H. Kaji, K. Schmidt-Rohr, Conformation and Dynamics of Atactic Poly(acrylonitrile). 2. Torsion Angle Distributions in Meso Dyads from Two-Dimensional Solid-State Double-Quantum 13C NMR, *Macromolecules* **2001,** *34* (21), 7368-7381, 10.1021/ma010657k.

[45] X.D. Liu, W. Ruland, X-ray studies on the structure of polyacrylonitrile fibers, *Macromolecules* **1993,** *26* (12), 3030-3036, 10.1021/ma00064a006.

[46] J. Xia, K. Matyjaszewski, Controlled/"Living" Radical Polymerization. Atom Transfer Radical Polymerization Catalyzed by Copper(I) and Picolylamine Complexes, *Macromolecules* **1999,** *32* (8), 2434-2437, 10.1021/ma981694n.

[47] H. Tang, M. Radosz, Y. Shen, CuBr2/N,N,N′,N′-Tetra[(2-pyridal)methyl]ethylenediamine/Tertiary Amine as a Highly Active and Versatile Catalyst for Atom-Transfer Radical Polymerization via Activator Generated by Electron Transfer, *Macromol. Rapid Commun.* **2006,** *27* (14), 1127-1131, 10.1002/marc.200600258.

[48] M. Lamson, M. Kopeć, H. Ding, M. Zhong, K. Matyjaszewski, Synthesis of well-defined polyacrylonitrile by ICAR ATRP with low concentrations of catalyst, *J. Polym. Sci., Part A: Polym. Chem.* **2016,** *54*, 1961-1968, 10.1002/pola.28055.

Chapter 3: Laser Pyrolysis of Polyacrylonitrile-Based Polymers Under Ambient Conditions

This work was initiated when a middle school student, Ben Tarr, came to us with an interest in making supercapacitors using laser pyrolyzed carbon electrodes. Working with Ben, I prepared polymer films for him to take to a laser cutter and systematically probe irradiate using a CO_2 laser. While the pristine polymers did not carbonize, oxidatively stabilized polymers did carbonize. Using the laser carbonized films Ben successfully built a basic coin cell supercapacitor with vinegar, which he went on to win the state level science fair for. The results presented in this chapter represent a draft of a communication that we are proud to have Ben on as a coauthor.

3.1 Abstract

Films of polyacrylonitrile (PAN) containing block copolymers with and without oxidative stabilization were exposed to CO_2 laser irradiation to assess the viability of fast laser pyrolysis for efficient carbonization. While PAN that had not undergone stabilization did not produce carbon, stabilized PAN readily carbonized, forming structures ranging from nanocrystalline graphite to amorphous carbon depending on the exposure conditions. Based on analysis of Raman spectra, faster exposure profiles resulted in a surprisingly high degree of microstructural order and a large amount of zigzag edges. A large amount of nitrogen and oxygen was observed in X-ray photoelectron spectra, which, in conjunction with the abundance of zigzag edges, make the material a promising candidate for electrocatalysis.

3.2 Introduction

Carbon materials have become critical in many facets of modern society, being used as electrodes, filters, sorbets, and fibers.[1-4] Carbonization and graphitization typically utilize inert gas conditions with temperature treatments as low as 500 °C to create

highly disordered partially graphitic materials and temperatures in excess of 3000 °C to form extended graphite structures.[5, 6] Such methods can be expensive, energy intensive, time consuming, and are limited to uniformly being applied to the material, closing off options such as spatial control. The temperature requirements of pyrolysis constrain the synthetic routes available, but one possible option is through laser exposure, which can rapidly induce localized heating. Herein, we report the use of CO_2 laser exposure of stabilized polyacrylonitrile (PAN) containing block copolymers in ambient conditions as a fast and economical way to produce films with spatially controlled localized carbon.

Laser treatment has been an integral component in the exploration of carbons, having been used to synthesize of nanotubes, fullerenes, and other carbon materials often using directed vapor deposition.[7-11] Laser exposure has also been used as a means of pretreatment of polymers,[12] pyrolysis of polymers,[13, 14] and post-carbonization induced graphitization.[14] But despite this breadth of work on laser treatments and synthesis methods, exploration of direct carbonization from polymeric precursors, especially in a "direct laser writing" setup, has been limited. This approach has the potential to make complex carbons imbedded in polymers or patterned on surfaces, greatly expanding the possible applications carbons can be used in.

Effective carbon formation from such a setup can be difficult because the precursor needs to interact favorably with the laser, as opposed to simply burning, volatilizing, ablating, or forming undesired carbons such as fullerenes. There has been some limited success in overcoming these problems through metal incorporations,[15] and with select polymeric precursors, namely Kapton polyimide and Bakelite phenolic resin.[16-18] Both of these polymeric precursors have easy means of crosslinking and carbonization, so it is

reasonable to expect that similar other precursors with similar properties could also be promising candidates for laser pyrolysis.[19-22]

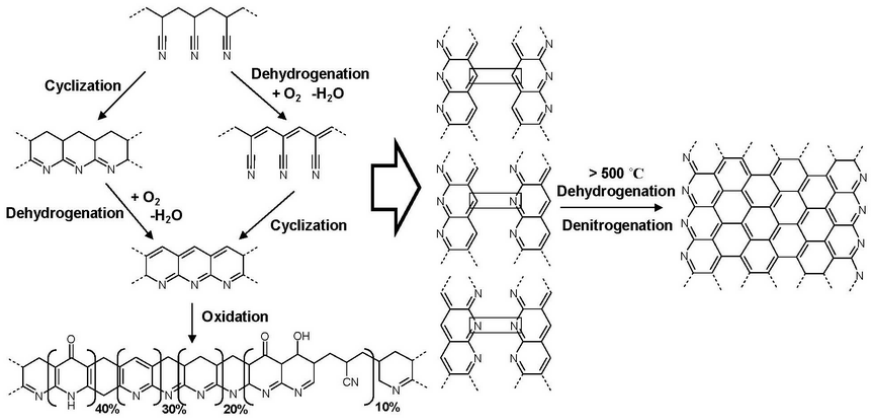

Figure 3.1 The idealized stabilization and pyrolysis mechanism for PAN. The first step, occurring in air, produces a ladder polymer that then fuses into a carbon at higher temperatures under inert atmosphere.[23]

PAN, a widely used polymer in fibers and as a precursor to carbon fibers, would be a logical precursor choice, and had the benefit of an extensive body of research behind it for its industrial relevance.[23] With the goal of developing a simple procedure that can be used to synthesize carbons quickly and economically, laser carbonization of PAN films was assessed using a commercial CO_2 laser cutter. Specifically, it was determined that thermal stabilization of the PAN was necessary to produce a carbon upon exposure to the CO_2 laser, pointing to the need of the presence of the ladder polymer to facilitate rapid carbonization by the irradiation (**Figure 3.1**). Another possibility is that by stabilizing, PAN more readily interacts with the wavelength of light produced by the CO_2 laser (**Figure 3.2** and **Figure 3.3**), thereby changing the achievable local temperature that induces carbonization.[24, 25]

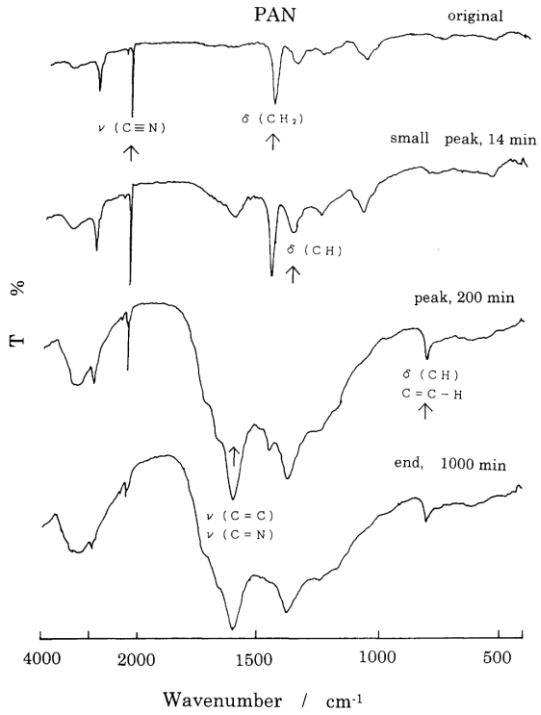

Figure 3.2 Fourier transform infrared (FTIR) spectra of PAN at different stages of the stabilization process. The energy range over which CO_2 lasers operate has nearly full transmittance in the pristine PAN, but over the course of the stabilization process, a broad absorption band develops that includes the region Reproduced from [26].

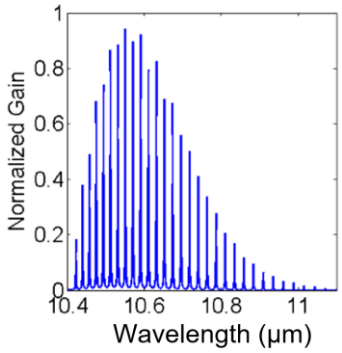

Figure 3.3 The range over which CO_2 lasers irradiate, the center of which corresponds to approximately 950 cm^{-1}. Reproduced from [27].

3.3 Results and Discussion

(Butyl acrylate)$_{91}$-*b*-(acrylonitrile)$_{146}$ films drop cast onto silicon wafers both without any modifications and oxidatively stabilized at 280 °C were exposed to CO_2 laser exposure of differing powers and speeds. Unmodified films did not show any indication of carbonization optically, only showing a different diffuse reflection from the pristine film,

while the stabilized PAN showed a darkening that is consistent with carbonization (**Figure 3.4**). Raman spectra of the films only showed broad scattering without any distinguishing features that could be attributed to any chemical or physical features, while stabilized films showed a variety of signals that are consistent with carbons containing a range of structures (discussed further below) (**Figure 3.5**).

Figure 3.4 Drop cast PAN-*b*-PBA films on silicon exposed to CO_2 laser radiation of differing speeds and powers, both without any prior stabilization of the film (left) and with oxidative stabilization (middle). (Right) Optical microscopy image (10× objective) of a stabilized PAN-*b*-PBA film on silicon. Stabilized PAN-*b*-PBA that was not exposed to the laser is on the left and laser exposed is on the right with visible effects from lines from the CO_2 laser's rastering.

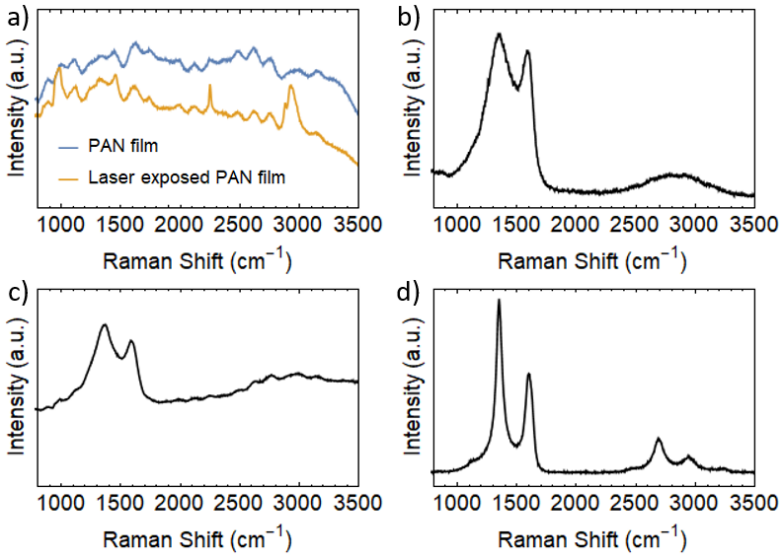

Figure 3.5 Raman spectra of a) PAN-*b*-PBA films before and after laser exposure, b) bulk copolymer templated nitrogen enriched nanocarbons pyrolyzed at 800 °C following normal procedures according to prior publications,[28, 29] and laser exposed stabilized PAN-*b*-PBA films at slower (c) and faster (d) raster speeds.

X-ray photoelectron spectra (XPS) indicated that the films did undergo chemical changes with laser exposure regardless of if the film was stabilized (**Figure 3.6**). This is also reflected in the overall atomic percentages of the samples (**Table 3.1**). XPS of films without stabilization both show less nitrogen than would be expected by the polymer's composition. While X-rays can penetrate relatively deep into the sample, photoelectron scattering limits the depth that can effectively be probed by XPS. This indicates that the PBA block is preferentially exposed on the surface, which is consistent with its lower surface tension. The N1s signal staying low after laser exposure also indicates that the surface PBA layer was not removed by the laser exposure. That said, the O1s and C1s spectra of not stabilized films shows chemical modifications, with broad higher binding energy signals emerging after irradiation. In the N1s spectrum, unmodified polymer film shows a peak that can be attributed to nitriles and remains mostly unchanged after irradiation but shows a shift to lower binding energies and a narrower linewidth. For stabilized polymers before with and without irradiation, the N1s spectra look similar, but the expected types of chemical states in the ladder structure of the stabilized film is very different than what can be expected in the final carbon.

Table 3.1 Surface heteroatom atomic content relative to carbon from XPS

Sample	N/C Ratio	O/C Ratio
PAN-*b*-PBA	2.3%	27.8%
Laser exposed PAN-*b*-PBA	3.7%	23.7%
Stabilized PAN-*b*-PBA	13.8%	18.0%
Laser exposed stabilized PAN-*b*-PBA	14.7%	19.9%
CTNC[29]	13.5%	7.3%

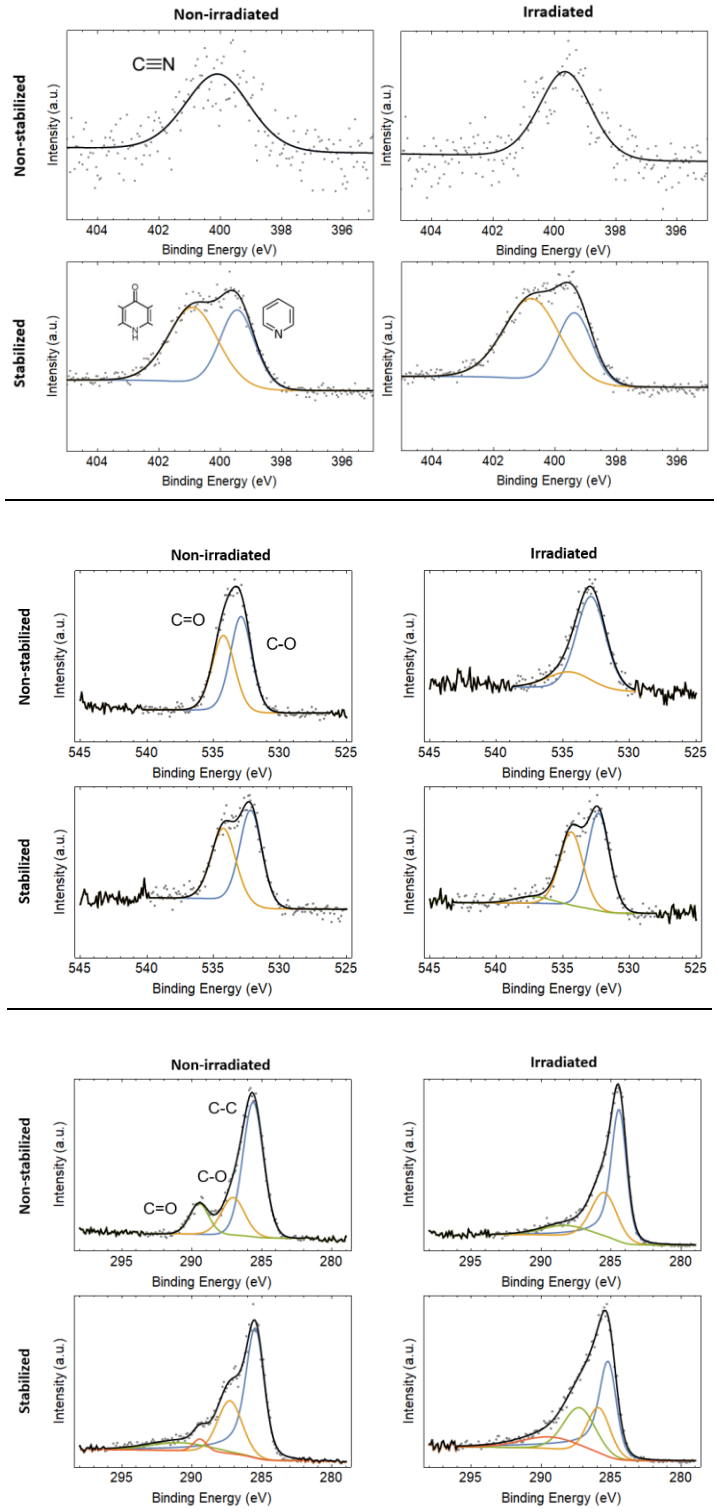

Figure 3.6 High resolution XPS spectra in the N1s, O1s, and C1s regions of PAN-*b*-PBA films: unmodified, after laser exposure, after stabilization, and after stabilization with subsequent laser exposure.

One notable difference between the carbons produced by laser irradiation compared to more typical pyrolysis under anaerobic conditions, is the oxygen content (**Table 3.1**). The oxygen content in laser exposed sample was much higher than that of CTNCs, which may be due to either the irradiation being performed in air. However, since the atomic content is similar to that of the stabilized, unirradiated film, it is likely related to the rate at which the pyrolysis is occurring. More effective control of the oxygen content as a result of laser pyrolysis will be the subject of future work.

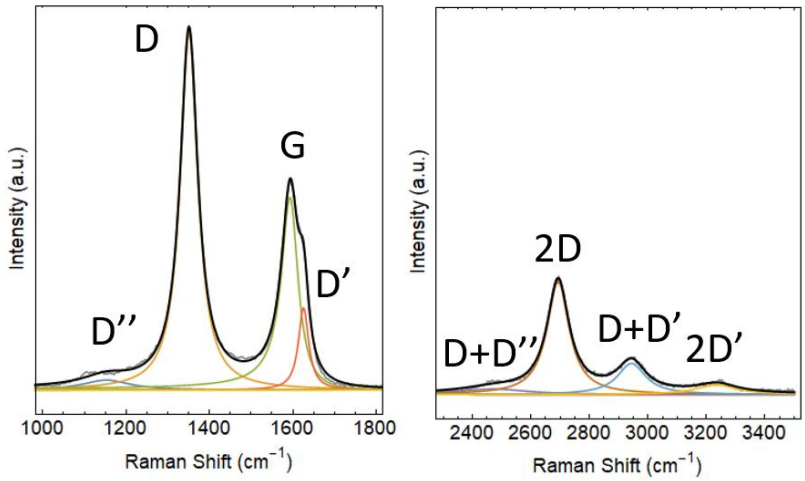

Figure 3.7 Decomposed Raman spectrum of an irradiated stabilized PAN-*b*-PBA film in the so-called "first order region" (left) and "second order region" (right).

Looking more in depth at the Raman spectrum with very narrow linewidths, many higher order D-band can be observed (**Figure 3.7**) and fitting parameters of the spectrum's decomposition (**Table 3.2**) can be used to determine structural features of the carbon. The many observable second order D-bands, as well as the narrowness of the D and G bands are indicative of a surprisingly well-ordered carbon with an abundance of edges.[30] Furthermore, the I(D)/I(G) value of 1.86, which corresponds to an approximate crystallite size of 2 nm, and the G position of 1595 cm^{-1} all point to the laser irradiation producing a nanocrystalline graphite.[31] This is in surprising contrast to the PAN-derived carbons

pyrolyzed in a furnace under inert atmosphere, which could be more readily characterized as amorphous carbons (**Figure 3.5b**). Previously, the broad D and G bands of furnace pyrolyzed PAN obscured the other modes, limiting what could be learned about their structures. For example, the D'' band at ~1150 cm^{-1}, also sometimes referred to as the "*trans*-polyacetylene band" might suggest that zigzag edges are the predominant type of edge formed, which would fit with the established mechanism for PAN carbonization (**Figure 3.1**).

Table 3.2 The main features of Raman band decomposition

Raman Feature	Value
G-band position	1595 cm^{-1}
G-band width	49 cm^{-1}
D-band position	1351 cm^{-1}
D-band width	51 cm^{-1}
I(D)/I(G)	1.86

3.4 Conclusion

Laser pyrolysis of PAN-*b*-PBA films was assessed by Raman and XPS, and while pristine polymer films could not be carbonized, oxidatively stabilized PAN was able to rapidly carbonize into nanocrystalline graphite with high nitrogen content. The exposure parameters of irradiation were qualitatively investigated, finding that shorter doses yielded the nanocrystalline graphite while slower speeds produced amorphous carbons that were more similar to stabilized and furnace pyrolyzed PAN-*b*-PBA. The retention of both nitrogen and oxygen heteroatoms from stabilized to laser pyrolyzed carbon is likely caused by the short time course of rapid laser induced carbonization, which facilitates kinetic

trapping of the heteroatoms. Whereas resulting properties of the carbon are very sensitive to the conditions, *i.e.* power and total dosage, in ways that still need to be investigated, the obtained results point to the potential to further control the process. These findings suggest that stabilized PAN-containing polymers can be effectively, rapidly and economically carbonized as films.

3.5 Experimental

Materials. Sulfuric acid (95 - 98%, Fischer), dimethylformamide (DMF, >99.8 %, Fischer) and polyacrylonitrile (molecular weight 150,000; Sigma-Aldrich) were used as received. The block copolymer precursors were synthesized *via* atom transfer radical polymerization (ATRP) as reported previously.[29, 32-36] ATRP involves the use of copper-based catalyst, thus all polymer samples were purified by three-fold precipitation into methanol/water (1:1 *v/v*) and re-dissolution in DMF.

Synthesis of CTNC as Films on Silicon. Monocrystalline silicon wafers were cut, washed with double distilled water and acetone, sonicated in water and finally dried in air. The insert was then treated under UV to remove organic residues. The as-prepared BCP was drop-cast from a 10 mg/mL solution in DMF onto the silicon wafer using a microliter syringe and dried under ambient conditions. The annealed films were stabilized at 280 °C for 1 h under air flow (150 mL/min) with a heating rate of 1 °C/min. Films were also produced by drop casting followed by stabilization in air on a hot plate without annealing to assess the efficacy of simpler, “low tech” procedures. Laser pyrolysis was performed using a CO_2 laser cutter (10.6 μm wavelength) at TechShop Pittsburgh.

Characterization. XPS was performed using an ESCALAB 250Xi X-ray Photoelectron Spectrometer Microprobe, with a 900 mm spot size. All high resolution

spectra were decomposed with Sherley baselines and standard Gaussian/Lorentzian lineshapes, except for the signal that corresponds to sp^2 conjugated carbons, which were fit with mix of a Lorentzian with a dampened asymmetric tail. Raman spectroscopy was performed using a Horiba XploRA ONE Raman Microscope with a 532 nm laser and a 50× objective. Raman peaks were decomposed using Lorentzian lineshapes for all peaks except for the signal corresponding to the G-and, which was fit with an asymmetric Breit–Wigner–Fano (BWF) profile.[30, 31, 37, 38]

3.6 References

[1] F. Rodriguez-Reinoso, The role of carbon materials in heterogeneous catalysis, *Carbon* **1998,** *36* (3), 159-175, Doi 10.1016/S0008-6223(97)00173-5.

[2] P. Serp, J.L.s. Figueiredo, Carbon materials for catalysis, John Wiley & Sons, Hoboken, N.J., 2009.

[3] P. Serp, Carbon nanotubes and nanofibers in catalysis, *Appl. Catal., A* **2003,** *253* (2), 337-358, 10.1016/s0926-860x(03)00549-0.

[4] Y. Zheng, J. Liu, J. Liang, M. Jaroniec, S.Z. Qiao, Graphitic carbon nitride materials: controllable synthesis and applications in fuel cells and photocatalysis, *Energy and Environmental Science*
2012, *5* (5), 6717, 10.1039/c2ee03479d.

[5] A. Hirsch, The era of carbon allotropes, *Nat Mater* **2010,** *9* (11), 868-71, 10.1038/nmat2885.

[6] V. Georgakilas, J.A. Perman, J. Tucek, R. Zboril, Broad family of carbon nanoallotropes: classification, chemistry, and applications of fullerenes, carbon dots, nanotubes, graphene, nanodiamonds, and combined superstructures, *Chem. Rev.* **2015,** *115* (11), 4744-822, 10.1021/cr500304f.

[7] Y. Zhang, H. Gu, S. Iijima, Single-wall carbon nanotubes synthesized by laser ablation in a nitrogen atmosphere, *Applied Physics Letters* **1998,** *73* (26), 3827-3829, 10.1063/1.122907.

[8] C.D. Scott, S. Arepalli, P. Nikolaev, R.E. Smalley, Growth mechanisms for single-wall carbon nanotubes in a laser-ablation process, *Applied Physics A Materials Science & Processing* **2001,** *72* (5), 573-580, 10.1007/s003390100761.

[9] S. Iijima, T. Wakabayashi, Y. Achiba, Structures of Carbon Soot Prepared by Laser Ablation, *The Journal of Physical Chemistry* **1996,** *100* (14), 5839-5843, 10.1021/jp953400v.

[10] A. Galvez, N. Herlin-Boime, C. Reynaud, C. Clinard, J.-N. Rouzaud, Carbon nanoparticles from laser pyrolysis, *Carbon* **2002,** *40* (15), 2775-2789, 10.1016/s0008-6223(02)00195-1.

[11] Y. Zhao, Q. Han, Z. Cheng, L. Jiang, L. Qu, Integrated graphene systems by laser irradiation for advanced devices, *Nano Today* **2017,** *12*, 14-30, 10.1016/j.nantod.2016.12.010.

[12] N.V. Platonova, I.B. Klimenko, B.M. Tarakanov, B.A. Vinogradov, K.E. Boyarkin, S.P. Maiburov, M.L. Syrkina, Pyrolysis of polyacrylonitrile fibres subjected to laser irradiation, *Fibre Chemistry* **1992,** *23* (3), 189-190, 10.1007/bf00545860.

[13] D.L. Fanter, R.L. Levy, C.J. Wolf, Laser pyrolysis of polymers, *Analytical Chemistry* **2002,** *44* (1), 43-48, 10.1021/ac60309a037.

[14] Y. Sha, W. Yang, S. Li, L. Yao, H. Li, L. Cheng, H. Yan, W. Cao, J. Tan, Laser induced graphitization of PAN-based carbon fibers, *RSC Advances* **2018,** *8* (21), 11543-11550, 10.1039/c8ra00497h.

[15] L.M. Zemtsov, G.P. Karpacheva, M.N. Efimov, D.G. Muratov, K.A. Bagdasarova, Carbon nanostructures based on IR-pyrolyzed polyacrylonitrile, *Polymer Science Series A* **2006,** *48* (6), 633-637, 10.1134/s0965545x06060125.

[16] S. Luo, P.T. Hoang, T. Liu, Direct laser writing for creating porous graphitic structures and their use for flexible and highly sensitive sensor and sensor arrays, *Carbon* **2016,** *96*, 522-531, 10.1016/j.carbon.2015.09.076.

[17] F. Wang, K. Wang, X. Dong, X. Mei, Z. Zhai, B. Zheng, J. Lv, W. Duan, W. Wang, Formation of hierarchical porous graphene films with defects using a nanosecond laser on polyimide sheet, *Applied Surface Science* **2017,** *419*, 893-900, 10.1016/j.apsusc.2017.05.084.

[18] F. Wang, W. Duan, K. Wang, X. Dong, M. Gao, Z. Zhai, X. Mei, J. Lv, W. Wang, C. Zhu, Graphitized hierarchically porous carbon nanosheets derived from bakelite induced by high-repetition picosecond laser, *Applied Surface Science* **2018,** *450*, 155-163, 10.1016/j.apsusc.2018.04.130.

[19] H.V. Shah, S.T. Brittain, Q. Huang, S.J. Hwu, G.M. Whitesides, D.W. Smith, Bis-o-diynylarene (BODA) derived polynaphthalenes as precursors to glassy carbon microstructures, *Chem. Mater.* **1999,** *11* (10), 2623-2625, DOI 10.1021/cm9903780.

[20] H. Suda, K. Haraya, Gas permeation through micropores of carbon molecular sieve membranes derived from Kapton polyimide, *J. Phys. Chem. B* **1997,** *101* (20), 3988-3994, DOI 10.1021/jp963997u.

[21] D.E. Jiang, A.C. van Duin, W.A. Goddard, 3rd, S. Dai, Simulating the initial stage of phenolic resin carbonization via the ReaxFF reactive force field, *J. Phys. Chem. A* **2009,** *113* (25), 6891-4, 10.1021/jp902986u.

[22] E. Fitzer, W. Schaefer, S. Yamada, The formation of glasslike carbon by pyrolysis of polyfurfuryl alcohol and phenolic resin, *Carbon* **1969,** *7* (6), 643-648, 10.1016/0008-6223(69)90518-1.

[23] P. Bajaj, A.K. Roopanwal, Thermal stabilization of acrylic precursors for the production of carbon fibers: An overview, *J. Macromol. Sci., Rev. Macromol. Chem. Phys.* **1997,** *C37* (1), 97-147, 10.1080/15321799708014734.

[24] M. von Allmen, A. Blatter, Heating by Laser Light, Laser-Beam Interactions with Materials1995, pp. 41-67.

[25] T. Ueda, K. Yamada, K. Nakayama, Temperature of Work Materials Irradiated with CO 2 Laser, *CIRP Annals* **1997,** *46* (1), 117-122, 10.1016/s0007-8506(07)60788-4.

[26] H. Kakida, K. Tashiro, Mechanism and Kinetics of Stabilization Reaction of Polyacrylonitrile and Related Copolymers II. Relationships between Isothermal DSC Thermograms and FT-IR Spectral Changes of Polyacrylonitrile in Comparison with the Case of Acrylonitrile/Methacrylic Acid Copolymer, *Polymer Journal* **1997,** *29* (4), 353-357, 10.1295/polymj.29.353.

[27] D. Haberberger, S. Tochitsky, C. Joshi, Fifteen terawatt picosecond CO_2 laser system, *Optics Express* **2010,** *18* (17), 10.1364/oe.18.017865.

[28] M.J. Zhong, S.Y. Jiang, Y.F. Tang, E. Gottlieb, E.K. Kim, A. Star, K. Matyjaszewski, T. Kowalewski, Block copolymer-templated nitrogen-enriched nanocarbons with morphology-dependent electrocatalytic activity for oxygen reduction, *Chem. Sci.* **2014,** *5* (8), 3315-3319, 10.1039/c4sc01477d.

[29] M. Zhong, E.K. Kim, J.P. McGann, S.E. Chun, J.F. Whitacre, M. Jaroniec, K. Matyjaszewski, T. Kowalewski, Electrochemically active nitrogen-enriched nanocarbons with well-defined morphology synthesized by pyrolysis of self-assembled block copolymer, *J. Am. Chem. Soc.* **2012,** *134* (36), 14846-57, 10.1021/ja304352n.

[30] A. Merlen, J. Buijnsters, C. Pardanaud, A Guide to and Review of the Use of Multiwavelength Raman Spectroscopy for Characterizing Defective Aromatic Carbon Solids: from Graphene to Amorphous Carbons, *Coatings* **2017,** *7* (10), 10.3390/coatings7100153.

[31] A.C. Ferrari, J. Robertson, Interpretation of Raman spectra of disordered and amorphous carbon, *Physical Review B* **2000,** *61* (20), 14095-14107, 10.1103/PhysRevB.61.14095.

[32] C. Tang, T. Kowalewski, K. Matyjaszewski, Preparation of Polyacrylonitrile-block-poly(n-butyl acrylate) Copolymers Using Atom Transfer Radical Polymerization and Nitroxide Mediated Polymerization Processes, *Macromolecules* **2003,** *36* (5), 1465-1473, 10.1021/ma025894h.

[33] K. Matyjaszewski, J. Xia, Atom Transfer Radical Polymerization, *Chem. Rev.* **2001,** *101* (9), 2921-2990, 10.1021/cr940534g.

[34] K. Matyjaszewski, N.V. Tsarevsky, Nanostructured functional materials prepared by atom transfer radical polymerization, *Nature chemistry* **2009,** *1* (4), 276-288, 10.1038/nchem.257.

[35] K. Matyjaszewski, Atom Transfer Radical Polymerization (ATRP): Current Status and Future Perspectives, *Macromolecules* **2012,** *45* (10), 4015-4039, 10.1021/ma3001719.

[36] K. Matyjaszewski, N.V. Tsarevsky, Macromolecular engineering by atom transfer radical polymerization, *J. Am. Chem. Soc.* **2014,** *136* (18), 6513-33, 10.1021/ja408069v.

[37] C. Thomsen, Second-order Raman spectra of single and multiwalled carbon nanotubes, *Physical Review B* **2000,** *61* (7), 4542-4544, 10.1103/PhysRevB.61.4542.

[38] A.C. Ferrari, Raman spectroscopy of graphene and graphite: Disorder, electron–phonon coupling, doping and nonadiabatic effects, *Solid State Communications* **2007,** *143* (1-2), 47-57, 10.1016/j.ssc.2007.03.052.

Chapter 4: Metal-Free Oxygen Reduction Reaction Using Copolymer Templated Nitrogen Enriched Carbons

This was the first project I was involved in as a graduate student, working initially with Dr. Mingjiang Zhong, and eventually on my own to quantify the evolution of nanostructure connectivity at the surface of binder-free films using extensive data processing and interpretation of atomic force microscopy (AFM). While all of the AFM measurements collected included both height and phase data, each of them is generally better suited to different system. In the non-pyrolyzed films, the heights are relatively uniform, but mechanical differences between blocks create phase contrast. In the pyrolyzed films, the two components are carbon and void as opposed to different polymer blocks, which leads to large height differences for imaging but no mechanical contrast for phase images. Thus, I used only height images, including from the block copolymer (BCP) films, to produce directly comparable datasets that could be uniformly processed. To elicit usable data from height images of BCP films, subtleties of the proportional–integral–derivative (PID) controller measurements were leveraged. The PID controls the height of the AFM head (the same height used to create height images) to try and maintain a setpoint voltage, the measure of which is based on the deflection of the tip. Tapping mode AFM can also produce so-called "phase images" based on oscillatory phase shifts of the tip as compared to the drive oscillation. These phase shifts can be produced by differences in in mechanical responses in a film, but with the right tapping conditions, those same mechanical differences can result in small changes in tip amplitude, and consequently the height images. Thus, the phase images of BCP films can be somewhat embedded in the height images. These images were then analyzed using image analysis methods to assess connectivity of the carbons in comparison to their BCP precursors to show the nanostructure collapse in thin films

4.1 Abstract

Binder-free films of nitrogen-enriched nanocarbons, prepared by the pyrolysis of polyacrylonitrile-block-poly(*n*-butyl acrylate) copolymer drop-casted on glassy carbon disk electrode, exhibited high electrocatalytic activity for the oxygen reduction reaction (ORR), matching that of Pt-based electrocatalyst. Dependence of the activity on pyrolysis temperature revealed that it is governed by the interplay of nitrogen content and electrical conductivity of the material. It was demonstrated that a nanocarbon formed by pyrolysis at 800 °C provided both large number of electrons transferred and high kinetic current density. ORR performance has been shown to critically depend on the presence of a nanoporous structure, suggesting that it facilitates high density and accessibility of catalytic sites, such as nitrogen-terminated edges of nanographitic domains.

Table of Contents Figure

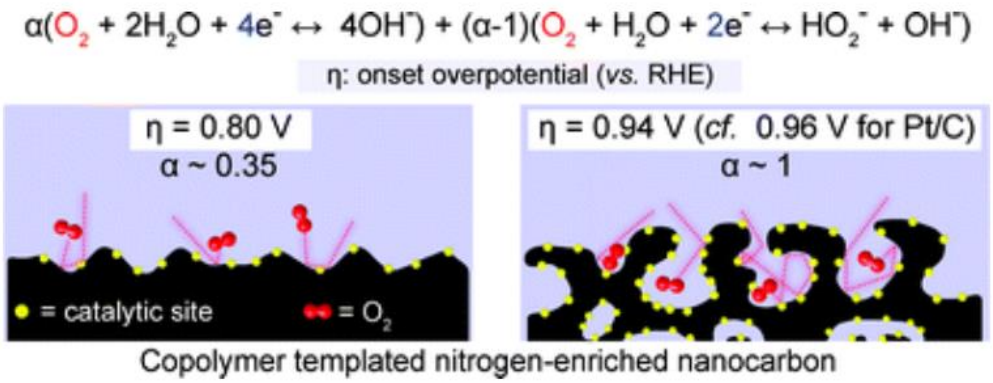

M.J. Zhong, S.Y. Jiang, Y.F. Tang, E. Gottlieb, E.K. Kim, A. Star, K. Matyjaszewski, T. Kowalewski, Block copolymer-templated nitrogen-enriched nanocarbons with morphology-dependent electrocatalytic activity for oxygen reduction, *Chemical Science* **2014,** *5* (8), 3315-3319, 10.1039/c4sc01477d.

4.2 Introduction

The oxygen reduction reaction (ORR) has been the subject of extensive research in recent years due to its applications in fuel cells, biosensors, and H_2O_2 production.[1-4]

Depending on the type of the electrocatalyst, ORR can proceed either through a 2- or 4-electron (2e or 4e) pathway, with the former desirable in H_2O_2 production and the latter preferred in fuel cells. The most commonly used electrocatalysts for ORR in fuel cells are based on platinum (Pt). The main advantage of these systems is their electrocatalytic activity and facile 4e-transfer process. However, their relatively high cost, limited stability, and susceptibility towards methanol crossover effect motivate considerable efforts aimed at identifying viable replacements, including non-precious metal[5-7] and non-metal based electrocatalytic systems.[8-11] Transition metals, e.g., Fe, Co, are typically placed on a carbon catalyst support which, in order to facilitate good binding, is doped with electron-donor heteroatoms such as nitrogen.

Heteroatom-enriched nanocarbon materials are currently receiving a significant level of attention due to their versatility in applications such as catalysis, energy storage, and gas sorption.[12-16] Among these materials,, nitrogen-enriched nanocarbons have been most widely investigated due to well-developed synthetic routes and the abundance of nitrogen-containing carbon precursors ranging from small molecules[8, 17-20] to synthetic polymers,[15, 21, 22] and bio-macromolecules.[23] Nitrogen-enriched carbons including carbon nanotubes,[8, 19] graphene,[14] and porous nanocarbons,[15, 21, 24, 25] carbon nitride,[26] have been all demonstrated to be capable of electrocatalyzing ORR with higher stability than Pt and with a negligible crossover to methanol.[21] While these catalysts show better long term stability and less crossover, one of the remaining challenges is that they rarely exhibit overpotentials matching those afforded by Pt-based systems. Moreover, the mechanism of remarkable catalytic activity of such metal-free system is still not well understood.

Herein we describe efficient, morphology-dependent ORR activity exhibited by copolymer templated nitrogen-enriched nanocarbons (CNTCs). CTNCs are obtained through the combination of pyrolysis and thermal decomposition of nanophase-separated block copolymers (BCPs) containing polyacrylonitrile (PAN) which serves as a nitrogen rich carbon precursor and porogenic sacrificial poly(*n*-butyl acrylate) (PBA).[15, 24, 27-31] We have previously shown that, for certain PAN/PBA ratios, the original morphology of the bulk precursor is well retained upon pyrolysis. The resulting materials show high surface area and accessibility of nitrogen functionalities as inferred from their performance as electrodes for supercapacitors[24] and as sorbents for CO_2 capture.[31] We have also reported preliminary evidence of ORR activity of these materials.[24] Herein, we demonstrate that ORR performance of binder free CTNC films pyrolyzed directly on glassy carbon (GC) matches Pt-based electrocatalysts, with consistent 4e-transfer and low overpotentials. As shown below, such a binder-free system offers multiple advantages for mechanistic study of ORR. Most importantly, we provide the evidence of striking dependence of catalytic activity on film thickness/morphology.

CTNCs used in this study were prepared from a BCP with number average degrees of polymerization (DP_n) of 70 and 99 for PBA and PAN, respectively, which has shown good preservation of nanoscale morphology upon pyrolysis.[24, 28] A control sample was prepared from PAN homopolymer (DP_n = 101) to assess the impact of nanostructure on ORR performance. Low dispersity index BCP ($Đ$ = 1.18) and homopolymer ($Đ$ = 1.09) were synthesized using atom transfer radical polymerization (ATRP).[32-35] Since ATRP involves the use of a Cu-based catalyst, the polymers were purified by three-fold precipitation to minimize the possibility of activity due to residual metal content. X-ray

photoelectron spectra of resulting carbons showed no signs of Cu 2*p* signal (Figure S1) and inductively coupled plasma mass spectroscopy did not reveal Cu content within a detection limit of 0.1 ppm. Another control carbon sample was prepared from PAN, synthesized using conventional free radical polymerization (FRP) without any catalyst.

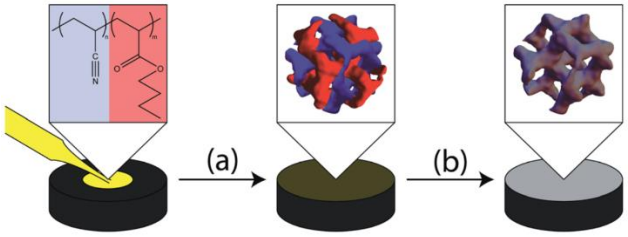

Figure 4.1 Preparation of binder-free CTNC film on GC disk electrode. (a) Evaporate at ambient conditions and thermally anneal at 160 °C; (b) 280 °C, air then 600–900 °C, Ar.

As shown in **Figure 4.1**, the fabrication of binder-free CTNC electrodes was facilitated by solution-processability of the polymeric precursor. Precursors were casted as a film onto the GC disk electrode and then pyrolyzed. One of the advantages of the binder-free electrode fabrication is that it allows for more precise determination of catalyst loading and eliminates the potential of the binder to limit the accessibility of catalytic sites. Casted BCP films were pyrolyzed at different temperatures, yielding materials labelled as CTNC-T, with T = 600, 700, 800, 900 indicating pyrolysis temperature (T_p) in °C. Nitrogen/carbon atomic ratios in CTNCs decreased with T_p from ~0.17 to ~0.06 (**Table 4.1**) while oxygen content remained nearly constant. Control samples of carbon supported Pt-catalyst were prepared from suspensions of commercial Pt/C catalyst kits using standard procedures.

Table 4.1 Characterization of bulk CTNCs synthesized under different pyrolysis conditions.

Entry	S_{BET} (m^2/g)	N/C (%)	Carbonization Yield (%)
CTNC-600	461	16.9	25.9
CTNC-700	491	13.5	23.6
CTNC-800	485	9.1	21.6
CTNC-900	509	6.1	20.5

4.3 Results and Discussion

Electrochemical characterization of CTNCs was carried out using cyclic voltammetry (CV) in 0.1 M KOH solutions. Comparison of CV curves obtained for CTNC-700 with solutions saturated with O_2 or N_2 provided the initial evidence of ORR activity of CTNC (**Figure 4.2a**). Linear scanning voltammograms (LSV) were then carried out using a rotating disk electrode (RDE) to assess the electrocatalytic activity from onset/half-wave overpotential (η_{os} and η_{hw}) and number of electrons transferred (n_e). Comparison of CTNC-700 with the Pt/C-catalyst demonstrates equally good ORR performance, seen from the low overpotential ($\eta_{os} \approx 0.95$ V *vs*. RHE) observed in both cases (**Figure 4.2b**, red and green traces). The control sample, prepared under the same conditions, but using a suspension containing Nafion binder, exhibited η_{os} higher by *ca*. 0.14 V (**Figure 4.2b**, black trace). The undesirable increase of overpotential in the presence of a binder demonstrates a clear advantage of the direct deposition method developed in this study.

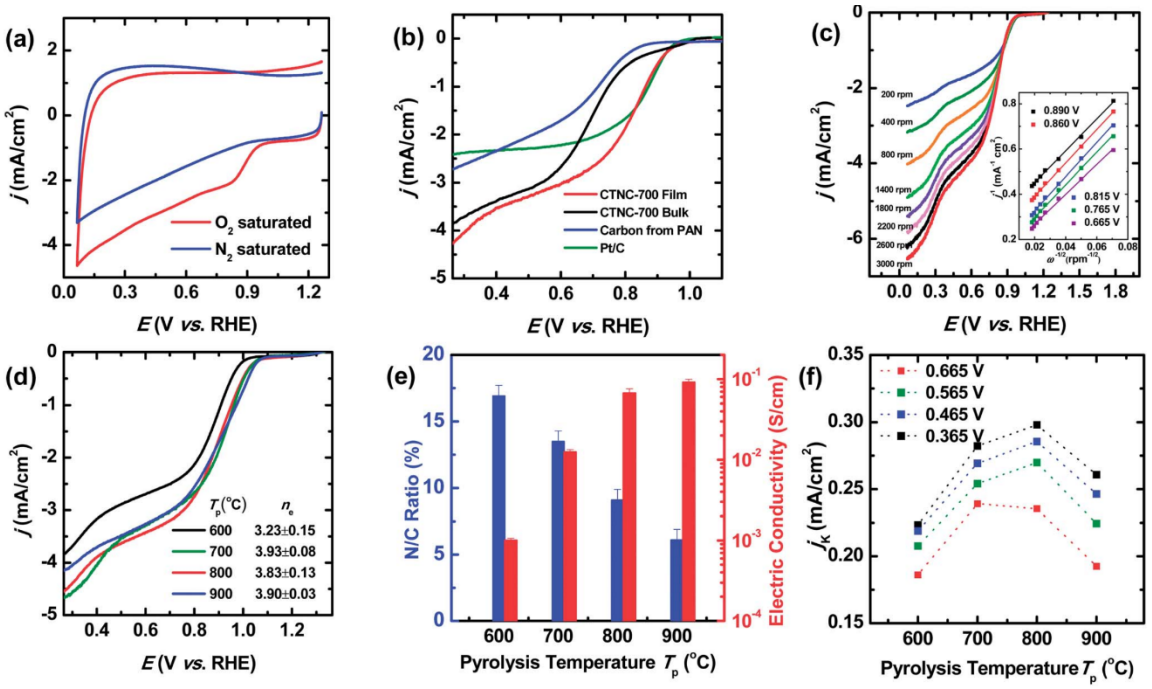

Figure 4.2 (a) CV of CTNC in O_2-and N_2-saturated 0.1 mol/L KOH solutions; (b) Polarization curves at rotating speed of 1400 rpm; (c) Polarization curves of CTNC-700 at different rotating speeds and K-L plots derived from (c) (inset). (d) Polarization curves of CTNC pyrolyzed at different T_p at rotating speed of 1400 rpm; (e) Effect of T_p on the N/C ratio (blue bars), electrical conductivity (red bars); (f) Kinetic currents at different potentials calculated from the K-L equation.

Long time stability of CTNC electrodes under electro-chemical load was assessed by evaluation of prolonged chronoamperometric response under a 0.865 V bias *vs*. RHE and by comparison of polarization curves acquired before and after this measurement. Nearly constant current observed over the course of 10 hours and virtually no changes in polarization curves between 0.4 V and 0.8 V are both indicators of excellent ORR stability of binder-free CTNCs.

The importance of nanoscale morphology of CTNC be-came evident from comparison of its LSV trace with a control sample prepared from the equivalent PAN homopolymer (**Figure 4.2b**, blue trace). The lower η_{os} and higher current density (j) exhibited by CTNCs indicates higher accessibility/density of catalytic sites facilitated by nanoporosity. Contribution of residual Cu to the observed effects was ruled out by similar

LSV traces of control carbon samples prepared from PAN obtained by ATRP and FRP. Koutecky-Levich (K-L) analysis[36] (Equation S1-3) of polarization curves at different rotating speeds (**Figure 4.2c**) revealed that ORR catalyzed by CTNC-700 in the potential range of 0.365 V ~ 0.890 V proceeded through a 4e-transfer, with $n_e = 3.93 \pm 0.11$.

Comparison of polarization curves with composition and electrical properties of CTNCs pyrolyzed at different T_p (**Figure 4.2d-f**) indicated that ORR performance depends on the interplay of nitrogen content and electrical conductivity. While CTNC-600 had the highest nitrogen content (**Figure 4.2e**, blue bars), it exhibited higher η_{os}, lower j, and the lowest n_e (**Figure 4.2d**, black trace). CTNC-600's inferior performance could be related to its low electrical conductivity (**Figure 4.2e**, red bars). Accordingly, while the values of overall j, η_{os} and ne for the other samples were very similar, the highest kinetic current (j_K) as determined from the K-L analysis, was observed for CTNC-800.

The impact of physical structure on catalytic activity was also manifested by pronounced dependence of performance on film thickness (**Figure 4.3**). RDE experiments were performed using samples of CTNC-700 with thicknesses ranging from *ca*. 90 nm to 4.4 μm (CTNC loadings: 12 - 180 μg/cm^2). CNTC thickness was controlled by varying the total volume of BCP solution used in the deposition of precursor film on GC electrode. The catalyst loadings, in such prepared CTNC films were estimated based on the mass of the deposited BCP under the assumption that the thin-film pyrolysis proceeded with the same yield as in the bulk. The decrease of the CTNC catalyst loading below *ca*. 120 μg/cm^2 led to a marked decrease of ORR performance shown by the increase of overpotential magnitude, decrease of n_e (**Figure 4.3a**) and decrease of cathodic current density. Optical

microscopy of entire GC surfaces with CNTC films did not reveal any film discontinuities or dewetting, which could have been responsible for the observed loss of ORR activity.

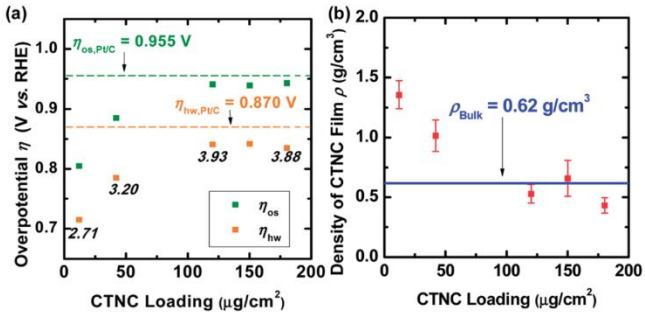

Figure 4.3 (a) Plot of onset/half-wave overpotential (η_{os} and η_{hw}) *vs.* CTNC-700 catalyst loading (italic numbers indicate n_e for corresponding CTNC shown above); (b) Comparison of estimated CTNC-700 film densities with bulk CTNC.

The observed decrease of ORR performance may be related to the change of surface morphology of CTNC with decreasing film thickness. Morphology was quantified by the analysis of domain topology in tapping mode atomic force microscopy (AFM) height images of BCPs (**Figure 4.4,** left column) and CTNCs (**Figure 4.4,** right column). For the purpose of this analysis the images were bandpass-filtered to remove the height variations not related to morphology. Characteristic brighter (*i.e.*, taller) features in BCP images correspond to PAN domains. These regions appear higher due to mechanical contrast between rigid PAN and soft PBA. Similar size and appearance of carbon domains in images of CTNCs point to overall preservation of nanoscale morphology upon pyrolysis. Preservation of the average size of nanoscale domains is also evident from the comparison of azimuthally averaged power spectra of AFM images of BCPs and CTNCs (**Figure 4.6a**), in which the domain size is reflected by the position of the characteristic change of slope (indicated by red arrows).

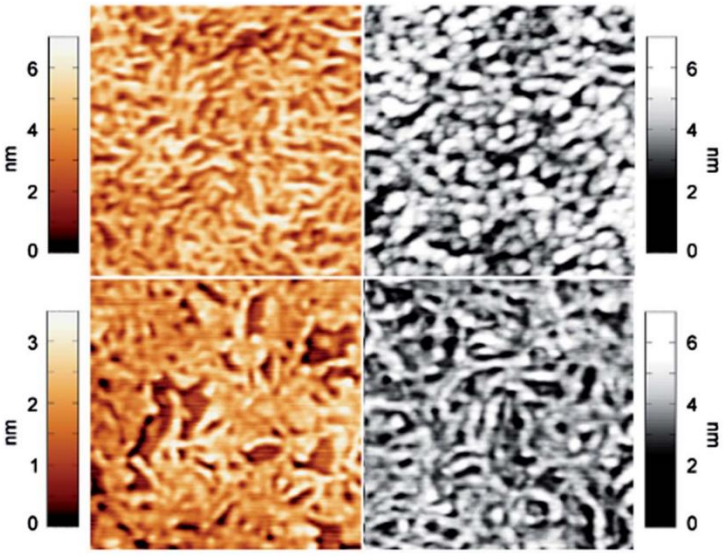

Figure 4.4 AFM images of BCP film (left column) and resultant CTNC-700 (right column) for two extreme catalyst loadings: 12 μg/cm^2 (top row) and 180 μg/cm^2 (bottom row).

Figure 4.5 Overlay of AFM image shown in Figure 3 and their domain traces with three largest connected clusters coloured in red, blue and magenta and all remaining clusters coloured in green.

Careful inspection of AFM images for CTNC samples from extreme catalyst loadings (**Figure 4.4,** right column) indicates that while characteristic domain sizes remain very similar, nanocarbon domains in the thinnest samples appear to be less interconnected. Such loss of interconnectivity could be indicative of the loss of bicontinuous bulk

morphology, which has been shown in the past to be the prerequisite for preventing nanostructure collapse upon pyrolysis.[24, 27, 28] In order to quantify domain connectivity in AFM images, we have developed a novel mathematical morphology based analysis method involving computing image skeletons, which trace the crests of height domains. The overlays of such produced domain traces with the filtered original AFM images are shown in **Figure 4.5**. Indeed, inspection of domain traces of BCPs shows that PAN domains form a highly interconnected network (**Figure 4.5**), likely reflecting the interconnected, bicontinuous bulk morphology.

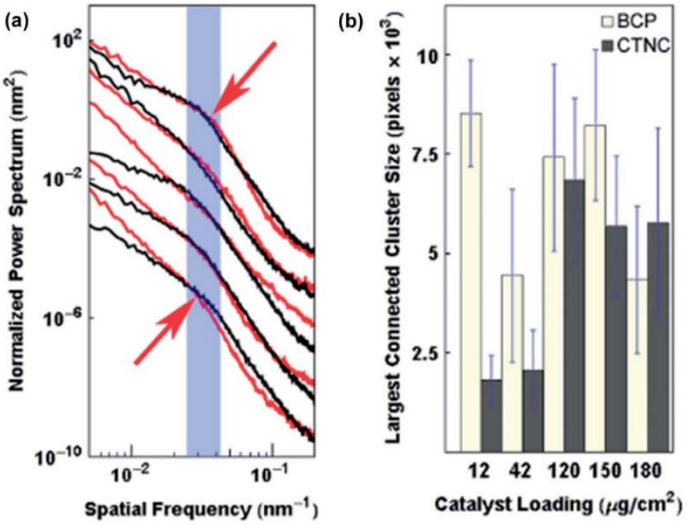

Figure 4.6 (left) Azimuthally averaged power spectra of AFM images of BCP (red traces) and CTNC-700 (black traces) films corresponding to catalyst loadings ranging from 12 μg/cm^2 (top) to 180 μg/cm^2 (bottom); (right) Size of the largest connected domain clusters in the AFM images of BCP (light red) and CTNC-700 for different catalyst loading (film thickness).

In order to obtain a quantitative measure of the degree of network connectivity, all AFM images obtained in this study were piecewise skeletonized to produce domain traces in 500 nm × 500 nm sub-regions. Such traces were then analyzed by counting the number and size of connected objects. Results of this analysis (**Figure 4.6b**) show that while average size of connected network objects for BCPs did not vary systematically with film

thickness, it dropped sharply for CTNCs with catalyst loadings below roughly *ca.* 120 μg cm^{-2}. This parallels the observed increase of overpotential below the same catalyst loading (**Figure 4.3a**). The density of CTNC films was estimated by calculating the ratio of catalyst loading to thicknesses, determined by profilometry. Results (**Figure 4.3b**) indeed show an increase in film density with a decrease in catalyst loading, pointing to the collapse of three-dimensional nanostructure in the thinnest films. This collapse is presumably due to the interaction between the GC substrate and carbonizing material. It is not difficult to envision that such a collapse could cause a loss of porosity and effective density of nitrogen-based catalytic sites, leading to the decrease in ORR performance of the thinnest CTNC films.

4.4 Conclusion

In summary, we have demonstrated that CTNC prepared from a PAN-b-PBA can act as electrocatalysts of ORR, with performance matching that of Pt based catalysts. The ability to prepare CTNC electrodes in a binder-free form uniquely allowed us to reveal the sharp decrease of electrocatalytic performance with the loss of bulk, nanoporous morphology, concomitant with the decrease of film thickness. The ORR performance of CTNCs has also been shown to be strongly affected by the interplay of the nitrogen content and electrical conductivity. We propose that one of the structural features of nitrogen-enriched carbons which might be responsible for their widespread electrochemical activity is nitrogen's stabilizing effect on the edges of nanographitic domains. The latter are known to be associated with the presence of non-bonding electron states, which could offer considerable advantage for facilitating electrochemical reduction processes.[37, 38] Moreover, nanoporosity of CTNCs may greatly increase the availability and accessibility of such sites. In this regard the key benefit of the copolymer-templating method discussed

is that it generates nanoporosity through thermal decomposition of the sacrificial block prior to carbonization. As such, this technique does not require harsh chemical treatment, like those used in the fabrication of activated carbons, or hard-templating methods. Some subtle characteristics could have an effect, such as preferential exposure of nitrogen-terminated zigzag edges of nanographitic domains from orientation of PAN chains at the domain interface in copolymer. It is worth noting that although the way of utilizing binder-free system in real devices is currently challenging, such electrode fabrication method is an effective tool for performing mechanistic studies on the ORR. Fundamental structural insights such as those discussed above could provide a stimulus for further developments of next generation sustainable heteroatom enriched carbon electrocatalysts for important energy applications.

4.5 Experimental

Materials. Acrylonitrile (AN), *n*-butyl acrylate (BA), methyl 2-bromopropionate (MBP), *N*,*N*,*N*′,*N*″,*N*″-pentamethyldiethylenetriamine (PMDETA), 2,2′-bipyridyl (bpy), CuBr, CuCl, $CuBr_2$, anisole, dimethylformamide (DMF), dimethylsulfoxide (DMSO), tetrahydrofuran (THF), N-methyl-2-pyrrolidone (NMP), ethanol, methanol, and Nafion®117 solution (5 wt %), polyacrylonitrile homopolymer (M_w = 150,000) were all obtained from Sigma-Aldrich. 20 wt% platinum on Vulcan carbon black was purchased from E-tek. CuCl and CuBr were purified by stirring in glacial acetic acid followed by washing with ether and dried overnight under vacuum. Monomers were passed through a basic alumina column prior to use. All other chemicals were used as received.

Preparation of Bulk Copolymer-Templated Nitrogen-Enriched Nanocarbon (CTNCs). The block copolymer and homopolymer precursors were synthesized *via* atom

transfer radical polymerization as reported previously.[24] The polymer samples were stabilized at 280 °C for 1 h under air flow (150 mL/min) with a heating rate of 1 °C/min, purged with nitrogen gas for one hour during cooling, and then pyrolyzed at 600 ~ 900 °C for 0.5 h under nitrogen gas flow (150 mL/min) with a heating rate of 10 °C/min. 1 mg of CTNC was dispersed in 1 mL solvent mixture of Nafion (5%) and ethanol (v/v = 1/9) by sonication. 20 μL of the solution was drop-casted on the glassy carbon (GC) electrode surface and dried in air. Pt/C based electrocatalysts were prepared using similar procedure.

Preparation of Binder-Free CTNC Films. Detachable GC disk insert (5 mm diameter, 4 mm thick, Pine AFED050P040GC) was carefully polished with 3 μm, 1 μm, and 0.25 μm diamond successively to obtain mirror-like surface. Then the electrode was washed with double distilled water and acetone and finally dried in air. The insert was then treated under UV to remove organic residues. The DMF solution of as-made block copolymer (BCP) (10 mg/mL) were drop-cast onto the GC insert using a microliter syringe pump and dried first at ambient condition followed by a 160 °C thermal annealing under vacuum. CNTC thickness was varied by varying the total volume of BCP solution used in the deposition of precursor film on GC electrode. The catalyst loadings, in such prepared CTNC films were estimated based on the mass of the deposited BCP under the assumption that the thin-film pyrolysis proceeded with the same yield as in the bulk.

Electrochemical Characterization. All of the voltammograms were recorded at 25 °C with a Gamry Reference 600 potentiostat. Measurements were carried out at a scan rate of 10 mV/s in N_2-saturated or O_2-saturated 0.1 M KOH aqueous solution. The as-prepared GC insert assembled onto the rotating electrode set-up (Pine E5TQ Series) was used as a working electrode and a platinum mesh as the counter electrode. Potentials were

recorded versus Ag/AgCl reference electrode and converted to reversible hydrogen electrode (RHE) by *E* (RHE) = *E* (Ag/AgCl) + 0.965 V in 0.1 M KOH aqueous solution.[36]

Details of Calculating the Koutecky - Levich Plots. Kinetic parameters of oxygen reduction reaction (ORR) were analyzed on the basis of the Koutecky - Levich equations[36]:

$$\frac{1}{j}=\frac{1}{j_L}+\frac{1}{j_K}=\frac{1}{B\omega^{1/2}}+\frac{1}{j_K} \quad \text{(eq. S1)}$$

$$B=0.62n_eFC_0D_0^{2/3}v^{-1/6} \quad \text{(eq. S2)}$$

$$j_K=n_eFkC_0 \quad \text{(eq. S3)}$$

where j (mA/cm^2) is the measured current density, j_K and j_L (mA/cm^2) are the kinetic- and diffusion-limiting current densities, ω is the angular velocity of the rotating disk ($\omega = 2\pi N$, where N is the linear rotating speed in rpm), n_e is the overall number of electrons transferred in ORR, F is the Faraday constant (97485 C/mol), C_0 is the bulk concentration of O_2 (1.2×10^{-3} mol/L), D_0 is diffusion coefficient of O_2 (1.9×10^{-5} cm^2 s^{-1}), v is the kinematic viscosity of the electrolyte (0.01 cm^2 s^{-1}), and k is the electron transfer rate constant, respectively. According to the Equations S1 to S3, the number of electrons transferred (n_e) and the kinetic-limiting current j_K can be obtained from the slope and intercept of the Koutecky–Levich plots (1/j versus $\omega^{-1/2}$), respectively.

Characterization. X-ray photoelectron spectroscopy (XPS) measurements were performed with a Kratos Axis Ultra spectrometer under the pressure of 10^{-8} torr. The monochromatic X-ray source was Al Kα (1486.6 eV) and the power was 208 W (14 kV, 20 mA). The voltage step size was 0.5 eV for surveys and 0.1 eV for high resolution. The

dwell time at every step was 150 ms for surveys, 600 ms for O and C, and 2000 ms for N high resolution. Quantification was performed by applying the appropriate relative sensitivity factors (RSFs, C 1*s* = 0.297, O 1*s* = 0.703, N 1*s* = 0.491) after subtracting Shirley-type background. The deconvolution into component peaks in high resolution peaks were carried out using 7:3 product of Gaussian-Lorentzian. Binding energy was corrected with reference to C 1*s* at 285.0 eV. The content of copper was also determined using an inductively coupled plasma mass spectrometer (ICP-MS) by Analytical Consulting Services (ACS) Labs in Houston, TX.

The pore structure of carbon sample was assessed from the N_2 isotherm curve measured by a gas adsorption analyzer (NOVA2000 series, Quantachrome Instruments). Prior to the adsorption experiments, all samples were degassed at 300 °C for 3 h to eliminate the surface contaminants (water or oils). The standard analysis of nitrogen sorption isotherms recorded for all samples studied provided the Brunauer-Emmett-Teller (BET) surface area, S_{BET}, evaluated in the range of relative pressure between 0.04-0.2. For the carbonized material, calculation of volume fractions of carbon and pores was based on the total pore volume per gram (V_{tot}) obtained from nitrogen adsorption analysis. V_{total} was calculated as 0.67 cm^3/g based on the amount adsorbed at a relative pressure of 0.99. Conversion of this value to volume fractions of carbon and pores still required the knowledge of density of carbon matrix. This was estimated using the known relationship between the density of carbon materials as a function of the H/C ratio.[39] Using this relationship and the H/C ratio (~0.20) obtained for the bulk CTNC from elemental analysis, the carbon matrix density was estimated to be equal to ~1.75 g/cm^3. From the V_{tot} and

carbon matrix density, the volume fractions of pore and carbon was, ϕ_{pore}= 0.539, ϕ_{carbon} = 0.461. Therefore, the density of CTNC can be calculated.

Tapping mode-atomic force microscopy (TM-AFM) measurements were taken using a Veeco Metrology Group Digital Instruments Dimension V with NanoScope V controller and NanoScope 7 software. A Veeco TESPA cantilever with a spring constant of 20–80 N/m and resonance frequency of 320–375 kHz was used. Filtered height images were generated by 7th order 2D polynomial flattening, followed by a "soft edge" bandpass filter (2 nm to 50 nm). Image skeletons were computed by digital thinning of non-overlapping 500 nm x 500 nm sub-panels of each filtered height image (using the procedure above), binarized by thresholding at the mean height. To obtain the measure of domain connectivity on the surface, connected clusters in the skeletonized images were detected using morphological processing tools and then sorted by size. All digital image processing was performed with custom scripts written in MATLAB R2013a (The MathWorks Inc., Natic, MA) and *Mathematica* 9 (Wolfram Research, Champaign, IL).

4.6 References

[1] J. Wang, Electrochemical Glucose Biosensors, *Chem. Rev.* **2007,** *108* (2), 814-825, 10.1021/cr068123a.

[2] X. Jin, V.V. Balasubramanian, S.T. Selvan, D.P. Sawant, M.A. Chari, G.Q. Lu, A. Vinu, Highly Ordered Mesoporous Carbon Nitride Nanoparticles with High Nitrogen Content: A Metal-Free Basic Catalyst, *Angew. Chem. Int. Ed.* **2009,** *48* (42), 7884-7887, 10.1002/anie.200903674.

[3] K. Otsuka, I. Yamanaka, Electrochemical cells as reactors for selective oxygenation of hydrocarbons at low temperature, *Catal. Today* **1998,** *41* (4), 311-325, http://dx.doi.org/10.1016/S0920-5861(98)00022-4.

[4] T.-P. Fellinger, F. Hasché, P. Strasser, M. Antonietti, Mesoporous Nitrogen-Doped Carbon for the Electrocatalytic Synthesis of Hydrogen Peroxide, *J. Am. Chem. Soc.* **2012,** *134* (9), 4072-4075, 10.1021/ja300038p.

[5] M. Lefevre, E. Proietti, F. Jaouen, J.P. Dodelet, Iron-Based Catalysts with Improved Oxygen Reduction Activity in Polymer Electrolyte Fuel Cells, *Science* **2009,** *324* (5923), 71-74, 10.1126/science.1170051.

[6] G. Wu, K.L. More, C.M. Johnston, P. Zelenay, High-Performance Electrocatalysts for Oxygen Reduction Derived from Polyaniline, Iron, and Cobalt, *Science* **2011,** *332* (6028), 443-447, 10.1126/science.1200832.

[7] D.S. Su, G. Sun, Nonprecious-Metal Catalysts for Low-Cost Fuel Cells, *Angew. Chem. Int. Ed.* **2011,** *50* (49), 11570-11572, 10.1002/anie.201106166.

[8] K. Gong, F. Du, Z. Xia, M. Durstock, L. Dai, Nitrogen-Doped Carbon Nanotube Arrays with High Electrocatalytic Activity for Oxygen Reduction, *Science* **2009,** *323* (5915), 760-764, 10.1126/science.1168049.

[9] L. Qu, Y. Liu, J.-B. Baek, L. Dai, Nitrogen-Doped Graphene as Efficient Metal-Free Electrocatalyst for Oxygen Reduction in Fuel Cells, *ACS Nano* **2010,** *4* (3), 1321-1326, 10.1021/nn901850u.

[10] S. Yang, X. Feng, X. Wang, K. Müllen, Graphene-Based Carbon Nitride Nanosheets as Efficient Metal-Free Electrocatalysts for Oxygen Reduction Reactions, *Angew. Chem. Int. Ed.* **2011,** *50* (23), 5339-5343, 10.1002/anie.201100170.

[11] D. Yu, Q. Zhang, L. Dai, Highly Efficient Metal-Free Growth of Nitrogen-Doped Single-Walled Carbon Nanotubes on Plasma-Etched Substrates for Oxygen Reduction, *J. Am. Chem. Soc.* **2010,** *132* (43), 15127-15129, 10.1021/ja105617z.

[12] H. Wang, T. Maiyalagan, X. Wang, Review on Recent Progress in Nitrogen-Doped Graphene: Synthesis, Characterization, and Its Potential Applications, *ACS Catal.* **2012,** *2* (5), 781-794, 10.1021/cs200652y.

[13] P. Ayala, R. Arenal, M. Rümmeli, A. Rubio, T. Pichler, The doping of carbon nanotubes with nitrogen and their potential applications, *Carbon* **2010,** *48* (3), 575-586, http://dx.doi.org/10.1016/j.carbon.2009.10.009.

[14] C. Zhu, S. Dong, Recent progress in graphene-based nanomaterials as advanced electrocatalysts towards oxygen reduction reaction, *Nanoscale* **2013,** *5* (5), 1753-1767, 10.1039/c2nr33839d.

[15] J.P. McGann, M. Zhong, E.K. Kim, S. Natesakhawat, M. Jaroniec, J.F. Whitacre, K. Matyjaszewski, T. Kowalewski, Block Copolymer Templating as a Path to Porous Nanostructured Carbons with Highly Accessible Nitrogens for Enhanced (Electro)chemical Performance, *Macromol. Chem. Phys.* **2012,** *213* (10-11), 1078-1090, 10.1002/macp.201100691.

[16] J.P. Paraknowitsch, A. Thomas, Doping carbons beyond nitrogen: an overview of advanced heteroatom doped carbons with boron, sulphur and phosphorus for energy applications, *Energy Environ. Sci.* **2013,** *6*, 2839-2855, 10.1039/c3ee41444b.

[17] X. Wang, K. Maeda, A. Thomas, K. Takanabe, G. Xin, J.M. Carlsson, K. Domen, M. Antonietti, A metal-free polymeric photocatalyst for hydrogen production from water under visible light, *Nat. Mater.* **2009,** *8* (1), 76-80, http://www.nature.com/nmat/journal/v8/n1/suppinfo/nmat2317_S1.html.

[18] X. Wang, X. Li, L. Zhang, Y. Yoon, P.K. Weber, H. Wang, J. Guo, H. Dai, N-Doping of Graphene Through Electrothermal Reactions with Ammonia, *Science* **2009,** *324* (5928), 768-771, 10.1126/science.1170335.

[19] Y. Tang, B.L. Allen, D.R. Kauffman, A. Star, Electrocatalytic Activity of Nitrogen-Doped Carbon Nanotube Cups, *J. Am. Chem. Soc.* **2009,** *131* (37), 13200-13201, 10.1021/ja904595t.

[20] W. Yang, T.-P. Fellinger, M. Antonietti, Efficient Metal-Free Oxygen Reduction in Alkaline Medium on High-Surface-Area Mesoporous Nitrogen-Doped Carbons Made from Ionic Liquids and Nucleobases, *J. Am. Chem. Soc.* **2010,** *133* (2), 206-209, 10.1021/ja108039j.

[21] R. Silva, D. Voiry, M. Chhowalla, T. Asefa, Efficient Metal-Free Electrocatalysts for Oxygen Reduction: Polyaniline-Derived N- and O-Doped Mesoporous Carbons, *J. Am. Chem. Soc.* **2013,** *135* (21), 7823-7826, 10.1021/ja402450a.

[22] X. Yang, D. Wu, X. Chen, R. Fu, Nitrogen-Enriched Nanocarbons with a 3-D Continuous Mesopore Structure from Polyacrylonitrile for Supercapacitor Application, *J. Phys. Chem. C* **2010,** *114* (18), 8581-8586, 10.1021/jp101255d.

[23] L. Chen, Z.-H. Huang, H. Liang, Z.-Y. Yu, S.-H. Yu, Flexible all-solid-state high-power supercapacitor fabricated with nitrogen-doped carbon nanofiber electrode material derived from bacterial cellulose[dagger], *Energy Environ. Sci.* **2013,** *6*, 3331-3338,

[24] M. Zhong, E.K. Kim, J.P. McGann, S.-E. Chun, J.F. Whitacre, M. Jaroniec, K. Matyjaszewski, T. Kowalewski, Electrochemically Active Nitrogen-Enriched Nanocarbons with Well-Defined Morphology Synthesized by Pyrolysis of Self-Assembled Block Copolymer, *J. Am. Chem. Soc.* **2012,** *134* (36), 14846-14857, 10.1021/ja304352n.

[25] J. Liang, Y. Zheng, J. Chen, J. Liu, D. Hulicova-Jurcakova, M. Jaroniec, S.Z. Qiao, Facile Oxygen Reduction on a Three-Dimensionally Ordered Macroporous Graphitic C3N4/Carbon Composite Electrocatalyst, *Angew. Chem. Int. Ed.* **2012,** *51* (16), 3892-3896, 10.1002/anie.201107981.

[26] S.B. Yang, X.L. Feng, X.C. Wang, K. Müllen, Graphene-Based Carbon Nitride Nanosheets as Efficient Metal-Free Electrocatalysts for Oxygen Reduction Reactions, *Angew. Chem. Int. Ed.* **2011,** *50* (23), 5339-5343, DOI 10.1002/anie.201100170.

[27] T. Kowalewski, N.V. Tsarevsky, K. Matyjaszewski, Nanostructured carbon arrays from block copolymers of polyacrylonitrile, *J. Am. Chem. Soc.* **2002,** *124* (36), 10632-10633,

[28] M. Zhong, C. Tang, E.K. Kim, M. Kruk, E.B. Celer, M. Jaroniec, K. Matyjaszewski, T. Kowalewski, Preparation of porous nanocarbons with tunable morphology and pore size from copolymer templated precursors, *Mater. Horiz.* **2014,** *1*, 121-124, 10.1039/c3mh00084b.

[29] C. Tang, T. Kowalewski, K. Matyjaszewski, Preparation of Polyacrylonitrile-block-Poly(n-butyl acrylate) Copolymers Using Atom Transfer Radical Polymerization and Nitroxide Mediated Polymerization Processes, *Macromolecules* **2003,** *36* (5), 1465-1473,

[30] C. Tang, A. Tracz, M. Kruk, R. Zhang, D.M. Smilgies, K. Matyjaszewski, T. Kowalewski, Long-range ordered thin films of block copolymers prepared by zone-casting and their thermal conversion into ordered nanostructured carbon, *J. Am. Chem. Soc.* **2005,** *127* (19), 6918-6919,

[31] M. Zhong, S. Natesakhawat, J.P. Baltrus, D. Luebke, H. Nulwala, K. Matyjaszewski, T. Kowalewski, Copolymer-templated nitrogen-enriched porous nanocarbons for CO2 capture, *Chem. Commun.* **2012,** *48* (94), 11516, 10.1039/c2cc36652e.

[32] C. Tang, B. Dufour, T. Kowalewski, K. Matyjaszewski, Synthesis and morphology of molecular brushes with polyacrylonitrile block copolymer side chains and their conversion into nanostructured carbons, *Macromolecules* **2007,** *40* (17), 6199-6205, 10.1021/ma070892o.

[33] C.B. Tang, T. Kowalewski, K. Matyjaszewski, Preparation of polyacrylonitrile-block-poly(n-butyl acrylate) copolymers using atom transfer radical polymerization and nitroxide mediated polymerization processes, *Macromolecules* **2003,** *36* (5), 1465-1473, Doi 10.1021/Ma025894h.

[34] K. Matyjaszewski, Atom Transfer Radical Polymerization (ATRP): Current Status and Future Perspectives, *Macromolecules* **2012,** *45* (10), 4015-4039, 10.1021/ma3001719.

[35] K. Matyjaszewski, J. Xia, Atom Transfer Radical Polymerization, *Chem. Rev.* **2001,** *101* (9), 2921-2990, 10.1021/cr940534g.

[36] A.J. Bard, L.R. Faulkner, Electrochemical Methods: Fundamentals and Applications, Wiley, New York, 2001.

[37] S. Fujii, T. Enoki, Nanographene and Graphene Edges: Electronic Structure and Nanofabrication, *Acc. Chem. Res.* **2012,** *46*, 2201-2210, 10.1021/ar300120y.

[38] I.-Y. Jeon, S. Zhang, L. Zhang, H.-J. Choi, J.-M. Seo, Z. Xia, L. Dai, J.-B. Baek, Edge-Selectively Sulfurized Graphene Nanoplatelets as Efficient Metal-Free Electrocatalysts for Oxygen Reduction Reaction: The Electron Spin Effect, *Adv. Mater.* **2013,** *25* (42), 6138-6145, 10.1002/adma.201302753.

[39] K. Kinoshita, Carbon : electrochemical and physicochemical properties, Wiley, New York, 1988.

Chapter 5: In-situ Platinum Deposition on Nitrogen-doped Carbon Films as a Source of Catalytic Activity in a Hydrogen Evolution Reaction

This work was in collaboration with Dr. Maciej Kopeć and was initially to just investigate metal-free hydrogen evolution using PAN-derived carbons. Following procedures common in literature, we observed some activity at first, but over the course of cyclic voltammetry, the activity improved to matching that of platinum. After electrochemical cycling, we checked the films by scanning electron microscopy and energy-dispersive X-ray spectroscopy, revealing platinum on the surface of the carbon. Delving into literature, it was known in the electrochemistry community that the types of conditions used in our experiments and the publications we based those procedures on causes trace amounts of the platinum counter electrode to dissolve into solution. The dissolved platinum can then plate onto the carbon working electrode. As opposed to abandoning the project as a failure, we did further analysis and characterization to understand how the platinum was being incorporated into the carbon, and to understand the effect the platinum was having on electrocatalytic activity. Furthermore, we believed it was very important to point out the procedure used in many already published works was likely causing platinum incorporation was likely the true source of the catalytic activity reported.

5.1 Abstract

Copolymer-templated nitrogen-doped carbon (CTNC) films deposited on glassy carbon were used as electrodes to study electrochemically driven hydrogen evolution reaction (HER) in 0.5 M H_2SO_4. The activity of these materials was extremely enhanced when a platinum counter electrode was used instead of a graphite rod and reached the level of commercial Pt/C electrodes. Postreaction scanning electron microscopy (SEM) and X-ray photoelectron spectroscopy (XPS) measurements of electrode surfaces revealed that

incorporation of even extremely low amounts of Pt resulted in this considerable gain of HER activity. High resolution XPS analysis and density functional theory (DFT) calculations confirmed that pyridinic nitrogen atoms act as active sites for Pt coordination and deposition. The Pt can be incorporated in both molecular (Pt^{2+}) and metallic (Pt^{0}) form. This study shows that great caution must be taken when designing "metal-free" HER catalysts based on N-doped carbons.

Table of Contents Figure

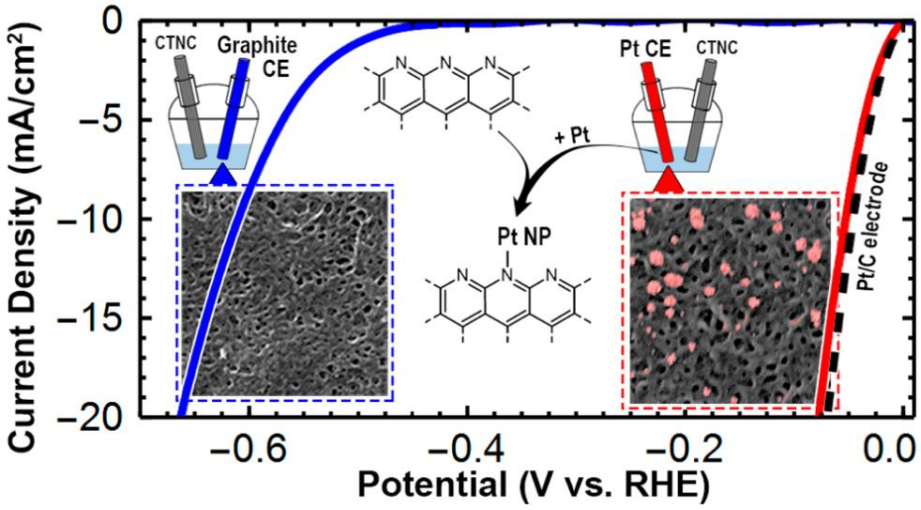

E. Gottlieb, M. Kopec, M. Banerjee, J. Mohin, D. Yaron, K. Matyjaszewski, T. Kowalewski, In-Situ Platinum Deposition on Nitrogen-Doped Carbon Films as a Source of Catalytic Activity in a Hydrogen Evolution Reaction, *ACS Appl Mater Interfaces* **2016,** *8* (33), 21531-8, 10.1021/acsami.6b03924.

5.2 Introduction

Carbon materials, such as activated carbon, are the most common catalyst supports due to their unique properties including large surface area, resistance to acids and bases, stability at high temperatures, and relatively easy regeneration of the active phase by combustion. The recent development of nanostructured carbons with unique electronic properties imparted by purity of graphitic basal planes and functionalized by heteroatoms has given way to extensive exploration of their application as standalone catalysts.[1, 2] In

the area of electrocatalysis, the discovery of catalytic activity of nitrogen-doped carbon nanotubes in the oxygen reduction reaction (ORR) by Dai *et al.*[3] spurred a broad interest in heteroatom-enriched nanocarbons as "metal-free" electrocatalysts for ORR,[4] oxygen evolution reaction (OER),[5, 6] CO_2 reduction,[7-10] and hydrogen evolution reaction (HER).[11-16]

Nitrogen atoms can be incorporated into graphitic and partially graphitic carbons either as pendant functionalities or as "structural" heteroatoms, integrated within the graphitic lattice as quartenary (graphitic), pyridinic, or pyrrolic species.[17] Structural heteroatoms are of particular interest for catalysis due to their chemical stability and good electronic communication with the π-electrons of the graphitic domains. The electron-withdrawing nature of these nitrogen atoms, owing to their electronegativity compared to carbon, results in a lowering of electron density for neighboring carbons. The resulting partially electropositive adjacent carbons can act as adsorption sites for oxygen molecules, which can subsequently be electrochemically reduced during ORR.[18] In the HER reaction, nitrogen atoms are believed to be active sites for proton adsorption and subsequent reduction.[11, 12] Additionally, the specific mechanisms of these processes, as well as roles of each type of structural and pendant nitrogen, are still being debated. These investigations are further complicated by a rising concern that the observed activities may be at least partially skewed by the presence of metal residues, usually originating from Fe, Co, or Ni catalysts used during synthesis.[19, 20] Whereas this problem has been addressed for ORR, e.g. by employing catalysts synthesized using all-metal-free approaches to confirm the catalytic activity of N-doped carbons,[19] a similar issue seems to have been overlooked in the case of "metal-free" HER.

In a typical HER experiment, a traditional three-electrode electrochemical cell is used to measure catalytic activity, which commonly comprises a Pt or graphite counter electrode (CE) and 0.5 M H_2SO_4 as the electrolyte. A critical concern, often not addressed, is the ability for Pt to dissolve in acidic media during potential cycling.[20-24] It has already been shown that dissolved Pt can contaminate a carbon working electrode, specifically under HER conditions.[25-28] Further complicating this concern is the fact that nitrogen heteroatoms in carbon materials are known to be active sites for nucleation and stabilization of metals.[29-32] Nevertheless, Pt is still commonly employed as a CE to investigate metal-free or noble-metal free systems, many of which comprise different forms of nitrogen-doped carbon.[33-43]

In addition to their activity as metal-free catalysts, heteroatom-enriched nanocarbons have been recently investigated for enhanced metal incorporation, which would take advantage of well-known metal coordinating properties of heteroatoms, such as nitrogen.[27] Pyridinic nitrogen is of particular interest, given widespread involvement of conjugated sp^2 nitrogens as metal coordination moieties (such as in bipyridine) in heterogeneous catalysis and in nature. Rational design of highly efficient and specific nitrogen-enriched nanocarbon supports could lead to the development of catalysts with significantly lower precious metal content and improved stability. As such, it could significantly alter the economics of a wide range of devices, including fuel cells, where the cost of precious metals is the main barrier to their widespread use. When investigating both metal-free catalysis and carbon-supported metal catalysis for HER, it is extremely important to separate the roles played by the metal and the support. Herein, we demonstrate

how this separation can be accomplished through the use of well-defined, porous, copolymer-templated nitrogen-enriched nanocarbons (CTNCs) as electrodes.

Synthesis of CTNCs utilizes soft templating through macromolecular self-assembly of a nanostructured block copolymer, specifically poly(butyl acrylate)-b-polyacrylonitrile (PBA-b-PAN).[44] The block copolymer (BCP) is composed of a heteroatom-rich carbon source, PAN, and an immiscible sacrificial block, PBA.[47, 48] The use of this synthetic pathway allows key aspects of CTNCs, such as surface area and mesoscale structure, to remain unchanged while varying the level of N doping and the size of the nanographitic domains through selection of the pyrolysis temperature.[45] The fabrication begins with self-assembly of block copolymers into well-defined nanoscale morphologies (Scheme 1). Upon pyrolysis, PAN serves as a heteroatom-rich carbon source for formation of graphitic domains, while the sacrificial PBA block is volatilized, generating a highly porous material. Maintaining a consistent nanostructure while varying conductive properties and N content/types allows for a more in-depth analysis of Pt incorporation and catalytic effectiveness in HER.

5.3 Results and Discussion

As with any work on HER, electrochemical experiments carried out in the current study were designed to provide insights into what constitutes the limiting step in the reaction. According to the generally accepted view, there are three possible limiting steps for HER in acidic media:

1) electrochemical hydrogen adsorption (Volmer step)

$$H^+ + e^- \rightarrow H_{ads}$$

2) electrochemical desorption (Heyrovsky step)

$$H_{ads} + H^+ + e^- \rightarrow H_{2(g)}$$

3) chemical desorption (Tafel step)

$$2H_{ads} \rightarrow H_{2(g)}$$

Thus, the reaction may occur either via the Volmer–Heyrovsky or Volmer–Tafel mechanism. The rate-controlling steps can be easily determined by evaluating the slopes of plots of overpotential as a function of the logarithm of current density in linear scanning voltammetry (Tafel plots).[46, 47]

HER activity of CTNC electrodes was studied by recording polarization curves in 0.5 M H_2SO_4. To study the effect of nitrogen content and conductivity, four sets of electrodes were prepared by deposition of block copolymer films on glassy carbon substrates, followed by stabilization through oxidative annealing. Stabilized films were then pyrolyzed under N_2 at temperatures ranging from 600 to 900 °C and used as electrodes in a standard HER electrochemical setup. Two sets of experiments were performed to ascertain the impact of Pt on catalytic activity: (i) cycling with a graphite counter electrode, referred to as metal-free conditions, and (ii) cycling with a Pt mesh counter electrode, referred to as Pt cycling. In order to fully equilibrate the system, each experiment involved performing 1000 cyclic voltammetry (CV) scans, followed by recording of linear sweeping voltammograms (LSV).

As shown in **Figure 5.1**, CTNCs cycled with a graphite rod counter electrode exhibited considerable electrochemical activity in comparison to a bare glassy carbon electrode and N-doped carbon prepared by pyrolysis of commercial PAN homopolymer. This comparison indicates that electrochemical activity of CTNCs is rooted in the combination of N doping and nanostructuring afforded by the copolymer templating

method used in their synthesis. Plotting the activity as measured by onset overpotential and overpotential at 10 mV/cm^2 (referred to as "operating overpotential") against pyrolysis temperature reveals the presence of a clear optimum for materials pyrolyzed at 700 °C with an operating overpotential of about 500 mV.

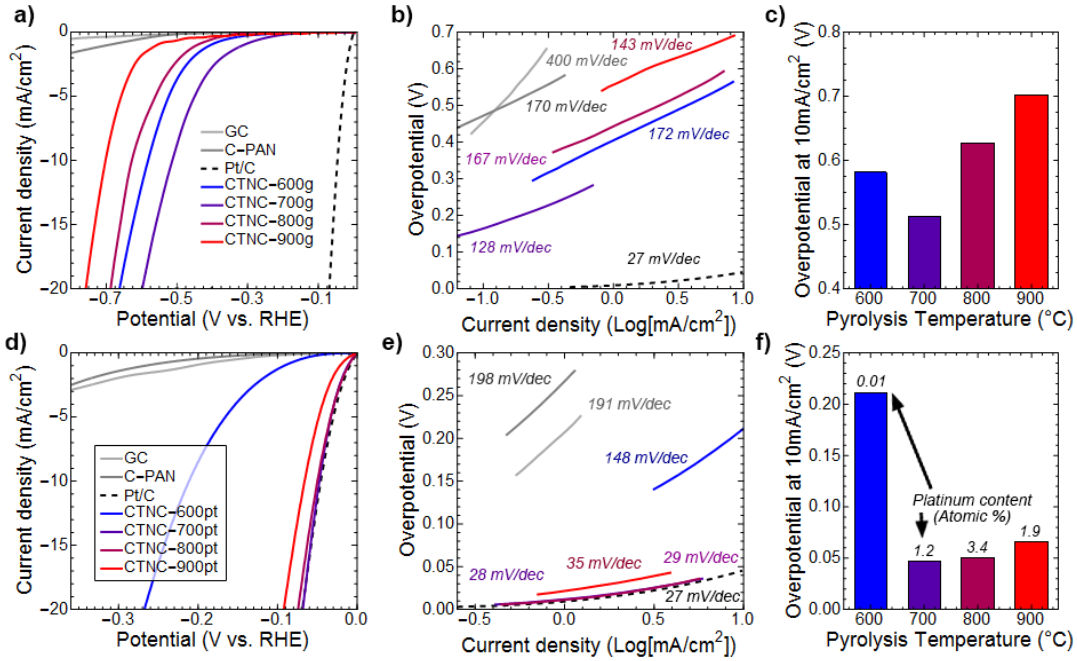

Figure 5.1 Electrochemical activity of CTNCs prepared under different pyrolysis temperatures. a) Linear sweep voltammograms (20 mV/s) recorded in 0.5 M H_2SO_4 with a graphite counter electrode after 1000 initial CV scans between 0 and -0.8 V vs SCE (at 100 mV/s); (b) Tafel plots and (c) operating overpotentials as a function of pyrolysis temperature corresponding to polarization curves and in (a). d) Linear sweep voltammograms (20 mV/s) recorded in 0.5 M H_2SO_4 with a Pt mesh counter electrode after 1000 initial CV scans between 0 and -0.8 V vs SCE (at 100 mV/s); (e) Tafel plots corresponding to polarization curves and in (d); (f) operating overpotentials and as a function of pyrolysis temperature; numbers above the bars indicate amount of Pt in the vicinity of the surface measured by XPS.

The presence of a similar optimum of performance for CTNC-700g analogues has been observed in our past studies of ORR.[45] As in that previous study, the optimum can be attributed to the interplay between the nitrogen content and the extent of graphitization (and thus electrical conductivity), which respectively decrease and increase with the increase of pyrolysis temperature. The paramount importance of nanoporosity of CTNC (surface area SBET = 472 m^2/g) as a factor providing high number of active sites per unit

area of the electrode is reflected by the relatively low HER activity of carbonized PAN homopolymer (SBET = 70 m^2/g). The levels of HER activity of CTNCs reported herein are comparable with activities reported recently for other N-doped carbons under similar electrochemical conditions.[11, 12] It should be noted, however, that in contrast with ORR, where N-doped carbons (including CTNCs) match the performance of Pt catalysts, no similar match is observed for HER. This can be explained by the different demands of ORR and HER with respect to the proximity of active sites. Specifically, the density of active sites for proton adsorption (pyridinic N atoms) is lower than the density of sites for O_2 adsorption (carbon atoms adjacent to pyridinic N atoms). Indeed, the slopes of Tafel plots derived from polarization curves (**Figure 5.1b**) ranged from 128 to 172 mV/dec, which is indicative of adsorption (the Volmer reaction) being the rate-determining step.

Most interestingly, as shown in **Figure 5.1d**, the electrochemical activity of CTNCs increased dramatically when the graphite counter electrode was replaced with a Pt mesh. As in the previous case, the optimum performance was observed for materials pyrolyzed under intermediate conditions (CTNC-700pt and CTNC-800pt), but this time it approached the performance of commercial Pt/C catalyst (onset potential ~0 mV vs RHE, operating overpotential <100 mV vs RHE, dashed line in **Figure 5.1a,d**). Furthermore, the slopes of Tafel plots for CTNC-700pt and CTNC-800pt were below 40 mV/dec, which is consistent with the Tafel mechanism for HER (**Figure 5.1e**). These results clearly indicate the paramount importance of the CE in investigations of HER activity using new catalysts in acidic media. Closer inspection of numerous reports of high HER activity of N-doped carbon-based catalysts reveals that the measurements were often performed with Pt CEs

whereas the activity improvements were attributed exclusively to electrocatalyst composition.[35-38, 41, 42, 44, 45]

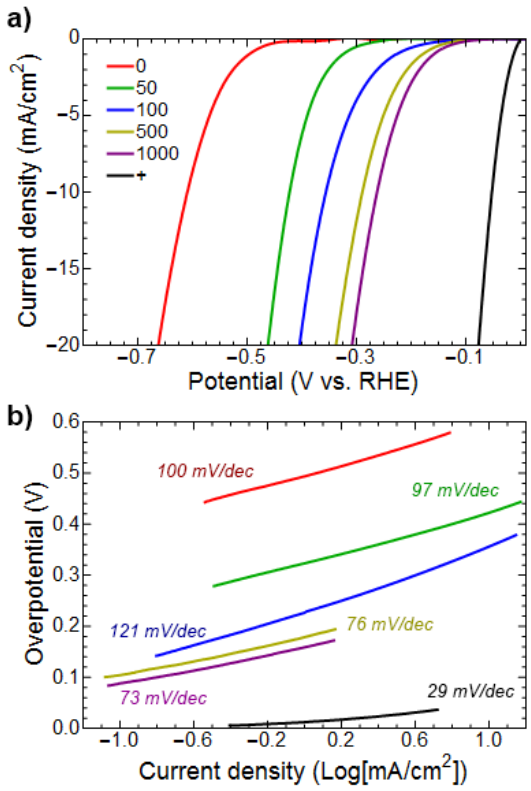

Figure 5.2 a) "Activation" of the CTNC-800 electrode upon potential cycling with Pt CE between 0 and -0.8 V vs SCE in 0.5 M H_2SO_4; dashed line denotes activity obtained after short cycling between -0.8 and +1 V vs SCE; b) Tafel plots for the corresponding cycle number and their slopes.

Given the existing reports of dissolution of Pt electrodes in acidic media,[20-23] one straightforward explanation of the marked increase in HER activity of CTNCs with Pt CE would be some mode of Pt deposition on CTNC surface. Cycling experiments performed with the CTNC-800 working electrode (**Figure 5.2**) revealed that HER activity increased gradually with the number of cycles. The overpotential at 10 mA/cm2 shifted from 600 mV vs RHE for pristine electrode to 420 mV vs RHE after only 50 cycles to eventually reach 280 mV vs RHE after 1000 potential cycles. This improvement in performance upon cycling was also evident in the progressive decrease of Tafel slopes,

from 100 to 73 mV/dec (**Figure 5.2b**). An even more dramatic effect was observed with only a few additional positive potential scans (between −0.8 and +1 V vs SCE), which is sometimes used to prepare electrodes prior to potential cycling. [37] The overpotential further decreased to 51 mV vs RHE at 10 mA/cm^2 (black line, **Figure 5.2**) which is close to the measured performance of commercial Pt/C electrodes. A similar enhancement of HER activity due to Pt deposition on a GC electrode upon very long cycling with Pt CE was recently observed by Dong *et al.*[28] Notably, in the case of CTNC, the gain in activity was observed as early as just after a few cycles. Furthermore, no activity gain was observed in a similar experiment conducted with a graphite CE.

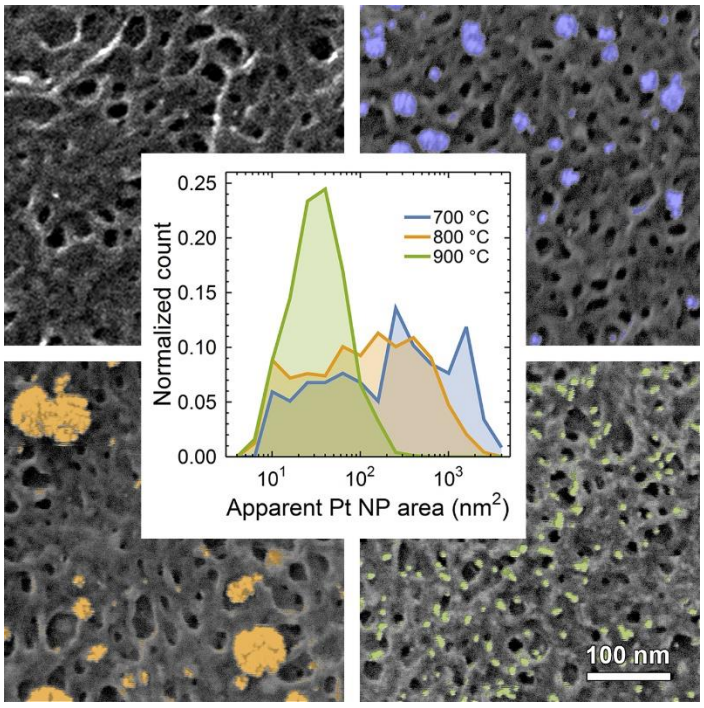

Figure 5.3 SEM images of CTNC-600pt (top left), 700pt (top right), 800pt (bottom left) and 900pt (bottom right) with false coloring of Pt nanoparticles corresponding to their histogram colors (center). CTNC-600pt did not show sufficiently large aggregates for size analysis.

SEM analysis of CTNC electrodes (**Figure 5.3**) revealed, in all cases, the presence of characteristic nanoscale morphology afforded by BCP templating. Consistent with this templating mechanism, the surface morphology of CTNCs did not appear to change in any

significant way with pyrolysis temperature. After cycling, the electrodes became decorated with distinct particulate aggregates, with sizes ranging from few to tens of nanometers in diameter. Based on EDX and XPS analysis, those aggregates were identified as Pt nanoparticles. With the increase of pyrolysis temperature, the initially broad particle size distributions narrowed toward the smallest size to become essentially monomodal for CTNC-900pt (**Figure 5.3**, bottom right). For CTNC-700pt and -800pt, the Pt aggregates appeared to be composed of smaller nanoparticles assembled into characteristic "cauliflower" structures. Similar structures have been reported by other authors for Pt deposited on carbon.[48] The evolution of the size distribution and appearance of aggregates suggest that their formation proceeds through the nucleation and further aggregation of sub-5 nm nanoparticles.

The presence of such particles is also evident upon the closer inspection of CTNC-600pt image which, at first glance, appears to be devoid of discernible deposits. The evolution of the abundance and appearance of Pt deposits with pyrolysis temperature of the CTNC substrate can be explained by the nucleation and growth mechanism. In general, one could expect that the size of Pt particles deposited on the surface should be inversely proportional to the nucleation density. Two factors that could control the nucleation density are the density of nitrogen sites and/or the overall current density. It is of note that the smallest particles (i.e., highest nucleation density) were observed on the surface of CTNC-900, which has the lowest surface density of N sites and highest conductivity. This suggests that the material's conductivity, which facilitates reduction of Pt ions, is the determining factor for nucleation density. This would also explain the larger particle sizes observed for CTNC-700 and CTNC-800. The formation of hierarchical, cauliflower aggregates on

CTNC-700pt and -800pt could be caused by local electric field concentrations due to the inhomogeneous connectivity of NG domains forming at these pyrolysis temperatures.

As demonstrated above, the HER activity of CTNC electrodes with a Pt counter electrode was clearly boosted by Pt deposition. This boost is manifested as a major drop of overpotential between CTNC-600pt and CTNC-700pt, concomitant with the observed increase of Pt content near the surface detected by XPS from 0.01 to >1 at. % (**Figure 5.1f**). Although superior HER activity of Pt-decorated carbon is not surprising (vis. well-known activity of Pt/C systems), it is important to note, however, that CTNCs exhibited considerable HER activity in a metal-free system. Under those circumstances, its most likely origin of activity was the presence of accessible N functionalities, which is widely believed to be the source of activity in N-doped carbons. For example, according to the currently held views, the ORR activity of N-doped carbons is attributed to C atoms adjacent to pyridinic N atoms.[18] Lone pair electrons of these N atoms are in turn pointed to as active sites for HER.[11] Given these observations, it is reasonable to expect that the same functionalities also serve as primary deposition sites for Pt atoms, which then effectively supersede N atoms as active sites for H^+ adsorption.

More insights into the role of N atoms in HER and Pt deposition were obtained through the analysis of high resolution 1s N and 4f Pt XPS spectra of CTNC electrodes used in electrochemical experiments. 1s N XPS spectra of pristine and Pt-cycled CTNC electrodes are shown respectively in **Figure 5.4**, top and bottom. The spectra of pristine CTNCs were dominated by two peaks, centered at 398 and 401 eV. The lower energy peak corresponds to pyridinic N, and its decrease with the increase of pyrolysis temperature reflects the concomitant decrease of nitrogen content which has been widely reported in

the literature for PAN derived carbons.[49] In contrast, the 398 eV feature is much less discernible in the spectra of Pt-cycled samples, which are dominated by a single feature centered at 400 eV.

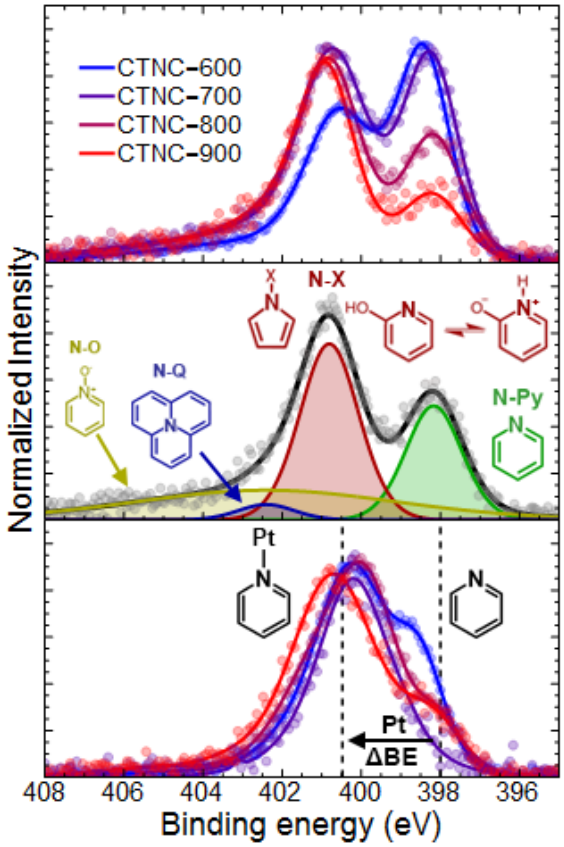

Figure 5.4 High resolution N 1s XPS spectra of CTNCs before (top) and after (bottom) Pt incorporation. Middle: CTNC-800 before Pt incorporation with shaded contours representing the components of fitting the spectrum to the superposition of different N species. The vertical dashed lines in the bottom panel indicate the DFT prediction of the difference between the 1s binding energies (ΔBE) of free and Pt-coordinating pyridinic nitrogen.

Decomposition of the 1s N XPS spectrum of pristine CTNC-800 into features corresponding to different N species according to widely accepted assignments is shown in **Figure 5.4**, middle. In agreement with the accepted mechanism of oxidative stabilization and anaerobic carbonization of PAN,[49] two dominant types of N in this material are unperturbed (N-Py, 398 eV) and partially oxidized (N-X, 401 eV) pyridinic species. The elimination of N-Py from the carbon framework as a cause of diminution of N-Py feature

can be ruled out since the overall nitrogen content, as determined by survey spectra, remained constant. Conversion of N-Py to N-X (for example through oxidation of adjacent C atoms) can be ruled out as well, since the spectrum of Pt-cycled samples peaks at a binding energy about 1 eV lower than expected for N-X species. An alternative, natural explanation for the shape change of the spectrum of Pt-cycled electrodes is that it is caused by the upward shift of binding energy of pyridinic N atoms upon coordination with Pt atoms. Indeed, the observed shift is in very good agreement with the shift predicted by DFT calculations performed on pyridine and Pt-coordinating pyridine (**Figure 5.4**, bottom).

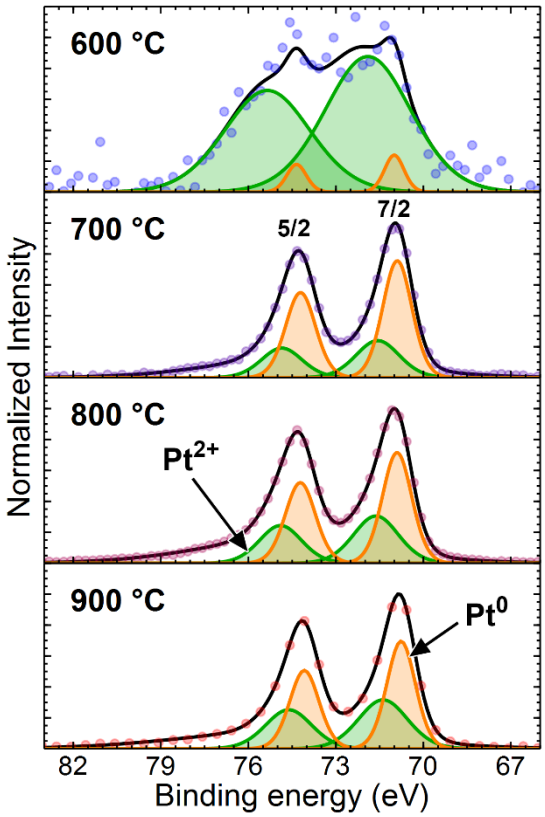

Figure 5.5 High resolution 4f Pt XPS spectra of CTNC-600 through 900 cycled with a Pt counter electrode. The presence of two maxima is due to 7/2 to 5/2 spin-orbit coupling. Shaded contours represent the decomposition of the spectra into Pt^0 (orange) and Pt^{2+} (green) lines.

The presence of such N-coordinated, "molecular" Pt species could also be inferred from high-resolution 4f Pt XPS spectra of all Pt-cycled electrodes. As shown in **Figure**

5.5, in all cases, the spectra exhibited two maxima due to familiar spin–orbit coupling in Pt. The common way of analyzing Pt XPS spectra involves their decomposition into lines corresponding to Pt^0 and Pt^{2+} species.[50] These lines differ in binding energies and width, with the broader, higher energy component corresponding to Pt^{2+}.[51] Results of such decomposition, shown in **Figure 5.5**, indicate that while both types of species were present in all of the samples, the spectrum of CTNC-600pt was dominated by the lines corresponding to Pt^{2+}. The presence of Pt^{2+} in all instances is consistent with the proposed coordination of Pt to pyridinic nitrogens inferred from 1s N XPS spectra. The prevalence of Pt^0 species on electrodes pyrolyzed at higher temperatures agrees well with the SEM observations, which revealed the presence of numerous platinum aggregates deposited on their surfaces. Even with Pt content that is barely detectable, there is a clear shift in the nitrogen content, as shown by CTNC-600pt in **Figure 5.4**, bottom, blue curve. While increased Pt incorporation does not appear to induce further shifting in N distribution, there is a clear shift in the distribution of Pt content with pyrolysis temperature (**Figure 5.5**). In the cycled CTNC-600pt electrode, the nonmetallic Pt content relative to metallic Pt is approximately 12 times higher than in all other samples.

5.4 Conclusion

The results presented demonstrate the impact of nanostructuring on boosting the HER activity of metal-free N-doped carbons. They also demonstrate that high HER activity of cycled CTNCs used herein is paralleled by their high efficiency in sequestration of minute amounts Pt due to trace dissolution of Pt counter electrodes. Results of detailed XPS analysis provides strong indication that in both cases the high activity of N-doped carbons can be attributed to the presence of pyridinic nitrogens. The high electrochemical

availability of these functionalities appears to be facilitated by the copolymer templating method used in the synthesis of CTNCs as seen by the lack of activity in pyrolyzed commercial PAN. One of the possible sources of this availability is molecular orientation of precursor polymer chains, inherent in the copolymer templating process. This aspect of this method points to its potential benefits in synthesis of highly efficient, functional nanocarbons. The ability of CTNC to sequester and bind Pt can lead to the development of novel catalyst supports based on nitrogen-doped carbon that will utilize significantly lower amounts of precious metals.

5.5 Experimental and Computational Methods

Materials. Sulfuric acid (95 - 98%, Fischer), dimethylformamide (DMF, >99.8 %, Fischer) and polyacrylonitrile (molecular weight 150,000; Sigma-Aldrich) were used as received. Pt/C catalyst (*HiSPEC® 3000*, 20 wt. % Pt on carbon black) was purchased from Alfa Aesar. The block copolymer precursors were synthesized *via* atom transfer radical polymerization (ATRP) as reported previously.[52-57] ATRP involves the use of copper-based catalyst, thus all polymer samples were purified by three-fold precipitation into methanol/water (1:1 *v/v*) and re-dissolution in DMF. A block copolymer with composition $(BA)_{91}$-*b*-$(AN)_{146}$ and narrow molecular weight distribution (MWD = 1.25) was used in this study. Milli-Q water (Milipore) was used in all experiments.

Synthesis of CTNC as Thin Film Electrodes. A detachable glassy carbon (GC) disk insert (5 mm diameter, 4 mm thick, Pine AFED050P040GC) was carefully polished with 3 μm, 1 μm, and 0.25 μm diamond successively to obtain a mirror-like surface. The electrode was then washed with double distilled water and acetone, sonicated in water and finally dried in air. The insert was then treated under UV to remove organic residues. The

as-prepared BCP was drop-cast from a 10 mg/mL solution in DMF onto the GC insert using a microliter syringe and dried under ambient conditions, followed by a 160 °C thermal annealing under vacuum. The annealed films were stabilized at 280 °C for 1 h under air flow (150 mL/min) with a heating rate of 1 °C/min, purged with nitrogen gas for one hour during cooling, and then pyrolyzed at 600 ~ 900 °C for 0.5 h under nitrogen gas flow (150 mL/min) with a heating rate of 10 °C/min. Electrodes prepared in this fashion are referred to as CTNC-XXX, where XXX indicates the pyrolysis temperature. Pt/C electrode was prepared by dispersing 1 mg of a commercial Pt black in 1 mL of ethanol/Nafion solution (9:1 v/v). The dispersion was sonicated for 30 min and 20 μL were cast on a polished GC disk.

Electrochemical Measurements. All of the measurements were recorded at 25 °C with a Gamry Reference 600 potentiostat. Linear sweep voltammograms were carried out at a scan rate of 20 mV/s in N_2-saturated 0.5 M H_2SO_4. The carbon-coated prepared GC insert was assembled into a rotating electrode set-up (Pine E5TQ Series) and used as the working electrode, with a graphite rod or platinum mesh as the counter electrode. The electrode was cycled between the measurements at 100 mV/s. All metal-free measurements were performed in a separate cell, which was not exposed to Pt. Likewise, in order to further rule out cross-contamination, the graphite counter electrode was never used with electrolyte previously cycled with Pt. Potentials were recorded versus a saturated calomel electrode (SCE) reference electrode and converted to reversible hydrogen electrode (RHE) by E (RHE) = E (SCE) + 0.241 + 0.059 × pH V. CTNC electrodes cycled with graphite and platinum counter electrode are referred to as CTNC-XXXg and CTNC-XXXpt, respectively.

Characterization. Brunauer-Emmet-Taller (BET) specific surface area measurements were performed using a Micromeritics Gemini VII 2390 Surface Area Analyzer with VacPrep 061 degasser. Degas Conditions: 300C at 20mTorr or less vacuum for a minimum of 3 hours. Scanning Electron Microscopy and Energy Dispersive X-Ray Spectroscopy (SEM/EDX) was performed on FEI Quanta 600 FEG Scanning Electron Microscope equipped with an XMAX 80mm SDD EDX detector and Oxford INCA EDS System full analytical suite. XPS was performed using an ESCALAB 250Xi X-ray Photoelectron Spectrometer Microprobe, with a 900 mm spot size.

Computational Methods. Simulations of 1s binding energies were calculated using CP2K. All structures were geometry optimized by conjugate gradient. All calculations were performed using the Gaussian Augmented-Plane Wave method and Becke, Lee, Yang, Parr (BLYP) functional. X-ray absorption spectrum (XAS) binding energies were calculated by delta self-consistent field (dSCF) in accordance with methods developed by Hutter et al.[58] Aug-cc-pVdZ basis was used for all electrons in non-Pt atoms and DZV-GTH-PADE was used for outer electrons of Pt. GTH-PADE-q18 was used for core electron potential.

5.6 References

[1] D.S. Su, S. Perathoner, G. Centi, Nanocarbons for the Development of Advanced Catalysts, *Chem. Rev.* **2013,** *113* (8), 5782-5816, 10.1021/cr300367d.

[2] S. Navalon, A. Dhakshinamoorthy, M. Alvaro, H. Garcia, Carbocatalysis by Graphene-Based Materials, *Chem. Rev.* **2014,** *114* (12), 6179-6212, 10.1021/cr4007347.

[3] K. Gong, F. Du, Z. Xia, M. Durstock, L. Dai, Nitrogen-doped carbon nanotube arrays with high electrocatalytic activity for oxygen reduction, *Science* **2009,** *323* (5915), 760-4, 10.1126/science.1168049.

[4] L. Dai, Y. Xue, L. Qu, H.-J. Choi, J.-B. Baek, Metal-Free Catalysts for Oxygen Reduction Reaction, *Chemical Reviews* **2015,** *115* (11), 4823-4892,

[5] J. Zhang, Z. Zhao, Z. Xia, L. Dai, A metal-free bifunctional electrocatalyst for oxygen reduction and oxygen evolution reactions, *Nat. Nanotechnol.* **2015,** *10* (5), 444-452, 10.1038/nnano.2015.48
http://www.nature.com/nnano/journal/v10/n5/abs/nnano.2015.48.html#supplementary-information.

[6] R. Li, Z. Wei, X. Gou, Nitrogen and Phosphorus Dual-Doped Graphene/Carbon Nanosheets as Bifunctional Electrocatalysts for Oxygen Reduction and Evolution, *ACS Catal.* **2015**, 4133-4142, 10.1021/acscatal.5b00601.

[7] B. Kumar, M. Asadi, D. Pisasale, S. Sinha-Ray, B.A. Rosen, R. Haasch, J. Abiade, A.L. Yarin, A. Salehi-Khojin, Renewable and metal-free carbon nanofibre catalysts for carbon dioxide reduction, *Nat. Commun.* **2013,** *4*, 10.1038/ncomms3819.

[8] S. Zhang, P. Kang, S. Ubnoske, M.K. Brennaman, N. Song, R.L. House, J.T. Glass, T.J. Meyer, Polyethylenimine-Enhanced Electrocatalytic Reduction of CO2 to Formate at Nitrogen-Doped Carbon Nanomaterials, *J. Am. Chem. Soc.* **2014,** *136* (22), 7845-7848, 10.1021/ja5031529.

[9] J. Wu, R.M. Yadav, M. Liu, P.P. Sharma, C.S. Tiwary, L. Ma, X. Zou, X.-D. Zhou, B.I. Yakobson, J. Lou, P.M. Ajayan, Achieving Highly Efficient, Selective, and Stable CO2 Reduction on Nitrogen-Doped Carbon Nanotubes, *ACS Nano* **2015,** *9* (5), 5364-5371, 10.1021/acsnano.5b01079.

[10] P.P. Sharma, J. Wu, R.M. Yadav, M. Liu, C.J. Wright, C.S. Tiwary, B.I. Yakobson, J. Lou, P.M. Ajayan, X.-D. Zhou, Nitrogen-Doped Carbon Nanotube Arrays for High-Efficiency Electrochemical Reduction of CO2: On the Understanding of Defects, Defect Density, and Selectivity, *Angew. Chem. Int. Ed.* **2015,** *54* (46), 13701-13705, 10.1002/anie.201506062.

[11] Y. Zheng, Y. Jiao, Y. Zhu, L.H. Li, Y. Han, Y. Chen, A. Du, M. Jaroniec, S.Z. Qiao, Hydrogen evolution by a metal-free electrocatalyst, *Nat. Commun.* **2014,** *5*, 3783, 10.1038/ncomms4783.

[12] Y. Zheng, Y. Jiao, L.H. Li, T. Xing, Y. Chen, M. Jaroniec, S.Z. Qiao, Toward Design of Synergistically Active Carbon-Based Catalysts for Electrocatalytic Hydrogen Evolution, *ACS Nano* **2014,** *8* (5), 5290-5296, 10.1021/nn501434a.

[13] B.R. Sathe, X. Zou, T. Asefa, Metal-free B-doped graphene with efficient electrocatalytic activity for hydrogen evolution reaction, *Catal. Sci. Technol.* **2014,** *4* (7), 2023-2030, 10.1039/c4cy00075g.

[14] Y. Ito, W. Cong, T. Fujita, Z. Tang, M. Chen, High catalytic activity of nitrogen and sulfur co-doped nanoporous graphene in the hydrogen evolution reaction, *Angew. Chem. Int. Ed.* **2015,** *54* (7), 2131-2136, 10.1002/anie.201410050.

[15] J. Duan, S. Chen, M. Jaroniec, S.Z. Qiao, Porous C3N4 Nanolayers@N-Graphene Films as Catalyst Electrodes for Highly Efficient Hydrogen Evolution, *ACS Nano* **2015,** *9* (1), 931-940, 10.1021/nn506701x.

[16] Y. Zhao, F. Zhao, X. Wang, C. Xu, Z. Zhang, G. Shi, L. Qu, Graphitic carbon nitride nanoribbons: graphene-assisted formation and synergic function for highly efficient hydrogen evolution, *Angew. Chem. Int. Ed.* **2014,** *53* (50), 13934-13939, 10.1002/anie.201409080.

[17] H. Wang, T. Maiyalagan, X. Wang, Review on Recent Progress in Nitrogen-Doped Graphene: Synthesis, Characterization, and Its Potential Applications, *ACS Catal.* **2012,** *2* (5), 781-794, 10.1021/cs200652y.

[18] D. Guo, R. Shibuya, C. Akiba, S. Saji, T. Kondo, J. Nakamura, Active sites of nitrogen-doped carbon materials for oxygen reduction reaction clarified using model catalysts, *Science* **2016,** *351* (6271), 361-365,

[19] S. Zhang, S. Tsuzuki, K. Ueno, K. Dokko, M. Watanabe, Upper Limit of Nitrogen Content in Carbon Materials, *Angewandte Chemie International Edition* **2015,** *54* (4), 1302-1306, 10.1002/anie.201410234.

[20] K.-I. Ota, S. Nishigori, N. Kamiya, Dissolution of platinum anodes in sulfuric acid solution, *J. Electroanal. Chem.* **1988,** *257* (1–2), 205-215, http://dx.doi.org/10.1016/0022-0728(88)87042-6.

[21] Y. Sugawara, T. Okayasu, A.P. Yadav, A. Nishikata, T. Tsuru, Dissolution Mechanism of Platinum in Sulfuric Acid Solution, *J. Electrochem. Soc.* **2012,** *159* (11), F779-F786,

[22] L. Xing, M.A. Hossain, M. Tian, D. Beauchemin, K. Adjemian, G. Jerkiewicz, Platinum Electro-dissolution in Acidic Media upon Potential Cycling, *Electrocatalysis* **2014,** *5* (1), 96-112, 10.1007/s12678-013-0167-9.

[23] Y. Furuya, T. Mashio, A. Ohma, M. Tian, F. Kaveh, D. Beauchemin, G. Jerkiewicz, Influence of Electrolyte Composition and pH on Platinum Electrochemical and/or Chemical Dissolution in Aqueous Acidic Media, *ACS Catal.* **2015,** *5* (4), 2605-2614, 10.1021/cs5016035.

[24] Y. Jiao, Y. Zheng, M. Jaroniec, S.Z. Qiao, Design of electrocatalysts for oxygen- and hydrogen-involving energy conversion reactions, *Chem. Soc. Rev.* **2015,** *44* (8), 2060-2086, 10.1039/c4cs00470a.

[25] A.B. Laursen, K.R. Patraju, M.J. Whitaker, M. Retuerto, T. Sarkar, N. Yao, K.V. Ramanujachary, M. Greenblatt, G.C. Dismukes, Nanocrystalline Ni5P4: a hydrogen evolution electrocatalyst of exceptional efficiency in both alkaline and acidic media, *Energy Environ. Sci.* **2015,** *8* (3), 1027-1034, 10.1039/C4EE02940B.

[26] P.C.K. Vesborg, B. Seger, I. Chorkendorff, Recent Development in Hydrogen Evolution Reaction Catalysts and Their Practical Implementation, *J. Phys. Chem. Lett.* **2015,** *6* (6), 951-957, 10.1021/acs.jpclett.5b00306.

[27] H.-W. Liang, S. Bruller, R. Dong, J. Zhang, X. Feng, K. Mullen, Molecular metal-Nx centres in porous carbon for electrocatalytic hydrogen evolution, *Nat. Commun.* **2015,** *6*, 10.1038/ncomms8992.

[28] G. Dong, M. Fang, H. Wang, S. Yip, H.-Y. Cheung, F. Wang, C.-Y. Wong, S.T. Chu, J.C. Ho, Insight into the electrochemical activation of carbon-based cathodes for hydrogen evolution reaction, *J. Mater. Chem. A* **2015,** *3* (24), 13080-13086, 10.1039/C5TA02551F.

[29] C.-L. Sun, L.-C. Chen, M.-C. Su, L.-S. Hong, O. Chyan, C.-Y. Hsu, K.-H. Chen, T.-F. Chang, L. Chang, Ultrafine Platinum Nanoparticles Uniformly Dispersed on Arrayed CNx Nanotubes with High Electrochemical Activity, *Chem. Mater.* **2005,** *17* (14), 3749-3753, 10.1021/cm050107r.

[30] D.C. Higgins, D. Meza, Z. Chen, Nitrogen-Doped Carbon Nanotubes as Platinum Catalyst Supports for Oxygen Reduction Reaction in Proton Exchange Membrane Fuel Cells, *J. Phys. Chem. C* **2010,** *114* (50), 21982-21988, 10.1021/jp106814j.

[31] X. Tuaev, J.P. Paraknowitsch, R. Illgen, A. Thomas, P. Strasser, Nitrogen-doped coatings on carbon nanotubes and their stabilizing effect on Pt nanoparticles, *Phys. Chem. Chem. Phys.* **2012,** *14* (18), 6444-6447, 10.1039/c2cp40760d.

[32] L. Jia, D.A. Bulushev, O.Y. Podyacheva, A.I. Boronin, L.S. Kibis, E.Y. Gerasimov, S. Beloshapkin, I.A. Seryak, Z.R. Ismagilov, J.R.H. Ross, Pt nanoclusters stabilized by N-doped carbon nanofibers for hydrogen production from formic acid, *J. Catal.* **2013,** *307*, 94-102, 10.1016/j.jcat.2013.07.008.

[33] X. Huang, Y. Zhao, Z. Ao, G. Wang, Micelle-template synthesis of nitrogen-doped mesoporous graphene as an efficient metal-free electrocatalyst for hydrogen production, *Sci. Rep.* **2014,** *4*, 7557, 10.1038/srep07557.

[34] Y. Liu, H. Yu, X. Quan, S. Chen, H. Zhao, Y. Zhang, Efficient and durable hydrogen evolution electrocatalyst based on nonmetallic nitrogen doped hexagonal carbon, *Sci. Rep.* **2014,** *4*, 6843, 10.1038/srep06843.

[35] B. Zhang, Z. Wen, S. Ci, J. Chen, Z. He, Nitrogen-doped activated carbon as a metal free catalyst for hydrogen production in microbial electrolysis cells, *RSC Adv.* **2014,** *4* (90), 49161-49164, 10.1039/c4ra08555h.

[36] X. Liu, W. Zhou, L. Yang, L. Li, Z. Zhang, Y. Ke, S. Chen, Nitrogen and sulfur co-doped porous carbon derived from human hair as highly efficient metal-free electrocatalysts for hydrogen evolution reactions, *J. Mater. Chem. A* **2015,** *3* (16), 8840-8846, 10.1039/C5TA01209K.

[37] M. Tavakkoli, T. Kallio, O. Reynaud, A.G. Nasibulin, C. Johans, J. Sainio, H. Jiang, E.I. Kauppinen, K. Laasonen, Single-shell carbon-encapsulated iron nanoparticles: synthesis and high electrocatalytic activity for hydrogen evolution reaction, *Angew. Chem. Int. Ed.* **2015,** *54* (15), 4535-4538, 10.1002/anie.201411450.

[38] K. Xie, H. Wu, Y. Meng, K. Lu, Z. Wei, Z. Zhang, Poly(3,4-dinitrothiophene)/SWCNT composite as a low overpotential hydrogen evolution metal-free catalyst, *J. Mater. Chem. A* **2015,** *3* (1), 78-82, 10.1039/c4ta04671d.

[39] W. Zhou, Y. Zhou, L. Yang, J. Huang, Y. Ke, K. Zhou, L. Li, S. Chen, N-doped carbon-coated cobalt nanorod arrays supported on a titanium mesh as highly active electrocatalysts for the hydrogen evolution reaction, *J. Mater. Chem. A* **2015,** *3* (5), 1915-1919, 10.1039/C4TA06284A.

[40] W. Zhou, J. Zhou, Y. Zhou, J. Lu, K. Zhou, L. Yang, Z. Tang, L. Li, S. Chen, N-Doped Carbon-Wrapped Cobalt Nanoparticles on N-Doped Graphene Nanosheets for High-Efficiency Hydrogen Production, *Chem. Mater.* **2015,** *27* (6), 2026-2032, 10.1021/acs.chemmater.5b00331.

[41] S.S. Shinde, A. Sami, J.-H. Lee, Electrocatalytic hydrogen evolution using graphitic carbon nitride coupled with nanoporous graphene co-doped by S and Se, *J. Mater. Chem. A* **2015,** *3* (24), 12810-12819, 10.1039/C5TA02656C.

[42] H. Jiang, Y. Zhu, Y. Su, Y. Yao, Y. Liu, X. Yang, C. Li, Highly dual-doped multilayer nanoporous graphene: efficient metal-free electrocatalysts for the hydrogen evolution reaction, *J. Mater. Chem. A* **2015,** *3* (24), 12642-12645, 10.1039/C5TA02792F.

[43] H. Zhang, Z. Ma, J. Duan, H. Liu, G. Liu, T. Wang, K. Chang, M. Li, L. Shi, X. Meng, K. Wu, J. Ye, Active Sites Implanted Carbon Cages in Core–Shell Architecture: Highly Active and Durable Electrocatalyst for Hydrogen Evolution Reaction, *ACS Nano* **2016,** *10* (1), 684-694, 10.1021/acsnano.5b05728.

[44] T. Kowalewski, N.V. Tsarevsky, K. Matyjaszewski, Nanostructured Carbon Arrays from Block Copolymers of Polyacrylonitrile, *J. Am. Chem. Soc.* **2002,** *124*, 10632-10633,

[45] M. Zhong, S. Jiang, Y. Tang, E. Gottlieb, E.K. Kim, A. Star, K. Matyjaszewski, T. Kowalewski, Block copolymer-templated nitrogen-enriched nanocarbons with morphology-dependent electrocatalytic activity for oxygen reduction, *Chemical Science* **2014,** *5* (8), 3315-3315,

[46] B.E. Conway, B.V. Tilak, Interfacial processes involving electrocatalytic evolution and oxidation of H2, and the role of chemisorbed H, *Electrochim. Acta* **2002,** *47*, 3571 - 3594,

[47] W. Wu, L. Zhan, W. Fan, J. Song, X. Li, Z. Li, R. Wang, J. Zhang, J. Zheng, M. Wu, H. Zeng, Cu-N Dopants Boost Electron Transfer and Photooxidation Reactions of Carbon Dots, *Angewandte Chemie International Edition* **2015,** *54* (22), 6540-6544, 10.1002/anie.201501912.

[48] H. Zhang, F. Jiang, R. Zhou, Y. Du, P. Yang, C. Wang, J. Xu, Effect of deposition potential on the structure and electrocatalytic behavior of Pt micro/nanoparticles, *Int. J. Hydrogen Energy* **2011,** *36* (23), 15052-15059, 10.1016/j.ijhydene.2011.08.072.

[49] P. Bajaj, A.K. Roopanwal, Thermal Stabilization of Acrylic Precursors for the Production of Carbon Fibers: An Overview, *J. Macromol. Sci. Polym. Rev.* **1997,** *37* (1), 97-147, 10.1080/15321799708014734.

[50] J.S. Hammond, N. Winograd, XPS spectroscopic study of potentiostatic and galvanostatic oxidation of Pt electrodes in H2SO4 and HClO4, *J. Electroanal. Chem.* **1977,** *78* (1), 55-69, http://dx.doi.org/10.1016/S0022-0728(77)80422-1.

[51] K. Ebitani, H. Konno, T. Tanaka, H. Hattori, In-situ XPS study of zirconium oxide promoted by platinum and sulfate ion, *J. Catal.* **1992,** *135* (1), 60-67, http://dx.doi.org/10.1016/0021-9517(92)90268-M.

[52] C. Tang, T. Kowalewski, K. Matyjaszewski, Preparation of Polyacrylonitrile-block-poly(n-butyl acrylate) Copolymers Using Atom Transfer Radical Polymerization and Nitroxide Mediated Polymerization Processes, *Macromolecules* **2003,** *36* (5), 1465-1473, 10.1021/ma025894h.

[53] M. Zhong, E.K. Kim, J.P. McGann, S.E. Chun, J.F. Whitacre, M. Jaroniec, K. Matyjaszewski, T. Kowalewski, Electrochemically active nitrogen-enriched nanocarbons with well-defined morphology synthesized by pyrolysis of self-assembled block copolymer, *J. Am. Chem. Soc.* **2012,** *134* (36), 14846-57, 10.1021/ja304352n.

[54] K. Matyjaszewski, J. Xia, Atom Transfer Radical Polymerization, *Chem. Rev.* **2001,** *101* (9), 2921-2990, 10.1021/cr940534g.

[55] K. Matyjaszewski, N.V. Tsarevsky, Nanostructured functional materials prepared by atom transfer radical polymerization, *Nature chemistry* **2009,** *1* (4), 276-288, 10.1038/nchem.257.

[56] K. Matyjaszewski, Atom Transfer Radical Polymerization (ATRP): Current Status and Future Perspectives, *Macromolecules* **2012,** *45* (10), 4015-4039, 10.1021/ma3001719.

[57] K. Matyjaszewski, N.V. Tsarevsky, Macromolecular engineering by atom transfer radical polymerization, *J. Am. Chem. Soc.* **2014,** *136* (18), 6513-33, 10.1021/ja408069v.

[58] J. Hutter, M. Iannuzzi, F. Schiffmann, J. VandeVondele, cp2k: atomistic simulations of condensed matter systems, *Wiley Interdisciplinary Reviews: Computational Molecular Science* **2014,** *4* (1), 15-25, 10.1002/wcms.1159.

Chapter 6: Dispersed Carbon Catalysts in Photo-Driven Hydrogen Evolution

This research was started as a collaboration with Dr. Husain Kagalwala to assess the hydrogen evolution activity of nitrogen-enriched carbons in a dispersed system. The first part of this chapter is the paper that resulted from that collaboration. All photocatalysis studies were performed by Husain and the carbon characterization and analysis was done by me.

The second part is an ongoing follow-up that started as a result of observations made in during characterization of ball-milled copolymer-templated nitrogen-enriched carbons (CTNCs) used in the first part. Small, extractable carbon dots were first observed components of ball-milled CTNCs during both scanning electron microscopy (SEM) and dynamic light scattering (DLS). Using a disk filter to separate them from the bulk carbon, they were found to be highly fluorescent and initial photocatalysis studies found them to be highly active. The low yields (~1%) of the carbon dots has generally made them quite difficult to study, and so much of the efforts have gone into trying to modify the synthetic procedure, which thus far has successfully increasing yields to as much as ~15%. Much of that exploration has been done by Mingkang Sun, who will also be the person to continue this work. The improved yields have enabled better characterization, but inconsistencies between samples made by different methods have raised questions about their composition that still need to be addressed. Further improving yields and more rigorous characterization will be an ongoing effort, as well as understanding what is causes the dots to be formed in the first place and determining methods to tune their optical and chemical properties.

6.1 Commodity Carbons as Water Reducing Catalysts in Photo-Driven Hydrogen Evolution

6.1.1 Abstract

Renewable fuel production is currently limited by precious-metal catalysts, and while there are alternative catalysts, price to performance is still insufficient for practical usage. Herein, multiple activated carbons (ACs) were investigated as water reducing catalysts (WRCs) in photo-driven hydrogen evolution. Polyacrylonitrile (PAN) derived carbons were used as model catalysts, to which N content and microporosity were found to be important for activity. ACs initially tested were further characterized, revealing consistent feature dependencies with PAN-based carbons. These results are encouraging for the use of ACs as WRCs and point to possible improvements to catalytic activity by increasing N content and microporosity. surface areas carbon materials.

Table of Contents Figure

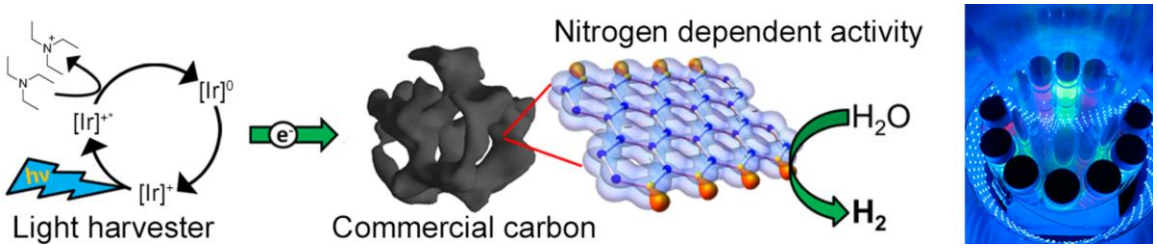

6.1.2 Introduction

Replacing traditional expensive metals and semiconductors with cheaper variants in energy conversion, storage, and fuel production has become a major focal point in applied research. As catalysts, carbon-based materials are especially attractive because of their abundance, cost, and tunability.[1-4] One of the most prominent examples of such an application is the replacement of platinum in catalysis, where the scarcity and cost often outweighs the metal's effectiveness.[5-7]

In energy applications, carbon has been explored to replace platinum in reactions including the oxygen reduction reaction (ORR), oxygen evolution reaction (OER), hydrogen oxidation reaction (HOR) and hydrogen evolution reaction (HER). In the cases of energy harvesting, OER and HER, the ultimate goal is to drive both reactions simultaneously. However, given the thermodynamically demanding nature of "total water splitting", it is prudent to address each half reaction separately. In photocatalysis this is accomplished through the use of sacrificial reductants or oxidants.

The reactions mentioned above can be driven either electrocatalytically, or photocatalytically. Between these two broad categories, electrocatalysis has generally seen more successes in carbons surpassing platinum performance. Presumably, this is because in photocatalysis, the carbon must either be photoactive, or able to interact with a light harvester. Graphitic carbon nitride (g-C_3N_4), the most notable example, has been used for this purpose due to its light absorbing band gap (approximately 2.7 eV) and nitrogen functionalities for interacting with protons.[8-12] However, g-C_3N_4 suffers from low quantum efficiency and slow hydrogen production, despite having suitable properties for both aspects of photocatalytic HER.

In photocatalytic HER, comparatively little research has been done using carbon materials solely as the water reducing catalyst (WRC), separating out light harvesting functionality. The requirements of a WRC arguably seem mutually exclusive to the requirements of light harvesting. It would not be surprising to find the limitations on g-C_3N_4's catalytic effectiveness stemmed from such an effect. Therefore, the use of a photosensitizer that is proven to be robust in photocatalytic HER can allow for the exploration and optimization of carbons acting solely as WRCs.

In choosing carbon systems to explore, a growing array of options have become available due to developments in hydrothermal,[13-16] chemical vapor,[17-22] and macromolecular[23, 24] synthetic techniques. By having a large set of synthetic options, carbon materials have seen tailored electronic properties, active sites, and multi-length-scale 3D structures. Subsequently, those carbons have been applied to catalysis. Despite carbon's progress as a catalyst, there are two significant areas that lag behind: low cost performers and fundamental understanding of what governs nanocarbon based catalysts. Expensive to produce, highly specific carbons are necessary to explore metal-free catalysts, but the insights they yield then need to be applied to low cost, bulk carbons.

Herein, we show that commercially available activated carbons can be used as WRCs with an Ir based photosensitizer. The commercial carbons assessed showed a variety of activity, but all showed activity. With this promising result, more in depth analysis of photo-HER with a carbon WRC was needed, but commercial carbons lack a well-defined structure suitable for such a study.

Deconvoluting the activity in heterogeneous systems from their structural and chemical properties can be notoriously difficult. To more effectively analyze individual factors that may influence activity, such as nanostructure and heteroatom content, it would be desirable to carry out a systematic study of catalytic activity using a thoroughly characterized, tunable material. The structural features of such a carbon-based water reducing catalyst (WRC) should include a 3D nanostructure, which would assure accessibility of catalytically active sites to protons and facilitate efficient charge transport. A study of material properties such as conductivity and heteroatom content, reaction

conditions, and resulting activity, with a consistent nanostructure could provide valuable insights across dispersed metal-free catalysts.

In past years, we developed a synthetic strategy that meet these criteria, involving the use of nanostructured block copolymer (BCP) precursors. By using controlled radical polymerizations (CRP) to tune block lengths, we can assure their self-assembly into well-defined nanostructures.[25-27] Copolymer-templated nitrogen-enriched nanocarbons (CTNCs) prepared using this method have been shown to be electrochemically active as supercapacitor electrodes,[25] electrocatalysts for the oxygen reduction reaction (ORR),[28] and catalytic counter-electrodes in dye-sensitized solar cells.[29]

In the present study, we demonstrate the use of both commercial carbons and metal-free CTNCs as WRCs in light-driven HER. The carbons were found to be effective WRCs with the use of a robust and highly efficient Ir-based photosensitizer, $[Ir(ppy)_2(dtbbpy)](PF_6)$ and triethylamine (TEA) as a sacrificial reductant (SR) (Scheme 1). Ir-based systems have been previously known to exhibit thousands of turnovers with a range of WRCs.[30-35] Commercial carbons were found to have activity that correlated with nitrogen content. The CTNCs (in particular $CTNC_{800}$) were found to outperform all of the commercial carbons as well as K_2PtCl_4/colloidal Pt used under similar conditions. More importantly, through the systematic variations in CTNCs, a deeper understanding of catalysis with heteroatom-enriched carbons was obtained.

6.1.3 Results and Discussion

Initial photo-HER experiments were performed using a variety of commercial activated carbons as water reducing catalysts (WRCs). All experiments were carried out with the carbons suspended in a mixture of acetonitrile (CH_3CN), water, sacrificial

reductant triethylamine (TEA) and an efficient Ir photosensitizer, $[Ir(ppy)_2(dtbbpy)](PF_6)$, to ensure photosensitization was not a limiting factor when assessing performance (Figure 1a) (details in SI).[36] All carbons produced H_2 with their activities showing an approximate trend with their corresponding surface area (**Figure 6.1**). Linear regression of the commercial carbons analyzed revealed a surface area normalized yield of 0.056 mmol H_2/m^2. These results were compared against a standard control of *in situ* formed Pt nanoparticles. Approximating the nanoparticles' radii as 2 nm,[36] surface area normalized activity of Pt was 4.0 mmol H_2/m^2. Although the initial results show Pt to be between 10 and 100 times more active per m^2, the observed activity is already well within the many orders of magnitude cost difference between Pt and commercial activated carbons.

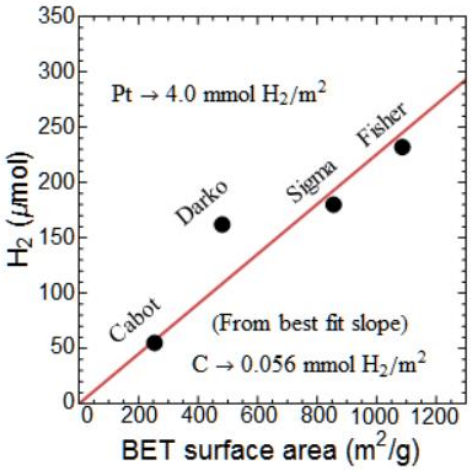

Figure 6.1 H_2 yields using commercial activated carbons as WRCs against their measured BET surface areas. All carbon experiments used 4 mg WRC and 0.1 mM PS, with CH_3CN/H_2O/TEA as specified in the experimental section. *In situ* formed Pt nanoparticles were used as a control (100 μM K_2PtCl_4), with surface area estimated from an average Pt nanoparticle radius of 2 nm.

To further investigate factors affecting the catalytic activity in such carbons, a set of polyacrylonitrile (PAN) derived carbons were used as model catalysts. Commercial carbons typically have a variety of trace metals, which are not present in the PAN-derived carbons.[37] Additionally, the use of model catalysts allowed for more systematic

variations and control of heteroatom composition, nanostructure, and microstructure. The PAN-derived carbons exhibit well-characterized variations in their graphitic domain sizes, meso/microporous structures, and nitrogen content.[26] The first set of systematic photo-HER studies used series of carbons derived from a block copolymer (BCP), polyacrylonitrile-*b*-poly(butyl acrylate) (PAN-*b*-PBA), pyrolyzed at different temperatures (**Figure 6.2a**). The copolymer templated nitrogen-enriched carbons (CTNCs) produced had consistent nanostructures, owing to the retained block copolymer induced morphology (**Figure 6.2b**).

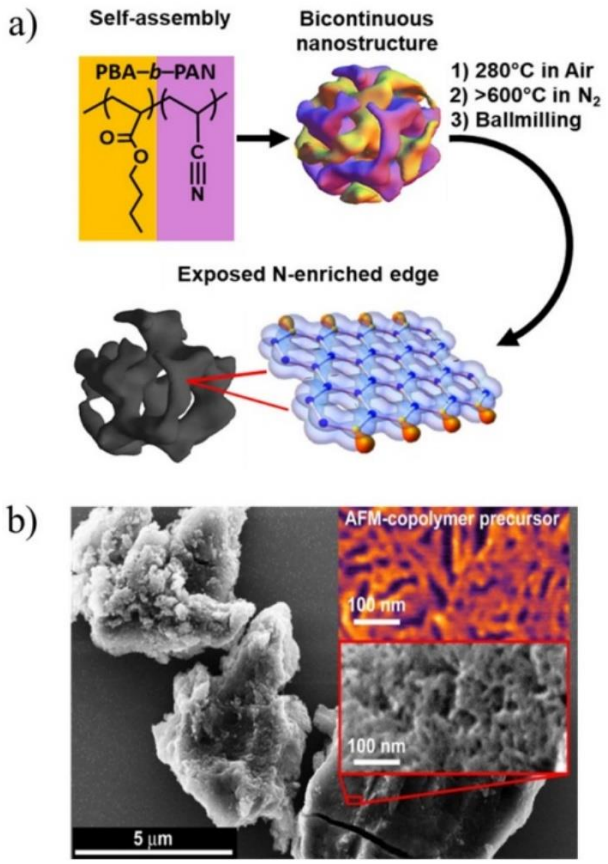

Figure 6.2 a) Synthesis of copolymer templated nitrogen-enriched carbons (CTNCs) from PAN-*b*-PBA. Cyclization of PAN through thermal stabilization allows for the nanostructure to be retained during pyrolysis, resulting in a carbon that has mesopores left by the sacrificial PBA block. b) An SEM image of ball milled CTNC. The inset shows an AFM image of the copolymer used to produce the CTNC and an SEM of the resulting carbon, showing retention of nanostructure through the pyrolysis process.

CTNCs were pyrolyzed at temperatures ranging from 600 to 1000 °C and tested for WRC activity (**Figure 6.3a**). Consistent with prior work applying CTNCs as an electrocatalyst, 800 °C was the optimal pyrolysis temperature for catalytic performance.[38] In accordance with the accepted carbonization mechanism of PAN,[26, 39] pyrolysis at higher temperatures yielded carbons with lower nitrogen content and larger crystallite domains (**Figure 6.3b**). Specifically, the established view of structural changes occurring upon increasing the pyrolysis temperature of PAN, and in line with our previous results, graphitic domains progressively fuse through denitrogenation into more extended nanographitic sheets. The superior performance of CTNCs pyrolyzed at 800 °C likely reflects the optimum balance between the increasing size of the pi-electron pool (nanographitic domain size) and the decreasing content of N-catalytic sites.

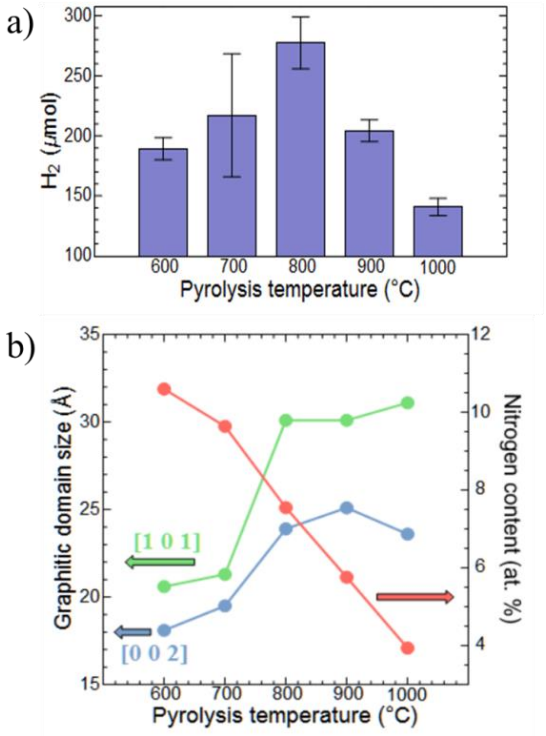

Figure 6.3 a) The effect of pyrolysis temperature on WRC performance (error bars correspond to ±1 standard deviation). b) Evolution of CTNC structure with pyrolysis temperature. Nanographitic domain size, determined by Scherrer analysis of XRD peak widths (blue and green) and nitrogen content from XPS (red).

The accessibility of catalytic sites was investigated by using carbons produced by the same thermal treatment, but derived from different PAN precursors, thereby producing carbons with consistent microstructures, but differing pore structures. Using the optimal pyrolysis conditions determined above, PAN-*b*-PBA, high molecular weight (MW) PAN, and low MW PAN (RAFT PAN) were all assessed as WRCs. As shown in prior work, CTNCs have both mesopores and micropores.[26] CTNC mesoporosity is the result of copolymer templating, in which PBA acts as a sacrificial porogen, volatilizing and leaving behind mesopores during the pyrolysis process. Micropores, on the other hand, form to varying degrees when simply pyrolyzing PAN. Therefore, since all of the resulting carbons were PAN derived, they were similar on an atomic-scale, but had different pore structures (**Table 6.1**).

Table 6.1 H_2 yields for different PAN-based carbons with respective nitrogen content and surface area data.

Carbon precursor	Nitrogen (at.%)[a]	Total SA (m^2/g)[b]	Micro-SA (m^2/g)[c]	H_2 yield (μmol)
PAN-*b*-PBA	7.6	460	220	278
RAFT PAN	10.7	150	120	253
Sigma PAN	6.3	80	25	91

[a] Measured by XPS. [b] From isotherms fit to the BJH model. [c] Estimated from the *t*-plot method.

Surprisingly, CTNCs and carbon from low MW PAN performed similarly, while carbon from high MW PAN produced dramatically smaller quantities of H_2 (**Table 6.1**). Despite lower overall surface area (SA), carbon from low MW PAN was able to produce almost the same quantity of H_2. In contrast to low MW PAN, pyrolyzed high MW PAN produced little H_2. This indicates that microporous SA is important for carbon performance as a WRC, while mesopores do not appreciably improve performance.

The importance of micropores was further corroborated by solvent studies, correlating H_2 production with solvent properties (using an otherwise optimized

procedure). While there was no clear trend between any single solvent property and catalytic performance, principal component analysis showed both surface tension and viscosity together to correlate with H_2 yields (**Figure 6.4a**). The importance of using a solvent with both low surface tension and viscosity is likely related to improved wettability of micropores. Furthermore, the importance of having specifically micropores, shown to be important in optimizing performance, and a solvent with both low surface tension and viscosity indicates the active sites are likely primarily located within micropores.

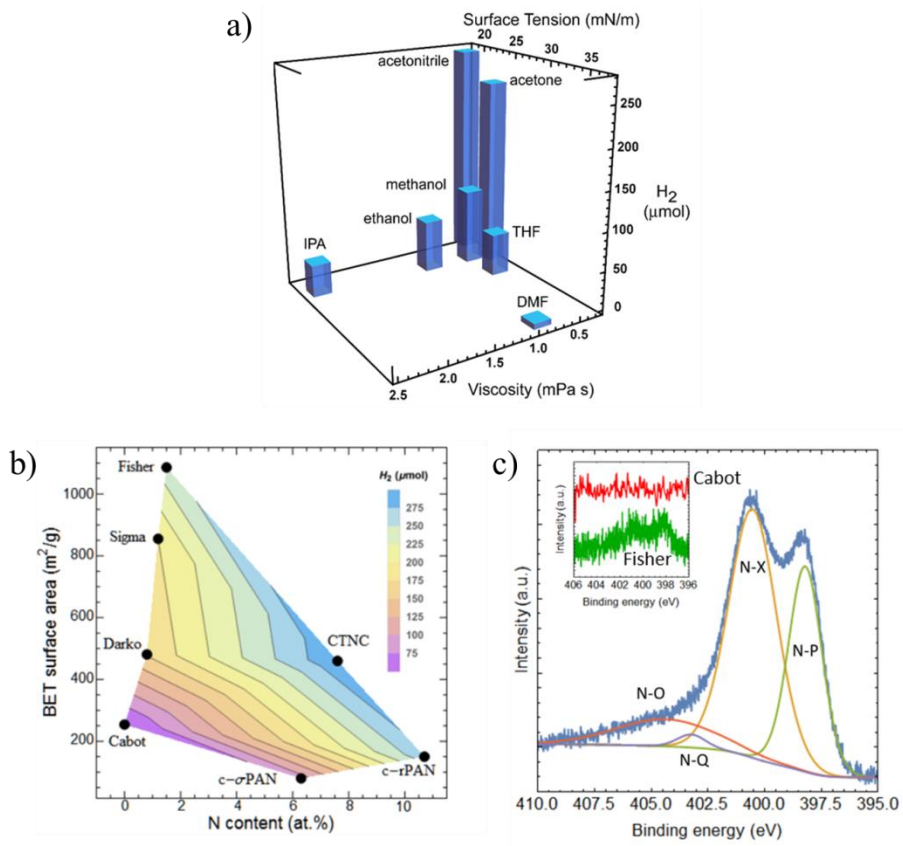

Figure 6.4 a) H_2 production in a variety of solvents, shown as a function of the two strongest correlated solvent properties (viscosity and surface tension), determined by principal component analysis. b) A contour plot of H_2 yields for commercial carbons, carbonized PAN samples, and CTNCs (800 °C) against their BET surface areas and nitrogen content from XPS. Points shown represent individual data points, and contours are the result of linear interpolations between those points. c) High resolution XPS of CTNC-800 with deconvolution peaks for pyridinic (N-P), pyrrolic (N-X), quaternary (N-Q), and pyridinic oxide (N-O). Inset: High resolution XPS of the highest and lowest %N commercial carbons, Cabot and Fisher.

The important material properties to catalytic activity, revealed by assessing PAN-derived carbons, were further validated by evaluating the consistency of the findings with the commercial carbons originally investigated as WRCs. The H_2 yields from commercial carbons as well as PAN-derived carbons pyrolyzed at 800 °C were plotted against their nitrogen content, measured by XPS, and BET surface areas (**Figure 6.4b**). Indeed, the commercial carbons, as well as CTNCs and pyrolyzed PAN samples, all show a strong correlation with both surface area and nitrogen content. From these results, it seems that nitrogen could be the determining factor of catalytic activity, as long as surface area is above a threshold to provide sufficient access to catalytic sites.

6.1.4 Conclusion

In conclusion, cost effective carbons can be used as water reducing catalysts in photo-driven hydrogen evolution. Model carbons derived from acrylonitrile containing polymers were studied to identify the source of catalytic activity. Catalytic activity was compared across model carbons with controlled variations in N content, graphitic domain size, and pore structure. These systematic studies revealed a dependence of catalytic activity on both N content and microporosity. This relationship was also observed when considering the commercial carbons. These preliminary results indicate that cost-effective water reducing catalysts could be developed from commercial carbons with increasing N content and enhancing microporosity.

6.1.5 Experimental

Materials. Acrylonitrile (AN), *n*-butyl acrylate (BA), methyl 2-bromopropionate (MBP), *N*,*N*,*N*′,*N*″,*N*″-pentamethyldiethylenetriamine (PMDETA), 2,2′-bipyridyl (bpy), CuBr, CuCl, $CuBr_2$, anisole, dimethylformamide (DMF), dimethylsulfoxide (DMSO),

tetrahydrofuran (THF), N-methyl-2-pyrrolidone (NMP), ethanol, methanol, polyacrylonitrile homopolymer (M_w = 150,000) and K_2PtCl_4 were all obtained from Sigma-Aldrich. CuBr was purified by stirring in glacial acetic acid followed by washing with ether and dried overnight under vacuum. Monomers were passed through a basic alumina column prior to use. HPLC grade solvents were used for photostudies, procured from Fischer, EMD or Pharmaco-Aaper. All other chemicals were used as received.

Synthesis. The block copolymer and homopolymer precursors were synthesized *via* atom transfer radical polymerization as reported previously.[40-44] The BCP precursors used in all studies had degrees of polymerization (DP_n) 140 and 90 for PAN and PBA respectively. The polymer samples were stabilized at 280 °C for 1 h under air flow (150 mL/min) with a heating rate of 1 °C/min, purged with nitrogen gas for one hour during cooling, and then pyrolyzed at 600 ~ 1000 °C for 0.5 h under nitrogen gas flow (150 mL/min) with a heating rate of 10 °C/min. In order to assure their dispersability in the reaction medium, CTNCs were pulverized by ball-milling for 5 minutes using a Spex 8000M mill in a silicon nitride container and ball. Samples were stored in a vacuum oven at 200 °C before use (henceforth called BM-CTNC). Since one of the main aims of the study was to investigate the use of CTNCs as metal-free catalysts, at all synthesis and processing steps, special attention was given to avoiding the introduction of trace amount of metals into the material. The iridium-based photosensitizer, $[Ir(ppy)_2(dtbbpy)](PF_6)$, was synthesized according to procedures described in literature.[45, 46]

Characterization. Brunauer-Emmett-Teller (BET) surface area was measured using Micromeritics Gemini VII 2390 with a nitrogen adsorbate, after degassing under vacuum and heating to 300 °C for at least 3 hours. Small Angle X-ray Scattering (SAXS)

was performed using Rigaku S-MAX3000 instrument equipped with a sealed microfocus source and a wire-array detector. X-ray Photoelectron Spectroscopy (XPS) was performed using an ESCALAB 250Xi X-ray Photoelectron Spectrometer Microprobe. Scanning electron microscopy (SEM) was performed on a FEI Quanta 600 FEG. All analyses were carried out using a gas phase Raman spectrometer (ENWAVE OPTRONICS, GasRaman-NOCH-1, max. output power = 500 mW, excitation wavelength = 532 nm). The spectra were recorded via a ProRaman XC1V79XNT software program. Small quantity of the respective carbon was spread evenly on a pre-cleaned silicon slide. The slide was then placed under a vertically mounted laser. An acquisition time of 15 minutes was used for all measurements. Care was taken to ensure the focal point of the beam was at the center of the carbon spot at all times. Three reaction vials were prepared, each containing 0.3 mM Ir and 4 mg BM-$CTNC_{900}$ in an 8:1:1 MeCN/water/TEA mixture. Either 1ml H_2O, D_2O or 1:1 H_2O/D_2O was added. After 24 hours of reaction time, the vial headspace was analyzed by the Raman spectrometer. The spectrometer was pre-calibrated for H_2 and D_2. For the H_2 calibration, a degassed vial containing 10 ml of MeCN was placed in a cylindrical laser chamber and injected with increasing amounts pure H_2. After each injection, the laser was turned on, (acquisition time = 3 minutes). For D_2, a similar approach was taken. Pure D_2 for this purpose was generated separately via reaction of pure lithium metal with D_2O. After recording the spectra, the peaks of interest, namely H_2 (4110 cm^{-1}) and D_2 (2988 cm^{-1}) were numerically integrated and the corresponding calibration curves were generated. The content of sample vials was analyzed in a similar fashion, following which H_2, D_2 and HD (3612 cm^{-1}) were quantified using the curves. A 10 ml 8:1:1 MeCN/H_2O/TEA solution containing 0.5 mM Ir and 30 mg BM-$CTNC_{700}$ was degassed and illuminated for 24 h

following the regular protocol. After H_2 evolution ceased, the solution was vacuum filtered to isolate the carbon, which was then washed with acetonitrile (3 x 5 ml) and acetone (3 x 5 ml) and then left for drying. The powder was then subject to XPS analysis using an ESCALAB 250Xi X-ray Photoelectron Spectrometer Microprobe. A 40 ml EPA vial containing 0.1 mM Ir and 4 mg BM-$CTNC_{800}$ in a 10 ml 8:1:1 MeCN/H_2O/TEA solution was subject to illumination following the regular protocol. After a 24 h period, the solution was vacuum filtered to isolate the carbon. Thereafter, the filtrate was concentrated to dryness via rotary evaporation. The residue was then subject to ESI-MS (50-100 μM, MeOH) using a Thermo-Fisher LCQ instrument equipped with an ESI ion source.

Photoloysis Protocol. A specified quantity of CTNC was weighed into 40 mL pre-cleaned EPA vials equipped with septa caps (VWR International, USA). The samples were then dispersed thoroughly in 7 mL of solvent via sonication for a 2 hour period. 1 mL aliquots of the photosensitizer, $[Ir(ppy)_2(dtbbpy)](PF_6)$ in the same solvent were added to the carbon samples, followed by water and TEA. The final solutions (10 mL) contained the required amounts of photosensitizer and CTNC catalyst in an 8:1:1 solvent / water / TEA ratio. Comparison with Pt was done using K_2PtCl_4 (100 μM) as the catalyst. A stir bar was placed into each vial, the septa caps were screwed back on and the samples were subject to degassing by application of vacuum and subsequent back-filling with Ar. This cycle was repeated 7 times to ensure an inert atmosphere. After bringing the vials to atmospheric pressure, the samples were magnetically stirred for 1 hour after which they were illuminated using a home built photoreactor with side illumination (24 W 460 nm LED strip with 300 diodes, Solid Apollo SA-LS-BL-3528-300-24 V).[47] After the specified illumination period, the vial headspace was analyzed for H_2 by gas chromatography

(GOW-MAC, series 400 G/C, thermal conductivity detector, Ar carrier gas). The instrument was pre-calibrated using 10% H_2-Ar gas mixtures. To obtain H_2 evolution traces, septa caps were replaced by pressure transducers. Following the same photoreaction protocol, the pressure readings were recorded *via* a LabView PC interface and converted to H_2 traces post headspace quantification.

6.2 Carbon Dots Synthesized from Thermally Treated Polyacrylonitrile

6.2.1 Abstract

Carbon dots were extracted from thermally treated polyacrylonitrile-containing polymers. They exhibit strong fluorescence and are narrowly dispersed around 20 – 30 nm without any clear nanostructuring to direct them to only form at this size. Their optical properties in conjunction with preliminary time-dependent density functional theory suggest that the dots contain conjugated components that are much smaller than the dots themselves, perhaps containing multiple electronically isolated conjugated domains. Yields were improved compared to pyrolysis by not oxidatively stabilizing and only thermally treating the polymer at lower (< 400 °C) temperatures under inert atmosphere. This means that the dots are formed without needing oxygen at moderate temperatures, but the precise mechanisms and conditions are still under investigation. The dots also exhibited significant activity as hydrogen reducing catalysts in a dispersed photocatalytic system.

6.2.2 Introduction

Carbon materials can exhibit an expansive range of electrical, physical, and chemical properties. While carbons have been used extensively across human history, more sophisticated and controlled synthetic processes continue to be developed, thereby expanding the range of attainable carbon-based structures.[48, 49] Within extended sp^2

conjugated systems, these structures can have electronic properties ranging from that of a semi-metal to a semiconductor, effective control over which would be immensely valuable in areas such as catalysis and electronics.[50, 51] That said, opening the bandgap in carbons is not a trivial task. It requires more carefully controlled final structures and there are many features that affect the bandgap in carbons including domain size, topological features, and the size of contiguous conjugated clusters. Furthermore, the synthetic methods needed to produce carbons with this type of control are often complicated processes, making the procedures less transferable into industrial settings.

Carbon dots make up a new and extremely interesting class of materials, exhibiting strong fluorescence with stability across different chemical conditions and solution processability. They can be synthesized many ways, including from small molecules such as citric acid, laser ablation, and arc-discharge.[52] While many of these carbon dots can exhibit similar UV-Vis spectra and photoluminescence, the origin of these properties are still under debate. With respect to synthesis, there are an ever increasing number of methods emerging, but few reports of producing carbon dots from polymers without the use of a template or encapsulation. We report the synthesis of narrowly dispersed carbon dots from simple and scalable thermal treatment and extraction by filtration of polyacrylonitrile (PAN) containing polymers that exhibit strong fluorescence and photocatalytic properties. These results point to a promising approach for scalable and inexpensive synthesis of functional carbon dots.

The microstructure of PAN and the multistep thermal treatments used to carbonize it have some interesting facets that may make it a particularly well-suited precursor for discrete nanometer scale carbons. PAN is a semicrystalline polymer that takes on a flat,

all-*trans* orientation when atactic to minimize the dipole interactions between nitrile groups. The flat, all-*trans* conformation, depending on the length of the polymer, may fold onto itself like other semicrystalline polymers.[53, 54] This microstructure in conjunction with the nitrile groups are what enable PAN to form ladder structures upon oxidative stabilization. With the prevalence and consistency of these extractable fractions across variations of PAN precursors and temperature treatments, these carbon dots seem to be the result of properties of PAN and the way it reacts at elevated temperatures.

6.2.3 Results and Discussion

When analyzing SEM of copolymer-templated nitrogen-enriched carbons (CTNCs), synthesized by oxidatively stabilizing then pyrolyzing PAN-*b*-PBA, small specks on the silicon wafer were observed. These specks were seen both scanning electron microscopy (SEM) and dynamic light scattering (DLS) (**Figure 6.5**) and were the first inclination that there might be nanometer size components among the bulk carbon. DLS showed a distinct component with hydrodynamic radii of approximately 150 nm, which was consistent with what was observed by SEM. To separate the carbon dots from the bulk

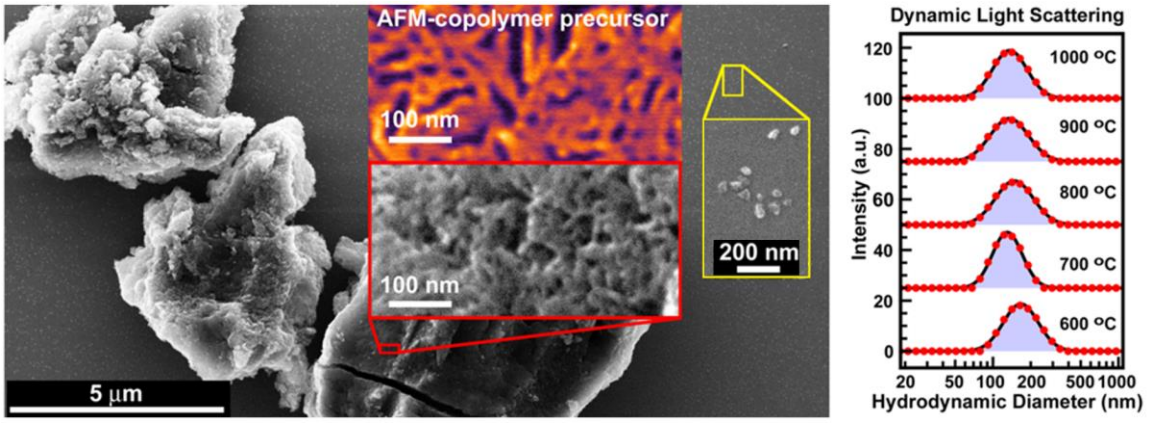

Figure 6.5 SEM of ball-milled CTNCs on a silicon wafer. On the silicon wafer, the carbon dots are the small specks in the background (left). Zoomed in on a region of the surface without bulk CTNCs (inset), amorphous but relatively monodisperse particles about 20 nm in diameter can be seen. DLS of CTNCs passed through a 0.22 µm filter with differing pyrolysis temperatures showing no appreciable effect on the size of the resulting nanoparticles (right).

CTNCs, the powder was suspended in chloroform, sonicated, and passed through a 0.22 µm polytetrafluoroethylene (PTFE) filter. The resulting solutions were transparent varying from completely colorless to slight yellow and exhibited fluorescence with exposure to long wave UV light that is characteristic of many carbon dot systems (**Figure 6.6**).[52] It was determined that the yield was quite low, with the nanoparticles only making up approximately 1 wt. % of the total CTNC mass.

Interestingly, in contrast to what might be expected given previous work on CTNCs and temperature dependence, no appreciable differences were observed by either DLS (**Figure 6.5, right**) or UV-Vis spectroscopy (**Figure 6.6, right**) for carbon dots from different pyrolysis temperature. This indicates that the process which leads to the observed size and optical properties of the dots are either not related to pyrolysis temperature or are independent of pyrolysis temperature above some threshold. Also, the UV-Vis spectra are very similar to spectra reported for other carbon dot systems, further verifying that these are indeed carbon dots.[52]

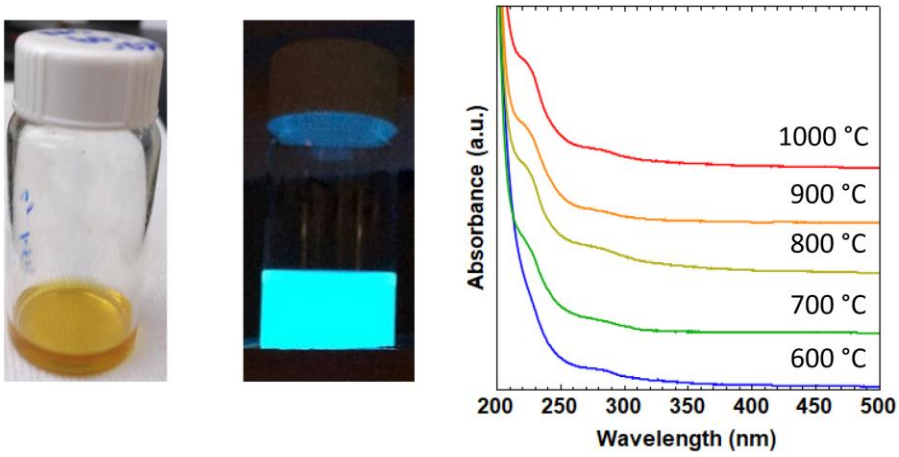

Figure 6.6 Photographs of carbon dots suspended in water (left) and dots fluorescing under longwave UV light (wavelength approximately 360 nm) (middle). UV-Vis spectra of carbon dots extracted from CTNCs pyrolyzed at 600 – 1000 °C (left).

Possible catalytic properties of the dots were of interest, given that they were extracted from carbons that have been demonstrated to be catalytically active. To investigate, two identical dispersions of ball-milled CTNC pyrolyzed at 800 °C (4 mg in 7 ml MeCN) were prepared as per the protocol described in Section 6.1.5, with one of the samples was filtered through a 0.22 μm syringe filter to obtain to clear solution. The filtered suspensions were still highly active, producing an amount of H_2 corresponding to approximately 10% of the output obtained with unfiltered suspensions (**Figure 6.7**). Simple mass comparison indicates that the carbon dot fraction is at least 10 times more active than its micron sized (*i.e.* bulk) counterpart. While the improved activity could simply be a result of a higher surface area to volume ratio, other factors relating to its chemical make-up and properties cannot be ruled out and are continuing to be explored. Regardless, using carbon dots appears as a straight-forward strategy to further increase the already high catalytic activity of ball-milled CTNCs, but requires higher synthetic yields to be effective.

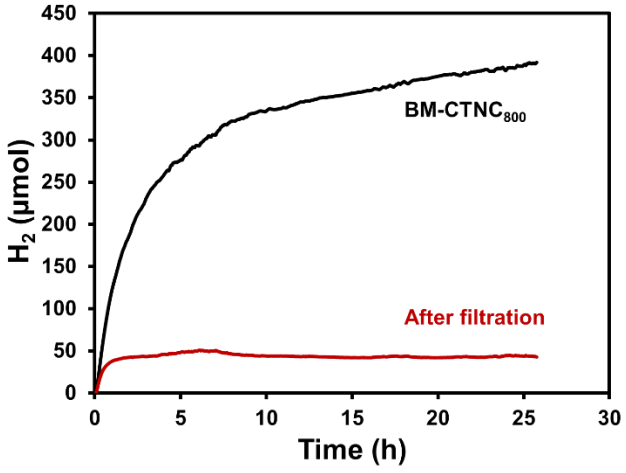

Figure 6.7 H_2 evolution traces comparing the water reducing activities of ball-milled CTNC pyrolyzed at 800 °C and nanoparticles extracted by filtration from CTNCs prepared under the same conditions. The nanoparticles (~1 wt% of the total CTNC mass) display high activity, showing up to 10 % of the performance of bulk CTNC without mass normalization.

While the results presented thus far were encouraging, yields needed to be improved to more effectively study the properties of the carbon dots. Using homopolymer PAN in place of block copolymer containing PAN seemed to make little difference in the carbon dots' properties. Similarly, dots produced from a range of pyrolysis temperatures showed remarkable consistency, as mentioned earlier. For these reasons, we predicted that the carbon dots were in fact being made in the lower temperature stages of thermal treatment, and the dots that were extracted were actually the ones that "survived" the pyrolytic conditions. Thus, PAN without oxidative stabilization was exposed to temperatures ranging from 250 – 350 °C for one hour under N_2, producing carbon dots with yields much higher than what is extracted from CTNCs (**Table 6.2**). (The lack of a trend in yields is likely a result of incomplete extraction, as more carbon dots can often be separated from the bulk by multiple passes of sonication and filtration.) PAN mixed with $CuBr_2$ (~24 wt.%) was also assessed under the same conditions, producing similar yields. The goal with copper doping was to enhance photoredox behavior in the resulting dots, which has been shown in other carbon dot systems.[55]

Table 6.2 Variations in carbon dot synthesis and the percent yields

Precursor	Stabilized	Temperature	Yield
PAN	Yes	700 °C	< 3%
PAN	No	250 °C	15%
PAN	No	300 °C	4%
PAN	No	350 °C	6%
PAN-$CuBr_2$	No	250 °C	12%
PAN-$CuBr_2$	No	300 °C	9%
PAN-$CuBr_2$	No	350 °C	7%

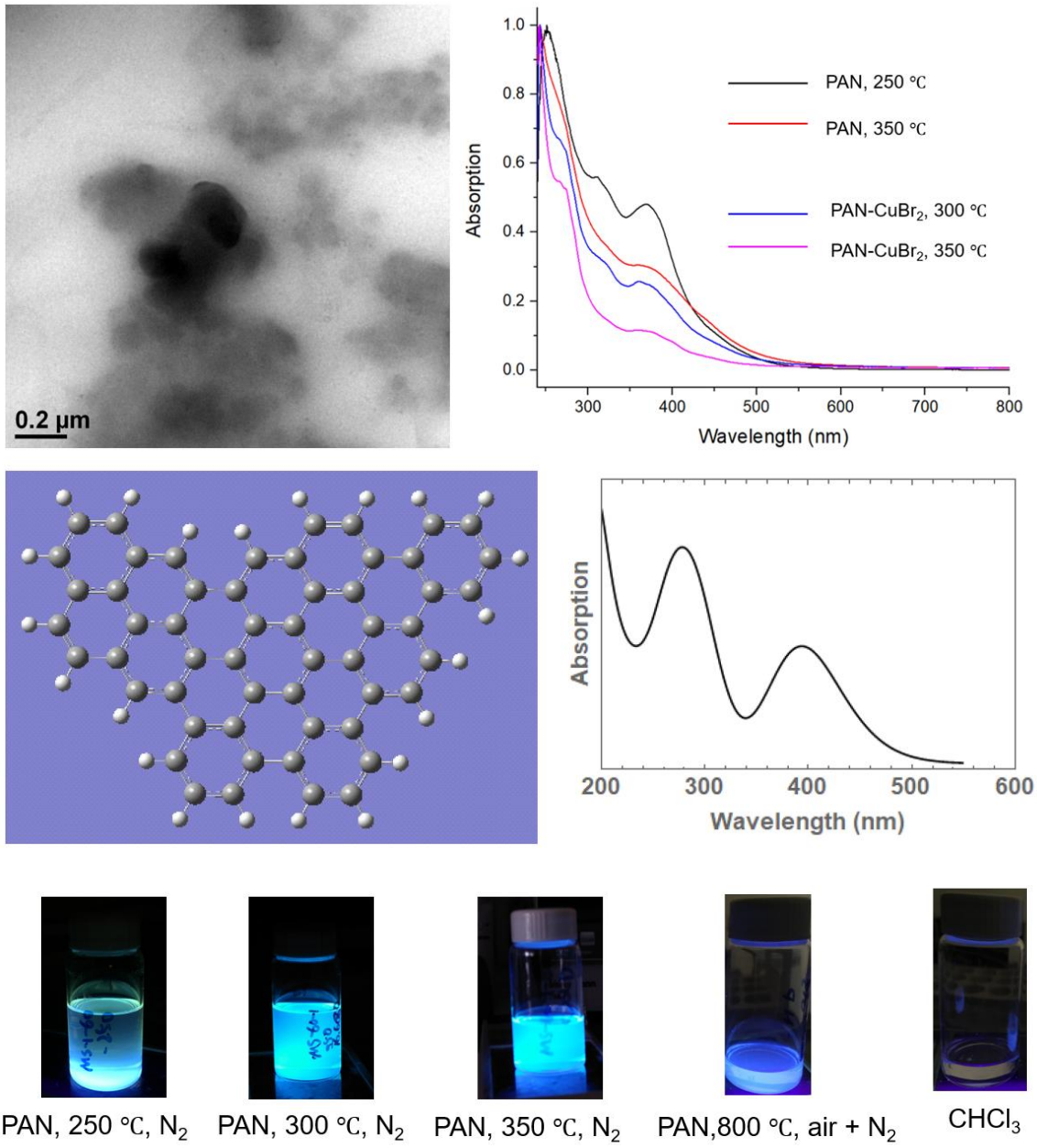

Figure 6.8 Preliminary TEM of a carbon dot from not stabilized PAN thermally treated under N_2 at 350 °C (top left). UV-Vis spectra of a range of carbon dots produced by low-temperature treatment (top right). The much higher concentrations of dots enabled by the lower temperature treatments allowed for better characterization of longer wavelength absorptions. A graphitic carbon nanoflake (middle left) was modeled using time dependent density functional theory with rCAM-B3LYP and STO-3G with 50 states, producing a simulated UV-Vis spectrum that is similar to the experimental results (middle, right). Compared to carbon dots from stabilized and pyrolyzed PAN, the lower temperature treated dots exhibited much stronger fluorescence (bottom)

Despite the very different synthetic processes undergone by the precursors, the resulting carbon dots were qualitatively similar in size, light absorption, and fluorescence,

both between each other compared to the dots from pyrolytic carbons (**Figure 6.8**). The dots from lower temperature treatment did exhibited stronger fluorescence as well as more defined features in UV-Vis spectra, though the lack of defined features in the CTNC extracted dots could simply be attributed to insufficient concentration. With fluorescence spectra, both samples showed a redshift in their λ_{max}, but the lower temperature dots showed less emission dependence on excitation while the higher temperature dots steadily increased fluorescence intensity from 350 to 410 nm (**Figure 6.9**). The samples with $CuBr_2$ did show more defined features in their spectra, which, on further inspection, can also be seen to a limited extent in the dots that were not made with $CuBr_2$. This may indicate that the presence of $CuBr_2$ during thermal treatment may somehow be improving the crystallinity of the resulting dots, but further studies will be needed.

XPS spectra of carbon dots were collected, in most cases showing mostly carbon with oxygen, and some nitrogen. The dots extracted from CTNCs showed almost unmeasurable nitrogen content in the pyridinic range, while dots extracted from low temperature treated PAN with $CuBr_2$ only had low (~1 at. %) quaternary nitrogen signal, and dots from low temperature PAN treatment showed no nitrogen content at all (**Figure 6.10**). This result will require continued efforts to determine the source of the unexpected variations in both nitrogen content and nitrogen chemical state for carbon dots from different synthetic procedures.

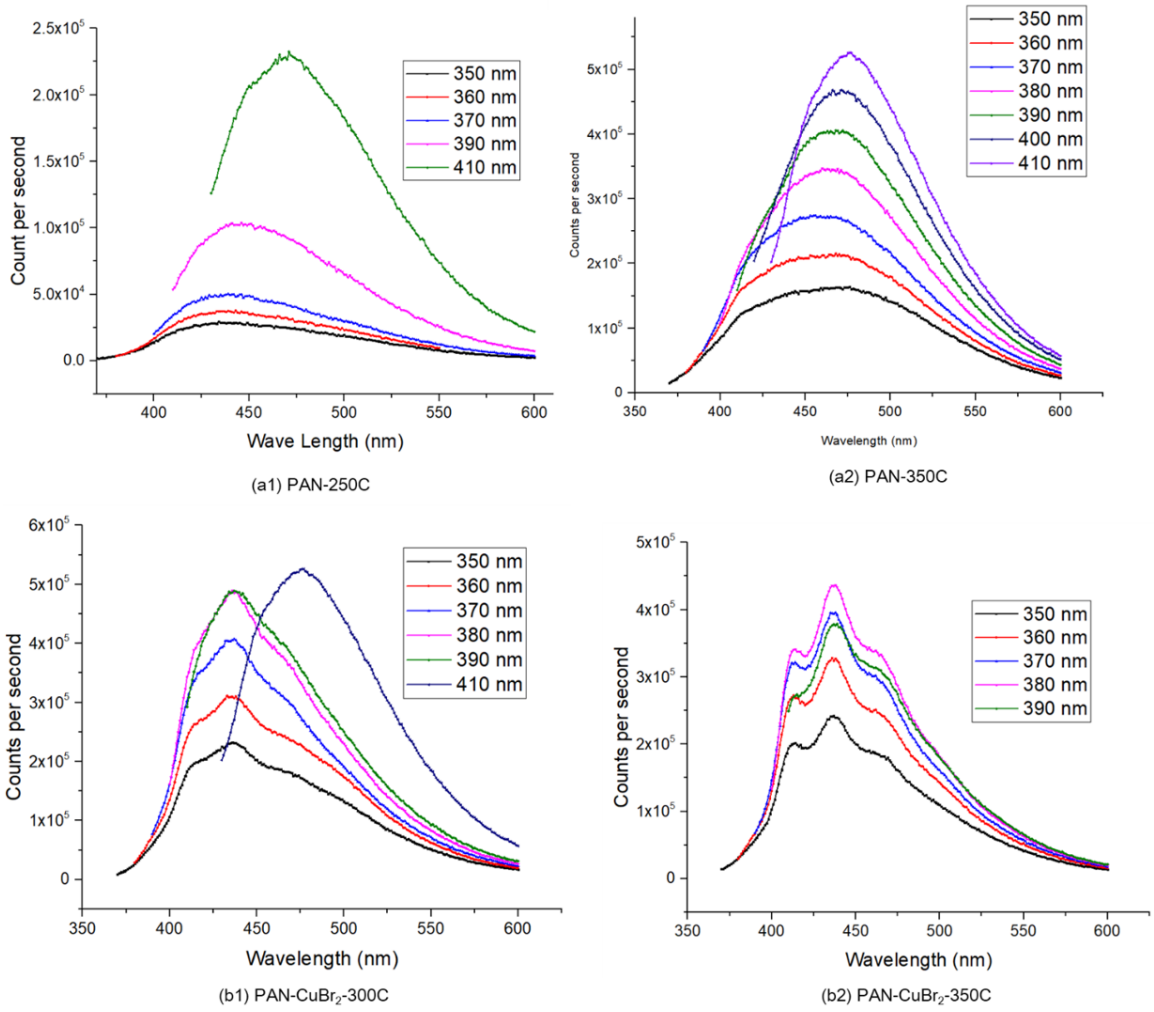

Figure 6.9 Fluorescence spectra of carbon dots extracted from PAN treated at 250 °C (a1) and 350 °C (a2), and PAN with $CuBr_2$ treated at 300 °C (b1) and 350 °C (b2). Fluorescence from both samples prepared with $CuBr_2$ show three features that mostly do not move with the excitation wavelength. Carbon dots prepared at higher temperature with $CuBr_2$ show the most definition for the three features, with the corresponding features broadened in the lower temperature sample.

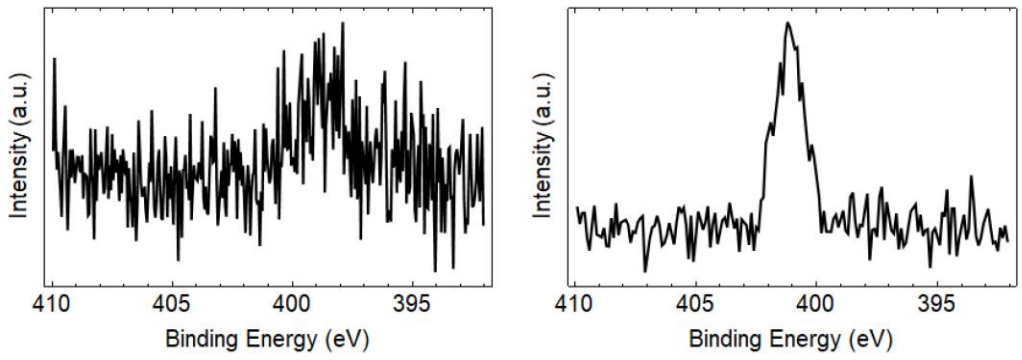

Figure 6.10 High resolution XPS spectra of the N1s region for carbon dots extracted from PAN pyrolyzed at 700 °C (left) and PAN with $CuBr_2$ thermally treated at 250 °C. The nitrogen content of dots from PAN thermally treated without $CuBr_2$ showed now measurable nitrogen.

6.2.4 Conclusion

Carbon dots were prepared from thermal treatments of PAN and filtration. The carbon dots were able to be extracted from both homopolymer PAN and PAN-*b*-PBA block copolymer, with remarkable consistency in size and optical properties across the different thermal treatments in their synthesis. The higher yields from lower temperature treatments suggest that the dots form at moderate temperatures, while the lower yields of carbon dots extracted from CTNCs are because many of them are incorporated into the graphitic structures during pyrolysis.

Preliminary results of hydrogen evolution revealed carbon dots to be extremely active in photocatalytic hydrogen production. Future work will involve further optimization of the photocatalytic hydrogen evolution system, as well as investigation of the source of catalytic activity in the carbon dots. Another key factor will be extending control over the optical properties of the carbon dots to increase their bandgap into the visible range, which is more practical for photo-driven fuel production.

Lastly, investigating the underlying mechanisms that lead to well-controlled carbon dots from PAN will be an ongoing effort. The ease with which these carbon dots make them an extremely promising material. Understanding what causes them to form will be important in both continuing to improve synthetic yields, as well as tuning their electronic properties.

6.2.5 Experimental

Materials. Acrylonitrile (AN), *n*-butyl acrylate (BA), methyl 2-bromopropionate (MBP), *N*,*N*,*N*′,*N*″,*N*″-pentamethyldiethylenetriamine (PMDETA), 2,2′-bipyridyl (bpy), CuBr, CuCl, $CuBr_2$, anisole, dimethylformamide (DMF), dimethylsulfoxide (DMSO),

tetrahydrofuran (THF), N-methyl-2-pyrrolidone (NMP), ethanol, methanol, polyacrylonitrile homopolymer (M_w = 150,000) and K_2PtCl_4 were all obtained from Sigma-Aldrich. CuBr was purified by stirring in glacial acetic acid followed by washing with ether and dried overnight under vacuum. Monomers were passed through a basic alumina column prior to use. HPLC grade solvents were used for photostudies, procured from Fischer, EMD or Pharmaco-Aaper. All other chemicals were used as received.

Synthesis. The block copolymer and homopolymer precursors were synthesized *via* atom transfer radical polymerization as reported previously.[40-44] The BCP precursors used in all studies had degrees of polymerization (DP_n) 140 and 90 for PAN and PBA respectively. The polymer samples were stabilized at 280 °C for 1 h under air flow (150 mL/min) with a heating rate of 1 °C/min, purged with nitrogen gas for one hour during cooling, and then pyrolyzed at 600 ~ 1000 °C for 0.5 h under nitrogen gas flow (150 mL/min) with a heating rate of 10 °C/min. In order to assure their dispersability in the reaction medium, CTNCs were pulverized by ball-milling for 5 minutes using a Spex 8000M mill in a silicon nitride container and ball. Samples were stored in a vacuum oven at 200 °C before use. Nanoparticles were initially synthesized by following the same procedure for synthesizing CTNCs, but with an additional step of suspending the powder in chloroform and passing the suspension through a 0.22 μm filter. The iridium-based photosensitizer, $[Ir(ppy)_2(dtbbpy)](PF_6)$, was synthesized according to procedures described in literature.[45, 46]

Photoloysis Protocol. A specified quantity of CTNC was weighed into 40 mL pre-cleaned EPA vials equipped with septa caps (VWR International, USA). The samples were then dispersed thoroughly in 7 mL of solvent via sonication for a 2 hour period. 1 mL

aliquots of the photosensitizer, $[Ir(ppy)_2(dtbbpy)](PF_6)$ in the same solvent were added to the carbon samples, followed by water and TEA. The final solutions (10 mL) contained the required amounts of photosensitizer and CTNC catalyst in an 8:1:1 solvent / water / TEA ratio. A stir bar was placed into each vial, the septa caps were screwed back on and the samples were subject to degassing by application of vacuum and subsequent back-filling with Ar. This cycle was repeated 7 times to ensure an inert atmosphere. After bringing the vials to atmospheric pressure, the samples were magnetically stirred for 1 hour after which they were illuminated using a home built photoreactor with side illumination (24 W 460 nm LED strip with 300 diodes, Solid Apollo SA-LS-BL-3528-300-24 V).[47] To obtain H_2 evolution traces, septa caps were replaced by pressure transducers. Following the same photoreaction protocol, the pressure readings were recorded *via* a LabView PC interface and converted to H_2 traces post headspace quantification.

Characterization.

6.3 References

[1] M. Batmunkh, M.J. Biggs, J.G. Shapter, Carbon Nanotubes for Dye-Sensitized Solar Cells, *Small* **2015**,

[2] K.S. Fernando, S. Sahu, Y. Liu, W.K. Lewis, E.A. Guliants, A. Jafariyan, P. Wang, C.E. Bunker, Y.-P. Sun, Carbon Quantum Dots and Applications in Photocatalytic Energy Conversion, *ACS applied materials & interfaces* **2015,** *7* (16), 8363-8376,

[3] J. Wang, H.L. Xin, D. Wang, Recent progress on mesoporous carbon materials for advanced energy conversion and storage, *Particle & Particle Systems Characterization* **2014,** *31* (5), 515-539,

[4] M.S. Dresselhaus, M. Terrones, Carbon-based nanomaterials from a historical perspective, *Proceedings of the IEEE* **2013,** *101* (7), 1522-1535,

[5] H. Shi, Y. Shen, F. He, Y. Li, A. Liu, S. Liu, Y. Zhang, Recent advances of doped carbon as non-precious catalysts for oxygen reduction reaction, *Journal of Materials Chemistry A* **2014,** *2* (38), 15704-15716,

[6] J.P. Paraknowitsch, A. Thomas, Doping carbons beyond nitrogen: an overview of advanced heteroatom doped carbons with boron, sulphur and phosphorus for energy applications, *Energy & Environmental Science* **2013,** *6* (10), 2839-2855,

[7] G. Wu, P. Zelenay, Nanostructured nonprecious metal catalysts for oxygen reduction reaction, *Accounts of chemical research* **2013,** *46* (8), 1878-1889,

[8] S. Cao, J. Low, J. Yu, M. Jaroniec, Polymeric Photocatalysts Based on Graphitic Carbon Nitride, *Advanced Materials* **2015,** *27* (13), 2150-2176,

[9] Z. Zhao, Y. Sun, F. Dong, Graphitic carbon nitride based nanocomposites: a review, *Nanoscale* **2015,** *7* (1), 15-37,

[10] S. Cao, J. Yu, g-C3N4 Based Photocatalysts for Hydrogen Production, *The Journal of Physical Chemistry Letters* **2014**,

[11] C.A. Caputo, M.A. Gross, V.W. Lau, C. Cavazza, B.V. Lotsch, E. Reisner, Photocatalytic Hydrogen Production using Polymeric Carbon Nitride with a Hydrogenase and a Bioinspired Synthetic Ni Catalyst, *Angewandte Chemie* **2014,** *126* (43), 11722-11726,

[12] J. Liu, J. Huang, D. Dontosova, M. Antonietti, Facile synthesis of carbon nitride micro-/nanoclusters with photocatalytic activity for hydrogen evolution, *RSC Advances* **2013,** *3* (45), 22988-22993,

[13] P. Zhang, Z.-A. Qiao, S. Dai, Recent advances in carbon nanospheres: synthetic routes and applications, *Chemical Communications* **2015,** *51* (45), 9246-9256,

[14] Z.L. Xie, D.S. Su, Ionic Liquid Based Approaches to Carbon Materials Synthesis, *European Journal of Inorganic Chemistry* **2014**,

[15] M. Antonietti, N. Fechler, T.-P. Fellinger, Carbon Aerogels and Monoliths: Control of Porosity and Nanoarchitecture via Sol–Gel routes, *Chemistry of Materials* **2013,** *26* (1), 196-210,

[16] M. Yoshimura, J. Senthilnathan, Hydrothermal Synthesis of Nano-Carbons, Carbon Nanomaterials, 2013, p. 395.

[17] M.X. Wu, Y.N. Lin, H.Y. Guo, W.Y. Li, Y.D. Wang, X. Lin, Design a novel kind of open-ended carbon sphere for a highly effective counter electrode catalyst in dye-sensitized solar cells, *Nano Energy* **2015,** *11*, 540-549, 10.1016/j.nanoen.2014.11.032.

[18] J.A. Elliott, Y. Shibuta, H. Amara, C. Bichara, E.C. Neyts, Atomistic modelling of CVD synthesis of carbon nanotubes and graphene, *Nanoscale* **2013,** *5* (15), 6662-6676,

[19] V. Jourdain, C. Bichara, Current understanding of the growth of carbon nanotubes in catalytic chemical vapour deposition, *Carbon* **2013,** *58*, 2-39,

[20] D. Wei, Y. Liu, Y. Wang, H. Zhang, L. Huang, G. Yu, Synthesis of N-Doped Graphene by Chemical Vapor Deposition and Its Electrical Properties, *Nano Letters* **2009,** *9* (5), 1752-1758,

[21] Y. Xia, R. Mokaya, Synthesis of Ordered Mesoporous Carbon and Nitrogen-Doped Carbon Materials with Graphitic Pore Walls via a Simple Chemical Vapor Deposition Method, *Advanced Materials* **2004,** *16* (17), 1553-1558,

[22] P. Delhaes, Chemical vapor deposition and infiltration processes of carbon materials, *carbon* **2002,** *40* (5), 641-657,

[23] S. De, A.M. Balu, J.C. van der Waal, R. Luque, Biomass-Derived Porous Carbon Materials: Synthesis and Catalytic Applications, *ChemCatChem* **2015**,

[24] X. Feng, Y. Liang, L. Zhi, A. Thomas, D. Wu, I. Lieberwirth, U. Kolb, K. Müllen, Synthesis of microporous carbon nanofibers and nanotubes from conjugated polymer network and evaluation in electrochemical capacitor, *Advanced Functional Materials* **2009,** *19* (13), 2125-2129,

[25] M. Zhong, E.K. Kim, J.P. McGann, S.-E. Chun, J.F. Whitacre, M. Jaroniec, K. Matyjaszewski, T. Kowalewski, Electrochemically active nitrogen-enriched nanocarbons with well-defined morphology synthesized by pyrolysis of self-assembled block copolymer, *Journal of the American Chemical Society* **2012,** *134* (36), 14846-14857,

[26] J.P. McGann, M.J. Zhong, E.K. Kim, S. Natesakhawat, M. Jaroniec, J.F. Whitacre, K. Matyjaszewski, T. Kowalewski, Block Copolymer Templating as a Path to Porous Nanostructured Carbons with Highly Accessible Nitrogens for Enhanced (Electro)chemical Performance, *Macromol. Chem. Phys.* **2012,** *213* (10-11), 1078-1090, 10.1002/macp.201100691.

[27] M.J. Zhong, S. Natesakhawat, J.P. Baltrus, D. Luebke, H. Nulwala, K. Matyjaszewski, T. Kowalewski, Copolymer-templated nitrogen-enriched porous nanocarbons for CO2 capture, *Chem Commun* **2012,** *48* (94), 11516-11518, Doi 10.1039/C2cc36652e.

[28] M.J. Zhong, S.Y. Jiang, Y.F. Tang, E. Gottlieb, E.K. Kim, A. Star, K. Matyjaszewski, T. Kowalewski, Block copolymer-templated nitrogen-enriched nanocarbons with morphology-dependent electrocatalytic activity for oxygen reduction, *Chem. Sci.* **2014,** *5* (8), 3315-3319, 10.1039/c4sc01477d.

[29] M.J. Ju, I.T. Choi, M. Zhong, K. Lim, J. Ko, J. Mohin, M. Lamson, T. Kowalewski, K. Matyjaszewski, H.K. Kim, Copolymer-templated nitrogen-enriched nanocarbons as a low charge-transfer resistance and highly stable alternative to platinum cathodes in dye-sensitized solar cells, *Journal of Materials Chemistry A* **2015**,

[30] H.N. Kagalwala, E. Gottlieb, G. Li, T. Li, R. Jin, S. Bernhard, Photocatalytic Hydrogen Generation System Using a Nickel-Thiolate Hexameric Cluster, *Inorganic chemistry* **2013,** *52* (15), 9094-9101,

[31] D.R. Whang, K. Sakai, S.Y. Park, Highly Efficient Photocatalytic Water Reduction with Robust Iridium (III) Photosensitizers Containing Arylsilyl Substituents, *Angewandte Chemie* **2013,** *125* (44), 11826-11829,

[32] F. Gärtner, S. Denurra, S. Losse, A. Neubauer, A. Boddien, A. Gopinathan, A. Spannenberg, H. Junge, S. Lochbrunner, M. Blug, Synthesis and Characterization of New Iridium Photosensitizers for Catalytic Hydrogen Generation from Water, *Chemistry-A European Journal* **2012,** *18* (11), 3220-3225,

[33] S.y. Takizawa, C. Pérez-Bolívar, P. Anzenbacher, S. Murata, Cationic Iridium Complexes Coordinated with Coumarin Dyes–Sensitizers for Visible-Light-Driven Hydrogen Generation, *European Journal of Inorganic Chemistry* **2012,** *2012* (25), 3975-3979,

[34] F. Gärtner, A. Boddien, E. Barsch, K. Fumino, S. Losse, H. Junge, D. Hollmann, A. Brückner, R. Ludwig, M. Beller, Photocatalytic hydrogen generation from water with iron carbonyl phosphine complexes: improved water reduction catalysts and mechanistic insights, *Chemistry-A European Journal* **2011,** *17* (23), 6425-6436,

[35] E.D. Cline, S.E. Adamson, S. Bernhard, Homogeneous catalytic system for photoinduced hydrogen production utilizing iridium and rhodium complexes, *Inorganic chemistry* **2008,** *47* (22), 10378-10388,

[36] P.N. Curtin, L.L. Tinker, C.M. Burgess, E.D. Cline, S. Bernhard, Structure− Activity Correlations Among Iridium (III) Photosensitizers in a Robust Water-Reducing System, *Inorganic chemistry* **2009,** *48* (22), 10498-10506,

[37] O. Ioannidou, A. Zabaniotou, Agricultural residues as precursors for activated carbon production—a review, *Renewable and Sustainable Energy Reviews* **2007,** *11* (9), 1966-2005,

[38] E. Gottlieb, M. Kopec, M. Banerjee, J. Mohin, D. Yaron, K. Matyjaszewski, T. Kowalewski, In-Situ Platinum Deposition on Nitrogen-Doped Carbon Films as a Source of Catalytic Activity in a Hydrogen Evolution Reaction, *Acs Appl Mater Inter* **2016,** *8* (33), 21531-8, 10.1021/acsami.6b03924.

[39] P. Bajaj, A. Roopanwal, Thermal stabilization of acrylic precursors for the production of carbon fibers: an overview, *Journal of Macromolecular Science, Part C: Polymer Reviews* **1997,** *37* (1), 97-147,

[40] M. Kruk, B. Dufour, E.B. Celer, T. Kowalewski, M. Jaroniec, K. Matyjaszewski, Synthesis of mesoporous carbons using ordered and disordered mesoporous silica templates and polyacrylonitrile as carbon precursor, *J Phys Chem B* **2005,** *109* (19), 9216-9225, Doi 10.1021/Jp045594x.

[41] C.B. Tang, A. Tracz, M. Kruk, R. Zhang, D.M. Smilgies, K. Matyjaszewski, T. Kowalewski, Long-range ordered thin films of block copolymers prepared by zone-casting and their thermal conversion into ordered nanostructured carbon, *J Am Chem Soc* **2005,** *127* (19), 6918-6919, Doi 10.1021/Ja0508929.

[42] C.B. Tang, T. Kowalewski, K. Matyjaszewski, RAFT polymerization of acrylonitrile and preparation of block copolymers using 2-cyanoethyl dithiobenzoate as the transfer agent, *Macromolecules* **2003,** *36* (23), 8587-8589, Doi 10.1021/Ma034942a.

[43] C.B. Tang, T. Kowalewski, K. Matyjaszewski, Preparation of polyacrylonitrile-block-poly(n-butyl acrylate) copolymers using atom transfer radical polymerization and nitroxide mediated polymerization processes, *Macromolecules* **2003,** *36* (5), 1465-1473, Doi 10.1021/Ma025894h.

[44] T. Kowalewski, N.V. Tsarevsky, K. Matyjaszewski, Nanostructured carbon arrays from block copolymers of polyacrylonitrile, *J Am Chem Soc* **2002,** *124* (36), 10632-10633, Doi 10.1021/Ja0178970.

[45] J.D. Slinker, A.A. Gorodetsky, M.S. Lowry, J. Wang, S. Parker, R. Rohl, S. Bernhard, G.G. Malliaras, Efficient yellow electroluminescence from a single layer of a cyclometalated iridium complex, *Journal of the american chemical society* **2004,** *126* (9), 2763-2767,

[46] S. Sprouse, K. King, P. Spellane, R.J. Watts, Photophysical effects of metal-carbon. sigma. bonds in ortho-metalated complexes of iridium (III) and rhodium (III), *Journal of the American Chemical Society* **1984,** *106* (22), 6647-6653,

[47] A.C. Brooks, K. Basore, S. Bernhard, Photon-Driven Reduction of Zn2+ to Zn Metal, *Inorganic chemistry* **2013,** *52* (10), 5794-5800,

[48] V. Georgakilas, J.A. Perman, J. Tucek, R. Zboril, Broad family of carbon nanoallotropes: classification, chemistry, and applications of fullerenes, carbon dots, nanotubes, graphene, nanodiamonds, and combined superstructures, *Chem. Rev.* **2015,** *115* (11), 4744-822, 10.1021/cr500304f.

[49] A. Hirsch, The era of carbon allotropes, *Nat Mater* **2010,** *9* (11), 868-71, 10.1038/nmat2885.

[50] C. Hu, L. Dai, Carbon-Based Metal-Free Catalysts for Electrocatalysis beyond the ORR, *Angew. Chem. Int. Ed. Engl.* **2016,** *55* (39), 11736-58, 10.1002/anie.201509982.

[51] L. Dai, Y. Xue, L. Qu, H.J. Choi, J.B. Baek, Metal-free catalysts for oxygen reduction reaction, *Chem. Rev.* **2015,** *115* (11), 4823-92, 10.1021/cr5003563.

[52] X. Sun, Y. Lei, Fluorescent carbon dots and their sensing applications, *TrAC Trends in Analytical Chemistry* **2017,** *89*, 163-180, 10.1016/j.trac.2017.02.001.

[53] R.J. Hobson, A.H. Windle, Crystalline structure of atactic polyacrylonitrile, *Macromolecules* **1993,** *26* (25), 6903-6907, 10.1021/ma00077a030.

[54] P. Bajaj, A.K. Roopanwal, Thermal stabilization of acrylic precursors for the production of carbon fibers: An overview, *J. Macromol. Sci., Rev. Macromol. Chem. Phys.* **1997,** *C37* (1), 97-147, 10.1080/15321799708014734.

[55] W. Wu, L. Zhan, W. Fan, J. Song, X. Li, Z. Li, R. Wang, J. Zhang, J. Zheng, M. Wu, H. Zeng, Cu-N Dopants Boost Electron Transfer and Photooxidation Reactions of Carbon Dots, *Angewandte Chemie International Edition* **2015,** *54* (22), 6540-6544, 10.1002/anie.201501912.

Chapter 7: Computational and Electronic Structure Studies of Graphitic Carbon Systems

This chapter is presented in two parts. The first part was a collaboration with Professor John Keith and Karthikeyan Saravanan to study the thermodynamics of hydrogen adsorption on various periodic carbon systems with nitrogen incorporated to assess the viability and best arrangement of heteroatom doped carbons for CO_2 reduction. My contribution to the collaboration was the initial studies of basal plane carbon and nitrogen doped carbons, as well as zigzag edged ribbons without spin polarization. Those calculation were later repeated with spin polarization by Karthikeyan, with additional studies of basal carbons with different holes. This work was more of a solid state physics style approach with planewaves and periodic boundaries, and while it provided useful insights, it lacked the kind of information that chemists would look at.

The second part of this chapter presents more preliminary results of calculations for a variety of finite graphitic flakes. The goal was to take more of a "chemist's view", looking at molecular orbitals, edge states, and band structures. Since carbons are still comprised of organic, taking a more molecular view can provide insights and trends that would otherwise be missed. While this is still a work in progress, it has quickly provided useful results, which will be repeated with higher levels of theory to confirm the findings. The results also indicate that spin and the emergence of open shell states from even moderately sized carbons may be important to their catalytic properties; a finding which is consistent with views held by the physics community for "traditional" catalysis but has largely been unexplored in metal free systems.

This work also represents the frontier of my contributions to the Kowalewski group, in which the group's focus has steadily shifted from characterization, to application, to finally understanding the underlying electronic structure that leads to their activity.

7.1 DFT Investigations of Hydrogen Binding Energies to N-Doped Carbons and Implications for Electrocatalytic CO_2 Reduction

7.1.1 Abstract

We have used Kohn-Sham density functional theory with atomistic thermodynamics to identify various forms of N-doped graphene basal planes and nanoribbons that are thermodynamically relevant for CO_2 electroreductions. Using our computational results, we derive phase diagrams for different nanocarbon structures, and we report which structures are suitable for hydrogen transfers to CO_2 with low overpotentials. With the incorporation of N atoms, standard reduction potentials resulting in hydrogenated surfaces become less negative, and this effectively opens pathways for hydrogen atom shuttling to CO_2 with reversibly hydrogenating nanocarbon catalysts. Of all morphologies considered, N-doped zigzag nanocarbon edges are most favorable for energetically efficient CO_2 electroreductions.

Table of Contents Figure

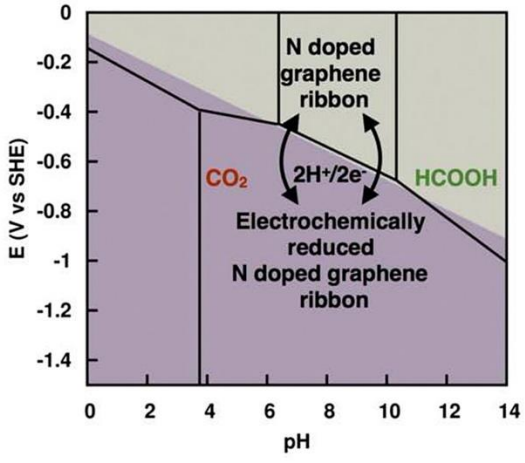

Low overpotential electrocatalysis with N-doped nanocarbons

7.1.2 Introduction

Catalysts are a cornerstone of modern society that enable large scale chemical and fuel production. Active catalysts are non-reactive materials that bind to and release chemically reacting intermediates, lowering activation barriers for desired products. Most catalysts today are precious metals because they resist oxidation (i.e. they are noble) while having *s* and *d* orbital states that can reversibly bind reaction intermediates.[1] However, precious metals are scarce, and alternatives are required for more economical and sustainable catalysis.[2-5]

Recent research has demonstrated that carbon materials are a promising avenue for advanced catalysis. Historically, activated carbons have been used as supports for metal catalysts because of their high surface area and electrical conductivity,[6, 7] but more recently they are being considered as catalysts themselves. Producing so-called 'metal-free' catalysts requires a great deal of synthetic control.[8] Synthetic routes include nanostructuring, heteroatom doping, and defect control.[9-13] Catalytic properties have been reported to depend on a myriad of factors relating to their synthesis, including confinement effects,[14, 15] material defects,[16, 17], and heteroatom dopants.[8] Additionally, it is difficult to draw meaningful conclusions from experimental works alone due to metal impurities.[18, 19]

Even with rapidly growing synthetic sophistication, the field of carbon as a catalyst is still in a relatively nascent stage. Factors that govern their catalytic performance are not well understood, and thus it is challenging to rationally improve their performance. Quantum chemical (QC) modeling can provide useful insights into why carbon catalysts might work and how to improve them, but the majority of QC studies to date have focused

on electronic structures and material properties of nanoscale carbon morphologies such as zigzag edges, armchair edges, and basal planes.[20-23] To a lesser but still sizable degree, QC studies have investigated catalytic reaction mechanisms on nanocarbons (e.g. the hydrogen evolution reaction,[24, 25] and the oxygen reduction reaction[20, 23, 26]). To an even lesser extent CO_2 reduction has been investigated, where experiment and theory have been used to identify specific active sites, product distributions (CO vs. formate), and catalyst stabilities.[9, 27-30]

Previous mechanistic studies on CO_2 reduction have focused on individual reaction steps involving CO_2 binding at different nanocarbon sites.[31, 32] However, it is also possible that a catalyst might undergo (electro-)chemical reactions itself under *in operando* conditions, thus resulting in a modified catalyst. Researchers have proposed that electrochemical $2H^+/2e^-$ reductions of pyridine molecules can form dihydropyridine molecules that facilitate energetically efficient CO_2 reduction processes originally reported by Bocarsly and coworkers.[33-37] A motivating factor for the current work is to determine if knowledge about the electrochemical behavior of pyridine is also transferable to the design of catalytically active N-doped nanocarbon materials.

The first step toward understanding catalytic reaction pathways is to quantify and understand reaction thermodynamics. The Sabatier Principle effectively states that an ideal catalyst will bind reactants just strongly enough to activate them while also minimizing barrier heights to form and release products. To understand reaction energetics of electrocatalytic reaction mechanisms, the computational hydrogen electrode model is a common starting point.[38]

Another related approach is to use QC modeling to generate Pourbaix diagrams to determine which morphologies might evolve during electrochemical reductions and which structures might participate in energetically efficient hydrogenations. Pourbaix diagrams do not provide kinetic information, but the insight into thermodynamics they provide is nevertheless useful. In particular, boundaries between different phases shown by a Pourbaix diagrams are loci of electrochemical conditions (pH and applied potential, E) where the chemical potentials of the phases are the same (example shown in **Figure 7.1**). If the different morphologies represent different reaction intermediates, the boundaries correspond to theoretically optimal conditions for energetically efficient catalysis according to the Sabatier Principle. For instance, the boundary between a hydrogenated surface and an unhydrogenated surface would correspond to the theoretically ideal pH and applied potentials for an energetically efficient hydrogen shuttling catalyst.

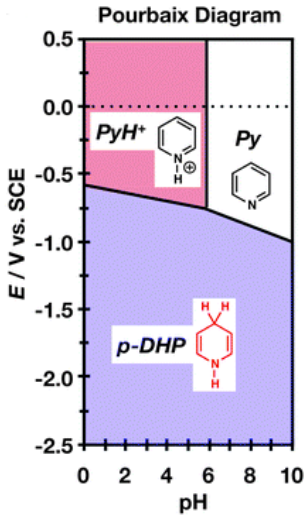

Figure 7.1 An example of a Pourbaix diagram for pyridine. The structures in each region represent the lowest energy species for the given pH and applied potentials.

To understand which carbon morphologies are best suited as CO_2 reduction catalysts, we use QC calculations to generate Pourbaix diagrams that identify

thermodynamically relevant structures at reducing conditions. Our approach follows a similar spirit to previous work regarding aromatic N-heterocycles present in homogeneous solution.[33-37] In these works, we screened a variety of catalyst intermediate states using molecular Pourbaix diagrams that identified electrochemical conditions for energetically efficient catalytic reactions. In the present work, we systematically explore the thermodynamic energies of different nanocarbon structures with different degrees of nitrogen defects and coverages of H atoms.

7.1.3 Results and Discussion

Using the computational hydrogen electrode model, we report the energetics for electrochemical reduction of various nanocarbon structures in terms of the energetics of different hydrogenation steps at different applied potentials. In our graphene basal plane (GBP) models, we consider the reductions of both structures containing different numbers of doping N atoms (**Figure 7.2**) and of common defect sites (**Figure 7.3**). We will first report energetics for different hydrogenations and then use those data to report phase diagrams that show relative stabilities of different N-doped carbon morphologies.

For the GBP systems (**Figure 7.2** and **Figure 7.3**), all structures were optimized without spin polarization, but we determined magnetic moments on the optimized structures using spin polarized calculations, and we found those contributions were negligible except for the GBP+1H system that optimized to 1 μB. Our 4 × 4 unit cell model can accommodate a large number of configurations involving doped N atoms and H atoms that may arise from electrochemical reductions (**Figure 7.2**). The substitutional energy of the first N atom or the binding energy of the first H atom is always the same due to the equivalence of binding sites on the GBP. We place the first N or H atom at the corner of

the graphene unit cell. Starting from the GBP with one H atom (the GBP + 1H system, which is uphill in energy by 1.44 eV) the second H atom preferentially binds one nearest neighbor away on the opposite side of the GBP at a site analogous to the ortho site for a pyridine molecule. These results are the same as previous computational studies by Boukhvalov *et al.* [39] who found that the energy of chemisorption at this site was uphill 0.54 eV.

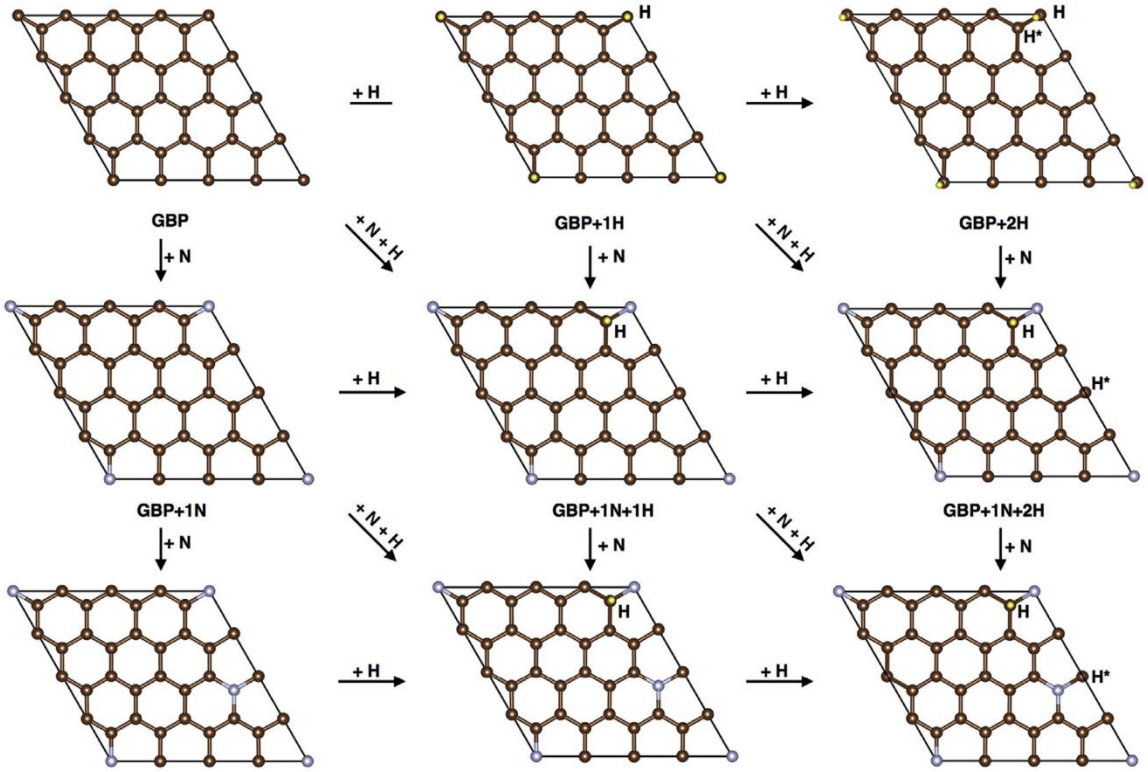

Figure 7.2 Lowest energy basal plane structures found in this work, consisting of different numbers of C (brown spheres), N (blue spheres), and H (yellow spheres) atoms. H and H* labels denote atoms on the top and bottom faces of the basal plane, respectively. The x × y unit cell is denoted by the black lines. The z direction has a 20 Å vacuum region.

The binding energy for the second H is even more uphill when it binds to the same side as the first H atom. Binding the first H atom to the GBP system disrupts aromaticity and results in a lattice distortion and a negative binding energy. One might assume that the second H atom would then bind more strongly since an energy penalty for disrupting

aromaticity has already been paid by adding the first H atom. That is the case here, but it is still energetically uphill to add a second H atom to the GBP system.

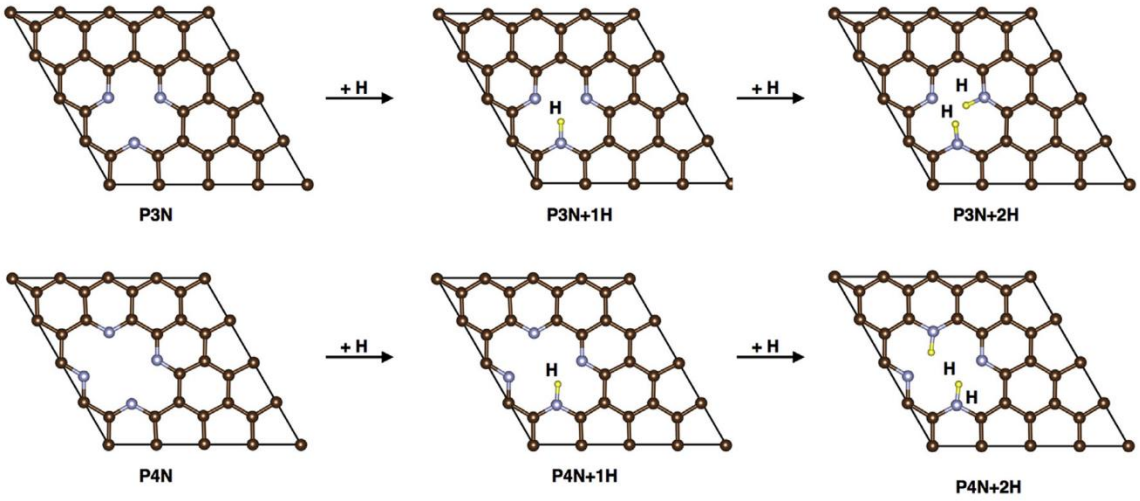

Figure 7.3 Basal plane structures with tri-pyridinic (P3N) and tetra-pyridinic (P4N) defects considered in this work showing different numbers of C (brown spheres), N (blue spheres), and H (yellow spheres) atoms. The x × y unit cell is denoted by the black lines. The z direction has a 20 Å vacuum region.

The next most favorable binding site is to a third nearest neighbor site (analogous to the *para* site for a pyridine molecule), which is further uphill by +0.40 eV compared to the *ortho* site. For our study we focus on lowest energy structures that would be relevant for thermodynamic phase diagrams, but all calculated binding energies are reported in **Table 7.1**.

When the pristine graphene is doped with an N atom at the corner of the unit cell, the second N atom in the unit cell preferentially substitutes away from the first N atom. This indicates that GBPs energetically prefer lower nitrogen doping densities, which agrees with previous studies. Since doping an N atom into graphene results in an increased magnetic moment at the adjacent carbon atoms, one might expect that these adjacent sites would accommodate binding H atoms having an unpaired electron. Indeed, the first adsorbed H atom on the singly and doubly nitrogenated graphene sheets will bind to sites adjacent to an N atom. The second H-adsorption site on the singly nitrogenated graphene

sheet is four nearest neighbor atoms away, halfway between the two N atoms. The second H-adsorption site on the doubly nitrogenated graphene sheet is *ortho* to the other N atom. The proximity of adsorbed H atoms next to N atoms is potentially significant for catalysis, since this indicates that frustrated Lewis base pair sites will exist on electrochemically reduced nitrogenated graphene basal planes, similar to molecular dihydropyridine structures reported by computational groups [33-37]. This structural motif is considered suitable for energetically efficient hydrogenation pathways.

Table 7.1 Binding energies (BE) of H to basal planes (GBP), planes with N-doped defects (P3N and P4N), and graphene ribbons (GR) with different concentration of N (positive values indicate bound states).

System	Binding Energy (eV)
GBP + 1H	-1.44
GBP + 2H/*ortho*	-0.54
GBP + 2H/*para*	-0.93
P3N + 1H	2.64
P3N + 2H	1.29
P4N + 1H	1.80
P4N + 2H	1.70
GR + 1H	0.54
GR + 2H	-0.05
GR + 1N + 1H	-0.40
GR + 1N + 2H	0.07
GR + 2N + 1H	-0.50
GR + 2N + 2H	-0.03

We also modeled the electrochemical reduction of two of the most common pyridinic defects found for graphene, tri-pyridinic (P3N, with up to three added H atoms) and tetra-pyridinic (P4N, with up to four added H atoms) vacancy defects.[40-42] A recent

study reported pyrrolic defects to be suitable for CO_2 reduction into formic acid with a low overpotential, but we find that the formation energy of this type of defect is significantly more uphill in energy than the energies to form the P3N and P4N defect sites.[32] Since the defective structures already incorporate N atoms, we did not study doping of additional N atoms to these structures. In accordance with previous reports,[43] H atoms preferentially bind to the N atoms within the pyridinic vacancy sites within the plane of the nanocarbon sheet. The first H atom binds to a tetra-pyridinic N atom by 1.8 eV. H atoms will not bind to other C atoms in this system (binding energies range from −1.3 to −0.8 eV). When one H atom is already bound to an N atom, the same trend holds where the second H atom binds much stronger to another N atom (1.7 eV). However, the presence of one H atom will allow a second H atom to bind to other C atoms (binding energies range from 0.3 to 0.8 eV). The positive binding energies for the tri-pyridinic and tetra-pyridinic defects are due to N-doped defects, which possess electron lone pairs that can bind to protons and allow electrons to enter the π-system of the GBP.

Structures we modeled for the GR system are illustrated in **Figure 7.4**. All data on GR systems were relaxed with spin polarization, where the starting magnetic moment on the system was 1 μB. The resulting spin moments for these systems always resulted in zero except for the GR saturated with H atoms, which had a magnetic moment of 1.3 μB. The presence of edge states in GR system makes their structural and electronic properties different from GBP systems. These edge states can be expected to cause preferential doping of N and addition of H on the edges of the ribbons. Indeed, we observe the first and second H atoms bind to the edges of the ribbons in our symmetric GR model, and our data are in good agreement with previous studies.[44] Furthermore, when the GR model is doped with

N atoms, these preferentially substitute with C atoms at the edges of the ribbons.[45] For N doping, the N atom substitution energies (per N atom added) are −0.7 eV, and 0.1 eV for the first and second N atoms respectively. After the first N substitution, removing an H atom is uphill by 1.2 eV. However, after the second N substitution, removing an H atom is energetically downhill −0.5 eV. Interestingly, when H atoms are added into the nitrogenated GR models, frustrated Lewis pairs form at the edges. Again, this finding is significant for catalysis on N-doped nanocarbon edges since these motifs are expected to open low energy pathways for CO_2 reduction.

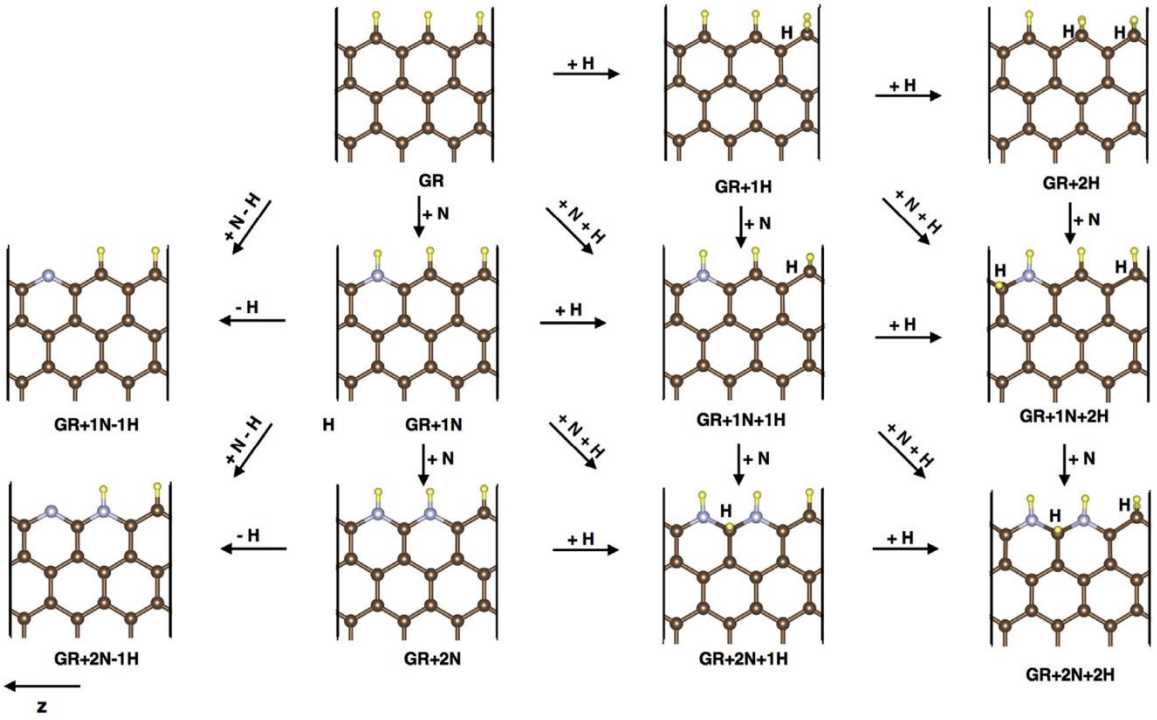

Figure 7.4 Nanoribbon structures considered in this work with different numbers of C (brown spheres), N (blue spheres), and H (yellow spheres) atoms. Only the top half of the symmetric ribbon is shown. The periodicity of the unit cell in the z direction is denoted by the dotted lines. H labels denote atoms on the top face of the nanoribbon. The x and y directions have 15 Å and 20 Å of vacuum separation their periodic images.

We now illustrate the electrochemical stability of the GBP systems in an N_2 environment using phase diagrams obtained with atomistic thermodynamics (**Figure 7.5**). The phase diagram for the GBP system includes the basal planes shown in **Figure 7.2** and

the defective sites in **Figure 7.3**. The free energies of these states were calculated as a function of the nitrogen concentration (ΔμN2) and applied potential, *E*. We note that these phase diagrams represent theoretical thermodynamic stabilities of different structures, but in reality, some structures may not be observed due to high kinetic barriers. Determination of these barriers in the presence of local solvation environments at electrochemical interfaces is left to future work.

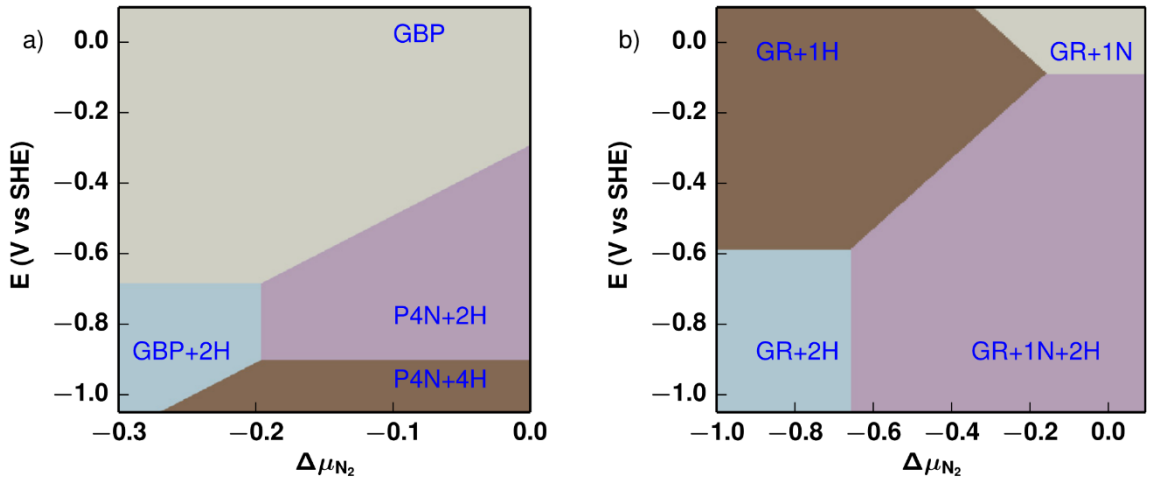

Figure 7.5 *Ab initio* atomistic thermodynamics phase diagrams for a) graphene basal planes (GBP) and b) graphene ribbons (GR) under electrochemical environments with nitrogen.

We find that the pristine GBP system (**Figure 7.5a**) is generally stable across large ranges of nitrogen concentration and applied potential. However, when ΔμN2 changes to reflect increased N content in tandem with more negative electrochemical potentials, structures involving the reduced forms of the P4N defective sites are thermodynamically more stable than the pristine GBP system. More negative than ΔμN2 = −0.18 eV, the most thermodynamically stable structure is either the reduced GBP structure with two H atoms or the P4N structure with four H atoms, depending on the values of ΔμN2 and applied potential.

For the GR systems (**Figure 7.5b**), N incorporation is energetically favorable when ΔμN2 is more positive than −0.2 eV. At ΔμN2 values more negative than −0.2 eV, a hydrogenated GR system is more stable. At slightly negative applied potentials, the thermodynamically most stable ribbon structure is the electrochemically reduced and nitrogenated GR system denoted as GR+1N+2H. Note that in this system, the two H atoms bind to sites at the ribbon edges that could be classified as frustrated Lewis pairs. At ΔμN2 values more negative than −0.67 eV and at *E* values more negative than −0.6 V vs. SHE, the reduced GR+1H system incorporates another H atom to form the GR+2H system. These results show that while it is energetically easier to dope a GR with a N atom than doping a GBP, the GBP with P4N defective sites can accommodate more N atoms and presumably even more with the formation of graphene nitride compounds. We also observed that it is easier to reduce the ribbons at all ranges of ΔμN2 when compared to basal planes. In summary, a potential of at least −0.3 V vs SHE is required to reduce a GBP system (into the P4N+2H system) while a less negative potential of −0.1 V is the lowest potential required to reduce the N doped GR systems (**Figure 7.5**).

We have shown Pourbaix diagrams to be useful descriptors for identifying participating catalyst morphologies in CO_2 reduction. When one Pourbaix diagram for a reactant (say, for CO_2) is superimposed on a Pourbaix diagram for a molecular or an extended structure catalyst, electrochemical conditions for low overpotentials are identified as the regions where boundaries from different Pourbaix diagrams are proximal to one another. We calculated Pourbaix diagrams for both graphene basal planes and graphene ribbons as a function of N concentration, and they are shown in **Figure 7.6**. The left and right panels show Pourbaix diagrams with increasing concentration of N in the GBP and

GR models respectively. In the case of the GBP model with no nitrogen present (**Figure 7.6a**), the GBP system is the more stable structure until −0.7 V vs. SHE, at which point the thermodynamic driving force favors a $2H^+/2e^-$ reduction process. In contrast, basal planes containing pyridinic defects are much more susceptible to electroreduction. Here, the P3N defect and the P4N defect would readily undergo $1H^+/1e^-$ and a $2H^+/2e^-$ reductions, respectively, at 0 V vs SHE. The boundary lines in the Pourbaix diagrams of the GBP and P4N models are several volts more negative than the standard redox potential needed to form formate from carbonic acid (a stable form of CO_2 in aqueous solution), indicating that reductions of the catalyst here would bring significantly higher overpotentials if they were needed to drive CO_2 reduction. However, the boundary lines denoting the reduction of the P3N+1H state into the P3N+2H state is relatively close to the boundary line for carbonic acid or bicarbonate reduction into formic acid or formate, suggesting that these processes on these morphologies would have lower overpotentials if coupled to CO_2 reduction.

The Pourbaix diagrams for zigzag edges of GR systems are somewhat different from those for the GBP systems. In the case of the undoped GR system, we see boundary lines that are not well-suited for energetically efficient CO_2 reduction. However, the $2H^+/2e^-$ reductions involving the GR+1N state (the nanoribbon with 1/3 coverage of N) and GR+2N (the nanoribbon with 2/3 coverage of N) into the GR+1N+2H and GR+2N+2H states are quite closely aligned to be coupled to energetically efficient CO_2 reduction. This indicates that zigzag edges of N-doped nanocarbons are good candidates for efficient CO_2 reduction via H-shuttling mechanisms. In principle, similar analyses as what has been reported here can be used to identify nanocarbon morphologies for energetically efficient catalysis.

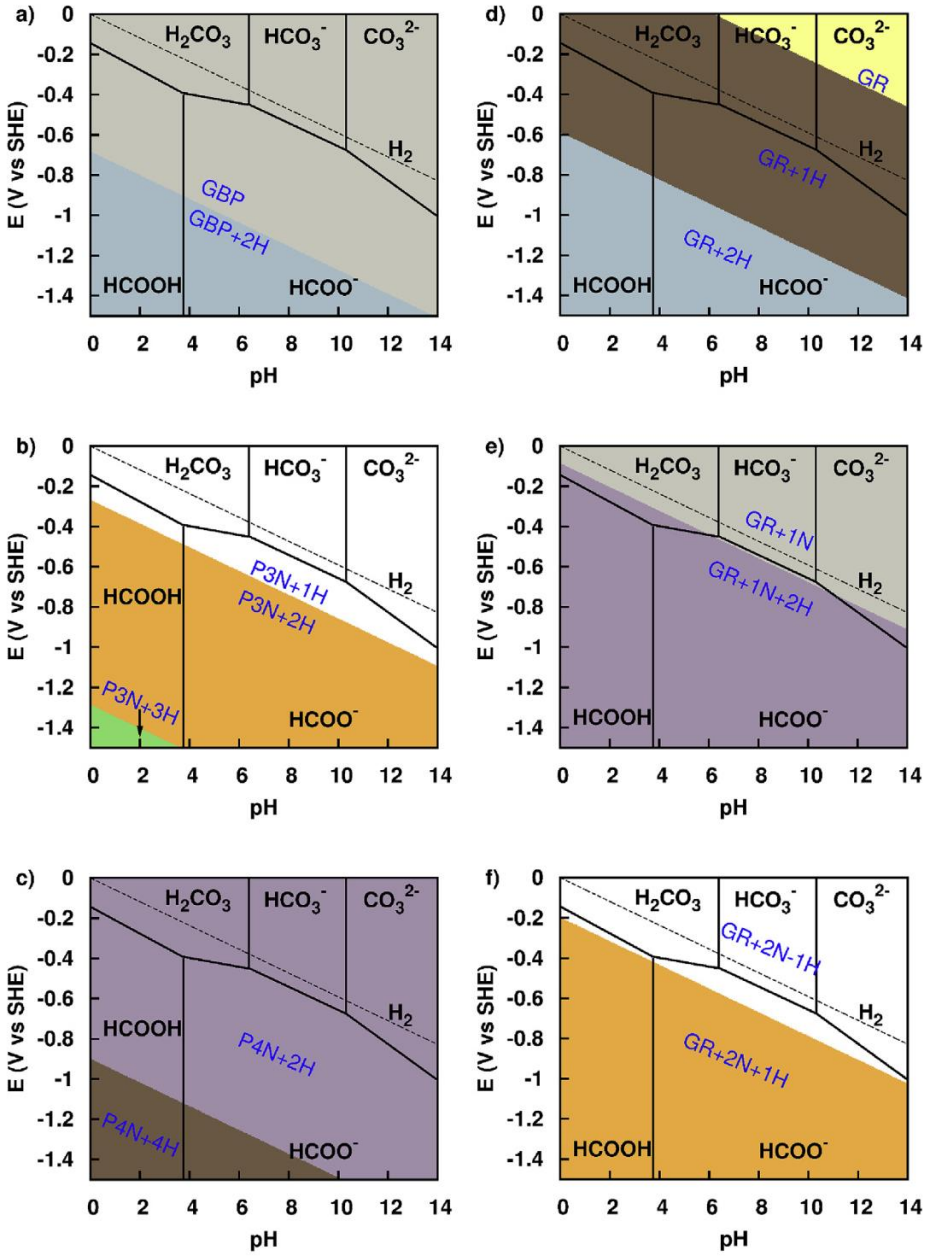

Figure 7.6 Pourbaix diagrams for basal plane structures (GBP (a)), tri-pyridinic defect (P3N (b)), tetra-pyridinic defect (P4N (c)) and graphene ribbon structures (GR (d), GR+1N (e),GR+2N (f)).

7.1.4 Conclusion

We have used density functional theory with atomistic thermodynamics to determine the energies of atomic scale N-doped nanocarbon morphologies under *in operando* electrochemical conditions. We find that zigzag edges are in general more susceptible to electrochemical reductions than graphene basal planes. However, tri-

pyridinic defects have suitable thermodynamic energies to undergo $2H^+/2e^-$ reductions at electrochemical operating conditions with moderately negative applied potentials. Our results show that if nitrogen concentration of carbonous materials can be well controlled, the reduction potentials for the materials should be tunable for energetically efficient catalysis. Of particular interest are the reduced states of these materials that can form frustrated Lewis pairs that would be applicable for energetically efficient (de)hydrogenation catalysis.

7.1.5 Computational Methods

We used ab initio atomistic thermodynamics [46] and computational hydrogen electrode model [38] to understand the thermodynamic stabilities of nanocarbon morphologies, graphene basal planes (GBP) and graphene ribbons (GR), having different N and H concentrations. We focused on a GR system with zigzag edges since this most closely resembles pyridine analogs that relate to our previous work.

The electronic energies of all GBP and GR structures were calculated using spin polarized Kohn-Sham density functional theory (DFT) as implemented in the Vienna *ab initio* simulation package (VASP), a plane wave based DFT package.[47, 48] We used the PBE [49, 50] exchange-correlation functional and projector augmented wave pseudopotentials [51, 52] to describe the valence electrons of atoms in the system. We have performed convergence tests by varying the energy cutoff and k points until the formation energy was converged up to 10 meV/Å^2 in the case of GBP and 10 meV/Å in the case of GR. Plane waves with an energy cutoff of 800 eV and 4 × 4 × 1 k-points were used for all calculations on the GBP systems while an energy cutoff of 500 eV and 3 × 1 × 1 k-points were used for GR systems. Convergence plots are included in the Supporting information.

All structures were relaxed using conjugate gradient iterative minimization until the difference in energies between consecutive geometry steps was less than 10^{-6} eV. The convergence of size of the unit cell was tested for the pristine GBP system, and we found the formation energies did not change by more than 1 meV/Å2 for a 4 × 4 unit cell. In the case of the GR system, the width of the zigzag ribbon was changed until the formation energies converged to less than 1 meV/Å. We found that a GR system with six zigzag lines across the ribbon width lead to converged energetics. Chemical modifications to the ribbon were made symmetrically to minimize dipoles.

7.2 Developing Catalytic Descriptors from Electronic Structure Models and Spin in Graphitic Carbons

7.2.1 Abstract

Density functional theory was used to investigate the electronic structure, molecular orbitals, and spin properties of nanographitic flakes. It was found that the energy of the highest occupied molecular σ orbital was relatively independent of the size of the graphitic flake while the highest occupied molecular π orbital increased with the size of the flake. Thus, controlling graphitic domain size could be a way to "tune" the catalytic activity of a carbon, by changing the alignment of the delocalized π band relative to the σ orbitals that can more readily form chemical bonds with reactants. Spin was also investigated and found to emerge at moderate sizes, specifically with respect to the zigzag edges. Natural bond orbitals showed that this could be due to the so-called "Clar sextet rule". Preliminary calculation on irregular flakes revealed a dependence of triplet singlet energy difference based on the lengths of the two largest zigzag edges. Lastly, the effect of nitrogen content on spin showed little dependence beyond a few notable exceptions, for which the origin of

the deviations is unclear. Future work will delve more into the effects of these properties on catalysis as well as the development of more thorough descriptors of these electronic and spin properties.

7.2.2 Introduction

Compared to the relatively burgeoning field of metal-free catalysis, the study of metal-based catalysis is more developed, with theories to explain and predict interaction strengths that dictate catalytic activity. Perhaps the most successful of these theories to date is the *d*-band model.[1, 53, 54] While the theory does not directly extend to metal-free catalysis, it may be instructive in coming to an understanding of graphitic systems and the underlying electronic structure features that lead to their catalytic activity. In the *d*-band model, the bonding strength between an adsorbate and metal can be explained by considering the interaction between the adsorbate-surface bonding and antibonding orbitals within the *d*-band of the metal (**Figure 7.7**).[1] More specifically, the interaction is determined by following the relative positions of the bonding and antibonding MO, the coupling strength of MOs to the *d*-band, and the filling of the antibonding MO by the Fermi level, E_F. The more filled the antibonding orbital is by coupling to the metal's *d*-band, the weaker the bond. These factors are often simplified into a single descriptor, the *d*-band center relative to E_F (since the antibonding MO is always above the E_F), denoted as ε_d.

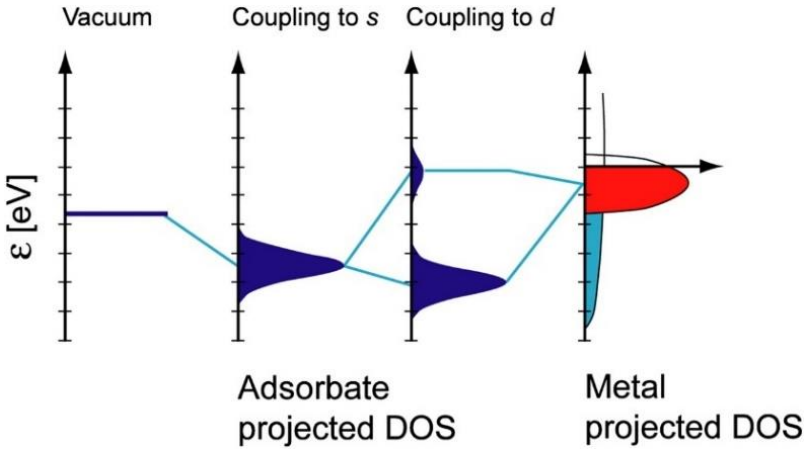

Figure 7.7 Schematic illustration of the *d*-band model. The adsorbate valence level (left) forms a bond with an *s* orbital of the metal (middle-left). The bond mixes with the *d*-band of the metal (right, in red), resulting in filling of the antibonding orbital based on its energy relative to E_F. Reproduced from [53].

These descriptive frameworks do not hold in carbon systems, of course, as they do not have any *d* orbitals, but parallels can still be drawn. At the core of these models, there are two key electronic features: a band of states with a highly delocalized pool of electrons, and localized states that act as donors or acceptors in forming bonds with an adsorbate. The electronic structure of carbons, depending on the arrangement, can actually have a similar picture. Ideal, infinite graphene has a cone shaped density of states, armchair edged graphene nanoribbons (GNRs) have a bandgap, and zigzag GNRs have their frontier orbitals at the fermi level and located on zigzag edges (**Figure 7.8**).[55-59] A key difference, though, is that metals can be effectively studied as periodic structures with planewave basis sets, while carbons are still "organic" systems with distinct molecular/frontier orbitals that make them behave very differently than metal-based systems in chemical processes.

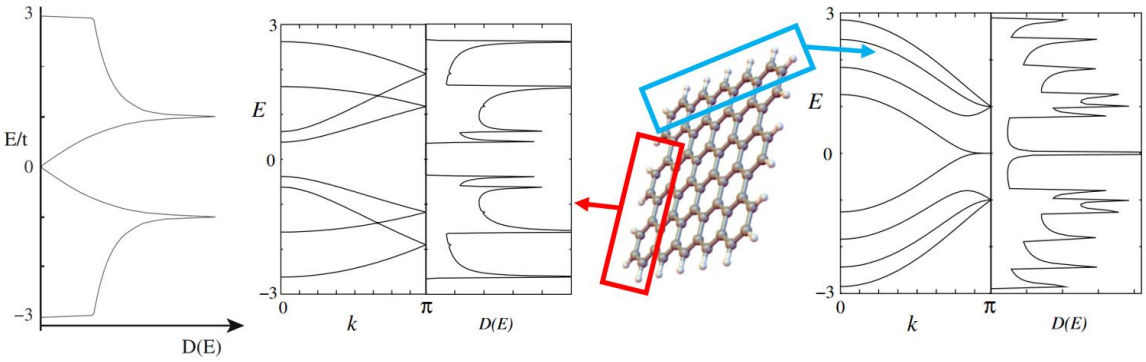

Figure 7.8 Density of states for infinite graphene (left plot). Energy band structures and density of states for the armchair (middle plot) and zigzag (right plot) graphene ribbons.[55] The armchair edged ribbon has a bandgap while the zigzag edged ribbon has an accumulation of states at the Fermi edge.

Another distinguishing aspect of carbons as compared to metals is spin. Although the mechanism by which magnetic order arises in carbons is still under debate, it is evident that it is distinct from the emergence of magnetism in metals, and that the spatial distribution of spin is subsequently also different.[60] With all of this said, the effects of spin on catalytic properties has generally not been a major focus of metal-free catalyst research, which is in strong contrast to other areas of catalysis, such as biocatalysis and traditional metal-based catalysis.

We hypothesize that the observed catalytic activity of nanocarbons is related to two aspects of their electronic structure: (i) the synergistic interaction of frontier π (non-bonding electrons on zigzag edges of nanographitic domains) and σ (lone pairs of zigzag edge nitrogens) orbitals, and (ii) the propensity of extended polyaromatic systems toward open shell states.[61-65] The role of (i) is related to the non-bonding and radical character of zigzag π electrons, which places them at the Fermi energy and enhances their ability to participate in reduction reactions such as ORR and HER, and the potential for lone pairs of zigzag-edge nitrogens to act as binding/coordination sites for reaction intermediates. The role of (ii) relates to the tendency of extended polyaromatic systems to develop open

shell states along their zigzag edges. Experimentally, we have seen this in preliminary EPR and valence band measurements, showing both the expected paramagnetic properties, and the dependence of the size of graphitic domains on the band edge of the π system, while not affecting the nitrogen lone pairs (**Figure 7.9**). Akin to the *d*-band model, we believe these concepts provide the tunable parameters that lead to differences in observed catalytic activity in graphitic systems that can then be leveraged to rationally design and improve their performance.

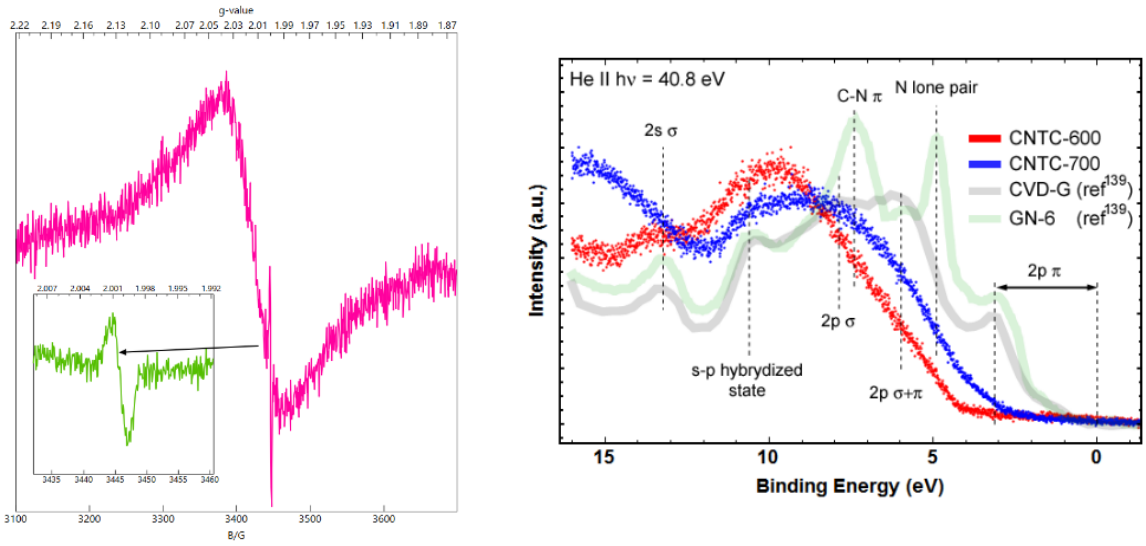

Figure 7.9 Preliminary EPR spectrum of polyacrylonitrile derived carbons (left) showing two distinct features: a narrow component corresponding to localized spins on zigzag edges in an open shell singlet state (inset), and a broad component originating from nonbonding π electrons.[66] UPS (right) spectra of PAN-derived carbons prepared at different pyrolysis temperatures. For comparison the UPS spectra of CTNC are overlayed with the spectra of graphene prepared by CVD (CVD-G) and of nitrogen doped nanographene (GN-6) published by other authors.[67]

It is important to mention that there is some controversy around calculating the so-called open shell singlet state, which requires a mixing of the highest occupied and lowest unoccupied molecular orbitals. These types of calculations can lead to spin contamination and produce wavefunctions that are not Eigenfunctions of the Hamiltonian.[68, 69] That said, such calculations have provided insights that have been corroborated experimentally and thus can still be instructive in qualitative exploration of chemical systems.

7.2.3 Results and Discussion

The evolution of electronic structure in nanocarbon systems with size was investigated computationally using B3LYP with a 6-31G basis on nitrogen substituted oligoacenes as a model for zigzag edges. Orbitals were grouped into either σ or π based on symmetry. With this grouping, a size dependence emerged for the π bonds while the σ bonds on the N atoms remain the same (**Figure 7.10**). As the length of the ladder is increased, the energy of the highest π electron state increases steadily in accord with the increase of its non-bonding nature. For *n*=3, the energy of the π electron state crosses above the lone pair energy, with the zigzag edge π electron state becoming the HOMO.

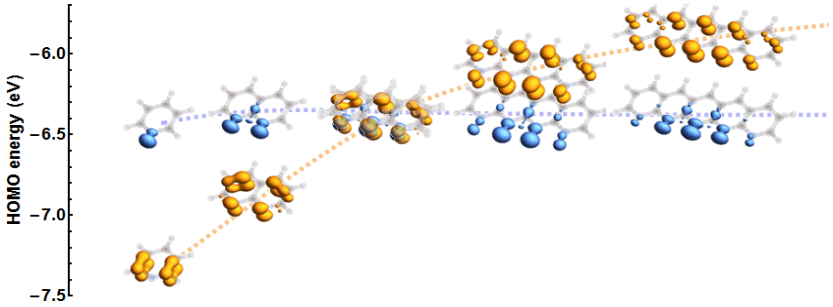

Figure 7.10 Results of DFT calculations showing the evolution of HOMO-π (orange) and HOMO- σ (blue) in the series of nitrogen substituted oligoacenes.

The importance of nitrogens in these systems can be seen further in comparing flakes both with and without nitrogens on zigzag edges. **Figure 7.11** compares a flake with hydrogen-terminated edges (left) with a flake in which one of the zigzag edges is terminated with nitrogen atoms (right). The central plots show the total density of electronic orbitals, with occupied orbitals colored in light brown and virtual orbitals colored in gray. The bars above and below the density of states separate the orbitals into σ (blue, above) and π (orange, below) symmetries (based on the absence or presence of a node in the plane of the graphene). For the hydrogen-terminated flake, the frontier orbitals

are non-bonded π-orbitals localized on the carbons of the zigzag edges. Substituents, such as the hydrogens, are strongly bonded to these edge carbons and sterically restrict access to the π orbitals. By replacing the C-H groups on the zigzag edge with nitrogen atoms, a set of non-bonding σ orbitals consisting of lone pairs on the nitrogen atoms are introduced (**Figure 7.11** in green). These pyridinic lone-pair orbitals provide the binding/coordination sites for the reaction intermediates and their energies do not seem to be size dependent.

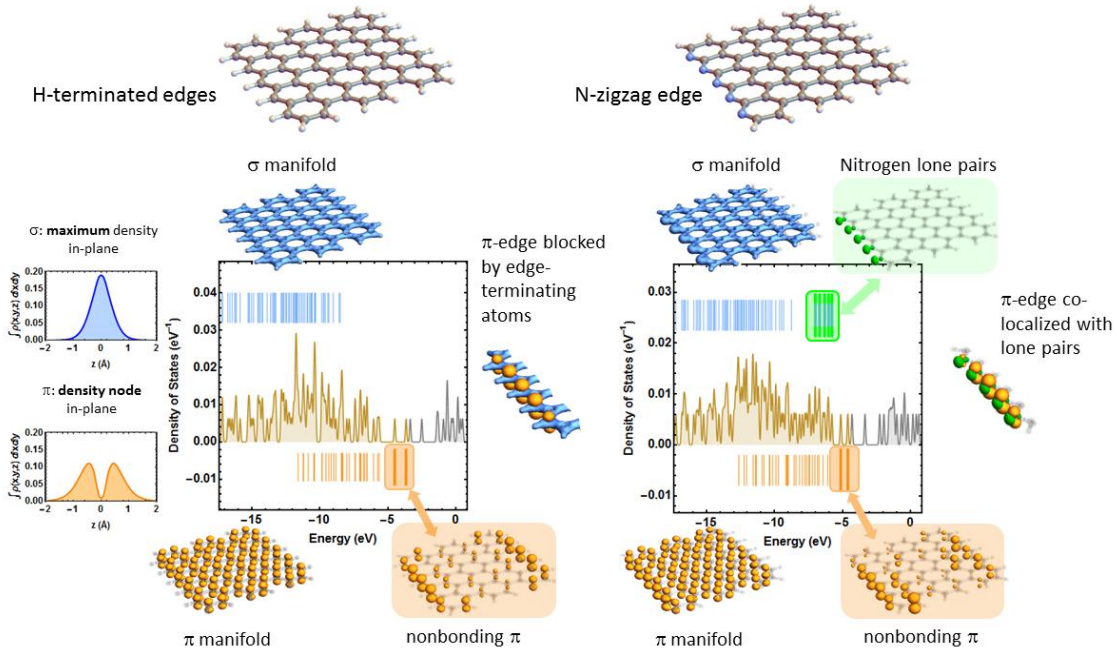

Figure 7.11 Results of DFT calculations of the electronic structure of nanographitic flakes. In the nanographitic flake shown on the left, the carbon dangling bonds are terminated with hydrogens. In the flake shown on the right the carbons on one of the zigzag edges were replaced with nitrogens.

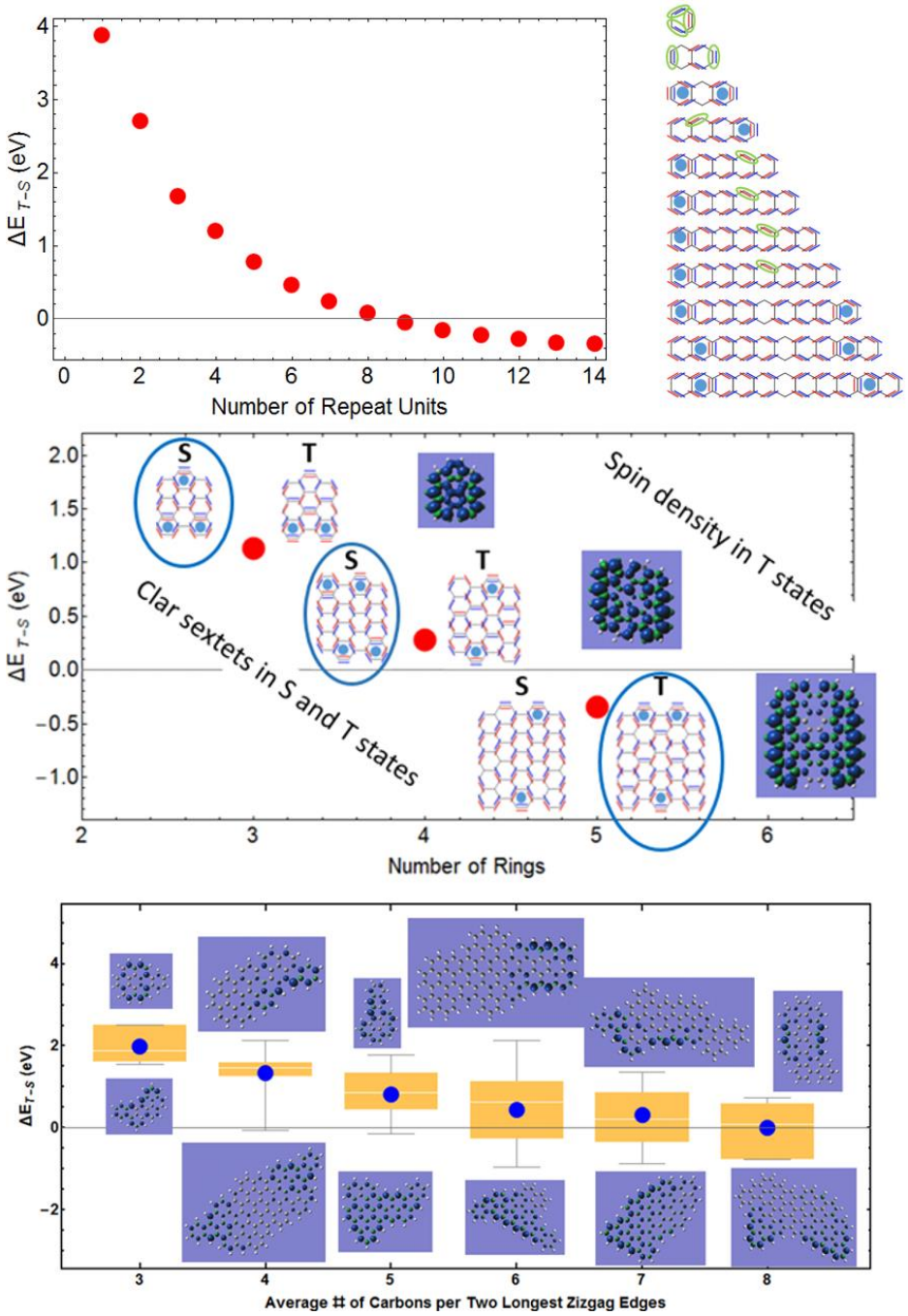

Figure 7.12 Emergence of open shell states on oligoacenes (top), on the zigzag edges of "square" graphitic nanoflakes comprised of n × n rings (middle), and on randomly generated irregular flakes (bottom). The energy difference between the triplet and singlet state, $\Delta E_{T\text{-}S}$ (red circles), becomes negative for 9 repeat units in oligoacenes and 5 × 5 nanoflakes. Spin density plots show that spin densities in the triplet state shift to zigzag edge as flake size increases. Bonding patterns from natural bond orbital analysis (middle plot, left of points) show that singlet-triplet state ordering is consistent with the lower-energy state having a higher number of Clar sextets (labeled by blue disks). For irregularly shaped nanoflakes, $\Delta E_{T\text{-}S}$ (blue circles) decreases and becomes negative as the length of the longest zigzag edges increases. The inset plots show the tendency of spin density to be localized for $\Delta E_{T\text{-}S} > 0$ and delocalized along zigzag edges for $\Delta E_{T\text{-}S} < 0$.

The size dependent emergence of spin properties in nanocarbons was probed in oligoacenes and idealized square flakes. By calculating the total energies of the singlet and triplet states, and looking at their natural bond orbitals. The calculations shown in **Figure 7.12** suggest that Clar sextet rules [64, 70-73] may be useful for understanding the tendency of spin density to accumulate at zigzag edges. These results show that the relative ordering of single and triplet states is consistent with the number of benzenoid sextets (Clar sextets). Within this picture, the energy-stabilization from formation of benzenoid sextets (Clar sextets) offsets loss in π-bonding associated with spin density on the zigzag edge. The calculations shown in **Figure 7.12, bottom**, on irregularly shaped structures provide additional insight into the role of zigzag edges. These show that single-triplet splitting is strongly correlated with the average length of the two longest zigzag edges. These results suggest that counts of Clar sextets and lengths of continuous zigzag edges are two useful features to consider in developing intuition for this family of catalysts.

The influence of zigzag edge nitrogens on the spin properties was assessed by generating random carbon flakes and modifying those structures with progressively higher nitrogen content on those edges. The total energies of the flakes were calculated for their singlet, triplet, and open shell singlet states (**Figure 7.13**). The pattern observed in **Figure 7.12** of spin emerging with long zigzag edges remained across all flakes regardless of nitrogen content. Almost no variance in triplet or open shell singlet energies relative to the closed-shell singlet energies were observed, except for a few notable cases when the triplet state was the lowest energy and the zigzag edges contained either 25 or 50% nitrogen. While these instances are very pronounced relative to the lack of an effect in all other cases, the effects do not manifest themselves appreciably in spin density surfaces (**Figure 7.14**).

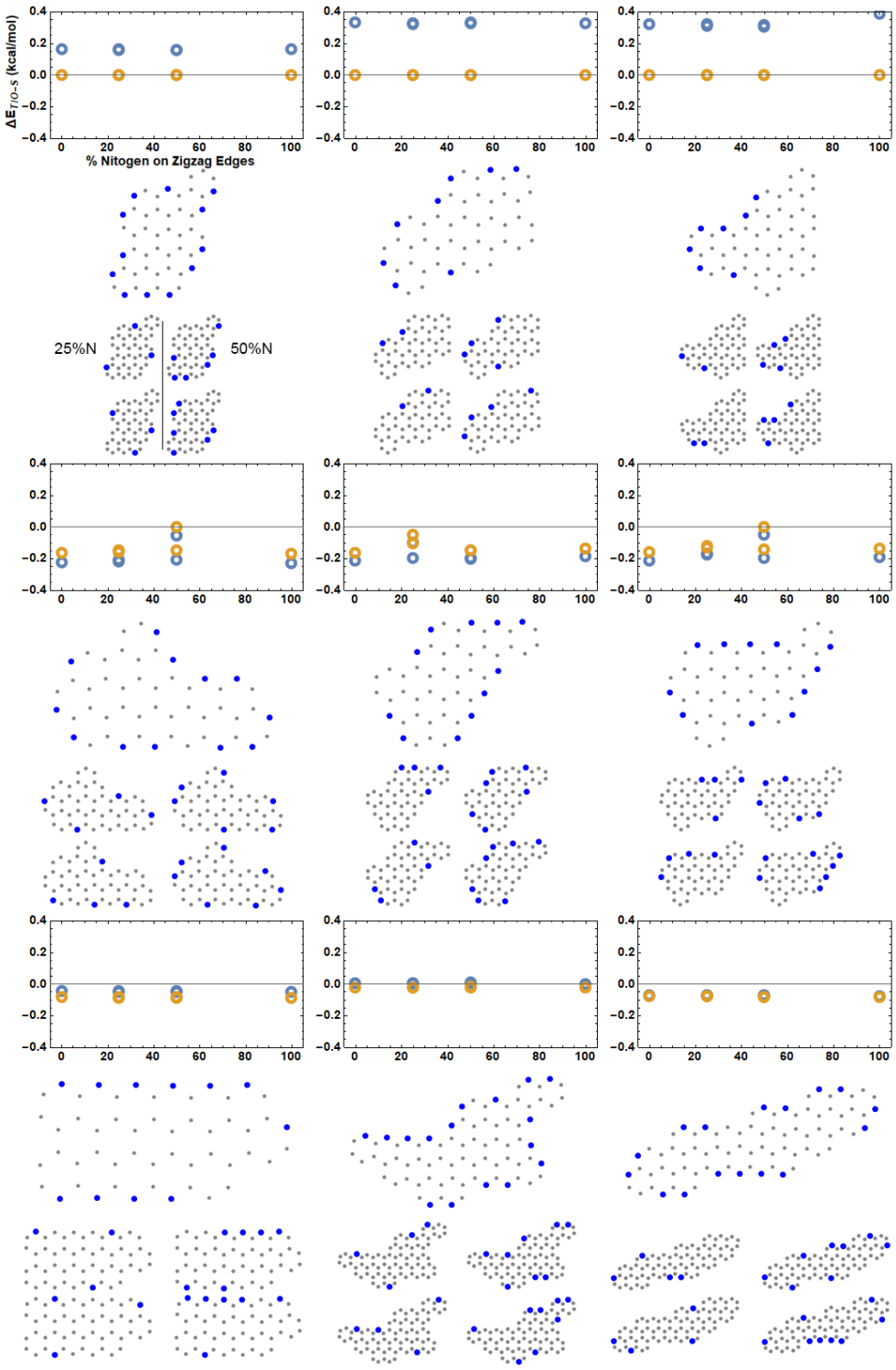

Figure 7.13 Energy differences between different spin states for carbon flake structures. Triplet minus closed-shell singlet is shown in blue, and open-shell singlet minus closed-shell singlet states is shown in orange. The first, second, and third rows group structures that have nitrogen-free structures with their lowest energy structures as singlet, triplet, and open shell singlet states respectively. Large structures show flakes with fully nitrogenated zigzag edges with the left 2 and right 2 smaller structures showing ~25% and ~50% N structures respectively.

Another interesting note is that the cases in which the open shell singlet is the lowest energy state occurs in structures with high aspect ratios and shorter distances between the zigzag edges. This indicates that in those structures, while breaking a π bond is energetically favorable, the zigzag edges are still close enough that the two electrons are not able to be truly free radicals, and as such are still interacting. For structures with the triplet state as the lowest energy, there is more distance between zigzag edges, allowing for full decoupling of the electrons.

7.2.4 Conclusion

The electronic structure of heteroatom nanocarbon flakes and their spin properties were investigated by DFT. It was found that there are two distinct components that comprise the overall electronic structure of a nanocarbon: the π orbitals, with a size dependent HOMO; and the σ orbitals, the higher energy states of which become accessible through heteroatom doping on the zigzag edge. By tuning the size of a carbon, it may be possible to tune the interactions between these two components to optimize redox properties to catalyze a particular reaction.

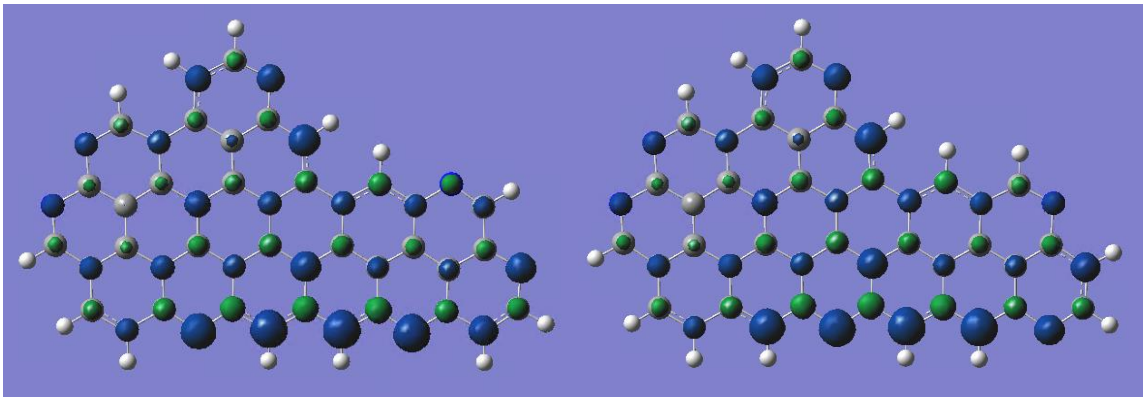

Figure 7.14 Spin densities of the flake shown in **Figure 7.15**, row 2, first column, with 50% nitrogen coverage on the zigzag edges. While the structure on the left has notably higher state for the triplet relative to the closed-shell singlet, there are no clear indications of its origin from spin densities.

The spin properties of the carbon flakes emerged as another size dependent feature but with strong topological effects as well. Triplet states become the ground state with the increase in the length of zigzag edges, but the threshold at which that occurs varies based on the size of the overall graphitic domain. The energy of the open shell singlet state was the lowest energy in cases where there were extended zigzag edges that were close to each other such that they remain in electronic communication. Surprisingly, nitrogen content did not have a strong effect on spin properties, except for a few cases for which the cause is not readily apparent and will be the subject of future investigations. These results point to an interplay between multiple features of carbon flakes (edges, topology, domain sizes, and heteroatom content) and electronic/spin properties that may be driving factors in metal-free catalysis.

7.2.5 Computational Methods

All calculations were performed using Gaussian 09 Revision D.01, using B3LYP and a basis set of 6-31G or STO-3G. All structures were geometry optimized for each spin state calculated. Structures were randomly generated by a custom script written in Mathematica.

7.3 References

[1] B. Hammer, J.K. Nørskov, Electronic factors determining the reactivity of metal surfaces, *Surface Science* **1995,** *343* (3), 211-220, https://doi.org/10.1016/0039-6028(96)80007-0.

[2] E. Nakamura, K. Sato, Managing the scarcity of chemical elements, *Nature materials* **2011,** *10* (3), 158-161,

[3] C. Jaffray, G. Hards, Precious metal supply requirements, *Handbook of Fuel Cells* **2003**,

[4] R.J. Farrauto, Y. Liu, W. Ruettinger, O. Ilinich, L. Shore, T. Giroux, Precious metal catalysts supported on ceramic and metal monolithic structures for the hydrogen economy, *Catalysis Reviews* **2007,** *49* (2), 141-196,

[5] R. Bashyam, P. Zelenay, A class of non-precious metal composite catalysts for fuel cells, *Nature* **2006,** *443* (7107), 63-66,

[6] D.S. Su, J. Zhang, B. Frank, A. Thomas, X. Wang, J. Paraknowitsch, R. Schlögl, Metal-free heterogeneous catalysis for sustainable chemistry, *ChemSusChem* **2010,** *3* (2), 169-80,

[7] E. Auer, A. Freund, J. Pietsch, T. Tacke, Carbons as supports for industrial precious metal catalysts, *Applied Catalysis A: General* **1998,** *173* (2), 259-271,

[8] J. Duan, S. Chen, M. Jaroniec, S.Z. Qiao, Heteroatom-Doped Graphene-Based Materials for Energy-Relevant Electrocatalytic Processes, *ACS Catalysis* **2015,** *5* (9), 5207-5234,

[9] X.-L. Wu, T. Wen, H.-L. Guo, S. Liu, X. Wang, A.-W. Xu, M. Mezger, Self-templated synthesis of novel carbon nanoarchitectures for efficient electrocatalysis, *Scientific Reports* **2016,** *6*, 28049-28049,

[10] J. Wei, D. Zhou, Z. Sun, Y. Deng, Y. Xia, D. Zhao, A Controllable Synthesis of Rich Nitrogen-Doped Ordered Mesoporous Carbon for CO 2 Capture and Supercapacitors, *Advanced Functional Materials* **2013,** *23* (18), 2322-2328,

[11] M. Zhong, S. Jiang, Y. Tang, E. Gottlieb, E.K. Kim, A. Star, K. Matyjaszewski, T. Kowalewski, Block copolymer-templated nitrogen-enriched nanocarbons with morphology-dependent electrocatalytic activity for oxygen reduction, *Chemical Science* **2014,** *5* (8), 3315-3315,

[12] Y. Zheng, J. Liu, J. Liang, M. Jaroniec, S.Z. Qiao, Graphitic carbon nitride materials: controllable synthesis and applications in fuel cells and photocatalysis, *Energy Environ. Sci.* **2012,** *5* (5), 6717-6731,

[13] E. Gottlieb, M. Kopeć, M. Banerjee, J. Mohin, D. Yaron, K. Matyjaszewski, T. Kowalewski, In-Situ Platinum Deposition on Nitrogen-Doped Carbon Films as a Source of Catalytic Activity in a Hydrogen Evolution Reaction, *ACS Applied Materials & Interfaces* **2016,** *8* (33), 21531-21538, 10.1021/acsami.6b03924.

[14] W. Ding, Z. Wei, S. Chen, X. Qi, T. Yang, J. Hu, D. Wang, L.-J. Wan, S.F. Alvi, L. Li, Space-Confinement-Induced Synthesis of Pyridinic- and Pyrrolic-Nitrogen-Doped Graphene for the Catalysis of Oxygen Reduction, *Angewandte Chemie* **2013,** *125* (45), 11971-11975,

[15] M. Seredych, T.J. Bandosz, Confined space reduced graphite oxide doped with sulfur as metal-free oxygen reduction catalyst, *Carbon* **2014,** *66*, 227-233,

[16] J.E. Trancik, S.C. Barton, J. Hone, Transparent and Catalytic Carbon Nanotube Films, *Nano Letters* **2008,** *8* (4), 982-987,

[17] J.-P. Tessonnier, A. Villa, O. Majoulet, D.S. Su, R. Schlögl, Defect-mediated functionalization of carbon nanotubes as a route to design single-site basic heterogeneous catalysts for biomass conversion, *Angewandte Chemie (International ed. in English)* **2009,** *48* (35), 6543-6,

[18] L. Wang, A. Ambrosi, M. Pumera, "Metal-free" catalytic oxygen reduction reaction on heteroatom- doped graphene is caused by trace metal impurities, *Angewandte Chemie (International ed. in English)* **2013,** *52* (51), 13818-21,

[19] G. Dong, M. Fang, H. Wang, S. Yip, H.-Y. Cheung, F. Wang, C.-Y. Wong, S.T. Chu, J.C. Ho, Insight into the electrochemical activation of carbon-based cathodes for hydrogen evolution reaction, *J. Mater. Chem. A* **2015,** *3* (24), 13080-13086, 10.1039/c5ta02551f.

[20] H. Kim, K. Lee, S.I. Woo, Y. Jung, On the mechanism of enhanced oxygen reduction reaction in nitrogen-doped graphene nanoribbons, *Physical chemistry chemical physics : PCCP* **2011,** *13* (39), 17505-10,

[21] W. Yuan, Y. Zhou, Y. Li, C. Li, H. Peng, J. Zhang, Z. Liu, L. Dai, G. Shi, The edge- and basal-plane-specific electrochemistry of a single-layer graphene sheet, *Scientific reports* **2013,** *3*, 2248-2248,

[22] A. Shen, Y. Zou, Q. Wang, R.A.W. Dryfe, X. Huang, S. Dou, L. Dai, S. Wang, Oxygen Reduction Reaction in a Droplet on Graphite: Direct Evidence that the Edge is More Active than the Basal Plane, *Angewandte Chemie (International ed. in English)* **2014,** *53* (40), 10804-8,

[23] L. Zhang, Z. Xia, Mechanisms of Oxygen Reduction Reaction on Nitrogen-Doped Graphene for Fuel Cells, *The Journal of Physical Chemistry C* **2011,** *115* (22), 11170-11176,

[24] Y. Zheng, Y. Jiao, Y. Zhu, L.H. Li, Y. Han, Y. Chen, A. Du, M. Jaroniec, S.Z. Qiao, Hydrogen evolution by a metal-free electrocatalyst, *Nature communications* **2014,** *5*, 3783-3783,

[25] Y. Zheng, Y. Jiao, L.H. Li, T. Xing, Y. Chen, M. Jaroniec, S.Z. Qiao, Toward Design of Synergistically Active Carbon-Based Catalysts for Electrocatalytic Hydrogen Evolution, *ACS Nano* **2014,** *8* (5), 5290-5296, 10.1021/nn501434a.

[26] W.A. Saidi, Oxygen Reduction Electrocatalysis Using N-Doped Graphene Quantum-Dots, *The Journal of Physical Chemistry Letters* **2013,** *4* (23), 4160-4165, 10.1021/jz402090d.

[27] B. Kumar, M. Asadi, D. Pisasale, S. Sinha-Ray, B.A. Rosen, R. Haasch, J. Abiade, A.L. Yarin, A. Salehi-Khojin, Renewable and metal-free carbon nanofibre catalysts for carbon dioxide reduction, *Nat Commun* **2013,** *4*,

[28] H. Wang, Y. Chen, X. Hou, C. Ma, T. Tan, Nitrogen-doped graphenes as efficient electrocatalysts for the selective reduction of carbon dioxide to formate in aqueous solution, *Green Chem.* **2016,** *18* (11), 3250-3256,

[29] S. Zhang, P. Kang, S. Ubnoske, M.K. Brennaman, N. Song, R.L. House, J.T. Glass, T.J. Meyer, Polyethylenimine-Enhanced Electrocatalytic Reduction of CO2 to Formate at Nitrogen-Doped Carbon Nanomaterials, **2014**,

[30] J. Wu, R.M. Yadav, M. Liu, P.P. Sharma, C.S. Tiwary, L. Ma, X. Zou, X.-D. Zhou, B.I. Yakobson, J. Lou, P.M. Ajayan, Achieving Highly Efficient, Selective, and Stable CO2 Reduction on Nitrogen-Doped Carbon Nanotubes, **2015**,

[31] G.-L. Chai, Z.-X. Guo, Highly effective sites and selectivity of nitrogen-doped graphene/CNT catalysts for CO2 electrochemical reduction, *Chem. Sci.* **2016,** *7* (2), 1268-1275,

[32] Y. Liu, J. Zhao, Q. Cai, Pyrrolic-nitrogen doped graphene: a metal-free electrocatalyst with high efficiency and selectivity for the reduction of carbon dioxide to formic acid: a computational study, *Phys. Chem. Chem. Phys.* **2016,** *18* (7), 5491-5498,

[33] J.A. Keith, E.A. Carter, Electrochemical reactivities of pyridinium in solution: consequences for CO2 reduction mechanisms, *Chemical Science* **2013,** *4* (4), 10.1039/c3sc22296a.

[34] A. Marjolin, J.A. Keith, Thermodynamic Descriptors for Molecules the Catalyze Efficient CO 2 Electroreductions, *ACS Catalysis* **2015,** *5* (2), 150106113904007-150106113904007,

[35] C.-H. Lim, A.M. Holder, J.T. Hynes, C.B. Musgrave, Roles of the Lewis Acid and Base in the Chemical Reduction of CO2 Catalyzed by Frustrated Lewis Pairs, **2013**,

[36] E. Barton Cole, P.S. Lakkaraju, D.M. Rampulla, A.J. Morris, E. Abelev, A.B. Bocarsly, Using a One-Electron Shuttle for the Multielectron Reduction of CO2to Methanol: Kinetic, Mechanistic, and Structural Insights, *Journal of the American Chemical Society* **2010,** *132* (33), 11539-11551, 10.1021/ja1023496.

[37] E.E. Barton, D.M. Rampulla, A.B. Bocarsly, Selective Solar-Driven Reduction of CO2to Methanol Using a Catalyzed p-GaP Based Photoelectrochemical Cell, *Journal of the American Chemical Society* **2008,** *130* (20), 6342-6344, 10.1021/ja0776327.

[38] J.K. Nørskov, J. Rossmeisl, A. Logadottir, L. Lindqvist, J.R. Kitchin, T. Bligaard, H. Jónsson, Origin of the Overpotential for Oxygen Reduction at a Fuel-Cell Cathode, *The Journal of Physical Chemistry B* **2004,** *108* (46), 17886-17892,

[39] D.W. Boukhvalov, M.I. Katsnelson, A.I. Lichtenstein, Hydrogen on graphene: Electronic structure, total energy, structural distortions and magnetism from first-principles calculations, *Physical Review B* **2008,** *77* (3), 10.1103/PhysRevB.77.035427.

[40] D. Wei, Y. Liu, Y. Wang, H. Zhang, L. Huang, G. Yu, Synthesis of N-Doped Graphene by Chemical Vapor Deposition and Its Electrical Properties, *Nano Letters* **2009,** *9* (5), 1752-1758, 10.1021/nl803279t.

[41] Z. Hou, X. Wang, T. Ikeda, K. Terakura, M. Oshima, M.-a. Kakimoto, S. Miyata, Interplay between nitrogen dopants and native point defects in graphene, *Physical Review B* **2012,** *85* (16), 10.1103/PhysRevB.85.165439.

[42] Y. Fujimoto, S. Saito, Formation, stabilities, and electronic properties of nitrogen defects in graphene, *Physical Review B* **2011,** *84* (24), 10.1103/PhysRevB.84.245446.

[43] Y. Fujimoto, S. Saito, Hydrogen adsorption and anomalous electronic properties of nitrogen-doped graphene, *Journal of Applied Physics* **2014,** *115* (15), 10.1063/1.4871465.

[44] T. Wassmann, A.P. Seitsonen, A.M. Saitta, M. Lazzeri, F. Mauri, Structure, Stability, Edge States, and Aromaticity of Graphene Ribbons, *Physical Review Letters* **2008,** *101* (9), 10.1103/PhysRevLett.101.096402.

[45] M. Li, L. Zhang, Q. Xu, J. Niu, Z. Xia, N-doped graphene as catalysts for oxygen reduction and oxygen evolution reactions: Theoretical considerations, *Journal of Catalysis* **2014,** *314*, 66-72, 10.1016/j.jcat.2014.03.011.

[46] K. Reuter, M. Scheffler, First-Principles Atomistic Thermodynamics for Oxidation Catalysis: Surface Phase Diagrams and Catalytically Interesting Regions, *Physical Review Letters* **2003,** *90* (4), 10.1103/PhysRevLett.90.046103.

[47] G. Kresse, J. Furthmüller, Efficiency of ab-initio total energy calculations for metals and semiconductors using a plane-wave basis set, *Computational Materials Science* **1996,** *6* (1), 15-50, 10.1016/0927-0256(96)00008-0.

[48] G. Kresse, J. Furthmüller, Efficient iterative schemes forab initiototal-energy calculations using a plane-wave basis set, *Physical Review B* **1996,** *54* (16), 11169-11186, 10.1103/PhysRevB.54.11169.

[49] J.P. Perdew, K. Burke, M. Ernzerhof, Generalized Gradient Approximation Made Simple, *Physical Review Letters* **1996,** *77* (18), 3865-3868, 10.1103/PhysRevLett.77.3865.

[50] J.P. Perdew, J.A. Chevary, S.H. Vosko, K.A. Jackson, M.R. Pederson, D.J. Singh, C. Fiolhais, Atoms, molecules, solids, and surfaces: Applications of the generalized gradient approximation for exchange and correlation, *Physical Review B* **1992,** *46* (11), 6671-6687, 10.1103/PhysRevB.46.6671.

[51] P.E. Blöchl, Projector augmented-wave method, *Physical Review B* **1994,** *50* (24), 17953-17979, 10.1103/PhysRevB.50.17953.

[52] G. Kresse, D. Joubert, From ultrasoft pseudopotentials to the projector augmented-wave method, *Physical Review B* **1999,** *59* (3), 1758-1775, 10.1103/PhysRevB.59.1758.

[53] B. Hammer, J.K. Nørskov, Theoretical surface science and catalysis—calculations and concepts, Impact of Surface Science on Catalysis2000, pp. 71-129.

[54] J.K. Norskov, F. Abild-Pedersen, F. Studt, T. Bligaard, Density functional theory in surface chemistry and catalysis, *Proceedings of the National Academy of Sciences* **2011,** *108* (3), 937-943, 10.1073/pnas.1006652108.

[55] K. Wakabayashi, K.-i. Sasaki, T. Nakanishi, T. Enoki, Electronic states of graphene nanoribbons and analytical solutions, *Science and Technology of Advanced Materials* **2016,** *11* (5), 10.1088/1468-6996/11/5/054504.

[56] A.H. Castro Neto, F. Guinea, N.M.R. Peres, K.S. Novoselov, A.K. Geim, The electronic properties of graphene, *Reviews of Modern Physics* **2009,** *81* (1), 109-162, 10.1103/RevModPhys.81.109.

[57] Z. Chen, Y.-M. Lin, M.J. Rooks, P. Avouris, Graphene nano-ribbon electronics, *Physica E: Low-dimensional Systems and Nanostructures* **2007,** *40* (2), 228-232, 10.1016/j.physe.2007.06.020.

[58] V. Barone, O. Hod, G.E. Scuseria, Electronic Structure and Stability of Semiconducting Graphene Nanoribbons, *Nano Letters* **2006,** *6* (12), 2748-2754, 10.1021/nl0617033.

[59] K. Nakada, M. Fujita, G. Dresselhaus, M.S. Dresselhaus, Edge state in graphene ribbons: Nanometer size effect and edge shape dependence, *Physical Review B* **1996,** *54* (24), 17954-17961, 10.1103/PhysRevB.54.17954.

[60] G.Z. Magda, X. Jin, I. Hagymási, P. Vancsó, Z. Osváth, P. Nemes-Incze, C. Hwang, L.P. Biró, L. Tapasztó, Room-temperature magnetic order on zigzag edges of narrow graphene nanoribbons, *Nature* **2014,** *514* (7524), 608-611, 10.1038/nature13831.

[61] Z. Sun, J. Wu, Open-shell polycyclic aromatic hydrocarbons, *J. Mater. Chem.* **2012,** *22* (10), 4151-4160, 10.1039/c1jm14786b.

[62] C. Lambert, Towards Polycyclic Aromatic Hydrocarbons with a Singlet Open-Shell Ground State, *Angew. Chem. Int. Ed.* **2011,** *50* (8), 1756-1758, 10.1002/anie.201006705.

[63] M. Ferbinteanu, C. Buta, A.M. Toader, F. Cimpoesu, The Spin Coupling in the Polyaromatic Hydrocarbons and Carbon-Based Materials, Carbon-related Materials in Recognition of Nobel Lectures by Prof. Akira Suzuki in ICCE2017, pp. 327-371.

[64] G. Trinquier, J.-P. Malrieu, Predicting the Open-Shell Character of Polycyclic Hydrocarbons in Terms of Clar Sextets, *J. Phys. Chem. A* **2018,** *122* (4), 1088-1103, 10.1021/acs.jpca.7b11095.

[65] M. Abe, Diradicals, *Chem. Rev.* **2013,** *113* (9), 7011-7088, 10.1021/cr400056a.

[66] V.Y. Osipov, A.I. Shames, T. Enoki, K. Takai, M. Endo, T. Hayashi, Y. Kaburagi, A.Y. Vul, Magnetic and EPR studies of edge-localized spin paramagnetism in multi-shell nanographites derived from nanodiamonds, *Diamond and Related Materials* **2009,** *18* (2-3), 220-223, 10.1016/j.diamond.2008.09.015.

[67] Z. Luo, S. Lim, Z. Tian, J. Shang, L. Lai, B. MacDonald, C. Fu, Z. Shen, T. Yu, J. Lin, Pyridinic N doped graphene: synthesis, electronic structure, and electrocatalytic property, *J Mater Chem* **2011,** *21* (22), 8038-8044, 10.1039/C1JM10845J.

[68] J. Gräfenstein, E. Kraka, M. Filatov, D. Cremer, Can Unrestricted Density-Functional Theory Describe Open Shell Singlet Biradicals?, *International Journal of Molecular Sciences* **2002,** *3* (4), 360-394, 10.3390/i3040360.

[69] A.S. Menon, L. Radom, Consequences of Spin Contamination in Unrestricted Calculations on Open-Shell Species: Effect of Hartree−Fock and Møller−Plesset Contributions in Hybrid and Double-Hybrid Density Functional Theory Approaches†, *The Journal of Physical Chemistry A* **2008,** *112* (50), 13225-13230, 10.1021/jp803064k.

[70] M. Solà, Forty years of Clar's aromatic π-sextet rule, *Front. Chem.* **2013,** *1*, 10.3389/fchem.2013.00022.

[71] Z.B. Maksić, D. Barić, T. Müller, Clar's Sextet Rule Is a Consequence of the σ-Electron Framework, *J. Phys. Chem. A* **2006,** *110* (33), 10135-10147, 10.1021/jp062917b.

[72] Y. Li, Z. Zhou, C.R. Cabrera, Z. Chen, Preserving the Edge Magnetism of Zigzag Graphene Nanoribbons by Ethylene Termination: Insight by Clar's Rule, *Sci. Rep.* **2013,** *3* (1), 10.1038/srep02030.

[73] S. Fujii, T. Enoki, Clar's Aromatic Sextet and π-Electron Distribution in Nanographene, *Angew. Chem. Int. Ed.* **2012,** *51* (29), 7236-7241, 10.1002/anie.201202560.